Utilisation de la maurocalcine dans des applications de délivrance intracellulaire de molécules ou de nanoparticules

Eloi Kamugisha Bahembera

Communauté
UNIVERSITÉ Grenoble Alpes

THÈSE

Pour obtenir le grade de

DOCTEUR DE LA COMMUNAUTÉ UNIVERSITÉ GRENOBLE ALPES

Spécialité : BIOTECHNOLOGIE

Arrêté ministériel : 7 août 2006

Présentée par

Eloi Kamugisha BAHEMBERA

Thèse dirigée par **Michel DE WAARD**

Préparée au sein du Laboratoire **Canaux Calciques Fonctions et Pathologies.**
Dans **l'École Doctorale Chimie et Sciences du Vivant.**

UTILISATION DE LA MAUROCALCINE DANS DES APPLICATIONS DE DELIVRANCE INTRACELLULAIRE DE MOLECULES OU DE NANOPARTICULES.

Thèse soutenue publiquement le 18 novembre 2015
Devant le jury composé de :

Mr Gilles FAURY,
Professeur des Universités, Université Joseph Fourier Grenoble, **Président**.
Mr Hervé DARBON,
Directeur de recherche, AFMB (UMR 7257), Marseille, **Rapporteur**.
Mr Guillaume SANDOZ,
Directeur de recherche, Université de Nice, **Rapporteur**.
Mr Peter REISS,
Directeur de recherche, CEA, Grenoble, **Examinateur.**
Mr Jean-Marc SABATIER,
Directeur de recherche, CNRS, INSERM (UMR 1097), Marseille, **Examinateur**.
Mr Michel DE WAARD,
Directeur de recherche, Grenoble Institut des Neurosciences, La Tronche, **Directeur de thèse**.

DEDICACES

Je dédie ce travail à tous les membres de ma famille large qui m'ont toujours soutenu et encouragé.

Je dédie également ce travail à tous ceux qui croient en leur capacité, s'investissent et persévèrent pour obtenir de bons résultats.

REMERCIEMENTS

Je remercie Dieu pour sa bienveillance à mon égard, particulièrement au cours de ce travail.

Je remercie les membres du jury Gilles FAURY, Hervé DARBON, Guillaume SANDOZ, Peter REISS, Jean-Marc SABATIER, et Michel DE WAARD pour avoir accepté de juger mon travail.

Je remercie le Directeur de thèse, Michel DE WAARD, d'avoir cru à mes capacités et de m'avoir accepté au sein de son équipe pour la préparation de cette thèse. Il s'est personnellement investi pour que cette thèse voie le jour et soit couronné de succès.

Merci à l'ANR pour le financement de cette thèse.

Je remercie Michel RONJAT pour son encadrement permanent et enrichissant aux côtés du Directeur de thèse.

Merci à tous les doctorants de l'équipe de Michel DE WAARD pour leur bonne collaboration.

Je remercie Christophe ARNOULT qui, au terme de mon stage de master 2 dans son équipe, s'est investi pour que j'accède à une thèse de doctorat. Je le remercie également pour ses remarques et conseils enrichissants au cours de la réunion du comité de suivi de thèse.

Mes remerciements s'adressent également à Jean-Luc LENORMAND pour ses conseils dont j'ai toujours bénéficié depuis mon stage de Master 1 réalisé dans son laboratoire, et particulièrement pour ses remarques enrichissantes dans le cadre du comité de suivi de thèse.

Je remercie Anne FELTZ et son équipe pour leur collaboration qui a significativement contribué au succès de ce travail.

Merci à Serge DIAGBOUGA et son équipe de m'avoir initié à la recherche biomédicale au Centre MURAZ au Burkina Faso, de m'avoir soutenu pour accéder aux formations des universités françaises, et de m'avoir toujours encouragé, depuis le Master 1 jusqu'à la thèse de doctorat.

Merci à toutes les autres personnes qui ont contribué de près ou de loin à l'aboutissement de ce travail.

RESUME

La Maurocalcine (MCa), excellent peptide de pénétration cellulaire (CPP, Cell Penetrating Peptide) issu du venin de scorpion, présente un grand intérêt pour des applications d'administration intracellulaire de molécules ou de nanoparticules expérimentales ou thérapeutiques. Afin de développer ces applications, le peptide a auparavant subi une série d'optimisations, dont la suppression de l'activité pharmacologique native et l'élimination des ponts disulfures intramoléculaires. Dans le présent travail, nous avons poursuivi l'optimisation du peptide par la réduction de la taille. Ensuite, nous avons développé une des applications possibles du peptide consistant en la vectorisation des nanobiodétecteurs du Ca^{2+} intracellulaire.

La taille de la MCa native (33 résidus) est plus longue que celle des CPPs usuels, telles que la Tat et la pénétratine (13 et 16 résidus, respectivement). Pour réduire la taille du peptide, nous avons procédé à la délétion de la MCa linéaire antérieurement conçue. Douze nouveaux puissants CPPs de courte taille ont été produits, dont la MCa_{UF1-9} qui s'est révélée la plus efficace de tous à de faibles concentrations. Le CPP MCa_{UF1-9} paraît donc très intéressant pour des applications utilisant de faibles concentrations. La caractérisation approfondie de la MCa_{UF1-9} a montré sa meilleure efficacité en pénétration cellulaire comparativement à la Tat, à la pénétratine, et à de petits analogues dérivés des peptides de la même famille des calcines, à l'exception de l'hadrucalcine$_{UF1-11}$ (Had_{UF1-11}) et de l'hadrucalcine$_{UF3-11}$ qui se sont révélés plus performants.

Comme l'une des applications possibles, l'analogue le plus efficace en pénétration cellulaire, l'Had_{UF1-11}, a été efficacement utilisé comme vecteur pour la délivrance intracellulaire des nanobiodétecteurs du Ca^{2+} cytosolique formés d'un quantum dot recouvert des molécules indicatrices de Ca^{2+}(CaRuby), en plus du CPP Had_{UF1-11}.

Les petits analogues de MCa (dérivés de MCa ou des autres peptides de la famille de calcine) pourraient être des CPPs de choix pour divers types d'applications de délivrance intracellulaire. Pour le confirmer (ou l'infirmer) leur caractérisation extensif est nécessaire.

Mots clés: Maurocalcine, hadrucalcine, nanoparticules, quantum dots, pénétration cellulaire, nanobiodétecteur de Ca^{2+}.

SUMMARY

The Maurocalcine (MCa), an excellent cell penetrating peptide (CPP) from the scorpion venom, presents a real interest for the development of applications for the intracellular delivery of experimental or therapeutic molecules or particles. In order for these applications to be developed, the peptide previously underwent a series of optimization processes, such as the suppression of native biological activity and the removal of intramolecular disulfide bonds. In this research, we carried on the optimization by reducing the size of the MCa and then developed one among other possible applications of this peptide which consists of the vectorization of the intracellular Ca^{2+} nanobiosensors.

The native size of MCa (33 residues) is much longer than the size of popular CPPs such as Tat and penetratin (13 and 16 residues, respectively). To reduce the size of the peptide, we truncated the previously designed linear MCa. Twelve new powerful small CPPs were produced, among which the MCa_{UF1-9} that was the best in cell penetration at low concentrations. Thus, the MCa_{UF1-9} appears very interesting for applications that require low concentrations. The MCa_{UF1-9} was further characterized and happened to be more efficient in cell penetration than the Tat, the penetratin, and other small analogous peptides derived from the peptides belonging to the same family as the MCa's, except from the $hadrucalcin_{UF1-11}$ (Had_{UF1-11}) and the $hadrucalcin_{UF3-11}$ which showed best performance.

As application, the most efficient analogous in cell penetration, the Had_{UF1-11}, was efficiently utilized as a vector for the intracellular delivery of intracellular Ca^{2+} nanobiosensors composed of a quantum dot coated with Ca^{2+} indicator (CaRuby) molecules, besides the CPP Had_{UF1-11}.

Small MCa analogous (derived from MCa or the other peptides of the calcin family) might be the choice CPPs for diverse intracellular delivery applications. In order to confirm this, their extensive characterization is necessary.

Key words: Maurocalcine, hadrucalcin, nanoparticles, quantum dots, cell penetration, Ca^{2+} nanobiosensor.

TABLE DES MATIERES

LISTE DES FIGURES

LISTE DES TABLEAUX

LISTE DES ABREVIATIONS

[Ca^{2+}]: Concentration du Ca^{2+}.

ADN: Acide Désoxyribo Nucléïque.

ARNm: Acide Ribo Nucléique messager.

BAPTA: 1,2 - bis (o-aminophenoxy) ethane-N,N,N',N'-tetraacetic acid.

BHE: Barrière Hémato-Encéphalique.

CaRuby: Calcium Ruby.

Ca_V: Canaux C^{2+} dépendants du potentiel membranaire.

ChTx: Charybdotoxine.

CICR: Ca^{2+} induced Ca^{2+} release.

ClTx: Toxines spécifiques des canaux Cl^-.

CPPs: Cell penetrating peptides.

DHPR: Dihydropyridine receptor.

FACS: Fluorescence Activated Cell Sorting.

FRET: Fluorescence Resonance Energy Transfer.

GAGs: Glycosaminoglycanes.

HA2: Hemmaglutinine A2.

IP_3: Inositol 1,4,5-triphosphate.

IP_3R: Récepteur d'IP_3.

KTx: Toxines spécifiques des canaux K^+.

LDL: Low-Density Lipoprotein.

MCa: Maurocalcine.

MCa_F: MCa repliée (folded).

MDR-1: Multi Drug Resistance-1.

NaTx: Toxines spécifiques des canaux Na^{+}.

NFkB: Nuclear Factor Kappa B.

NLS: Nuclear Localization Sequence.

NMDAR: Récepteur de la N-méthyl D-aspartate.

PAs: Protéines adaptatrices.

PEG: Polyéthylène glycol.

PGHS: Protéoglycane à héparane sulfate.

pH: Potentiel Hydrogène.

PMCA: Plasma Membrane Ca^{2+}-ATPase.

PMOs: Phosphorodiamidate morphorodiamidate morpholino oligomers.

PNA: Peptide Nucleic Acid.

QDs: Quantum Dots.

RE: Réticulum Endoplasmique.

RS: Réticulum sarcoplasmique.

RyR: Récepteur de la Ryanodine.

SERCA: Sarco/Endoplasmic Reticulum Ca^{2+} ATPase.

siRNA: short interfering Ribo Nucleic Acid.

SOC: Store-Operated Ca^{2+} Channels.

Tat: Trans-activatrice de la transcription.

TIRF: Total Internal Reflexion Fluorescence.

VP22: Viral Protein 22.

VULs: Vésicules phospholipidiques Unilamellaires Larges.

INTRODUCTION

La faible perméabilité de la membrane cytoplasmique des cellules eucaryotes aux médicaments et aux macromolécules constitue un obstacle majeur au développement de molécules ou particules thérapeutiques ou diagnostiques innovantes. Depuis ces 15 dernières années, des progrès significatifs ont été réalisés dans la conception de nouveaux outils pour l'amélioration de l'administration intracellulaire de molécules bioactives (*1-6*). L'un des outils les plus prometteurs sont des peptides de pénétration cellulaire (CPPs, cell penetrating peptides).

Les CPPs ont permis d'améliorer l'efficacité d'administration intracellulaire. Ils ont été utilisés avec succès *in vitro* et *in vivo*, pour l'administration de divers types de molécules dont l'ADN, les oligonucléotides, le siRNA (short interfering RNA), le PNA (Peptide Nucleic Acid), les protéines et peptides, ainsi que des nanoparticules liposomes (*2, 7*). Cependant, les CPPs couramment utilisés tels que la Tat (*8*), la pénétratine (*9*), la VP22 (*10*), l'Arg 8 (*11*) sont internalisés principalement par endocytose (*12*), ce qui présente des problèmes de biodisponibilité dus à leur séquestration et leur dégradation endosomales. Bien que des stratégies aient été mises au point pour remédier à ces problèmes, elles entraînent souvent une forte cytotoxicité qui limite leur usage (*13*). Plus récemment, il a été identifié un nouveau type de CPPs dont l'internalisation cellulaire se fait principalement par translocation, ce qui évite significativement la séquestration et la dégradation endosomales (*14-16*). Dans ce nouveau type de CPPs, figure la Maurocalcine (MCa), objet de nos travaux.

La MCa est un CPP particulièrement intéressant. Outre l'internalisation par la translocation, elle présente une stabilité remarquable : elle n'est pas dénaturée par de hautes températures allant même jusqu'à 100 °C ou par des conditions de pH extrêmes; sa pénétration cellulaire a lieu à de très faibles concentrations; sa toxicité est très faible (*16*). Cependant, l'utilisation de la MCa à l'état natif est limitée par son activité pharmacologique qui consiste en l'activation du canal récepteur de la ryanodine (RyR), ainsi que par sa taille relativement longue par rapport à des CPPs couramment utilisés (*8-11*) (Tableau 1). Des modifications pour supprimer l'activité pharmacologique ont été antérieurement réalisées avec succès (*16-18*). Quant à la réduction de la taille, elle a fait partie de nos travaux.

Au cours de mes travaux de thèse, j'ai contribué d'une part, à l'étude des propriétés de pénétration cellulaire des peptides analogues de la MCa de tailles réduites, et d'autre part, au

développement de l'une de leurs applications possibles consistant en la vectorisation d'un nanobiodétecteur du Ca^{2+} intracellulaire.

Les résultats de ces travaux sont présentés dans cet ouvrage. Afin de faciliter leur compréhension, ils sont précédés de notions sur les voies d'entrée de macromolécules et de particules dans les cellules, sur les CPPs, sur les toxines du venin de scorpion, et sur l'homéostasie calcique cytosolique.

1. GENERALITES

1.1. Voies d'entrée de macromolécules ou particules dans la cellule

Les macromolécules ou particules entrent dans la cellule par l'endocytose ou par la translocation. La voie empruntée dépend non seulement des caractéristiques de la macromolécule ou la particule, mais également d'autres facteurs, notamment la membrane cytoplasmique et la matrice extracellulaire.

1.1.1. Membrane cytoplasmique et matrice extracellulaire

Avant d'entrer dans la cellule, la macromolécule ou particule interagit avec la membrane cytoplasmique et la matrice extracellulaire.

La membrane cytoplasmique est formée d'une bicouche phospholipidique (*19*) dans ou sur laquelle sont insérées ou fixées des molécules lipidiques ou protéiques.
La bicouche phospholipidique forme une barrière stable entre deux compartiments aqueux, extra et intracellulaires. Elle est hydrophile à ses faces extracellulaire et cytosolique, et hydrophobe à ses faces intramembranaires (Figure 1). La couche phospholipidique externe est principalement composée de phosphatidylcholine et de sphingomyéline qui sont neutres. Quant à la couche phospholipidique interne, elle est principalement composée de phosphatidyléthanolamine qui est également neutre, phosphatidylsérine et phosphatidylinositol qui tous les deux sont chargés négativement. En plus des phospholipides, on trouve également le cholestérol distribué dans les deux couches, et des glycolipides insérés dans la couche externe (*20*).

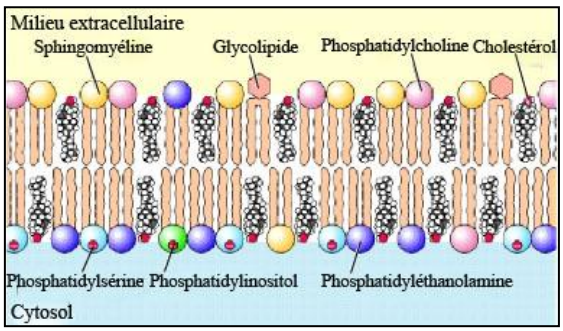

Figure 1: Schéma de la bicouche lipidique de la membrane cytoplasmique (*20*) (Modifiée).

Les molécules protéiques sont principalement des protéines, des glycoprotéines, et des protéoglycanes (Figure 2). Elles exercent des fonctions spécifiques de la membrane cytoplasmique telles que le transport sélectif de molécules, la détection et la transduction des signaux, la reconnaissance intercellulaire. Les glycoprotéines sont des protéines associées par liaison covalente à une courte chaîne glucidique, tandis que des protéoglycanes sont des protéines associées par liaison covalente à des glycosaminoglycanes (GAGs). Les GAGs eux-mêmes sont des polymères linéaires sulfatés (sauf l'acide hyaluronique) composés d'une répétition d'un disaccharide de base constitué d'un hexosamine (glucosamine ou galactosamine) et d'un autre ose (acide glucuronique, acide iduronique, galactose) (Figure 3). Les GAGs possèdent plusieurs charges négatives issues de leurs composants acides uroniques (qui donnent le groupement $-COO^-$) et sulfate ($-SO_3^-$). On distingue différentes familles de GAGs : l'acide hyaluronique, la chondroïtine sulfate/dermatane sulfate (globalement la même famille), l'héparine/héparane sulfate, et le kératane sulfate. L'héparane sulfate est le GAG le plus abondant dans la membrane cytoplasmique où il est l'un des composants de différents protéoglycanes membranaires. Les protéoglycanes à héparane sulfate (PGHS) jouent un rôle important dans la régulation des microdomaines de la surface cellulaire (*21*). Par ailleurs, les PGHS font partie des composants majoritaires de la matrice extracellulaire.

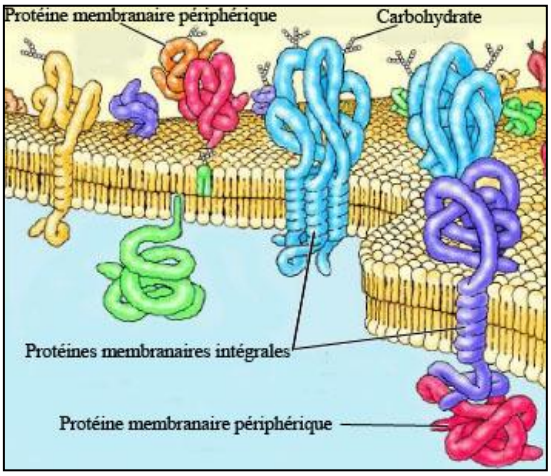

Figure 2: Schéma de la membrane cytoplasmique avec ses composants protéiques (*20*) (Modifiée).

La matrice extracellulaire est l'ensemble de macromolécules extracellulaires des tissus (tissu conjonctif, tissu épithélial, tissu musculaire, tissus nerveux). Ses principaux composants sont des protéines telle que l'élastine, des glycoprotéines telles que le collagène et la fibronectine, et des GAGs / protéoglycanes (*22*). Les GAGs / protéoglycanes sont les plus abondants et forment un gel hydraté où baignent les cellules (*23*).

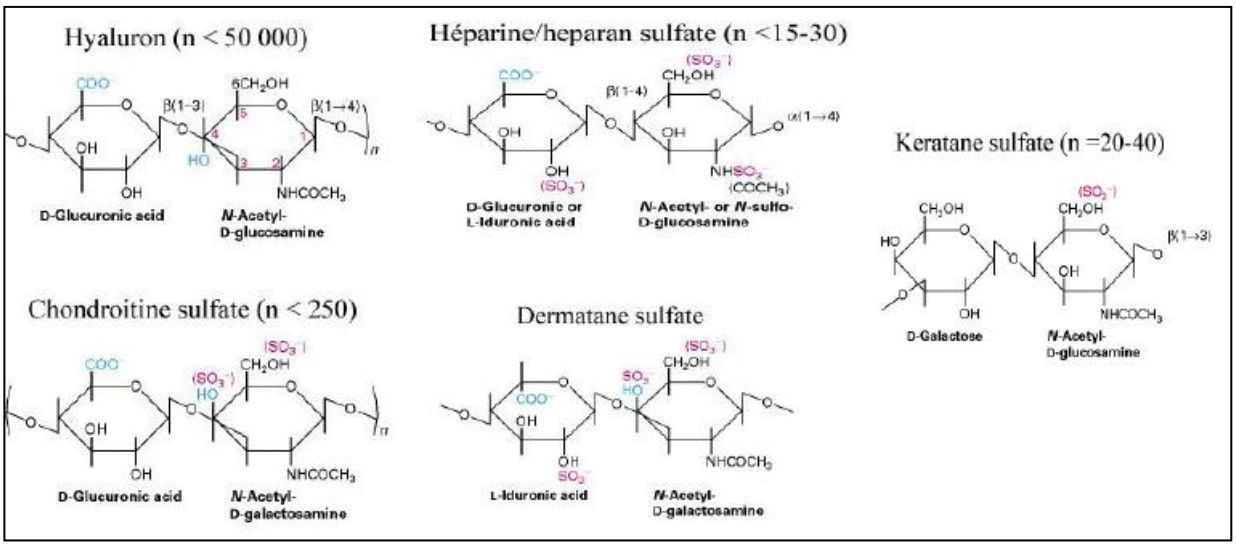

Figure 3: Familles de glycosaminoglycanes (*24*).
n : nombre d'unités disaccharidiques.

1.1.2. Endocytose

L'endocytose est un processus fondamental dans les cellules eucaryotes. Il joue un rôle clé dans plusieurs domaines de la biologie cellulaire, allant de la nutrition cellulaire à la régulation de la signalisation intercellulaire. L'endocytose consiste en l'internalisation par la cellule des composants de la membrane cytoplasmique (protéines, lipides…), des ligands, des nutriments, et des fluides, dans une vésicule issue de la membrane cytoplasmique. Arrivée à l'intérieur de la cellule, la vésicule fusionne avec un endosome; le résultat s'appelle toujours l'endosome. Les endosomes peuvent avoir différentes destinations : la réintégration dans la membrane cytoplasmique par exocytose (recyclage), l'évolution en endosomes tardifs et fusion avec des lysosomes pour la digestion des molécules internalisées, ou la migration vers d'autres compartiments cellulaires tels que l'appareil de Golgi. Il existe différents types d'endocytose selon la morphologie et la composition des structures naissantes de la membrane cytoplasmique au cours de la formation des vésicules endocytiques. Selon les connaissances actuelles, l'endocytose peut être subdivisé en quatre grands types : l'endocytose dépendante de la clathrine (EDC), l'endocytose par cavéoles/rafts, la macropinocytose, et la phagocytose.

1.1.2.1. Endocytose dépendante de la clathrine

L'EDC joue un rôle clé dans la nutrition et la signalisation cellulaire. Elle est caractérisée par le rôle central joué par la clathrine. Cependant, diverses autres protéines accessoires telles que les protéines adaptatrices (PAs) et la dynamine sont également impliquées (*25*).

Au cours de l'EDC les vésicules endocytiques se forment à partir des invaginations de la membrane cytoplasmique recouvertes de la clathrine. Sous une certaine stimulation, la face intracellulaire de la membrane cytoplasmique se couvre de la clathrine, entraînant la formation des invaginations. Les protéines de cette membrane cytoplasmique invaginée et recouverte de la clathrine sont alors sélectivement triées par des PAs cytosoliques (*26*). Sous l'action de la dynamine, une protéine cytosolique à activité GTPasique, la vésicule endocytique est formée et libérée dans le cytoplasme (*27-29*). Immédiatement après la libération de la vésicule endocytique dans le cytoplasme, le manteau composé de la clathrine et des PAs est relâché, avant la fusion de la vésicule avec l'endosome précoce.

La voie de l'EDC intervient non seulement dans la nutrition cellulaire mais aussi dans la signalisation cellulaire. L'EDC facilite l'ingestion par la cellule des nutriments tels que le fer transporté par la transferrine, et le cholestérol transporté par la LDL. Par ailleurs, elle intervient dans la transduction de signaux par l'internalisation de la plupart des récepteurs membranaires après la fixation du ligand.

1.1.2.2. Endocytose par les cavéoles /rafts

La membrane cytoplasmique comporte des domaines insolubles dans les détergents (résistants aux détergents) et riches en cholestérol appelés rafts (radeaux lipidiques). Les rafts sont le siège de phénomènes d'endocytose se développant sans l'intervention de la clathrine, mais avec celle de la dynamine. Diverses structures endocytiques sont observées, dont des cavéoles et des structures tubulaires. Les cavéoles sont de petites invaginations (50-100 nm) de la membrane cytoplasmique, régulières, avec une morphologie caractéristique bien définie en forme de flacon (*30*), riche en cavéoline 1 (*31*). En effet, sous des conditions normales, non stimulantes, les cavéoles n'interviennent pas significativement dans l'endocytose; elles restent stables (attachées) à la membrane cytoplasmique (*32-37*) grâce, principalement, à la cavéoline 1 (*37-39*). L'endocytose par les cavéoles est déclenchée par une stimulation, par exemple suite à la fixation d'un ligand par un récepteur membranaire. Il s'agit d'un processus régulé nécessitant des kinases de la famille Src, la dynamine, et une polymérisation locale de l'actine (*32, 40, 41*).

Des structures endocytiques sans cavéoline sont également observées au niveau des rafts. On distingue des structures morphologiquement similaires aux cavéoles (*42*) et des structures morphologiquement différentes des cavéoles (*36, 43*). Des structures morphologiquement similaires aux cavéoles comportent des protéines flotilline-1 et 2 qui, co-exprimées ensemble, sont responsables de la morphologie cavéolaire (*44, 45*). Des structures morphologiquement différentes des cavéoles sont par exemple celles de formes tubulaires impliquées dans l'internalisation des glycosphingolipides (*36, 43*).

1.1.2.3. Macropinocytose

La macropinocytose est une endocytose spécialisée, strictement dépendante de l'actine corticale (*46*). Elle consiste en l'internalisation par la cellule d'un grand volume de fluide extracellulaire dans de larges vésicules membranaires (pouvant atteindre 5µm de diamètre) formées suite au développement de prolongements de la membrane cytoplasmique (*46*) (Figure 4).

1.1.2.4. Phagocytose

Comme la macropinocytose, la phagocytose est aussi une endocytose spécialisée, strictement dépendante de l'actine corticale. Elle est réalisée par des cellules spécialisées (monocytes/macrophages, polynucléaires neutrophiles, cellules dendritiques…), et consiste en l'internalisation de larges particules telles que les bactéries.

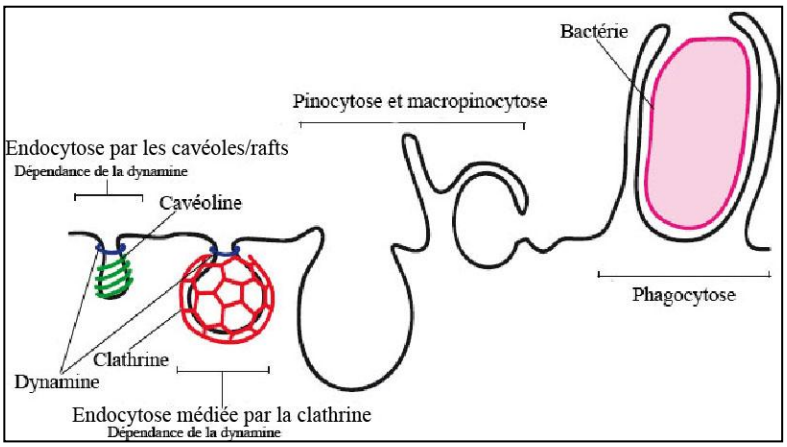

Figure 4: Différents types d'endocytose.
Quatre principaux types d'endocytose sont montrés (ceci pourrait être une simplification) : d'une part, l'endocytose par les cavéoles/rafts et l'endocytose médiée par la clathrine qui nécessitent la GTPase dynamine 1, et d'autre part, la pinocytose/macropinocytose et la phagocytose qui ne nécessitent pas la dynamine 1 (*47*) (Modifié).

Dans le processus de la phagocytose, la cellule phagocytaire est attirée vers la particule cible (bactérie, virus…) principalement par chimiotactisme. Arrivée au niveau de la particule, la cellule émet des prolongements de la membrane cytoplasmique, qui englobent la particule et forment une vésicule endocytique (Figure 4).

1.1.3. Translocation

La translocation est un processus d'internalisation non endocytique de macromolécules, de façon indépendante de l'énergie (*48*). Pour les peptides, la translocation se fait par divers mécanismes; les plus connus sont les mécanismes de carpet, de barrel-stave, et de micelle inversée (*49-51*).

1.1.3.1. Mécanisme de carpet

Le mécanisme de carpet (tapis) est ainsi appelé car le processus de translocation est initié par la couverture de la membrane cytoplasmique par les peptides à la manière d'un tapis (Figure 5). Le mécanisme comprend quatre étapes successives : 1) Etablissement de liaisons électrostatiques entre les peptides et les têtes des phospholipides, 2) Alignement des monomères des peptides sur la surface de la membrane de façon que leur face hydrophile soit en contact avec les têtes des phospholipides, 3) Rotation des molécules (peptides et phospholipides) conduisant à la réorientation des résidus hydrophobes des peptides vers le cœur hydrophobe de la membrane, et 4) Désintégration de la membrane du fait de la perturbation de la courbure de la bicouche (Figure 5). Contrairement au mécanisme de barrel-stave, dans le mécanisme de carpet, les peptides sont en contact avec la membrane sur toute leur longueur et ne sont pas insérés dans le cœur de la membrane. Pour agir selon le mécanisme de carpet, les peptides doivent comporter des acides aminés chargés positivement tout le long de la chaîne peptidique et avoir une charge nette fortement positive (*49, 52*).

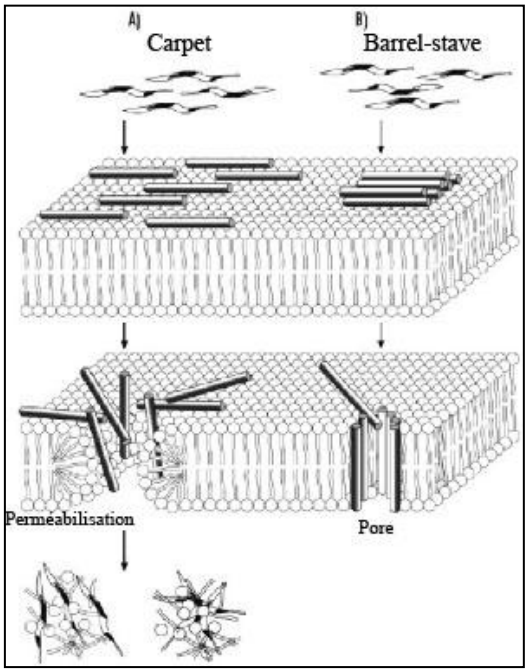

Figure 5: Translocation des peptides par les mécanismes de carpet et de barrel-stave.
(A) Le mécanisme de carpet : Les peptides couvrent la membrane cytoplsmique grâce aux interactions électrostatiques entre les parties du peptide chargées positivement et les têtes des phospholipides membranaires. Ensuite, le complexe peptides-phospholipides effectue une rotation en dirigeant les résidus hydrophobes des peptides vers le cœur de la bicouche phospholipidique. Ceci provoque une perturbation de la membrane aboutissant à sa perméabilisation, ce qui permet le passage des peptides vers le cytosol.
(B) Le mécanisme de barrel-stave (formation de pore). Les peptides s'accumulent sur la membrane cytoplasmique par leurs hélices amphipathiques. Ensuite, la partie hydrophobe des hélices amphipathiques s'insère à l'intérieur de la bicouche membranaire, conduisant à la formation d'un pore. Les peptides passent à travers le pore et arrivent dans le cytosol (*53*) (Modifiée).

1.1.3.2. <u>Mécanisme de barrel-stave</u>

Selon le modèle de barrel-stave, la translocation des peptides se fait au moyen des canaux formés par des peptides à travers la bicouche phospholipidique. Les peptides se positionnent en cylindre autour d'un pore aqueux (Figure 5). Les surfaces hydrophobes des hélices α ou des feuillets β forment la face extérieure du canal en contact avec les chaînes acyles des phospholipides membranaires, alors que les surfaces hydrophiles forment la face intérieure du canal, donc le « revêtement » du pore (*49, 52, 54, 55*). La première étape de la formation des pores de barrel-stave est la liaison des peptides à la surface membranaire, le plus souvent sous forme monomérique. Au moment de la liaison, les peptides peuvent entrer dans une phase de transition conformationnelle, forçant les têtes polaires des phospholipides à induire un amincissement localisé de la membrane. Cet amincissement permet l'insertion de

la partie hydrophobe des peptides dans la membrane. Quand les peptides liés atteignent une concentration suffisante, les peptides monomériques s'auto-assemblent et s'insèrent dans le noyau hydrophobe de la membrane aboutissant à la formation d'un canal peptidique. Les peptides sont alors transportés à travers le canal par gradient de concentration des peptides liés à la surface (*49*).

1.1.3.3. Mécanisme de micelle inversée

Dans le mécanisme de micelle inversée, le peptide est englobé par la bicouche phospholipidique de la membrane cytoplasmique avant d'être libéré dans le cytoplasme (Figure 6).

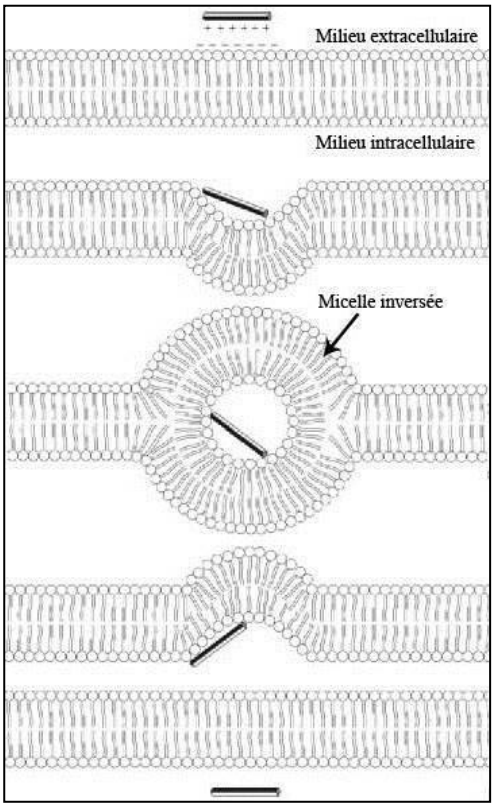

Figure 6: Translocation des peptides par le mécanisme de micelle inversée.

La partie du peptide chargée positivement interagit avec les phospholipides de la membrane, ensuite la partie hydrophobe du peptide interagit avec la membrane, ce qui crée une micelle inversée aboutissant à l'internalisation du peptide (*53*) (Modifiée).

Les peptides se fixent à la membrane cytoplasmique par les interactions électrostatiques établies entre les acides aminés basiques (chargés positivement) et les têtes des

phospholipides membranaires. Ensuite, les interactions entre les acides aminés hydrophobes des peptides et la membrane entraînent une réorganisation de la membrane conduisant à la translocation du peptide vers le cytoplasme par l'intermédiaire d'une micelle inversée (*51*).

1.2. Peptides de pénétration cellulaire (CPPs)

La membrane cytoplasmique constitue une barrière naturelle qui ne laisse passer que des molécules apolaires de moins de 500 daltons (*56*). Ceci a été un obstacle majeur au développement de stratégies thérapeutiques ou diagnostiques à action intracellulaire, car la plupart de molécules ou particules prometteuses ne peuvent pas traverser la bicouche lipidique. La découverte des CPPs, peptides spéciaux dotés d'une capacité de franchir la membrane cytoplasmique, a rendu possible le développement de stratégies de vectorisation permettant l'administration intracellulaire de divers types de molécules ou de particules.

1.2.1. Historique des CPPs

La notion de CPP a été proposée suite à des observations selon lesquelles certaines protéines, principalement des facteurs de transcription, pouvaient faire des navettes à l'intérieur de la cellule et d'une cellule à l'autre.

Historiquement, la première observation a été faite en 1988 par Frankel et Pabo, qui ont montré que la protéine Tat du VIH-1 pouvait entrer dans les cellules et migrer jusqu'à l'intérieur du noyau (*57*). En 1991, le groupe de Prochiantz a montré que l'homéodomaine de la protéine antennapedia de la drosophile pouvait être internalisé par des cellules neuronales (*58*). Cette observation a été à l'origine de la découverte, en 1994, du premier CPP appelé pénétratine, peptide de 16 résidus d'acides aminés (Tableau 1) dérivé du troisième hélice de l'homéodomaine d'antennapedia (*9*). En 1998, le groupe de Lebleu a identifié la séquence peptidique minimale de Tat nécessaire pour l'internalisation cellulaire (*59*). Ces premiers CPPs naturels ont inspiré la conception de CPPs artificiels pour des applications de vectorisation de molécules.

Tableau 1: Maurocalcine et les principaux CPPs décrits dans la littérature.

CPP	Nombre d'acides aminés	Charge électrique nette	Séquence d'acides aminés
Maurocalcine (*60, 61*)	33	+7	GDCLPHLKLCKENKDCCSKKCKR RGTNIEKRCR
Tat_{48-60} (*59, 62*)	13	+8	GRKKRRQRRRPPQ
Pénétratine (*9, 51*)	16	+7	RQIKIWFQNRRMKWKK
Transportan (*48, 63, 64*)	27	+4	GWTLNSAGYLLGKINLKALAALA KKIL
Pep-1(*65, 66*)	21	+3	KETWWETWWTEWSQPKKKRKV
MPG (*67, 68*)	27	+5	GALFLGFLGAAGSTMGAWSQPKK KRKV
Arg_9 (*69, 70*)	9	+9	RRRRRRRRR

- Les résidus acides (chargés négativement), c'est-à-dire l'acide aspartique (D) et l'acide glutamique (E), sont représentés en bleu.
- Les résidus basiques (chargés positivement), c'est-à-dire la lysine (K) et l'arginine (R), sont représentés en rouge.

Le groupe de Heitz et Divita a conçu, en 1997 le premier CPP non-covalent, le MPG, pour l'administration des acides nucléiques (*67*), et en 2001 un autre CPP non-covalent, le Pep-1, pour l'administration des protéines et des peptides (*65*). Les groupes de Wender et de Futaki ont démontré que des séquences peptidiques composées d'arginine (polyarginines) étaient suffisantes pour l'administration de molécules dans les cellules et ont proposé que les mécanismes de leur internalisation impliquaient des interactions de type liaison hydrogène entre le groupe guanidinium des résidus arginines et le groupe phosphate des phospholipides membranaires (*70, 71*).

Un intérêt majeur pour les CPPs est venu des premières preuves de concept de leur application *in vivo* par les groupes de Dowdy et de Langel. Le groupe de Dowdy a démontré la capacité des CPPs à faire pénétrer de petits peptides ou de larges protéines dans la cellule (*72*). Quant au groupe de Langel, il a réussi l'administration intracellulaire des PNAs grâce au CPP Transportan (*48*). Dès lors, beaucoup d'autres CPPs ont été conçus (*2, 7, 73, 74*) et quelques autres isolés des organismes naturels dont la maurocalcine (ci-dessous) issue du venin de scorpion (*60*).

1.2.2. Classification des CPPs

Les CPPs peuvent être classés en différents groupes en fonction de leurs propriétés individuelles ou en fonction de leur structure et leur mode d'interaction avec la membrane cytoplasmique.

1.2.2.1. Classification des CPPs en fonction de leur origine

Selon leur origine, les CPPs peuvent être classés en trois groupes : les CPPs dérivés des protéines, les CPPs chimériques, et les CPPs synthétiques.

Les CPPs issus des protéines résultent de la troncation des protéines naturellement dotées de la propriété de pénétration cellulaire. Il s'agit par exemple du CPP Tat issu de la troncation de la protéine Tat du VIH-1(*8*), et de la pénétratine issue de la protéine antennapedia de la drosophile (*9*).

Les CPPs chimériques sont constitués de deux ou plusieurs motifs provenant de peptides différents. C'est le cas du transportan et de sa version plus courte (TP10) dérivés de la mastoparane et de la galanine (*48, 63*).

Les CPPs synthétiques sont des CPPs artificiels, conçus selon les propriétés observées chez des CPPs naturels. On peut citer par exemple des CPPs constitués d'acides aminés basiques tels que les polyarginines (*70, 71*).

1.2.2.2. Classification des CPPs en fonction de la structure et du mode d'interaction avec la membrane cytoplasmique

Le mode d'interaction des CPPs et la membrane cytoplasmique dépend, entre autres facteurs, du caractère amphipathique des CPPs (*75*). Le caractère amphipathique résulte de la structure du peptide. Selon la structure à l'origine du caractère amphipathique, les CPPs peuvent être classés en trois principaux groupes : des CPPs amphipathiques primaires, des CPPs amphipathiques secondaires, et des CPPs non amphipathiques (*75*).

Des CPPs amphipathiques primaires sont typiquement composés de plus de 20 acides aminés, et comportent séquentiellement des résidus hydrophiles et des résidus hydrophobes

tout au long de leur structure primaire (*75*). Il s'agit des CPPs tels que le transportan (*48*) et son dérivé TP10 (*76*).

Les CPPs amphipathiques secondaires manifestent le caractère amphipathique par des structures secondaires, hélices α ou feuillets β, formées au cours de leurs interactions avec les phospholipides membranaires. Ils comportent le plus souvent moins d'acides aminés que les CPPs amphipathiques primaires. Ce sont par exemple des CPPs tels que la pénétratine (*9*), la pVEC (*77*), et la M918 (*78*).

Les CPPs non amphipathiques sont courts et comportent une forte proportion d'acides aminés basiques (cationiques). On peut citer par exemple la Tat_{48-60} (*8, 59*) et la polyarginine R_9 (*70*).

1.2.3. Méthodes d'étude des CPPs

Différentes méthodes sont utilisées pour suivre les CPPs et leurs cargaisons à l'intérieur de la cellule et déterminer leurs mécanismes d'internalisation cellulaire. Il n'y a pas de méthodes spécifiques pouvant répondre complètement à toutes ces questions. Ainsi, différentes méthodes sont combinées. On distingue des méthodes biologiques utilisant des cultures cellulaires et des méthodes biophysiques.

1.2.3.1. Méthodes biologiques utilisant des cultures cellulaires

Les cultures cellulaires sont utilisées pour évaluer l'efficacité de pénétration cellulaire des CPPs et pour déterminer leurs mécanismes d'internalisation. La méthode la plus courante est d'incuber les cellules avec les CPPs couplés à un fluorochrome et de mesurer la fluorescence des cellules.

a. Méthode d'évaluation de l'efficacité de pénétration cellulaire

L'efficacité de pénétration cellulaire des CPPs est évaluée à l'aide des méthodes qualitatives et des méthodes quantitatives, notamment la microscopie de fluorescence/confocale et le FACS (Fluorescence Activated Cell Sorting), respectivement. L'efficacité de pénétration cellulaire est généralement testée par l'incubation des CPPs (couplés à leur cargaison) avec des cellules de mammifères en culture, suivie d'une analyse par microscopie de fluorescence/confocale ou par FACS.

Analyses par microscopie confocale. L'imagerie par microscopie confocale réalisée sur des cellules vivantes non fixées, permet de suivre la localisation intracellulaire des CPPs-cargaison. En utilisant cette méthode, il est possible de distinguer les peptides fixés à la face externe de la membrane cytoplasmique des peptides internalisés par la cellule. Une évaluation correcte de la distribution intracellulaire des CPPs nécessite l'utilisation des cellules vivantes non fixées. En effet, il a été montré que les analyses faites sur des cellules fixées, même dans des conditions douces, conduisent à une redistribution artificielle des CPPs internalisés (*12, 79, 80*). Ceci soulève des doutes sur les conclusions des premières études sur la distribution intracellulaire des CPPs dont la plupart ont été réalisées sur des cellules fixées.

La limitation principale de la microscopie confocale est d'ordre statistique, car avec cette technique il est difficile d'analyser plusieurs cellules.

Analyse par FACS. Le FACS (cytométrie en flux) est utilisé pour une analyse quantitative de l'internalisation des CPPs. L'analyse est basée sur la détection de la fluorescence émise par la cellule grâce aux CPPs marqués par des fluorochromes. Le FACS ne permet pas une discrimination des CPPs internalisés et ceux fixés à la face externe de la membrane cytoplasmique. Ceci présente le risque de surestimation de l'internalisation des CPPs. En effet, les CPPs se fixent fortement sur la membrane cellulaire et restent associés aux cellules même après plusieurs lavages. Pour prendre en compte uniquement des CPPs internalisés, des stratégies permettant l'élimination des CPPs fixés à la face externe de la membrane cytoplasmique (*12*) ou l'inhibition de la fluorescence de ces CPPs externes (*81, 82*) ont été mises en place. La stratégie la plus courante est le traitement des cellules par la trypsine (*12*). Ce traitement enzymatique permet une élimination par digestion des CPPs fixés à la face externe de la membrane cytoplasmique, si ces CPPs contiennent des sites de protéolyse trypsique.

b. Méthodes d'étude des mécanismes moléculaires d'internalisation

Il existe plusieurs méthodes expérimentales pour l'investigation des mécanismes d'internalisation des CPPs. Les méthodes les plus utilisées mettent en évidence l'implication de l'endocytose.

L'implication de l'endocytose est couramment mise en évidence par l'inhibition d'une ou plusieurs voies d'endocytose. La méthode la plus utilisée est l'incubation des cellules avec des CPPs à 4°C ce qui permet l'inhibition de toutes les voies d'endocytose dépendantes d'énergies. La spécification des types d'endocytose impliqués est réalisée par l'incubation des cellules avec des inhibiteurs spécifiques. On utilise par exemple l'amiloride qui inhibe la macropinocytose (*13*, *83*), la cytochalasine D qui inhibe la macropinocytose et l'endocytose dépendante de clathrine en stoppant l'élongation de la F-actine nécessaire pour ces types d'endocytose, le méthyl-β-cyclodextrine qui inhibe la voie dépendante des radeaux lipidiques (lipid rafts) par déplétion du cholestérol membranaire, et le nocodazole qui empêche la formation des microtubules (*84*). Cependant ces inhibiteurs pourraient ne pas être totalement spécifiques.

L'internalisation par endocytose est également mise en évidence par des méthodes de colocalisation des complexes CPP-cargaison avec les endosomes. Ces méthodes utilisent des marqueurs d'endosomes tel que la transferrine ou FM 4-64 (*12*), ou de lysosomes tel que le lysotracker red (*85*, *86*).

1.2.3.2. Méthodes biophysiques

Les études des interactions entre les CPPs et des membranes contribuent à l'élucidation des mécanismes de translocation des CPPs (*87*). Ces études sont réalisées par des systèmes membranaires modèles et des techniques biophysiques. Les membranes modèles les plus couramment utilisées sont des vésicules phospholipidiques unilamellaires larges (VULs). Les analyses biophysiques de la fuite des VULs indiquent le degré de perturbation de la membrane causée par différents CPPs. Les résultats sont habituellement associés à une pénétration cellulaire directe ou à un échappement endosomal des CPPs.

1.2.4. Mécanisme d'internalisation des CPPs

Le mécanisme d'internalisation des CPPs dans le cytoplasme constitue la principale question pour le développement des applications thérapeutiques *in vivo*. Même si ce mécanisme reste sujet de discussions, il y a un consensus que les CPPs entrent d'abord en contact avec la surface cellulaire à travers des interactions électrostatiques avec des protéoglycanes, avant d'emprunter diverses voies d'internalisation.

1.2.4.1. Interactions des CPPs et les protéoglycanes de la surface cellulaire

Le premier contact entre les CPPs et la cellule se fait par des interactions électrostatiques avec des protéoglycanes de la surface cellulaire (*88*). Ces interactions s'établissent entre les charges positives portées par les résidus basiques des CPPs et les charges négatives portées par les GAGs. Néanmoins, en plus de la charge, des facteurs structuraux interviendraient, car il a été montré que les CPPs contenant l'arginine ont une meilleure affinité vis-à-vis des GAGs que ceux contenant la lysine, alors que les deux résidus ont la même charge positive (*89*). Après la première étape de contact entre les CPPs et la membrane, une réorganisation des lipides a lieu pour permettre l'internalisation des peptides.

1.2.4.2. Voies d'internalisation

Les voies d'internalisation des CPPs dans le cytoplasme sont encore sujet à discussions. Cependant, il semble y avoir un consensus que deux voies coexistent : une ou plusieurs formes d'endocytose et la translocation membranaire directe (*90*).

L'endocytose semble être le principal mode d'internalisation de la majorité des CPPs connus à ce jour (*12, 13, 56, 80, 91-93*). L'endocytose entraîne une accumulation cytoplasmique lente et limitée des CPPs. Bien que la macropinocytose ait été rapportée comme étant la voie majeure d'internalisation des CPPs cationiques (*13, 83*), l'internalisation des CPPs par d'autres voies d'endocytose dont l'endocytose dépendante de la clathrine ou des cavéoles/rafts ont été décrites (*93, 94*).

La coexistence de la translocation directe à travers la bicouche lipidique, est suggérée par plusieurs études qui montrent l'intervention d'un mécanisme non endocytique impliquant

le potentiel transmembranaire, qui permet un accès rapide des CPPs au cytoplasme (*73, 95-99*). Ce mécanisme est spécialement observé avec des peptides amphipathiques, qui ont tendance à interagir avec les lipides et, une fois dans la membrane, adoptent une structure secondaire qui modifie l'intégrité de la membrane (*100*).

Le niveau de contribution de chaque mode (translocation versus endocytose) dépend des conditions expérimentales, notamment la nature du CPP et sa concentration, la cargaison, le type cellulaire, et la température entre autres (*95, 96, 101*).

1.2.5. Devenir des CPPs au sein de la cellule

La distribution intracellulaire des CPPs et leur sort varient selon leur mode d'entrée. Si l'internalisation se fait par la translocation directe, le peptide s'accumule dans le cytoplasme et atteint le noyau (*102, 103*). Par ailleurs, si l'endocytose est la principale voie d'internalisation, la majorité des peptides sont transportés jusque dans les endosomes tardifs et lysosomes où ils sont dégradés (*102, 103*). Cependant, une petite fraction des CPPs peut s'échapper des endosomes, par leur propriété de briser l'endosome ou du fait de la faible intégrité des endosomes (*21*). En plus, plusieurs études rapportent que les CPPs peuvent emprunter une « voie rétrograde » à travers le réticulum endoplasmique (RE) et le réseau de Golgi, et être libérés dans le cytosol (*92*). Les CPPs comportant les motifs NLS (Nuclear Localization Sequence) fonctionnels peuvent également entrer directement dans le noyau (*104, 105*).

1.2.6. Modes de conjugaison de CPP et cargaison

Au regard du mode de conjugaison avec la cargaison, les CPPs peuvent être subdivisés en deux principales classes : les CPPs qui exigent une liaison covalente avec la cargaison et ceux qui forment des complexes stables non covalents.

1.2.6.1. Conjugaison par liaison covalente

La conjugaison par liaison covalente consiste en la formation d'une liaison covalente entre la cargaison et le peptide porteur. Elle est réalisée par des réactions chimiques ou par clonage génique suivi d'une expression d'une protéine de fusion comportant le CPP (*106-*

109). Différentes approches chimiques basées principalement sur des liaisons disulfures ou thio-esters, ont été proposées pour la conjugaison stable ou clivable. Pour garantir la stabilité et l'efficacité de la cargaison, plusieurs paramètres sont pris en considération, notamment le type de réaction chimique utilisée pour la liaison et la nature de l'espaceur (*107, 109*). Les stratégies covalentes sont principalement utilisées pour la vectorisation des peptides/protéines (*74*), ou des analogues d'ADN/oligonucléotides dont les PNAs (*110*) et les PMOs (*111, 112*). La stratégie de conjugaison par liaison covalente a plusieurs avantages pour des applications *in vivo,* notamment la reproductibilité de la procédure et le contrôle de la stœchiométrie du complexe CPP-cargaison. Cependant, cette stratégie est limitée du point de vue chimique, et risque d'altérer l'activité biologique de la cargaison. Une baisse de l'activité biologique a été particulièrement observée avec des oligonucléotides chargés ou des siRNA conjugués avec des CPPs par liaison covalente (*113*). Ainsi, pour ces types de molécules, les stratégies non covalentes semblent plus appropriées.

1.2.6.2. Conjugaison non covalente

La conjugaison non covalente est principalement utilisée avec des CPPs amphipathiques, c'est à dire des CPPs qui comportent un domaine hydrophile (polaire) et un domaine hydrophobe (non polaire) (*73*). Plusieurs CPPs capables de former des complexes non covalents avec des biomolécules et d'améliorer leur administration dans des cellules mammifères ont été rapportés (*114*). Des approches non covalentes ont été originellement développées pour l'administration de gènes. Plusieurs peptides capables de condenser l'ADN associé à des peptides qui favorisent l'échappement des endosomes ont été décrits (*115, 116*).

1.2.7. Application des CPPs

Le nombre d'applications des CPPs est en augmentation. Plus de 300 études sur des stratégies à base des CPPs ont été rapportées (*90, 117-119*). Ces stratégies ont été utilisées pour l'administration des cargaisons de nature et de taille diverses : des acides nucléiques, des peptides, des protéines, des nanoparticules...

1.2.7.1. Administration de gènes

L'un des obstacles majeurs du développement des stratégies thérapeutiques ou diagnostiques géniques est la difficulté pour l'ADN et d'autres acides nucléiques de traverser les membranes cellulaires pour atteindre leur cible intracellulaire. La vectorisation des acides nucléiques par des CPPs est l'une des approches utilisées pour surmonter cet obstacle.

Pour permettre l'administration intracellulaire des gènes, des CPPs ont été utilisés seuls ou combinés à d'autres méthodes de transfection. L'association des CPPs Tat, Transportan, ou polyarginines à des méthodes de transfection à base de lipides (par exemple des liposomes), de polyéthylèneimine, ou de nanostructures a permis l'amélioration de l'administration intracellulaire des gènes (*120-124*). D'autres CPPs combinant des propriétés de fixation d'ADN et de pénétration membranaire ont été également développés (*114*).

Le premier obstacle souvent rencontré par le complexe CPP-cargaison après son internalisation, est la difficulté de s'échapper de l'endosome. Pour favoriser l'échappement de l'ADN de l'endosome, différentes stratégies ont été exploitées. Des peptides amphipathiques dotés d'activités fusogénique et endosomolytique dépendantes du pH tels que le peptide de fusion de la sous-unité HA2 de l'hémagglutinine d'influenza ou des peptides riches en histidine, ont été associés à des CPPs et ont montré la capacité d'augmenter l'efficacité de transfection (pour la revue: (*114*)). Des peptides capables de condenser l'ADN et de favoriser l'échappement endosomal tel que le PPTG1 (*125*) ou de prévenir l'internalisation endosomale tel que le MPG (*126*) ont été également utilisés pour l'administration de gènes en cultures cellulaires. Cependant, seulement peu de CPPs ont été validés *in vivo* pour l'administration de gènes. A ce jour, le peptide amphipathique secondaire PPTG1, est le seul exemple rapportant une réponse significative d'expression de gènes *in vivo* après une injection intraveineuse (*125*).

Le second obstacle majeur des systèmes non viraux d'administration de gènes, est leur faible translocation nucléaire; la translocation nucléaire est pourtant nécessaire pour la transfection des cellules qui ne sont pas en division. Pour améliorer l'administration nucléaire de l'ADN, des peptides synthétiques contenant la séquence NLS ont été extensivement utilisés (*104*, *127*). La plupart de ces peptides ont été construits avec des séquences dérivées de la NLS de l'antigène T large de SV40. Cette séquence a été associée à des CPPs liés directement à la cargaison ou combinés à d'autres méthodes de transfection. Il a été montré

que le domaine NLS du MPG améliore la translocation nucléaire des acides nucléiques sans nécessiter de briser la membrane nucléaire pendant la mitose. La technologie MPG a été appliquée pour l'administration aussi bien de l'ADN plasmidique que d'oligonucléotides avec une efficacité élevée dans un grand nombre de lignées de cellules adhérentes et en suspension (*105, 128*).

1.2.7.2. Administration d'analogues nucléotidiques

Les PNAs et les « phosphorodiamidate morphorodiamidate morpholino oligomers » (PMOs), sont de petits analogues nucléotidiques neutres, puissants pour des applications anti-sens ou de correction d'épissage d'ARNm par blocage stérique. Comme des acides nucléiques, les PNAs et les PMOs ont un problème de pénétration à l'intérieur de la cellule à travers la membrane cytoplasmique. L'une des stratégies pour surmonter ce problème est l'utilisation des CPPs.

Différents CPPs, le Transportan (*48*), la Tat, la pénétratine, le TP10 (une version courte du Transportan), et les polyarginines (*107-109, 113*) ont été couplés à des PNAs ou des PMOs pour l'administration dans divers types cellulaires, *in vitro* et *in vivo.* Cependant, cette approche a rencontré un problème de séquestration endosomale du complexe CPP-PNA/PMO (*129*). La conception de nouveaux CPPs, tels que le R6-pénétratin et le (R-Ahx-R)4 (arginines espacés d'acide 6-aminohexanoïque), ont permis de réduire significativement la séquestration endosomale et d'obtenir une réponse anti-sens ou de correction d'épissage à des concentrations nanomolaires (*111, 130*).

1.2.7.3. Administration d'oligonucléotides et de siRNA

Des oligonucléotides et de courts RNAs interférants (siRNA) sont de puissants outils biomédicaux pour contrôler l'activation de protéines et/ou l'expression de gènes après la transcription (*131, 132*). Comme tous les acides nucléiques, des oligonucléotides et des siRNA ont un problème de pénétration à l'intérieur de la cellule à travers la membrane cytoplasmique. Leur administration à l'aide des CPPs est l'une des stratégies développées pour surmonter cet obstacle.

Différents CPPs, notamment le Transportan, le TP10, et le MPG ont été utilisés avec succès pour l'administration de types variés d'oligonucléotides ou de siRNA *in vitro* et *in*

vivo. Le Transportan et le TP10 ont été utilisés pour l'administration d'oligonucléotides qui interagissent avec NFkB ou Myc pour le contrôle de leur activité (*133, 134*). Quant aux peptides MPG, ils ont été utilisés avec succès pour l'administration de divers types d'oligonucléotides ou de siRNA qui inhibent l'expression des protéines, telles que la Multi Drug Resistance-1 (MDR-1) (*135*) et la télomérase (*136, 137*) de cellules cancéreuses.

1.2.7.4. Administration *in vivo* de protéines et de peptides

En général, des protéines / peptides pénètrent difficilement dans la cellule à travers la membrane cytoplasmique. Pour permettre l'administration intracellulaire de peptides/protéines d'intérêt thérapeutique ou expérimental, des stratégies à base de CPPs ont été développées.

La première preuve de concept de la capacité des CPPs à faciliter l'administration intracellulaire des protéines *in vivo*, a été donnée par Dowdy et collègues en 1999, en montrant que la protéine de fusion Tat-β galactosidase peut être administrée dans presque tous les tissus y compris le cerveau, par injection intra-péritonéale dans les souris (*72*). Par la suite, la vectorisation par les CPPs a été employée avec succès pour l'administration intracellulaire *in vivo* de diverses protéines ciblant surtout le cancer (*13, 106, 114, 118, 138-145*), mais aussi d'autres maladies telles que l'asthme (*146*) et l'ischémie (*147, 148*), ou pour la vaccination (*149*). Différents CPPs ont été utilisés, notamment la Tat (*13, 106, 140, 143, 144, 146-149*), la pénétratine (*138, 139, 142, 145*), et le Pep-1(*114, 118, 141*). Des résultats satisfaisants ont été obtenus avec diverses voies d'administration: injections intraveineuses, intra-tumorale, ou intra-trachéale, pulvérisation nasale, et application directe sur la peau (*114, 118*).

1.3. Toxines peptidiques du venin de scorpion

Le venin de scorpion est composé de diverses substances (*150, 151*), mais les plus abondantes, responsables du caractère toxique du venin sont des peptides. Ces toxines peptidiques agissent principalement sur des canaux ioniques, surtout des cellules excitables, sur lesquels elles se fixent spécifiquement et avec une très forte affinité (*152-154*). Elles ont en commun un motif structural très conservé qui consiste en un noyau compact comportant un ou deux hélices α et deux ou trois feuillets β interconnectés par deux à cinq ponts disulfures établis entre des résidus cystéines (*155-157*). Les toxines peptidiques du venin de scorpion se

distinguent essentiellement par leur taille et par leurs cibles pharmacologiques (canaux ioniques).

Selon la taille de la chaîne peptidique, on distingue les toxines de longue chaîne et les toxines de courte chaîne.

Les toxines de longue chaîne sont généralement des peptides composées de 60 à 76 résidus acides aminés et comportent quatre ponts disulfures intramoléculaires (*158-161*). Cependant, il existe également quelques peptides de 58 résidus acides aminés et qui comportent trois ponts disulfures (*162-164*).

Les toxines de courte chaîne sont composées de 29 à 41 résidus acides aminés et comportent trois ou rarement quatre ponts disulfures intramoléculaires (*158-161*).

En considérant les canaux ioniques spécifiquement ciblés, quatre différentes familles de toxines ont été décrites : les toxines des canaux sodiques (NaTx) (*152, 156*), les toxines des canaux potassiques (KTx) (*165, 166*), les toxines des canaux chloriques (ClTx) (*167*), et les toxines des canaux calciques (canaux Ca^{2+}) (*168*).

Les NaTx du venin de scorpion sont des peptides de longue chaîne (*158-161*). Elles modifient les mécanismes de fermeture/ouverture des canaux Na^+ dépendants du potentiel membranaire. On distingue des toxines α qui modifient la cinétique d'inactivation dépendante du potentiel membranaire (*169*), et des toxines β qui modifient la cinétique d'activation (*170, 171*).

Les KTx du venin de scorpion sont généralament des peptides de courte chaîne (*158-161*) telles que la noxiustoxine (*165*), la charybdotoxine (*172*), et la kaliotoxine (*173*). Elles bloquent spécifiquement plusieurs types de canaux K^+; non seulement des canaux K^+ des cellules excitables, mais également ceux de cellules non excitables telles que des érythrocytes (*174*) et des lymphocytes (*175*). Les KTx du venin de scorpion se fixent sur la face extracellulaire du canal et empêchent le passage des ions (*176*). Il convient de noter que certaines toxines de 58 acides aminés agissent également sur les canaux potassiques (*164*).

Les ClTx sont des peptides de courte chaîne telle que la chlorotoxine (*177*). Elles sont formées de 30 à 40 résidus d'acides aminés et comportent, inhabituellement pour les peptides de cette longueur, quatre ponts disulfures intramoléculaires (*178-180*). Les ClTx de scorpion bloquent les canaux Cl^- de faible conductance (*177*).

Les toxines du venin de scorpion spécifiques des canaux Ca^{2+} sont rarement connues et leur longueur est variable. Les toxines les plus connues sont celles qui sont spécifiques des

canaux RyR du réticulum sarco-plasmique, et qui forment la famille des calcines : l'impératoxine A, la maurocalcine, l'opicalcine 1 et 2, l'hémicalcine, et l'hadrucalcine. Ce sont des peptides de courte chaîne composés de 33 (*60, 181-183*) ou 35 (*184*) acides aminés avec trois ponts disulfures intramoléculaires. Elles se fixent spécifiquement et avec une forte affinité sur les canaux RyR et provoquent leur activation (ouverture) (*60, 153, 182-184*).

1.4. Homéostasie calcique cytosolique

La variation de la concentration du Ca^{2+} [Ca^{2+}] cytosolique libre constitue une signalisation impliquée dans la régulation de nombreux processus biologiques. Cette variation est transitoire, car la cellule est équipée d'un système d'homéostasie du Ca^{2+} cytosolique, c'est-à-dire un système de maintien de la concentration de Ca^{2+} de repos. L'homéostasie du Ca^{2+} cytosolique dépend des processus d'entrée et de sortie du Ca^{2+} du cytosol.

1.4.1. Entrée du calcium dans le cytosol

Lors de la dépolarisation membranaire, une grande quantité de calcium entre dans le cytosol à partir du milieu extracellulaire et /ou des stocks intracellulaires.

1.4.1.1. Entrée du calcium extracellulaire

Le Ca^{2+} extracellulaire entre dans le cytosol par des canaux Ca^{2+}. Ces canaux comprennent des canaux spécifiques du Ca^{2+} et des canaux cationiques non spécifiques, perméables au Ca^{2+} et à d'autres cations.

a. Canaux spécifiques du Ca^{2+}

On distingue plusieurs types de canaux spécifiques de Ca^{2+} en fonction de leur mode d'activation. On peut citer entre autres, des canaux Ca^{2+} dépendants du potentiel membranaire ou voltage (Ca_V) et des canaux Ca^{2+} dépendants des stocks calciques intracellulaires (SOCs, Store-Operated Ca^{2+} Channels).

Les canaux Ca_V se trouvent dans la membrane cytoplasmique principalement des cellules excitables telles que les cellules neuronales et musculaires; ils sont très rares dans des cellules non excitables. Ce sont des canaux Ca^{2+} activés par une dépolarisation de la

membrane cytoplasmique. Sur le plan structural (Figure 7), les canaux Ca_V sont des complexes protéiques formés de 5 sous-unités (*185-190*): la sous-unité $\alpha 1$ qui forme le pore perméable à Ca^{2+} (*191*), et les sous-unités auxiliaires $\alpha 2$, β, δ, et γ qui interviennent dans la régulation de l'expression et de l'activation du canal (*192-195*). Les canaux Ca_V conduisent différents types de courant Ca^{2+}, résultat de la diversité structurale de la sous-unité $\alpha 1$. Selon des critères physiologiques et pharmacologiques, on distingue des courants de types L, T, N, P, Q, et R.

Les courants Ca^{2+} de type L (Long lasting currents) sont désignés ainsi du fait de leur longue durée de passage (*196*). Ils sont en plus caractérisés par une activation à haut potentiel membranaire (faiblement négatif), une production en grande quantité (large conductance du canal), une lente inactivation dépendante du potentiel membranaire (qui explique leur longue durée), une inhibition spécifique par des drogues antagonistes de Ca^{2+} dont les dihydropyridines, les phénylalkylamines, et les benzothiazépines (*196, 197*).

Les courants Ca^{2+} de type T (**T**ransient currents) sont principalement caractérisés par leur durée de passage très courte d'où leur nom (*198*). Comparativement aux courants de types L, ils sont activés à des potentiels membranaires nettement plus bas (plus négatifs), s'inactivent plus rapidement, sont produits en quantité plus faible (faible conductance du canal), et sont insensibles à des drogues antagonistes du Ca^{2+} conventionnels.

Les courants Ca^{2+} de type N se distinguent par leurs potentiel membranaire d'activation et vitesse d'inactivation intermédiaires : valeurs du potentiel membranaire d'activation plus faibles (plus négatives) que celles des courants de type L, mais plus élevées (moins négatives) que celles des courants de type T; vitesse d'inactivation plus rapide que celle des courants de type L, mais plus lente que celle des courants de type T (*198*). Ils sont insensibles à des drogues organiques antagonistes des courants Ca^{2+} de type L; par contre, ils sont bloqués par la toxine peptidique d'escargot, la v-conotoxine GVIA, et par les toxines peptidiques proches (*196, 199*).

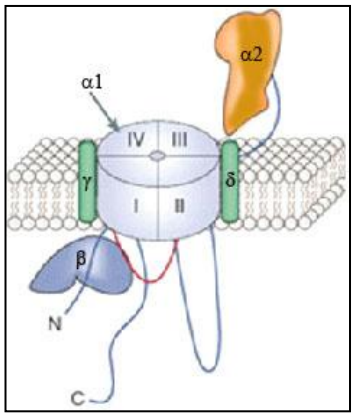

Figure 7: Schéma d'un canal calcique dépendant du potentiel membranaire. Section verticale montrant la sous-unité α1 avec ses quatre domaines formant le pore du canal, et les sous -unités auxiliaires α2δ, β, et γ (*200*).

Les courants Ca^{2+} de type P, initialement observés dans les neurones **P**urkinje (d'où leur nom) (*201, 202*), se distinguent par leur forte sensibilité à la toxine d'araignée v-agatoxine IVA (*203*).

Les courants Ca^{2+} de type Q sont également bloqués par la v-agatoxine IVA, mais avec une faible affinité. Ils ont été initialement observés dans les neurones des granules du cervelet (*204*).

Les courants Ca^{2+} de type R sont observés dans les neurones des granules du cervelet. Ils sont résistants à la plupart des bloqueurs des canaux Ca_V spécifiques de sous-type (*204*), d'où leur nom (**R** pour resistant). Cependant, dans certains types cellulaires ils peuvent être sélectivement bloqués par la toxine peptidique SNX-482 dérivée de la *tarantula Hysterocrates gigas* (*205*). De multiples sous-types de canaux peuvent produire des courants Ca^{2+} de type R (*206*).

Les canaux SOCs constituent la principale voie d'entrée du Ca^{2+} dans les cellules non électriquement excitables, notamment les cellules épithéliales et les cellules sanguines. Ce sont des canaux activés, non par le potentiel membranaire, mais plutôt par la diminution de la $[Ca^{2+}]$ des stocks calciques intracellulaires (*207-209*). Cependant, la molécule détectrice du Ca^{2+} dans les stocks, ainsi que le signal qui relie le contenu Ca^{2+} des stocks aux canaux SOCs dans la membrane cytoplasmique ne sont pas encore bien élucidés. La diminution de la $[Ca^{2+}]$ des stocks calciques intracellulaires est le résultat du relâchement du Ca^{2+}, physiologiquement stimulé principalement par l'inositol 1, 4, 5-triphosphate (IP_3). L'entrée du Ca^{2+} par les SOCs est régulée par divers mécanismes directs ou indirects qui entretiennent ou inhibent le courant

Ca^{2+}. Les mécanismes qui entretiennent le courant Ca^{2+} impliquent surtout les mitochondries. En absorbant le Ca^{2+} relâché par les stocks calciques, les mitochondries contribuent à l'accentuation de la diminution de la [Ca^{2+}] des stocks calciques, et par conséquent, à l'augmentation de l'activation des SOCs. En plus de cela, en absorbant le Ca^{2+} entrant par les SOCs, les mitochondries réduisent l'inactivation des SOCs dépendante de Ca^{2+} (*210*). Ainsi les mitochondries contribuent à la génération des courants Ca^{2+} plus intenses et plus durables (*210, 211*). L'inhibition des courants calciques entrant par les SOCs implique plusieurs mécanismes, notamment l'inactivation dépendante du Ca^{2+}. L'inactivation dépendante du Ca^{2+} se fait selon 3 mécanismes cinétiquement et spatialement distincts : l'inactivation rapide résultant de l'apparition de fortes concentrations de Ca^{2+} dans le voisinage des canaux ouverts (*212-214*), l'inactivation suite au re-remplissage des stocks Ca^{2+} intracellulaires (*215, 216*), et l'inactivation lente (*215, 217, 218*).

b. Canaux cationiques non spécifiques perméables au Ca^{2+}

Des canaux cationiques non spécifiques perméables au Ca^{2+} conduisent le Ca^{2+} et d'autres types de cations. Certains canaux peuvent conduire différents types de cations simultanément dans le même sens, vers l'intérieur de la cellule. C'est le cas du canal Récepteur de la N-méthyl-D-aspartate (NMDAR) utilisé dans nos travaux. D'autres canaux peuvent conduire différents types de cations en sens opposés. C'est le cas des échangeurs Na^{+}/Ca^{2+}.

Le canal NMDAR est l'un des récepteurs des neurotransmetteurs fondamentaux dans le cerveau, en raison de ses rôles clés dans les fonctions essentielles du cerveau, allant de la neurotransmission de l'excitation, aux fonctions d'apprentissage et de la mémoire. Le canal NMDAR appartient à la famille des récepteurs ionotropiques du glutamate, acide aminé neurotransmetteur excitateur. Le canal NMDAR est caractérisé par une forte affinité pour le glutamate, une forte conductance, une forte perméabilité au Ca^{2+}, et un blocage dépendant du potentiel membranaire par les ions Mg^{2+} (Figure 8). L'activation du NMDAR nécessite en plus du glutamate, la glycine comme co-activateur essentiel, et le potentiel d'excitation permettant l'enlèvement du blocage par le Mg^{2+}. Le potentiel d'excitation se développe suite à l'activation des récepteurs du glutamate dans la membrane postsynaptique, par le glutamate issu du relâchement présynaptique. L'activation du canal NMDAR conduit à l'ouverture de

son pore sélectif pour les cations, ce qui entraîne une entrée massive des ions Na^+ et Ca^{2+}, et une sortie massive des ions K^+.

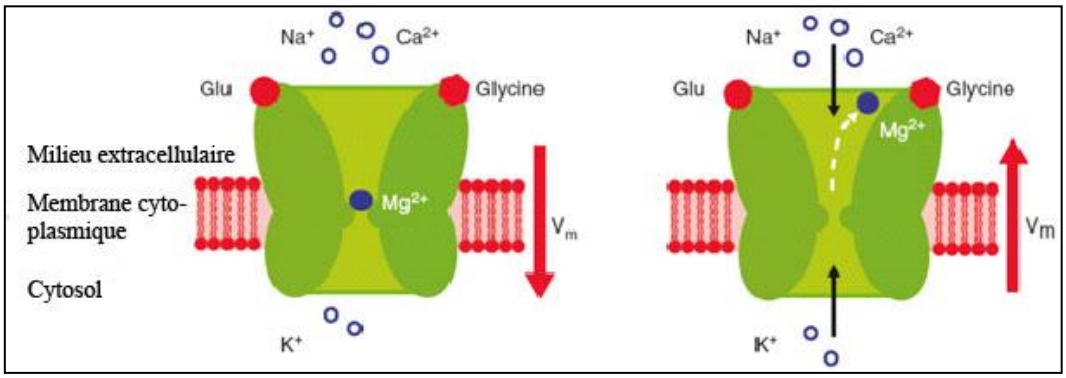

Figure 8: Schéma du mécanisme de blocage du canal NMDAR par les ions Mg^{2+}.
A gauche : Au potentiel membranaire (V_m) de repos, le pore du canal NMDAR est bloqué par des ions Mg^{2+}.
A droite : Suite à la dépolarisation, les ions Mg^{2+} sont enlevés du pore, et le canal peut laisser passer le courant ionique. (*219*) (Modifiée).

L'échangeur Na^+/Ca^{2+}, situé à la membrane cytoplasmique (ou du sarcolemme) peut, dans certaines conditions, faire entrer du calcium dans le cytoplasme (*220*), fonctionnant en mode inverse par rapport à sa principale fonction d'extrusion du calcium vers le milieu extracellulaire (Figure 12) (voir détails ci-dessous).

1.4.1.2. Entrée du calcium des stocks calciques intracellulaires

A l'intérieur de la cellule de fortes quantités de Ca^{2+} sont stockées dans des organelles spécialisées. La principale organelle intracellulaire de stockage et de relâchement du Ca^{2+} dans la plupart des cellules est le RE (réticulum endoplasmique), appelé réticulum sarcoplasmique (RS) dans des cellules des muscles striés. La membrane du RE/RS contient des canaux spécialisés à travers lesquels, sous une stimulation appropriée, le Ca^{2+} stocké est relâché dans le cytosol. On distingue deux familles: les canaux RyR et les canaux récepteurs d'IP_3 (IP_3R).

On distingue trois isoformes des canaux RyR : RyR1, RyR2, et RyR3 (*221-225*) exprimés de façon spécifique dans certains tissus. Les plus prédominants dans les muscles striés des mammifères sont, les canaux RyR1 prédominants dans les muscles squelettiques (*222, 226-228*), et les canaux RyR2 prédominants dans les muscles cardiaques (*223, 224*). Les canaux RyR3 sont faiblement présents dans les muscles striés des mammifères (*229*) et leur rôle physiologique n'est pas bien connu.

L'activité des canaux RyR1 est couplée à un «détecteur de potentiel membranaire » de la membrane cytoplasmique. Dans les cellules musculaires, le Ca^{2+} est relâché du RS en réponse à la dépolarisation des invaginations de la membrane cytoplasmique (sarcoplasmique) appelées tubules transverses (tubules t). Un mécanisme putatif du relâchement a été proposé (*230-233*).

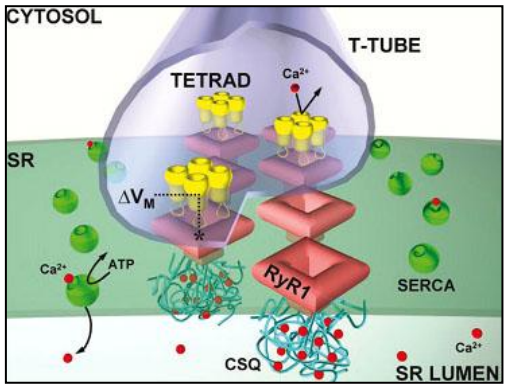

Figure 9: Environnement du canal récepteur de la ryanodine dans les muscles squelettiques.
Le réticulum sarcoplasmique (SR) des cellules musculaires squelettiques comporte des canaux récepteurs à la ryanodine de type 1(RyR1) et des pompes Ca^{2+} ATPase (SERCA). Les tubules t de la membrane cytoplasmique des cellules musculaires squelettiques contiennent des tétrades, regroupements de quatre canaux récepteurs de la dihydropyridine (DHPR). Les canaux RyR1 sont associés aux tétrades: chaque canal RyR1 sur deux est associé à une tétrade. Un changement de potentiel membranaire des tubules t (delta VM) active le canal DHPR. L'entrée du Ca^{2+} à travers le canal DHPR n'est pas importante pour l'activation du canal RyR1 dans les muscles squelettiques. Le signal delta VM des tubules t semble plutôt être transmis au canal RyR1 par une interaction physique directe entre le canal DHPR et le canal RyR1. Le signal delta VM des tubules t déclenche l'ouverture du canal RyR1 et le relâchement du Ca^{2+} stocké à l'intérieur du SR. La pompe SERCA, en utilisant l'énergie de l'ATP, repompe le Ca^{2+} vers l'intérieur du SR où le Ca^{2+} reste stocké fixé à la calséquestrine (CSQ), tampon de Ca^{2+} de forte capacité et de faible affinité (*234*)**.**

Le canal RyR1 de la membrane du RS interagit avec le récepteur de la dihydropyridine (DHPR, dihydropyridine receptor) se trouvant dans la membrane des tubules t et qui est un canal Ca_v de type L (*235-238*). Ces canaux sont disposés de manière à permettre une très rapide et efficace transduction du signal de dépolarisation, de la membrane des tubules t aux canaux RyR1: chaque canal RyR1 sur deux interagit avec un groupement de quatre canaux DHPR (*236, 239*) (Figure 9). La dépolarisation de la membrane des tubules t induit des changements conformationnels dans le DHPR qui conduisent à l'activation et l'ouverture du canal RyR1. L'ouverture du canal RyR1 entraîne le relâchement massif du Ca^{2+} du RS dans le cytosol. Ce mécanisme est généralement appelé relâchement de Ca^{2+} induit par la dépolarisation (depolarization-induced Ca^{2+} release) (*237, 240-243*).

Figure 10: Environnement du canal RyR2 dans un muscle cardiaque.
Le tubule t contient des canaux récepteurs de la dihydropyridine (DHPR) et des systèmes d'extrusion du Ca^{2+} comme l'échangeur Na^{+}/Ca^{2+}. Un changement de potentiel membranaire du tubule t active le canal DHPR qui s'ouvre et laisse entrer le Ca^{2+} dans le cytosol. L'entrée du Ca^{2+} déclenche l'ouverture des canaux RyR2, ce qui entraîne le relâchement dans le cytosol, du Ca^{2+} stocké dans le réticulum sarcoplasmique (SR), par le mécanisme de relâchemet du calcium induit par le calcium (calcium induced calcium release). La pompe Ca^{2+} ATPase du SR, en utilisant l'énergie de l'ATP, repompe le Ca^{2+} vers l'intérieur du SR où le Ca^{2+} reste stocké fixé à la calséquestrine, tampon Ca^{2+} de forte capacité et de faible affinité. L'échangeur Na^{+}/Ca^{2+} utilise l'énergie du gradient Na^{+} pour expulser le Ca^{2+} hors de la cellule (*234*).

L'activité du canal RyR2 est gouvernée par le processus du relâchement de Ca^{2+} induit par le Ca^{2+} (CICR, Ca^{2+} induced Ca^{2+} release). Dans le muscle cardiaque, il y a environ un canal DHPR pour tous les 5-10 canaux RyR2 (*236, 244*), et les canaux DHPR et RyR2 ne sont pas alignés de façon hautement ordonnée (*236, 244*) (Figure 10). Les canaux RyR2 ne sont donc pas facilement activables par des interactions directes avec le canal DHPR. Par contre, pendant le long potentiel d'action cardiaque (environ 100 ms), le canal Ca^{2+} DHPR a suffisamment de temps de s'ouvrir et laisser entrer le Ca^{2+} extracellulaire. C'est cette entrée du Ca^{2+} extracellulaire qui constitue le signal qui active les canaux RyR2. Ainsi activés, les canaux RyR2 s'ouvrent permettant le relâchement du Ca^{2+} du RS dans le cytosol par le processus de CICR (*245, 246*).

Les canaux IP_3R sont des canaux de relâchement sélectif de Ca^{2+} localisés de façon prédominante dans la membrane du RE (*247-249*). Les canaux IP_3R relâchent le Ca^{2+} dans le cytosol suite à une activation principalement par l'IP_3 (Figure 11), mais aussi par d'autres ligands, en particulier le Ca^{2+} cytosolique.

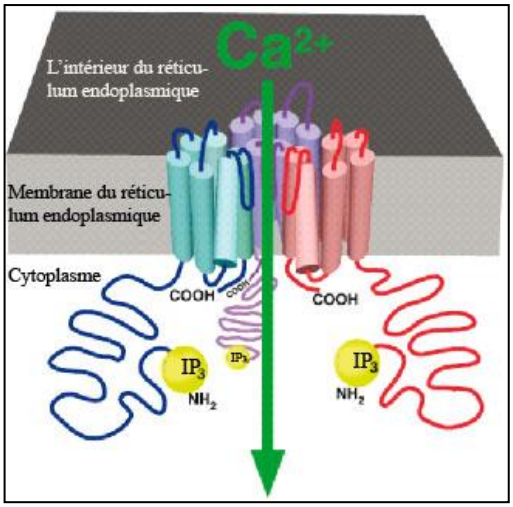

Figure 11: Canal de relâchement du Ca^{2+}, récepteur de l'inositol 1, 4, 5-triphosphate (IP_3R).
Le schéma montre trois des quatre molécules IP_3R formant le canal. Une partie de la boucle qui relie les hélices transmembranaires 5 et 6 de chaque molécule est enfoncée dans la lumière du canal pour former une voie de perméabilisation du canal aux ions Ca^{2+} relâchés du réticulum endoplasmique (*250*) (Modifiée).

Les courants Ca^{2+} issus des canaux IP_3R sont produits de façon répétitive (oscillations) avec une fréquence souvent dépendante du niveau de stimulation. Ces courants peuvent s'initier à un endroit spécifique et y rester bien localisés ou se propager sous forme d'ondes (*251-253*).

1.4.2. Evacuation du calcium cytosolique

Divers mécanismes interviennent dans l'évacuation du Ca^{2+} cytosolique pour rétablir la $[Ca^{2+}]$ de repos. On distingue des mécanismes d'évacuation consistant en la réabsorption par des organelles intracellulaires ou en la capture par des protéines intracellulaires, et des mécanismes d'extrusion du Ca^{2+} vers le milieu extracellulaire.

1.4.2.1. Réabsorption du Ca^{2+} par des organelles intracellulaires

Les principales organelles qui réabsorbent le Ca^{2+} sont le RE/RS et les mitochondries.

Le RE/RS réabsorbe le Ca^{2+} cytosolique par un pompage contre le gradient de la $[Ca^{2+}]$ au moyen de la pompe Ca^{2+}ATPase (pompe SERCA, Sarco/Endoplasmic Reticulum Ca^{2+} ATPase). La pompe SERCA est une protéine ubiquitaire qui se trouve dans la membrane du RE/RS ainsi que dans la membrane sarco/cytoplasmique. Cette pompe permet le transport de deux ions Ca^{2+} pour l'hydrolyse d'une molécule d'ATP (*254*).

Les mitochondries réabsorbent également une grande proportion du Ca^{2+} entré massivement dans le cytosol (*255, 256*). Le regroupement spatial des mitochondries dans

certains domaines de la cellule représente vraisemblablement un « tampon physiologique » qui empêche ou affaiblit la propagation de la vague calcique vers d'autres domaines où le signal calcique pourrait déclencher des réponses cellulaires non appropriées. La membrane interne mitochondriale est la seule barrière que doit franchir le calcium puisque la membrane externe est perméable à cet ion. L'absorption du Ca^{2+} par les mitochondries se fait par le gradient électrochimique selon deux modes : le mode uniport qui est lent et le mode RaM (Rapid Mode) qui est 300 fois plus rapide. Les molécules intervenant ne sont pas encore bien caractérisées, mais il semble que ce soit des canaux cationiques protéiques. Le Ca^{2+} absorbé est utilisé dans plusieurs fonctions cellulaires dont la régulation du métabolisme oxydatif, la régulation des évènements de libération calcique spontanée (*257*), et l'apoptose (*258*, *259*).

1.4.2.2. Capture du Ca^{2+} par des protéines cytosoliques

Le myoplasme contient des protéines capables de fixer le Ca^{2+} et donc de jouer le rôle de tampon calcique. Les trois protéines liant le Ca^{2+} avec une forte affinité dans le muscle sont la troponine C, la parvalbumine, et la calmoduline. Elles sont impliquées dans la régulation de la $[Ca^{2+}]$, ainsi que de la contraction et la relaxation musculaires (*260*).

La troponine C appartient à la famille des protéines fixant le Ca^{2+} par leurs domaines «EF hands» (*261*). C'est une protéine qui intervient dans la contraction musculaire. Lors de l'augmentation de Ca^{2+} intracellulaire induite par une dépolarisation membranaire, la troponine C fixe le Ca^{2+} par ses domaines « EF hands » ce qui déclenche le processus de contraction musculaire.

La parvalbumine est une protéine cytosolique soluble découverte en 1952 par J.G Henrotte (*262*). Elle appartient aussi à la famille des protéines à motif « EF hands » et possède deux sites de fixation du Ca^{2+}. Chez les mammifères, il existe deux isoformes de parvalbumine. L'isoforme α du muscle adulte et l'isoforme β de l'embryon (*263*).

La calmoduline fait aussi partie des protéines à domaines « EF hands » liant le Ca^{2+}. Cependant, étant beaucoup moins exprimée que la troponine C ou la parvalbumine, la calmoduline ne peut pas jouer de véritable rôle de tampon Ca^{2+}. En revanche, elle permet la régulation de l'activité des canaux Ca^{2+} du RS, tels que les canaux IP_3R (*264*) et les canaux RyR (*265*).

1.4.2.3. Extrusion du Ca^{2+} vers le milieu extracellulaire

L'extrusion du Ca^{2+} vers le milieu extracellulaire se fait principalement par la pompe Ca^{2+} ATPase de la membrane cytoplasmique ou du sarcolemme (pompe PMCA, Plasma Membrane Ca^{2+}-ATPase) et par l'échangeur Na^{+}/Ca^{2+}.

La pompe PMCA expulse le Ca^{2+} vers le milieu extracellulaire contre le gradient de la $[Ca^{2+}]$ grâce à l'énergie obtenue par l'hydrolyse de l'ATP.

L'échangeur Na^{+}/Ca^{2+} joue le rôle d'extrusion du Ca^{2+} vers le milieu extracellulaire, dans les conditions physiologiques normales. Cependant, dans certaines conditions, il peut fonctionner en mode inverse et faire entrer du Ca^{2+} dans le cytoplasme (*220*). Dans les conditions physiologiques normales, la stœchiométrie de l'échange est d'un ion de Ca^{2+} pour trois ions de Na^{+} (*266*). L'activité des échangeurs Na^{+}/Ca^{2+} est réversible et le sens des mouvements ioniques dépend des gradients électrochimiques des ions transportés. Le transport ne nécessite donc pas d'ATP (Figure 12). Quand la membrane est dépolarisée et que la concentration du Na^{+} intracellulaire augmente, l'échangeur peut fonctionner en mode inverse : faire sortir des ions Na^{+} et faire entrer des ions Ca^{2+}. A la fin de la dépolarisation membranaire et lorsque la $[Ca^{2+}]$ intracellulaire est élevée, l'échangeur Na^{+}/Ca^{2+} fonctionne en mode normal et permet l'extrusion du Ca^{2+}.

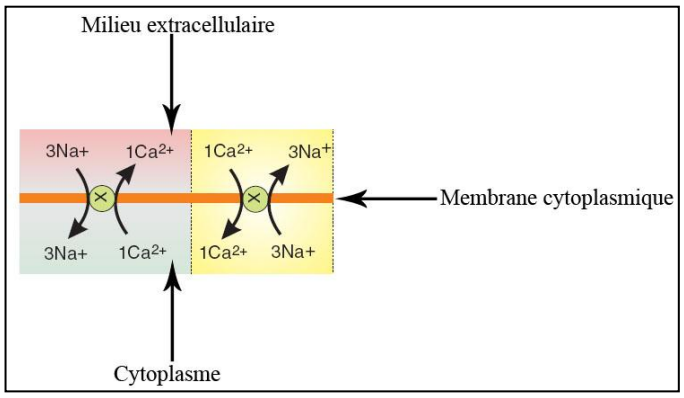

Figure 12: Mécanismes d'échange des ions Na^{+} et Ca^{2+} par l'échangeur Na^{+}/Ca^{2+}.
Partie gauche : Mode normal (Forward mode). L'échangeur fait entrer dans la cellule trois ions de Na^{+} et sortir un ion de Ca^{2+}.
Partie droite : Mode inverse (reverse mode). L'échangeur fait entrer un ion de Ca^{2+} et sortir trois ions de Na^{+} (*267*) (Modifiée).

1.4.3. Micro / Nanodomaines calciques

Le terme de micro/nanodomaines Ca^{2+} désigne des signaux Ca^{2+} qui consistent en une augmentation temporaire de la [Ca^{2+}] cytosolique, à proximité ou à distance d'un ou plusieurs canaux Ca^{2+} ouverts, et qui couvre des distances variant de centaines de nanomètres aux micromètres.

La diffusion de Ca^{2+} à travers un canal Ca^{2+} ouvert crée un gradient Ca^{2+} local, qui chute abruptement avec la distance sous l'effet des tampons Ca^{2+} intracellulaires. Dans quelques nanomètres du pore du canal Ca^{2+}, les tampons ne sont pas en mesure de capturer immédiatement tout le Ca^{2+} qui entre massivement dans le cytosol à partir du milieu extracellulaire ou des stocks intracellulaires (*268*), d'où les fortes concentrations de Ca^{2+} à ces endroits (*269*). Cependant, de fortes [Ca^{2+}] peuvent également se retrouver loin des canaux qui ont laissé entrer le Ca^{2+}. Ceci est rendu possible par le système de tunnel qui transporte le Ca^{2+} dans des conditions qui ne l'exposent pas aux tampons (*270*). La localisation des cibles sensibles au signal Ca^{2+} dans les zones recouvertes par les micro/nanodomaines Ca^{2+} permet leur activation rapide et sélective (*271*).

2. CONTEXTE DES TRAVAUX

La MCa (L-MCa) est le premier exemple démontré d'une toxine peptidique animale repliée ayant des propriétés de pénétration cellulaire. Elle a été découverte en 2000 dans le venin d'un scorpion tunisien, *Scorpio maurus palmatus*, pour son activité sur les canaux RyRs, canaux de relargage du Ca^{2+} intracellulaire situés dans la membrane du RS (Réticulum Sarcoplasmique) (*60*). Elle appartient à la famille des calcines qui comporte cinq autres peptides issus du venin de scorpion: l'imperatoxine A, l'opicalcine1, l'opicalcine 2, l'hémicalcine, et l'hadrucalcine. Ceux qui ont été caractérisés ont tous en commun la propriété d'activer les canaux RyRs (*182, 184, 272*).

La MCa est un peptide cationique composé de 33 résidus acides aminés. Le peptide comporte 7 charges positive : parmi les 33 résidus, 11 (33%) sont des résidus basiques chargés positivement, contre 4 (12%) résidus acides chargés négativement. Par ailleurs le peptide comporte six résidus cystéines qui forment trois ponts disulfures : Cys^{3}-Cys^{17}, Cys^{10}-Cys^{21}, et Cys^{16}-Cys^{32} (*60*). Le peptide est replié et rigidement structurée par les trois ponts

disulfures et comporte trois brins β s'étendant sur les résidus 9-11 (brin 1), 20-23 (brin 2), et 30-33 (brin 3) (*60*). Curieusement, ces brins β semblent correspondre à des étendus des résidus chargés positivement (Figure 14: Séquence d'acides aminés de la MCa repliée (MCaF). Globalement, le peptide peut être schématiquement représenté avec trois domaines: une tête hydrophobe, une seconde face plus large principalement basique, et un troisième domaine latéral qui contient le pharmacophore (Figure 13).

La MCa a une activité pharmacologique consistant en l'activation du canal RyR1 des muscles squelettiques entrainant le relargage du Ca^{2+}. L'activité de la MCa (L-MCa) a été démontrée par différents tests. Les tests réalisés sur les vésicules du RS (*273*) et sur les myotubes (*273, 274*) ont montré le relargage du Ca^{2+} induit par le MCa. Par ailleurs, les tests de liaison de la ryanodine par les canaux RyR1 ont montré une augmentation significative de la quantité de ryanodine liée en présence de la MCa comparativement à la quantité liée sans MCa (*273*). Cette augmentation indique l'ouverture des canaux RyR sous l'activité de la MCa, ce qui, d'une part conduit à la transformation des sites de liaison de la ryanodine de faible affinité en sites de forte affinité par changement de conformation, et d'autre part permet à la ryanodine de mieux accéder à ses sites de fixation situés à l'intérieur des canaux RyRs. L'activité de la MCa a par ailleurs été observée au moyen des canaux RyR1 incorporés la bicouche phospholipidique reconstituée (*274*). La MCa entraine le relargage du Ca^{2+} en mettant les canaux RyR1 dans un état de sous-conductance de longue durée (*60, 274, 275*). La surface du peptide chargée positivement constitue la principale région d'interaction avec le canal RyR1 (*274*). Les principaux résidus impliqués sont, dans l'ordre croissant d'implication, la Lys^{8}, la Lys^{20}, la Lys^{22}, l'Arg^{23}, et l'Arg^{24} (*274*). L'Arg^{24} est le plus déterminant dans l'activité pharmacologique du peptide. Sa substitution par l'Ala entraine la suppression de l'activité pharmacologique (*273*, *274*). Il a été montré que la MCa interagit également avec les canaux RyR2 des muscles cardiaques sans néanmoins provoquer le relargage du Ca^{2+} (*276*). Cependant l'absence du relargage du Ca^{2+} serait due à l'état de phosphorylation des canaux RyR2 dépendant des conditions expérimentales; les études en cours tenant compte de ce facteur pourraient donner des éclaircissements à ce sujet.

Par ailleurs, la maurocalcine a une propriété de pénétration cellulaire. L'activation des canaux RyR1, situés à l'intérieur de la cellule, a suggéré la capacité de la MCa de pénétrer dans la cellule pour atteindre sa cible. En plus, la MCa partage avec les CPPs connus avant, le caractère cationique par la forte proportion d'acides aminés basiques. La plupart de ses acides

aminés basiques sont regroupés sur une même face de la molécule en accord avec la distribution asymétrique observée sur des CPPs usuels (*18*) (Figure 13). Par la suite, différentes analyses réalisées ont confirmé que la MCa possède effectivement la propriété de pénétration cellulaire (*277*). Lors de sa pénétration cellulaire, la MCa établit d'abord des interactions avec les protéoglycanes de la surface cellulaire (*278*) et/ou les phospholipides chargés de la membrane plasmique (*279*). L'observation d'une libération calcique quasi instantanée (processus plus rapide que l'endocytose) suite à une application extracellulaire de la MCa à des myotubes (*273*), la découverte du site de fixation de la MCa dans la partie cytoplasmique de RyR1 (*280*), et la sensibilité de la pénétration cellulaire au potentiel électrostatique membranaire (*279*) ont suggéré une pénétration cellulaire de la MCa par un mécanisme de translocation membranaire directe. Cependant, il a été montré que l'endocytose, essentiellement la macropinocytose, contribue à la pénétration cellulaire de la MCa (*278*). Par ailleurs, la MCa s'est révélée un vecteur efficace pour la délivrance intracellulaire de divers types de cargaisons tels que des protéines (*277, 279*), des peptides (*18*), des fluorochromes (*16, 281*), des médicaments (*61*), ou des nanoparticules (*282*).

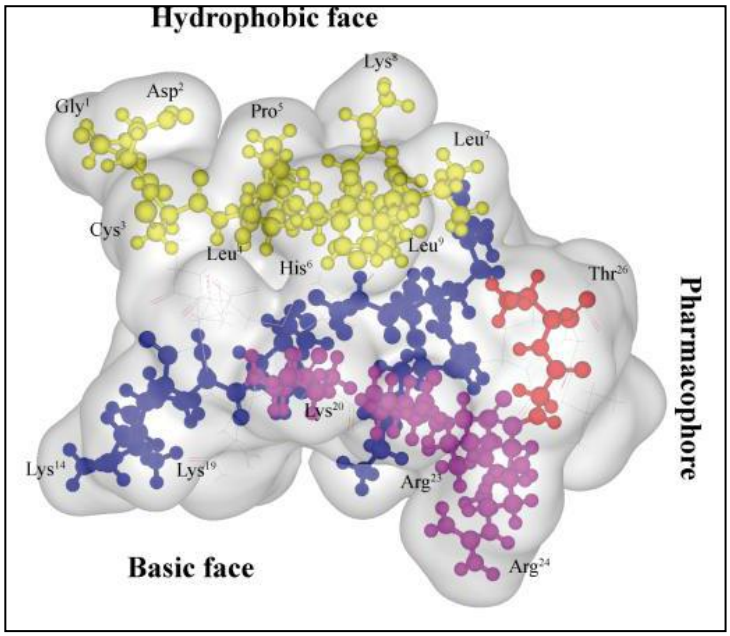

Figure 13: Représentation schématique de la structure 3D de la MCa

La face hydrophobe : formée essentiellement des résidus acides aminés hydrophobes. Elle est représentée en jaune.

La face basique : formée des résidus acides aminés basiques représentés en bleu ou en rose.

Le pharmacophore : formé des résidus acides aminés intervenant dans les interactions entre la MCa et les canaux RyR, représentés en rouge ou en rose.

En rose sont représentés des résidus basiques qui interviennent dans les interactions MCa-RyR; ils appartiennent à la fois à la face basique et au pharmacophore.

La MCa présente des avantages comparativement à d'autres CPPs. Elle pénètre dans la cellule à de très faibles concentrations, de l'ordre nanomolaire, et elle est peu toxique (*16, 279*). Elle a une excellente stabilité; elle n'est pas dénaturée par des conditions de pH extrêmes ni par des températures élevées pouvant aller jusqu'à 100°C (*16*). Par ailleurs, la MCa semble pénétrer dans la cellule principalement par la translocation membranaire directe (*16*), le mode de pénétration le plus avantageux car il préserve les cargaisons de la séquestration et la dégradation enzymatique dans les endosomes. En plus, elle est l'un de rares CPPs dont la pénétration cellulaire peut être étudiée indépendamment de l'attachement à une cargaison, car elle a un révélateur physiologique direct sous la forme d'un relâchement de Ca^{2+} des stocks calciques intracellulaires (*274*)

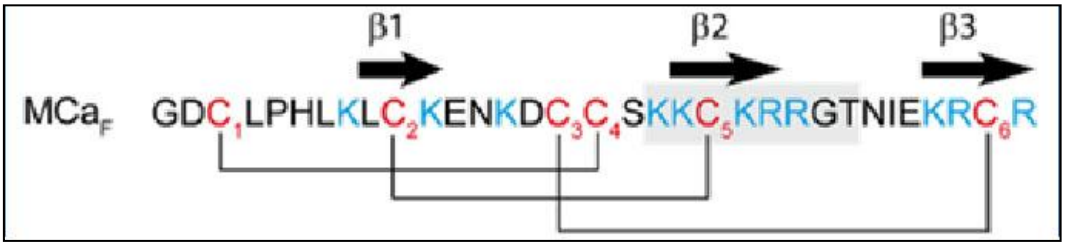

Figure 14: Séquence d'acides aminés de la MCa repliée (MCa_F)
La séquence d'acides aminés est écrite dans un code d'une seule lettre. Les résidus d'acide aminée cystéine sont représentés en rouge. Les résidus d'acides aminés basiques sont représentés en bleu. Les structures secondaires (feuillets β) sont indiquées par des flèches. La boîte grise est la séquence d'homologie de la MCa avec le canal Ca_v 1.1 sensible à la dihydropyridine.

Cependant, bien que la MCa soit un puissant vecteur de délivrance intracellulaire de diverses cargaisons, son utilisation dans la conformation native rencontrerait des obstacles. L'activité pharmacologique native de la MCa est indésirable pour la plupart des applications envisageables *in vivo*, car le relargage excessif du Ca^{2+} pourrait occasionner un dysfonctionnement fatal (*60*). Les trois ponts disulfures de la MCa native compliquent la synthèse chimique du peptide par des étapes de repliement/oxydation, qui en plus ont un faible rendement, ce qui rend le coup de production relativement élevé comparativement aux CPPs non repliés couramment utilisés. En outre, la présence des six résidus cystéines (formant les trois ponts disulfures) causerait des problèmes pour le greffage de la cargaison. La cargaison est souvent greffée au moyen d'un résidu cystéine supplémentaire. La présence d'autres résidus cystéine dans la chaine peptidique rend incontrôlable le site de fixation de la

cargaison et le nombre de cargaisons greffées car la cargaison pourrait également se greffer aux cystéines à l'intérieur du peptide. La taille du peptide est plus longue que celles des CPPs rapportés dans la littérature (Tableau 1). Pour toutes ces raisons, comme d'autres CPPs connus avant, la MCa native a été modifiée afin de faciliter son utilisation *in vivo* comme un nouveau système de délivrance intracellulaire de produits d'intérêts divers (*53*). La suppression de l'activité pharmacologique de la MCa s'est révélée très simple du fait que les exigences structurelles impliquées dans la liaison avec le RyR sont plus strictes que pour la pénétration cellulaire. Plusieurs stratégies biochimiques ont été utilisées avec succès. Il s'agit notamment de mutations ponctuelles (*17*), la linéarisation (empêcher le repliement) du peptide par la suppression des ponts disulfures (*18*), et la synthèse du peptide au moyen d'acides aminés isomères optiques D (*16*). La deuxième stratégie a eu l'avantage de donner un analogue de la MCa linéaire plus simple à produire car l'étape d'oxydation/repliement n'était plus nécessaire et plus simple à utiliser grâce à la présence d'un résidu cystéine supplémentaire réservé au greffage simple et rapide de la cargaison, sans interférence de cystéines internes car ils ont été substitués par l'Abu. Mais, cet analogue linéaire s'est révélé légèrement moins efficace en pénétration cellulaire que la MCa repliée/oxydée. Par ailleurs, l'analogue linéaire était toujours long, car composé de 33 résidus.

La présente thèse avait deux objectifs :

1. Poursuivre les optimisations du CPP analogue linéaire de la MCa pour le rendre plus simple et plus économique à produire et à utiliser, et améliorer ses performances.

2. Dans le cadre des applications possibles, valider la preuve de concept de l'utilisation des dérivés de la MCa comme outil de délivrance intracellulaire de nano-sondes, notamment les nanobiodétecteurs du Ca^{2+} cytosolique.

3. RESULTATS

Les résultats sont présentés sous forme d'articles. Trois principaux articles ont été publiés au cours de ces travaux de thèse:

(1). Small Efficient Cell-Penetrating Peptides Derived from Scorpion Toxin Maurocalcine:

Efficaces petits CPPs dérivés de la Maurocalcine.

(2). Cell Penetration Properties of a Highly Efficient Mini Maurocalcine Peptide:

Propriétés de pénétration cellulaire d'un puissant CPP « Mini-Maurocalcine ».

(3). Cell-Penetrating Nanobiosensors for Pointillistic Intracellular Ca^{2+}-Transient Detection:

Adressage intracellulaire des Nanobiodétecteurs de variations transitoires ponctuelles du Ca^{2+} intracellulaire.

3.1. Efficaces petits CPPs dérivés de la Maurocalcine

Résumé : La MCa est un excellent CPP issu du venin de scorpion, *Scorpio Maurus palmatus*. Afin de développer des applications, notamment in vivo, la MCa a subi des optimisations. Ces optimisations ont conduit à différents CPPs analogues de la MCa, notamment la MCa linéaire (MCa_{UF1-33}) dépourvue de ponts disulfures et d'activité pharmacologique, mais conservant d'excellentes propriétés de pénétration cellulaire. Dans ce travail, nous avons poursuivi les optimisations par la délétion de la $MCa_{UF1-33,}$ afin de simplifier la synthèse et de réduire le coût de production du CPP. Douze excellents CPPs de taille réduite ont été obtenus. D'après les tests réalisés sur les cellules CHO, les nouveaux CPPs ont manifesté une excellente efficacité de pénétration cellulaire; ils ont une faible cytotoxicité; leur pénétration cellulaire est essentiellement indépendante de la macropinocytose; ils sont pharmacologiquement inertes. Les différents analogues pourraient constituer une boîte à outils, utilisés chacun de façon adaptée aux besoins spécifiques de délivrance intracellulaire. Pour des besoins spécifiques en concentration intracellulaire, trois analogues manifestent un intérêt particulier : la MCa_{UF1-9} pour de faibles concentrations intracellulaires, et la $MCa_{UF18-33}$ ou la $MCa_{UF14-25}$ pour de fortes concentrations intracellulaires. Une caractérisation approfondie donnera plus de lumière sur de possibles développements d'applications.

3.1.1. Introduction

La MCa (L-MCa) est une toxine issue du venin de scorpion, *Scorpio maurus palmatus,* et dotée d'excellentes propriétés de pénétration cellulaire. La MCa a suscité l'intérêt, d'abord pour son activité pharmacologique consistant en l'activation des canaux RyR1 conduisant au relargage du Ca^{2+} du RS (réticulum sarcoplasmique) dans le cytosol (*60*). C'est l'observation de cette activité pharmacologique de la MCa qui a conduit à la découverte de ses propriétés de CPPs (*277*).

La MCa est un peptide cationique composé de 33 résidus acides aminés. Onze (33%) de ses résidus sont des résidus basiques donc chargés positivement. Par ailleurs, la MCa comporte six résidus cystéines formant trois ponts disulfures : Cys^{3}-Cys^{17}, Cys^{10}-Cys^{21}, et Cys^{16}-Cys^{32} (*60*). Le peptide est replié et rigidement structuré par les trois ponts disulfures. Il comporte trois brins β s'étendant sur les résidus 9-11 (brin 1), 20-23 (brin 2), et 30-33 (brin 3) (*60*).

La MCa a une activité pharmacologique qui consiste en l'activation des canaux RyR1 des muscles squelettiques. La MCa agit sur les canaux RyR1 en induisant un état de sous-conductance de longue durée qui se traduit par un relargage du Ca^{2+} du RS (*60, 274, 275*). L'activité pharmacologique de la MCa est dépend essentiellement de ses résidus basiques, donc chargés positivement, notamment la Lys^{8}, la Lys^{20}, la Lys^{22}, l'Arg^{23}, et l'Arg^{24} (*274*). L'Arg^{24} est le plus actif; sa substitution par l'alanine entraine une perte totale de l'activité pharmacologique (*273, 274*). La MCa interagit également avec les canaux RyR2 des muscles cardiaques, mais sans provoquer le relargage du Ca^{2+} (*276*).

La MCa, est un CPP particulièrement intéressant. Elle pénètre dans la cellule à de très faibles concentrations et essentiellement par translocation directe**;** elle a une stabilité remarquable (résistance à de hautes températures, à des conditions de pH extrêmes, à la digestion enzymatique) et une très faible toxicité (*16, 279*) ; elle délivre dans la cellule divers types de cargaisons : des protéines (*277, 279*), des peptides (*18*), des fluorochromes (*16*), des médicaments (*61*), ou des nanoparticules (*282*).

Cependant, dans son état natif, la MCa serait difficilement utilisable en qualité de vecteur. L'activité pharmacologique native consistant en l'activation des canaux RyR1 induisant le relargage du Ca^{2+} intracellulaire dans le cytosol, est indésirable dans la plupart des applications envisageables, particulièrement *in vivo,* car elle pourrait occasionner de graves dysfonctionnements (*60*). La présence de six Cys internes complique la synthèse du peptide par l'étape de repliement/oxydation, dont en plus le taux de réussite est faible, ce qui augmente le coup de production. Par ailleurs, les Cys internes compliquent le greffage de la cargaison, il serait difficile de greffer la cargaison au moyen d'un résidu cystéine supplémentaire (technique normalement simple et rapide), car les cystéines internes pourraient également se lier à la cargaison; le site de greffage et le nombre de molécules de la cargaison greffées seraient donc incontrôlables. Par ailleurs, la taille du peptide plus longue que celle des CPPs usuels rend le coût de production plus élevé. Pour toutes ces raisons il a été nécessaire d'optimiser le peptide pour faciliter son utilisation comme vecteur de délivrance intracellulaire, *in vivo,* de produits d'intérêts diagnostiques ou thérapeutiques.

Les optimisations du CPP MCa ont d'abord consisté en la suppression de l'activité pharmacologique et en l'élimination des ponts disulfures (Cys internes). Différentes stratégies ont permis de supprimer l'activité pharmacologique tout en conservant la propriété de

pénétration cellulaire. Des mutations ponctuelles, notamment la mutation R24A, ont donné des analogues pharmacologiquement inertes (*17, 273, 274*) ; cependant, bien que conservée, leur efficacité de pénétration cellulaire a baissé comparativement à celle de la MCa native (*17*). La synthèse du peptide au moyen des acides aminés isomères optiques D au lieu des isomères optiques L composant la MCa native, a abouti à un analogue (D-MCa) complètement dépourvu d'activité pharmacologique et ayant une efficacité de pénétration cellulaire comparable à celle de la MCa native (*16*)**.** La suppression des ponts disulfures a été réalisée par le remplacement des six résidus cystéines par l'acide isostérique 2-aminobutyrique (Abu). Le choix d'Abu a été motivé par sa similarité avec la cystéine; les deux molécules diffèrent seulement par le groupement thiol (-SH) de la cystéine (groupement par lequel se forme le pont disulfure) qui est remplacé par le groupement méthyl ($-CH_3$) dans la molécule d'Abu. Le peptide linéaire (MCa-Abu) obtenu est pharmacologiquement inactif et efficace en pénétration cellulaire; cependant, il est moins efficace que la MCa native (*18*). Globalement, les différentes stratégies ont conduit à des CPPs analogues de MCa pharmacologiquement inertes, mais qui conservent les résidus cystéines internes, à l'exception de la MCa-Abu. Cependant, la MCa-Abu, comme tous les autres analogues (à l'exception de la D-MCa) est moins efficace en pénétration cellulaire que la MCa native. Par ailleurs, elle est toujours composée de 33 résidus, taille relativement longue par rapport aux CPPs usuels. La poursuite des optimisations s'avère donc nécessaire.

Le présent travail a porté sur la réduction de la taille du CPP MCa. Douze analogues de la MCa de courte taille ont été conçus par la délétion de l'analogue linéaire, la MCa_{UF1-33}. Tous ces nouveaux analogues se sont avérés d'excellents CPPs. Ils sont, pratiquement tous, plus efficaces que la MCa linéaire non délétée (MCa_{UF1-33}). Ils pénètrent dans les cellules principalement par une voie indépendante de la macropinocytose, qui pourrait être la translocation directe. Ils sont pharmacologiquement inactifs et peu toxiques.

La MCa semble donc être un peptide hautement spécialisé pour la pénétration cellulaire, qui a les propriétés de pénétration cellulaire distribuées tout le long de sa séquence.

3.1.2. Article publié

Cell Biology:

Small Efficient Cell-penetrating Peptides Derived from Scorpion Toxin Maurocalcine

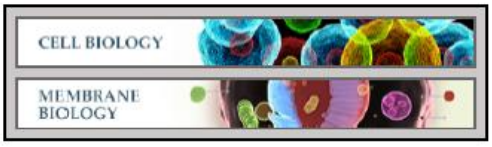

Cathy Poillot, Hicham Bichraoui, Céline Tisseyre, Eloi Bahemberae, Nicolas Andreotti, Jean-Marc Sabatier, Michel Ronjat and Michel De Waard

J. Biol. Chem. 2012, 287:17331-17342.
doi: 10.1074/jbc.M112.360628 originally published online March 20, 2012

THE JOURNAL OF BIOLOGICAL CHEMISTRY VOL. 287, NO. 21, pp. 17331–17342, May 18, 2012

Small Efficient Cell-penetrating Peptides Derived from Scorpion Toxin Maurocalcine*[S]

Received for publication, March 9, 2012 Published, JBC Papers in Press, March 20, 2012, DOI 10.1074/jbc.M112.360628

Cathy Poillot[‡§], Hicham Bichraoui[‡§1], Céline Tisseyre[‡§1], Eloi Bahemberae[‡§], Nicolas Andreotti[¶], Jean-Marc Sabatier[¶], Michel Ronjat[‡§], and Michel De Waard[‡§‖2]

From [‡]INSERM U836, Grenoble Neuroscience Institute, Site Santé La Tronche, Chemin Fortuné Ferrini, BP 170, 38042 Grenoble Cedex 9, France, the [§]Université Joseph Fourier, 38041 Grenoble, France, [¶]INSERM UMR1097, Luminy, 13288 Marseille, France, and [‖]Smartox Biotechnologies, Biopolis, 5 Avenue du Grand Sablon, 38700 La Tronche, France

Background: This study aimed at developing a new set of maurocalcine-derived cell-penetrating peptides from truncation.
Results: Several truncated peptides were designed and evaluated for Cy5 dye cell penetration.
Conclusion: All truncated peptides are competitive cell-penetrating peptides, many of them comparing favorably well with TAT.
Significance: Maurocalcine-derived truncated cell-penetrating peptides differ in their properties, enlarging the potential fields of applications.

Maurocalcine is the first demonstrated example of an animal toxin peptide with efficient cell penetration properties. Although it is a highly competitive cell-penetrating peptide (CPP), its relatively large size of 33 amino acids and the presence of three internal disulfide bridges may hamper its development for *in vitro* and *in vivo* applications. Here, we demonstrate that several efficient CPPs can be derived from maurocalcine by replacing Cys residues by isosteric 2-aminobutyric acid residues and sequence truncation down to peptides of up to 9 residues in length. A surprising finding is that all of the truncated maurocalcine analogues possessed cell penetration properties, indicating that the maurocalcine is a highly specialized CPP. Careful examination of the cell penetration properties of the truncated analogues indicates that several maurocalcine-derived peptides should be of great interest for cell delivery applications where peptide size matters.

Maurocalcine (MCa)[3] is a 33-mer peptide that was initially isolated from the venom of a Tunisian chactid scorpion, *Scorpio maurus palmatus* (1). The toxin belongs to a family of peptide that folds according to an inhibitor cystine knot motif and thus contains three disulfide bridges with a Cys^1-Cys^4, Cys^2-Cys^5, and Cys^3-Cys^6 connecting pattern (2). The solution structure, as defined by ^{1}H NMR, illustrates that MCa contains three β-strands (strand 1 from amino acid residues 9–11, strand 2 from 20–23, and strand 3 from 30–33). One distinctiveness of MCa is the fact that it is greatly enriched in basic amino acid residues. Of the 33 amino acids that compose MCa, 12 of them are basic, most of them represented by Lys residues. Interestingly, the β-strands of MCa encompass most of the basic domains (see Fig. 1*A*). MCa turned to be of interest to our research group for several reasons. First, it is an exquisite pharmacological activator of the ryanodine receptor type 1 (RyR1) from skeletal muscle because it promotes high Po gating modes and long lasting subconductance states of the ion channel (3, 4). On myotubes, application of MCa rapidly induces Ca^{2+} release from the sarcoplasmic reticulum (SR) (5), a result further confirmed by positive effect of MCa on the release of Ca^{2+} from purified SR vesicles (3, 5). The interaction of MCa with RyR1 has been witnessed by increased [^{3}H]ryanodine binding onto purified RyR1 (3, 5). The binding site for MCa on RyR1 has also been mapped and shown to correspond to domain(s) that have a predicted localization within the cytoplasm (6). Second, similarly to imperatoxin A (7) for which this was first noted, MCa has an interesting sequence homology with the II–III loop of the L-type calcium channel $Ca_v1.1$ subunit over a domain that is slightly larger than the second β-strand of MCa (see Fig. 1*A*) (5). This loop is predominantly involved in excitation-contraction coupling through direct molecular interactions with RyR1 (6, 8). This homology has been a source of inspiration to an understanding of how toxins may interfere with the process of excitation-contraction coupling (4, 8, 9). Third, and this is the scope of this paper, MCa has been shown to act as a cell-penetrating peptide (CPP) (10). This discovery stemmed from earlier criticisms that MCa may not be an activator of RyR1 because peptide toxins were not known to cross the plasma membrane, which would be required here to bind to RyR1. Studies that were undertaken to demonstrate the ability of MCa to reach its target showed that (i) MCa triggers Ca^{2+} release from the SR a few seconds after its application in the extracellular medium (5) and (ii) intracellular accumulation of fluorescent-streptavidin occurs if it incubated first with biotinylated MCa (10). Since these pioneering studies, MCa or analogues thereof proved powerful vectors for the cell entry of proteins, peptides (11),

* This work was supported by grants from Technology pour la Santé (Program TIMOMA2 of the Commissariat à l'Energie Atomique) and from Agence Nationale pour la Recherche PNANO (Programs SYNERGIE and NanoFret). Mass spectrometry analyses were performed by the Centre d'Investigation Clinique of Grenoble under the direction of Dr. Michel Sève.
[S] This article contains supplemental Figs. 1 and 2.
[1] Both authors contributed equally to this work.
[2] To whom correspondence should be addressed. Tel.: 33-4-56-52-05-63; Fax: 33-4-56-52-06-37; E-mail: michel.dewaard@ujf-grenoble.fr.
[3] The abbreviations used are: MCa, maurocalcine; Abu, 2-aminobutyric acid; CPP, cell-penetrating peptide; F, folded; Fmoc, *N*-(9-fluorenyl)methoxycarbonyl; MTT, 3-(4,5-dimethylthiazol-2-yl)-2,5-diphenyltetrazolium bromide; RyR, ryanodine receptor; SR, sarcoplasmic reticulum; UF, unfolded.

nanoparticles, or drugs such as doxorubicin (12–15). Although the mode of cell penetration of MCa may vary according to cargo nature, cell type, or chemical linkage employed, the data gathered so far suggest that the peptide may enter cells according to two priming steps onto the plasma membrane: first an interaction with proteoglycans with an affinity in the micromolar range, followed by a second interaction with negatively charged lipids which occurs with greater affinity (16, 17). The mode of cell entry of MCa is not altered by the absence of proteoglycans, but simply reduced quantitatively, suggesting that proteoglycans do not orient the mode of cell penetration. Two modes seem to concur to MCa cell entry, as far as observed, one related to macropinocytosis and another to membrane translocation. The balance between both modes of entry was found correlated to cargo nature and the type of MCa analogue used. It is of great interest to pursue the study of MCa as CPP despite the wealth of new CPP sequences that are discovered yearly. Among the competitive advantage of MCa over other CPP sequences are the facts that it has almost no associated toxicity *in vitro* and *in vivo*, penetrates into cells at very low concentrations, and is extremely stable *in vivo* upon intravenous injection (over 24 h).[4]

Although MCa appears as an elaborate and efficient CPP, its pharmacological properties represent a serious hindrance while envisioning *in vitro* and *in vivo* applications. In addition, because of its length (33 amino acid residues) and the presence of three disulfide bridges, MCa is a relatively difficult to synthesize CPP, compared with other CPPs, and would benefit from a downsizing approach. Several strategies have been employed successfully in the past to overcome one or both of these issues. The first strategy was based on single-point mutations of the MCa sequence. This strategy preserved the disulfide bridges and the three-dimensional structure of the analogues. Overall, mutations affected more seriously the pharmacology of MCa than the cell penetration properties (18). Many of the amino acids involved in RyR1 binding and pharmacology were located within the cluster of basic amino acids that presented sequence homology with the L-type $Ca_v1.1$ channel. Some of these residues, but not all, were also important for cell penetration properties. Hence, several analogues could be defined that kept close to intact cell penetration properties while entirely losing their pharmacological action (MCa R24A for instance). Some other analogues were actually better than MCa itself for cell penetration, suggesting that pairs of mutations, aiming at disrupting pharmacology and improving penetration, may be used in the future to define still better CPP analogues of MCa. The second strategy, which has yield success, is based on the chemical synthesis of D-MCa, an analogue entirely based on the use of D-amino acids. This peptide is a mirror image of the natural L-MCa but, like other D-CPPs, preserves its cell penetration properties while losing entirely its ability to interact with RyR1 (19). This method has several advantages. It no longer is sensitive to proteases that may be an additional advantage for *in vivo* experiments where the half-life of the circulating peptide matters. It is also possible to improve this analog by introducing point mutations shown previously to improve cell penetration (19). In these two strategies, although being effective, one may argue that (i) the peptides are still among the longest CPP known to date, implying increased costs of production, and (ii) the yield of production of these peptides is hampered by the folding process. Also, the use of peptides with internal disulfide bridges, despite have advantageous features in term of stability *in vivo*, makes chemical coupling of these CPPs to cargoes more complicated (difficulty to add extra Cys residues to the peptides for instance without interfering with the correct folding process). The third strategy that was used to circumvent one of this criticism was the chemical synthesis of an MCa analog in which all internal Cys residues were replaced by isosteric 2-aminobutyric acid residues (11). The resulting peptide was still 33-mer long but one step in production was saved by avoiding the folding process. In addition, an extra-Cys residue could be added to the N terminus of the peptide to favor simplified cargo grafting on this CPP analogue. This peptide, termed here C-MCa_{UF1-33} (C for extra-Cys, UF for unfolded, and 1–33 for its length; see Fig. 1*B*) no longer has any secondary structures, but efficiently penetrates into cells. Interestingly also, the peptide completely lacks pharmacological activity, indicating that folding and secondary structures are essential for binding onto RyR1. Although this peptide is an efficient CPP, it remains less potent than MCa in its folded version, suggesting that further optimization should be brought to this analogue. Such optimization appears feasible on the basis of the fact that MCa fulfills three different functions (pharmacology, obligation to resemble the L-type channel, and cell penetration). We reasoned that because only cell penetration was the quality we searched for, the peptide could be further simplified and novel analogues be designed.

In this study, we undertook to identify new more potent MCa analogues with three criteria in mind. First, these analogues should be shorter than the folded version of MCa (MCa_F) or the unfolded version (MCa_{UF}). Second, these peptides should be designed to better delimitate the domains of MCa responsible for cell penetration. Third, we should be able to design analogues with extra free SH functions for cargo grafting. We present several new analogues that have highly potent cell penetration capabilities, while losing pharmacological activity, preserving lack of cell toxicity, and with facilitated cargo grafting. This new generation of MCa analogues is predicted to have bright futures for CPP applications *in vitro* and *in vivo*.

EXPERIMENTAL PROCEDURES

Reagents—*N*-α-Fmoc-L-amino acid, Wang-Tentagel resin, and reagents used for peptide syntheses were obtained from Iris Biotech. Solvents were analytical grade products from Acros Organics. Cy5 maleimide mono-reactive dye was purchased from GE Healthcare.

Solid Phase Peptide Syntheses—Chemical syntheses of MCa analogues were performed as described previously (19). Briefly, analogues of MCa were chemically synthesized by the solid phase method (20) using an automated peptide synthesizer (CEM© Liberty). Peptide chains were assembled stepwise on 0.24 meq of Fmoc-D-Arg-Pbf-Wang-Tentagel resin using 0.24 mmol of Fmoc L-amino acid derivatives. The side chain pro-

[4] C. Poillot, H. Bichraoui, C. Tisseyre, E. Bahemberae, N. Andreotti, J.-M. Sabatier, M. Ronjat, and M. De Waard, unpublished data.

tecting groups were: Trityl for Cys and Asn; *tert*-butyl for Ser, Thr, Glu, and Asp; Pbf for Arg; and *tert*-butylcarbonyl for Lys. Reagents were at the following concentrations: Fmoc-amino acids (0.2 M Fmoc-AA-OH in dimethylformamide), activator (0.5 M 2-(1H-benzotriazole-1-yl)-1,1,3,3-tetramethyluronium hexafluorophosphate in dimethyformamide), activator base (2 M diisopropylethylamine in *N*-methyl-pyrrolidone) and deprotecting agent (5% piperazine/0.1 M 1-hydroxybenzotriazole in dimethyformamide), as advised by PepDriver (CEM©). After peptide chain assembly, resins were treated 4 h at room temperature with a mixture of TFA/water/triisopropylsilan/dithiothreitol (DTT) (92.5/2.5/2.5/2.5). The peptide mixtures were then filtered, and the filtrates were precipitated by adding cold *t*-butylmethyl ether. The crude peptides were pelleted by centrifugation (10,000 × *g*, 15 min), and the supernatants were discarded. MCa analogues were purified by HPLC using a Vydac C18 column (218TP1010, 25 × 10 cm). Elutions of the peptides were performed with a 10–60% acetonitrile linear gradient containing 0.1% TFA. The purified fractions were analyzed by analytical RP-HPLC (Vydac C18 column 218TP104, 25 × 4.6 cm). All analogues were characterized by MALDI-TOF mass spectrometry.

Labeling of Peptide with Cy5—Each peptide was labeled with Cy5 according to the manufacturer's protocol (GE Healthcare). Peptides were dissolved at 1 mg/ml in 0.1 M Na_2CO_3 buffer, pH 9.3. 300 μl of the solubilized peptides was added to Cy5-maleimide-containing tubes. The mixtures were incubated for 2 h at room temperature and then purified by HPLC using an analytical Vydac C18 column. Elution of the Cy5-labeled peptides was performed with a 10–60% acetonitrile linear gradient containing 0.1% TFA. The pure peak fractions were lyophilized and peptides quantified by UV spectrophotometer at 649 nm.

Cell Culture—Chinese hamster ovary (CHO) and F98 cell lines (from ATCC) were maintained at 37 °C in 5% CO_2 in F-12 nutrient medium (Invitrogen) supplemented with 10% (v/v, CHO) or 2% (v/v, F98) heat-inactivated fetal bovine serum (Invitrogen) and 100 units/ml streptomycin and penicillin (Invitrogen).

MTT Assay—Cells were seeded into 96-well micro plates at a density of ~8×10^4 cells/well. After 2 days of culture, the cells were incubated for 24 h at 37 °C with MCa analogues at a concentration of 10 μM. Control wells containing cell culture medium alone or with cells, both without peptide addition, were included in each experiment. 0.1% saponin was used as toxic agent for comparison. The cells were then incubated with MTT for 30 min. Conversion of MTT into purple colored MTT formazan by the living cells indicates the extent of cell viability. The crystals were dissolved with dimethyl sulfoxide, and the optical density was measured at 540 nm using a microplate reader (Biotek ELx-800; Mandel Scientific Inc.) for quantification of cell viability. All assays were run in triplicate.

Confocal Microscopy—For analysis of the subcellular localization of MCa-Cy5 analogues in living cells, cell cultures were incubated with the fluorescent peptides for 2 h and then washed with phosphate-buffered saline (PBS) alone. The plasma membrane was stained with 5 μg/ml rhodamine-conjugated concanavalin A (Molecular Probes) for 5 min. Cells were washed once more. Live cells were then immediately analyzed by confocal laser scanning microscopy using a Leica TCS-SPE operating system. Rhodamine (580 nm) and Cy5 (670 nm) were sequentially excited, and emission fluorescence was collected in z-confocal planes of 10–15-nm steps.

Fluorescence-activated Cell Sorting—CHO cells were incubated with various concentrations of Cy5-labeled peptides in F-12K culture medium without serum at 37 °C for 2 h. The cells were then washed with PBS to remove excess extracellular peptide and treated with 1 mg/ml trypsin (Invitrogen) for 5 min at 37 °C to detach cells from the surface and centrifuged at 200 × *g* before suspension in PBS. For experiments with the macropinocytosis inhibitor, amiloride, CHO cells were initially washed with F-12K and preincubated for 30 min at 37 °C with 1 mM amiloride (Sigma). The cells were then incubated for 2 h at 37 °C with 1 μM Cy5-MCa analogues. For all of these experimental conditions, flow cytometry analyses were performed with live cells using a Becton Dickinson FACS LSR II flow cytometer (BD Biosciences). Data were obtained and analyzed using FCS express software (De Novo). Live cells were gated by forward/side scattering from a total of 10,000 events.

Preparation of Heavy SR Vesicles—Heavy SR vesicles were prepared following the method of Kim *et al.* (21). Protein concentration was measured by the Biuret method.

[^{3}H]Ryanodine Binding Assay—Heavy SR vesicles (1 mg/ml) were incubated at 37 °C for 2 h in an assay buffer composed of 10 nM [^{3}H]ryanodine, 150 mM KCl, 2 mM EGTA, 2 mM $CaCl_2$ (pCa = 5), and 20 mM MOPS, pH 7.4. Truncated MCa analogues were added prior to the addition of heavy SR vesicles. [^{3}H]Ryanodine bound to heavy SR vesicles was measured by filtration through Whatman GF/B glass filters followed by three washes with 5 ml of ice-cold washing buffer composed of 150 mM NaCl, 20 mM HEPES, pH 7.4. [^{3}H]Ryanodine retained on the filters was measured by liquid scintillation. Nonspecific binding was measured in the presence of 80 μM unlabeled ryanodine. The data are presented as mean ± S.E. Each experiment was performed in triplicate.

Statistical Analyses—All data are given as mean ± S.D. for n number of observations, and statistical significance (p) was calculated using Student's t test.

RESULTS

Nonfolded Truncated Maurocalcine Peptides Are Efficient CPPs—Fig. 1*A* illustrates the primary structure of MCa with its secondary structures (β-strands) and its pattern of disulfide bridges. This peptide will be termed MCa_F, for folded (F) MCa. An earlier report has demonstrated that replacing the six internal cysteine residues of MCa by Abu residues results in a pharmacologically inert and unfolded (UF) CPP (MCa_{UF1-33}, Fig. 1*B*). This peptide loses its secondary structures (11). Because this project aims at identifying shorter CPP sequences based on MCa_{UF1-33} sequence by the delivery of Cy5 cargo, we first determined where at the N terminus (C-MCa_{UF1-33}) or C terminus (MCa_{UF1-33}-C) the cargo could be best grafted after addition of an extra cysteine residue (C) (Fig. 1*B*). As shown, both vector-cargo complexes Cy5-C-MCa_{UF1-33} and MCa_{UF1-33}-C-Cy5 penetrated efficiently within CHO cells, as estimated by confocal microscopy (Fig. 1*C*) or by FACS (Fig. 1*D*). At 3 μM, a slightly better cell penetration was observed with Cy5 localized

Small Cell-penetrating Maurocalcine Peptides

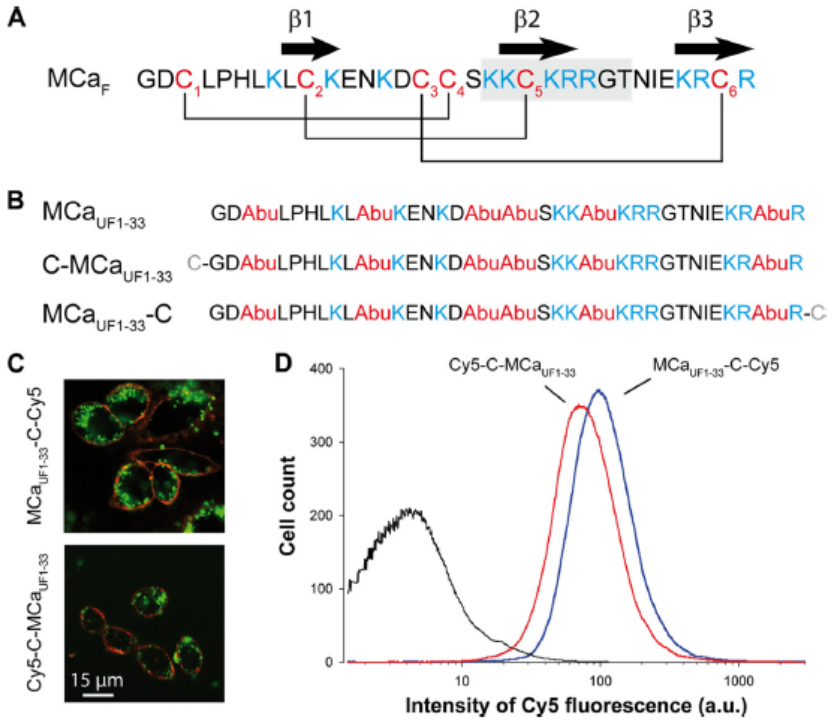

FIGURE 1. **Efficacy of cargo penetration as function of grafting position on MCa$_{UF1-33}$.** *A*, amino acid sequence of MCa$_F$ in single-letter code. The positions of half-cystine residues are *highlighted* in *red*. Cys residues are *numbered*, and basic amino acids are *highlighted* in *blue*. Secondary structures (β-strands) are indicated by *arrows*. The *gray box* is the sequence of homology of MCa with the dihydropyridine-sensitive Ca$_v$1.1 channel. *B*, amino acid sequences of unfolded MCa analogues in single-letter code. Cys residues are replaced by isosteric 2-aminobutyric acid residues (*Abu*, in *red*) to form MCa$_{UF1-33}$. An additional N-terminal (C-MCa$_{UF1-33}$) or C-terminal (MCa$_{UF1-33}$-C) Cys residue was added in two novel analogues competent for cargo grafting (shown in *gray*). *C*, confocal microscopy images illustrating cell penetration of Cy5-C-MCa$_{UF1-33}$ and MCa$_{UF1-33}$-C-Cy5 (*green labeling*). Plasma membranes are labeled with concanavalin A-rhodamine (in *red*). CHO cells were incubated 2 h with 1 μM peptide concentration. *D*, comparison of cell penetration efficacy between Cy5-C-MCa$_{UF1-33}$ and MCa$_{UF1-33}$-C-Cy5 as determined by FACS. CHO cells were incubated for 2 h with 3 μM peptide, washed and treated 5 min by 1 mg/ml trypsin before quantification of intracellular fluorescence. *a.u.*, arbitrary unit.

at the C terminus of MCa$_{UF1-33}$, but this difference was not significant. Because chemical syntheses of truncated MCa$_{UF1-33}$ analogues was facilitated by adding the extra cysteine residue at the C terminus of the sequence rather than at the N terminus, we kept on working on the basis of MCa$_{UF1-33}$-C sequence. Nevertheless, these data indicate for the first time that cargo grafting on the CPP MCa$_{UF1-33}$ can be performed likewise at both extremities of the sequence.

Next, we designed a series of truncated MCa$_{UF}$-C peptides comprising either a C-terminal truncation (three analogues: MCa$_{UF1-20}$-C, MCa$_{UF1-15}$-C, and MCa$_{UF1-9}$-C), a N-terminal truncation (7 analogues: MCa$_{UF8-33}$-C, MCa$_{UF11-33}$-C, MCa$_{UF14-33}$-C, MCa$_{UF18-33}$-C, MCa$_{UF20-33}$-C, MCa$_{UF22-33}$-C, and MCa$_{UF25-33}$-C), and Both N- and C-terminal truncations (2 analogues: MCa$_{UF6-25}$-C and MCa$_{UF14-25}$-C) (Fig. 2*A*). All of these analogues were then labeled with Cy5 to investigate their cell penetration properties. Every one of these peptides has been designed in such a way that the cargo would be removed from the peptide upon trypsin cleavage. This was useful for the FACS experiments in which the fluorescence associated to the cells is measured after trypsin treatment, thereby potentially removing the cargo from peptides that would eventually be associated with the outer part of the plasma membrane. The net positive charges of the peptides were drastically different, ranging from 0 (MCa$_{UF1-15}$-C and MCa$_{UF1-9}$-C) to +8 (MCa$_{UF8-33}$-C). However, many of the peptides contained a percentage of positively charged residues equal (MCa$_{UF-25-33}$-C) or superior to MCa$_F$ or MCa$_{UF1-33}$ (8 of 12 analogues). Three analogues had a lower percentage of basic residues than MCa$_F$ (all three C-terminal truncated analogues, MCa$_{UF1-20}$-C, MCa$_{UF1-15}$-C, and MCa$_{UF1-9}$-C).

We first evaluated by FACS the fluorescence accumulation within CHO cells that occurred after a 2 h incubation with 3 μM positively charged MCa peptides (net charge ≥ +5; Fig. 2*B*). This first study revealed several unexpected findings. First, all of the charged peptides (8 tested) demonstrated CPP properties. These peptides all had the K^{22}R^{23}R^{24} sequence in common, a cluster of basic amino acid residues shown to contribute to the dose efficacy of cell penetration of MCa$_F$ in an earlier study (18). Interestingly, removing the last 8 C-terminal amino acids of MCa had little impact on the cell penetration properties (if one compares MCa$_{UF14-25}$-C with MCa$_{UF14-33}$-C). Similarly, the removal of the amino acid region His^6-Asn^{13} did not drastically change cell penetration properties (MCa$_{UF6-25}$-C *versus* MCa$_{UF14-25}$-C). Second, all peptides appeared to behave better than the reference peptide MCa$_{UF1-33}$-C, suggesting that

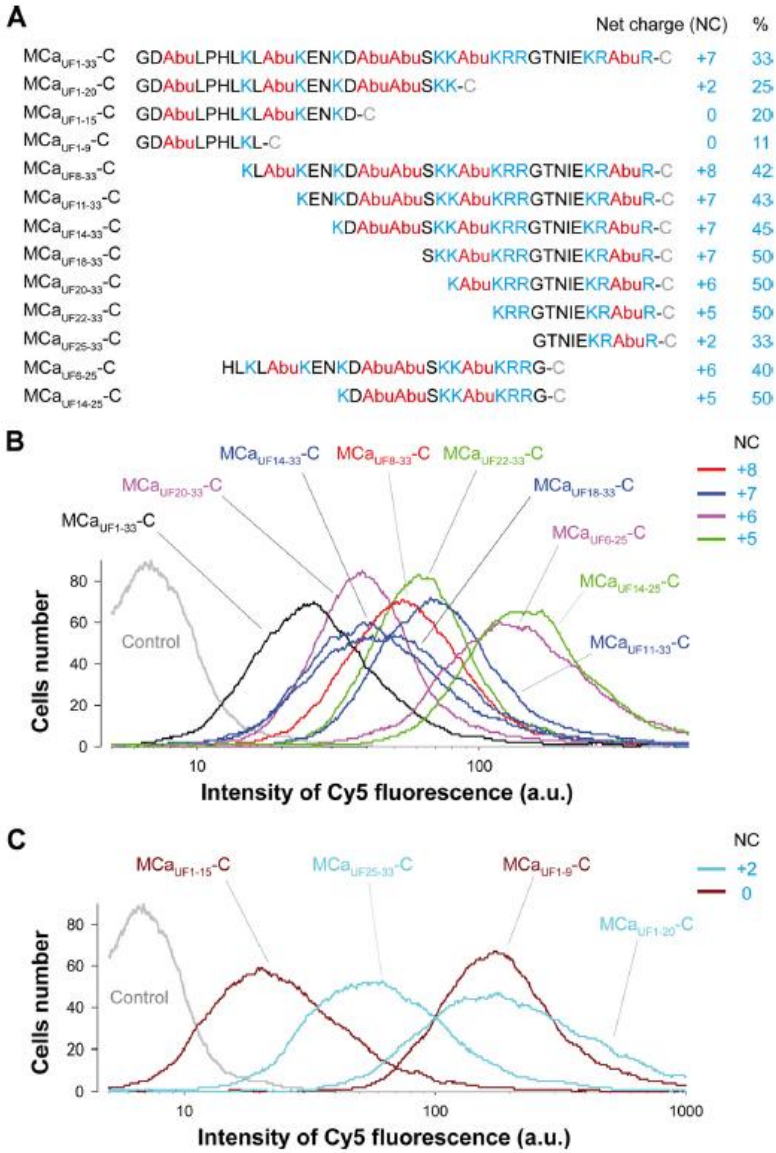

FIGURE 2. **Primary structure of truncated MCa$_{UF}$ analogues and comparison of cell penetration efficacies.** *A*, primary structures of truncated MCa$_{UF}$-C analogues and determination of their net positive charge and percentage of basic amino acid residues within the sequence. A total of 12 truncated MCa$_{UF}$-C analogues were produced (three with truncations in C terminus, seven in N terminus, and two in both N and C termini). Positively charged residues are in *blue* (His residues were not counted), whereas Abu residues that replace Cys residues are in *red*. *B*, comparative cell penetration efficacy of all MCa$_{UF}$-C-Cy5 truncated analogues that possess a net positive charge ≥ +5. Code colors: *red* (net charge +8), *blue* (+7), *pink* (+6), and *green* (+5). The nontruncated MCa$_{UF1-33}$-C-Cy5 analogue is shown as reference (*black line*) for the efficacy of cell penetration of all analogues. Experimental conditions: CHO cell incubation with 1 μM concentration of each analogue for 2 h and fluorescence quantification by FACS. *a.u.*, arbitrary unit. *C*, same as *B* but for truncated MCa$_{UF}$-C-Cy5 analogues with positive net charge ≤ +2.

sequence truncation of MCa$_{UF}$ may represent a potent strategy to define more efficient CPPs. Less positively charged peptides were also tested for their ability to penetrate into CHO cells (Fig. 2*C*). No less surprisingly, all peptides showed CPP properties, including two peptides with no net positive charge (MCa$_{UF1-9}$-C and MCa$_{UF1-15}$-C). MCa$_{UF1-9}$-C appeared as a better CPP than MCa$_{UF1-15}$-C, suggesting that the Abu^{10}-Asp^{15} region introduces no competitive advantage and confirming results shown in Fig. 2*B*. This may represent an inhibitory region because of the presence of Glu^{12} and Asp^{15}, two negatively charged residues. The finding that mutation of Glu^{12} to Ala enhances cell penetration of both MCa$_F$ (18) and MCa$_{UF}$ (11) further supports this conclusion. MCa$_{UF25-33}$-C turned out to have CPP properties also, even though this sequence did not confer a competitive advantage to other MCa CPP analogues as shown in Fig. 2*B*. Two additional experiments were conducted

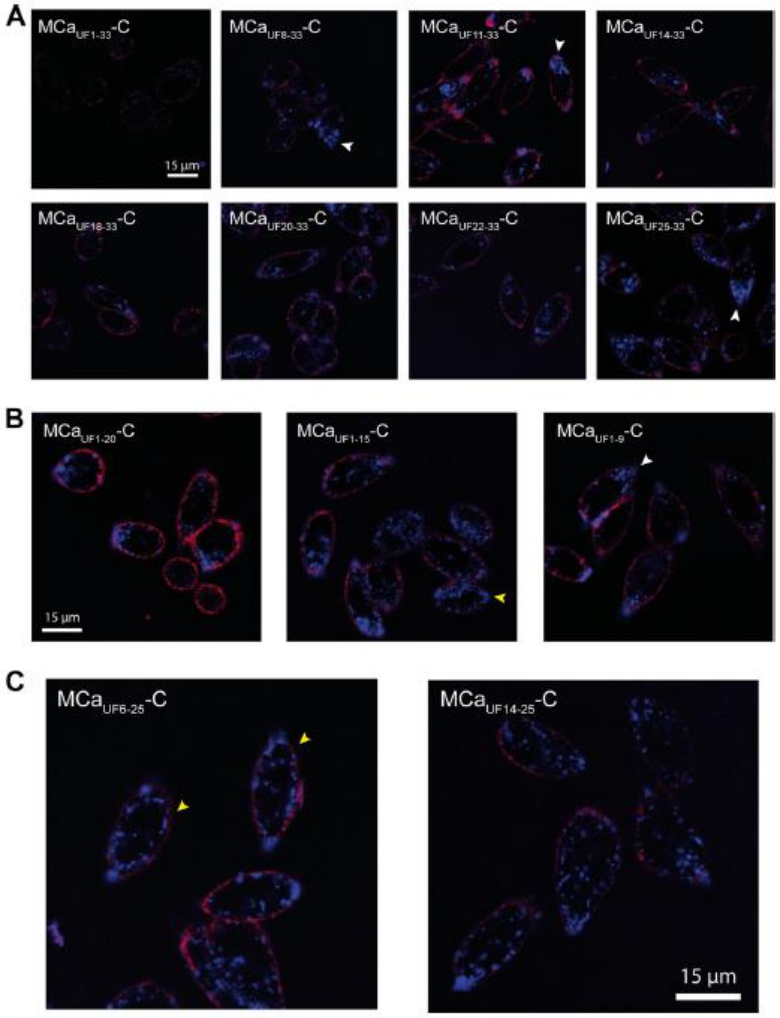

FIGURE 3. **All truncated MCa$_{UF}$-C-Cy5 vector-cargo complexes have resembling intracellular distributions.** *A*, intracellular distribution of N-terminal truncated MCa$_{UF}$ analogues. *B*, intracellular distribution of C-terminal truncated MCa$_{UF}$ analogues. *C*, intracellular distribution of N- and C-terminal truncated MCa$_{UF}$ analogues. CHO cells were incubated for 2 h with 3 μM MCa$_{UF}$-C-Cy5 vector-cargo complexes, before extensive washing, membrane labeling with rhodamine-conjugated concanavalin A, and live cell confocal microscopy imaging. Cy5 is in *blue*, and rhodamine is in *red*. *White arrows* illustrate a tendency for a preferential apical localization of the Cy5 dye. *Yellow arrows* illustrate the tendency for a subplasma membrane labeling of the Cy5 dye.

to confirm the specificity of these findings. First, a truncated charybdotoxin peptide was synthesized (ChTx$_{UF1-12}$-C) in which the internal Cys residue was replaced by Abu and an additional C-terminal Cys residue added for Cy5 labeling, as for our MCa$_{UF}$ analogues (supplemental Fig. 1*A*). As shown by confocal microscopy, ChTx$_{UF1-12}$-C was unable to deliver the Cy5 cargo at a higher concentration of 5 μM. Second, we also designed two MCa$_{UF}$ peptides in which, instead of using Abu derivatives, we mutated internal Cys residues by Ala residues. As shown, both MCa$_{UF1-9(Ala)}$-C and MCa$_{UF14-25(Ala)}$-C worked well for Cy5 delivery into CHO cells, demonstrating that Abu residues were not responsible by themselves for the cell penetration properties of the peptides (supplemental Fig. 1, *B* and *C*). Ala residues were, however, not fully equivalent to Abu residues as dose-response curve was slightly better for MCa$_{UF14-25(Ala)}$-C than for MCa$_{UF14-25}$-C, further arguing that Abu residues were not central to the cell penetration properties of truncated MCa$_{UF}$ peptides (supplemental Fig. 1*D*). The overall message from this first study is that all truncated MCa$_{UF}$ analogues can behave as CPPs at the concentration tested. The findings suggest that MCa is a peptide fully specialized to achieve cell penetration including in domains that are not highly charged.

Intracellular Distribution of All Truncated MCa$_{UF}$ Analogues Bears Resemblance to That of Full-length MCa$_{UF}$—Although all truncated derivatives of MCa$_{UF1-33}$ show cell penetration properties according to the FACS analyses, we examined whether there were differences in intracellular distribution among these peptides. This question was investigated by confocal microscopy after 2 h of peptide accumulation into CHO cells (Fig. 3). Interestingly, all peptides showed very sim-

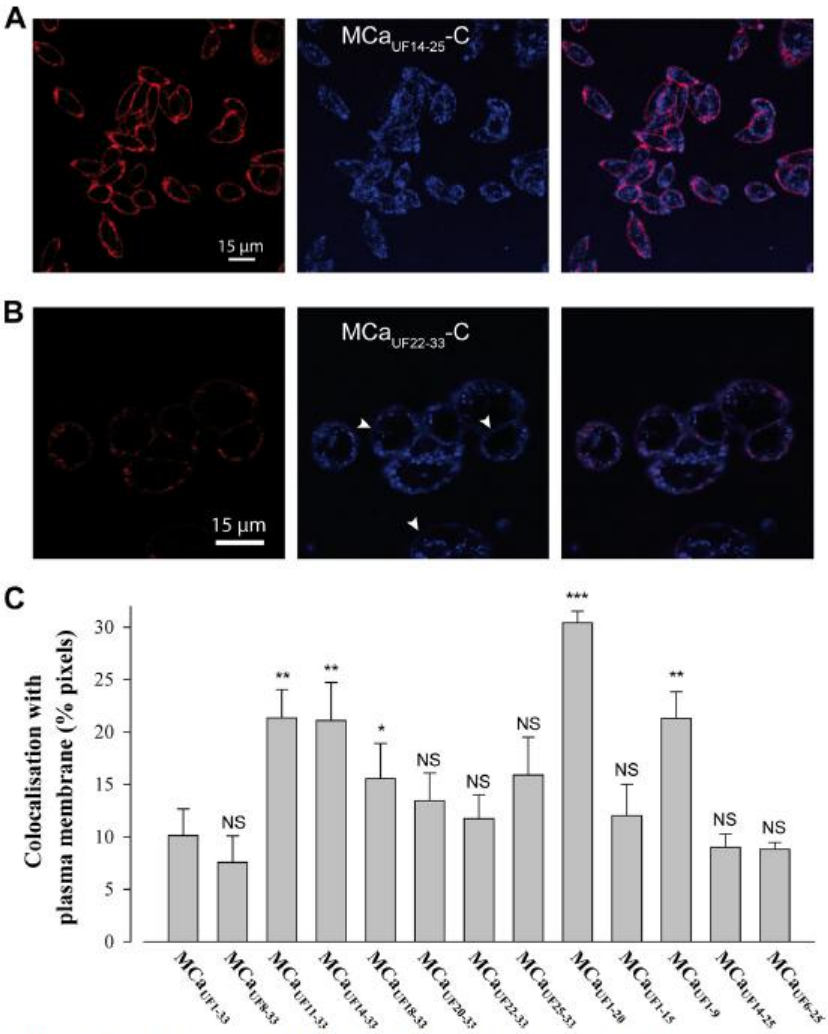

FIGURE 4. **Membrane staining is diffuse whereas intracellular staining is punctuated.** *A*, lower magnification image of CHO cells stained with 3 μM MCa$_{UF14-25}$-C-Cy5 that illustrates a predominant subplasma membrane rim-like distribution. *B*, diffuse membrane staining of CHO cells by MCa$_{UF22-33}$-C-Cy5. *White arrows* indicate domains of the plasma membrane where the diffuse staining of the peptide-cargo complex is the most evident. *C*, extent of colocalization of the Cy5-labeled peptides with the rhodamine-labeled plasma membrane. *NS*, nonsignificant; *, ≤0.1; **, ≤0.05; and ***, ≤0.001.

ilar intracellular distributions, although the degree of accumulated cell fluorescence varied somewhat with peptide sequences. In confirmation of the FACS results, the peptide that appeared to penetrate the least was the full-length unfolded MCa, MCa$_{UF1-33}$-C-Cy5 (Fig. 3*A*). The vast majority of the fluorescence appears in punctuate dots within the cells. In many cases, these dots appear at higher concentrations within one pole of the cell (see labeling of MCa$_{UF8-33}$-C-Cy5, MCa$_{UF11-33}$-C-Cy5, MCa$_{UF25-33}$-C-Cy5, and MCa$_{UF1-9}$-C-Cy5, for instance). On various occasions also, all of the peptides tend to present a subplasma membrane distribution, forming a rim of smaller circumference than the concanavalin A labeling itself. This subplasma membrane rim localization was more evident for CHO cells labeled with MCa$_{UF14-25}$-C-Cy5 as illustrated in Fig. 4*A*. Finally, more rarely, a direct plasma membrane labeling by the peptide-cargo complex was observable (Fig. 4*B*). This type of labeling could be observed with N-terminal truncated vectors exclusively and was most evident for MCa$_{UF22-33}$-C-Cy5. The staining of the plasma membrane was always diffuse in contrast to intracellular staining which was mainly punctuated. Diffuse membrane labeling was also observed for MCa$_{UF25-33}$-C-Cy5 and MCa$_{UF20-33}$-C-Cy5, two peptides that differ from 2 to 3 amino acids of MCa$_{UF22-33}$-C-Cy5. It was difficult to evidence for the other vector-cargo complexes. We propose that this staining coincides with an alteration of the duration of peptide plasma membrane residency for these truncated MCa$_{UF}$ analogues. The lower occurrence of this diffuse staining for the other truncated variants may reflect faster internalization by endocytosis and/or membrane translocation. Globally, these effects reflect cell entry and distribu-

tion tendencies that were hard to quantify, and they should therefore be interpreted with caution.

In an attempt to better apprehend peptide behavior at the plasma membrane, we quantified the extent of Cy5/rhodamine staining colocalization. Rhodamine-positive staining was also Cy5-positive for 63–86% of the pixels (best performing peptides were $MCa_{UF14-33}$-C-Cy5, $MCa_{UF18-33}$-C-Cy5, $MCa_{UF20-33}$-C-Cy5, and $MCa_{UF22-33}$-C-Cy5; data not shown). This finding indicates that the peptides invade large membrane areas and that membrane interaction is not limited to small specialized surface areas. In contrast, Cy5-positive pixels were rhodamine-positive to far more variable extents (Fig. 4*C*). For instance, 10.1 ± 2.6% of MCa_{UF1-33}-C-Cy5, the reference compound, was colocalized with the plasma membrane indicator. Despite the fact that short plasma membrane staining times were used (few minutes), a fraction of the colocalization that is quantified also corresponds to intracellular staining following ongoing endocytosis. Nevertheless, this result indicates that this peptide does not remain stuck within the plasma membrane during its 2-h incubation with CHO cells. It thus indicates relatively fast cell penetration. Many of the other peptides, however, behaved differently from MCa_{UF1-33}-C-Cy5. Indeed, several peptides show surprisingly higher colocalization with rhodamine (21.3 ± 2.6% for $MCa_{UF11-33}$-C-Cy5 and 30.4 ± 1.4% for MCa_{UF1-20}-C-Cy5, for instance). These higher values of colocalization indicate that some peptides remain for longer periods of time or at higher concentration within the plasma membrane. Alternatively, these peptides may rely more heavily on endocytosis for cell penetration and are present within intracellular organelles to which subsequent endocytotic vesicles that contain rhodamine labeling will fuse. Peptides most concerned by these behaviors were $MCa_{UF11-33}$-C-Cy5 and $MCa_{UF14-33}$-C-Cy5, which contained two or one of the CPP inhibitory negative charges (Glu^{12} and Asp^{15}), and MCa_{UF1-9}-C-Cy5 and MCa_{UF1-20}-C-Cy5, which were poorly charged peptides.

Amiloride Sensitivity of Cell Penetration of Truncated MCa_{UF} Analogues—In earlier studies, we have demonstrated that the cell entry of MCa_{UF1-33} was largely sensitive to amiloride. Because amiloride is an exquisite blocker of macropinosomes (22–24), this suggested a predominant macropinocytosis mechanism for its cell penetration (17). However, it was likely that such a predominant reliance on macropinocytosis was also conferred by the cargo type transported (streptavidin in that report). We therefore conducted an in-depth analysis of the amiloride sensitivity of the various truncated MCa_{UF} peptides with Cy5 as cargo and quantified by FACS the degree of cell penetration inhibition. Fig. 5*A* illustrates the amiloride sensitivity of four different truncated peptides. As shown, amiloride inhibits the cell penetration of MCa_{UF1-33}-C-Cy5 by 19.6% and of MCa_{UF1-15}-C-Cy5 by 39%. The finding that amiloride blocks to a far lesser extend the penetration of Cy5 compared with that of streptavidin (17) when MCa_{UF1-33} is the vector indicates the influence of the cargo nature on the mechanism of cell entry. Surprisingly, amiloride was found to enhance rather than inhibit the cell penetration of $MCa_{UF20-33}$-C-Cy5 and $MCa_{UF18-33}$-C-Cy5 (Fig. 5*A*). Preserving the plasma membrane from undergoing macropinocytosis may free surface areas for enhanced peptide translocation through the membrane. The effect of amiloride was always associated with a sharpening of the fluorescence intensity distribution in the *x* axis (see, for instance MCa_{UF1-15}-C-Cy5), reflecting reduced cell heterogeneity for the mechanisms underlying peptide penetration. The amiloride sensitivity of cell penetration was further investigated for all truncated MCa_{UF} peptides, and the results are presented in Fig. 5*B*. Four peptides showed higher amiloride sensitivity than MCa_{UF1-33}-C-Cy5 ($MCa_{UF11-33}$-C-Cy5, $MCa_{UF25-33}$-C-Cy5, MCa_{UF1-15}-C-Cy5, and $MCa_{UF14-25}$-C-Cy5). All other peptides showed reduced amiloride sensitivities or a tendency for greater cell penetration under the effect of amiloride. We conclude that the Cy5 cargo does not promote macropinocytosis as the main route of peptide entry and that truncation of MCa_{UF} may lead to analogues that rely to a lesser extent on macropinocytosis for cell entry.

Comparative Dose-dependent Cell Penetration of MCa_{UF} Analogues—Although we compared the properties of cell penetration of truncated peptides at rather mild concentrations, we also aimed at comparing the dose dependence of cell penetration of these peptides by FACS (Fig. 6). One example of such an analysis is shown for peptide MCa_{UF8-33}-C-Cy5 in Fig. 6*A*. 33 μM was the highest concentration that could be tested on CHO cells, and obviously cell penetration did not show any sign of saturation for cell incubation times with this peptide of 2 h. The dose-dependent cell penetrations were compared for all N-terminal truncated peptides (Fig. 6*B*), C-terminal truncated peptides (Fig. 6*C*), and double truncated analogues (Fig. 6*D*) with the same settings. These analyses confirm that MCa_{UF1-33}-C-Cy5 is the least performing cell-penetrating peptide. Most truncated peptides show detectable cell penetration at concentrations ≥1 μM. One remarkable exception to this rule was noticeable. MCa_{UF1-9}-C-Cy5 shows an unusual dose-dependent penetration with detectable cell penetration at 10 nM and only small progressive increases in fluorescence intensity with higher peptide concentrations (Fig. 6*C*). This peptide was therefore the best performing peptide for cell penetration at low concentrations. Finally, additional information that could be taken from these analyses is that the peptides differed significantly with regard to the maximal extent of cell penetration. Among the N-terminal truncated MCa_{UF} analogues, $MCa_{UF18-33}$-C-Cy5 performed drastically better than the other truncated peptides (Fig. 6*B*). The difference in cell penetration among $MCa_{UF11-33}$-C-Cy5 and $MCa_{UF18-33}$-C-Cy5 resides in the removal of the KENKDAbuAbu sequence which we presume is inhibitory to some extent because of the presence of Glu^{12} and Asp^{15}. Among the C-terminal truncated peptides, MCa_{UF1-20}-C-Cy5 was performing as well as MCa_{UF8-33}-C-Cy5, and although not tested at higher concentrations, MCa_{UF1-9}-C-Cy5 would be expected to perform still better. Finally, for N- and C-terminal truncated analogues, the best peptide turns out to be $MCa_{UF14-25}$-C-Cy5, which yields the greatest fluorescence accumulation at 33 μM compared with all other truncated MCa_{UF} analogues. Whereas all of these peptides performed quite well, we were curious to compare them with a classical CPP under similar experimental conditions. Cell penetration was observed for TAT-C in CHO cells, and the dose-response curve was equivalent or even less favorable for TAT than for many MCa_{UF} peptides (supplemental Fig. 1, *E*

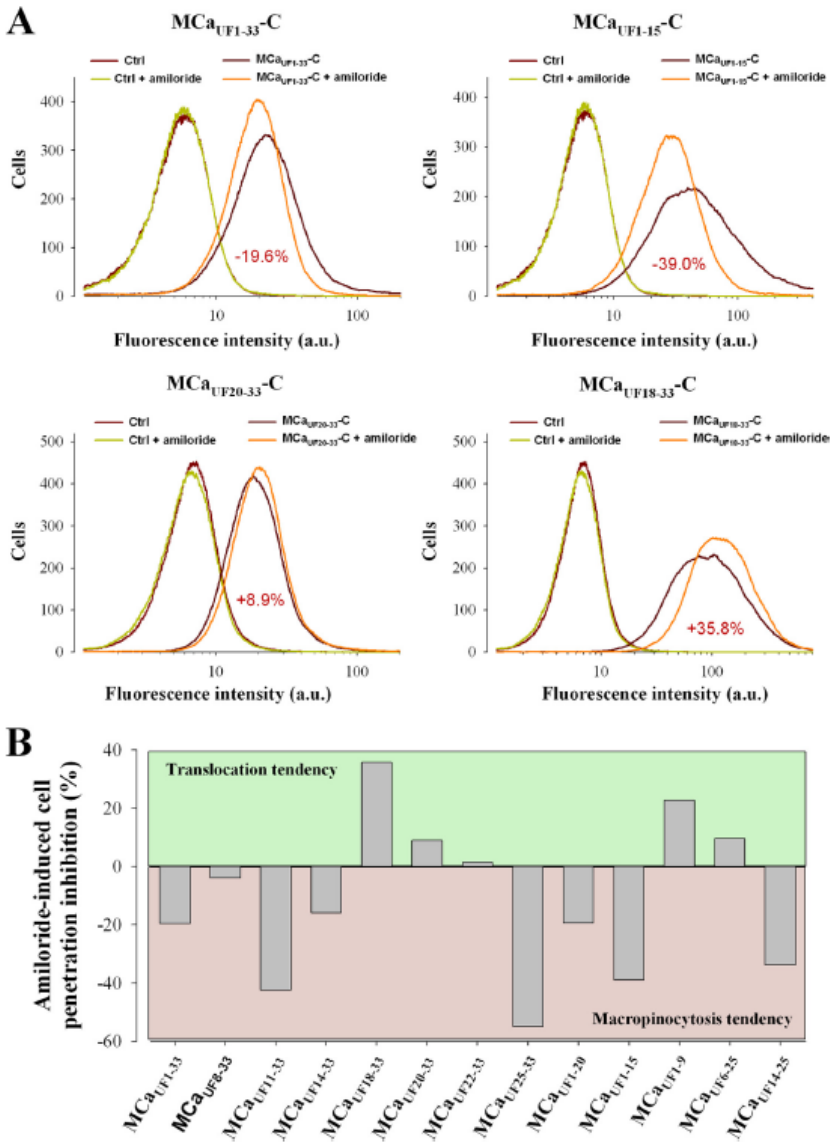

FIGURE 5. **Amiloride sensitivity of truncated MCa$_{UF}$ peptide cell entry.** *A*, representative FACS analyses of the effect of 5 mM amiloride on MCa$_{UF1-33}$-C-Cy5 (*upper left*), MCa$_{UF1-15}$-C-Cy5 (*upper right*), MCa$_{UF20-33}$-C-Cy5 (*lower left*), and MCa$_{UF18-33}$-C-Cy5 (*lower right*) entries. *Numbers* in *red* represent average decrease or increase in peptide entry upon amiloride treatment. Cells were treated for 2 h with 3 μM peptide concentration with or without 5 mM amiloride. *a.u.*, arbitrary unit. *B*, average effect of amiloride on mean cell entry of the truncated peptides. Positive values reflect increase in cell entries, whereas negative values indicate reduction in cell penetration.

and *F*). This was further largely confirmed when comparing the vector properties of TAT-C and MCa$_{UF1-9}$-C in yet another cell type, the glioma F98 rat cell line (supplemental Fig. 2). 3 μM MCa$_{UF1-9}$-C proved better than TAT-C at 3 and 10 μM.

Truncated MCa$_{UF}$ Peptides Lack Pharmacological Effects and Are Predominantly Nontoxic—An earlier report has shown that MCa$_{UF1-33}$ is unable to interact with the MCa target, RyR1 (11). This is due to the loss of secondary structures because of the lack of internal disulfide bridging. We did therefore expect that truncated analogues of MCa$_{UF}$ should also be pharmacologically inert. This hypothesis was challenged by testing the ability of the Cy5-free peptides to stimulate [^{3}H]ryanodine binding (Fig. 7*A*). As shown, contrary to MCa$_F$, which contains secondary structures and disulfide bridges, none of the peptides we designed had an effect on [^{3}H]ryanodine binding.

Finally, the peptides were challenged for their toxicity by incubating CHO cells with 1 or 10 μM peptide concentrations for an extended duration (24 h) that far exceeds the duration challenged for cell penetration (Fig. 7*B*). A 10 μM peptide concentration was generally slightly more toxic than 1 μM, except for MCa$_{UF14-25}$-C. At 1 μM, toxicity never exceeded 8%, and significances of these effects were negligible. In contrast, toxic-

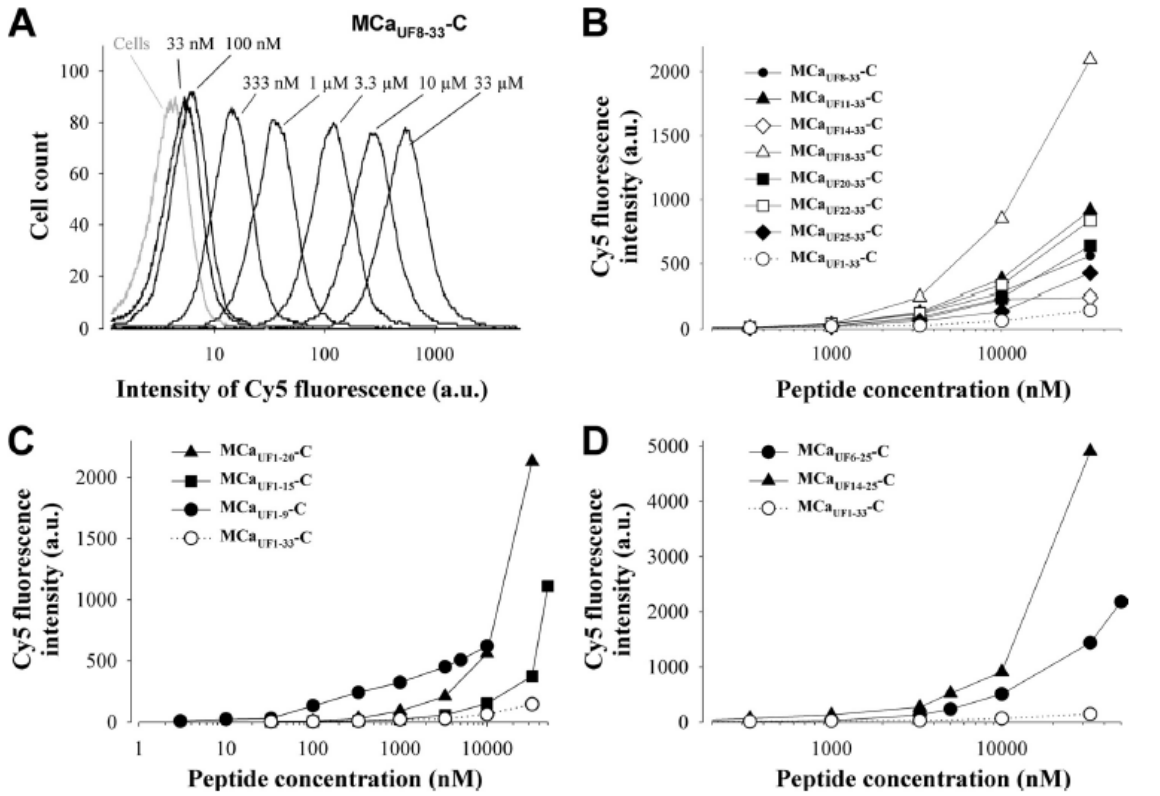

FIGURE 6. **Dose-dependent cell penetration of truncated MCaUF peptides.** *A*, representative example of the dose-dependent cell penetration of MCa$_{UF8-33}$-C -Cy5 in CHO cells as analyzed by FACS. The peptide was incubated for 2 h with the cells before analyses. There was no saturation of cell entry for a concentration up to 33 μM. *B*, dose-dependent cell penetration of N-terminal truncated MCa$_{UF}$ peptides compared with MCa$_{UF1-33}$-C-Cy5 (*open circles, dotted line*). *a.u.*, arbitrary unit. *C*, dose-dependent cell penetration of C-terminal truncated MCa$_{UF}$ peptides. *D*, dose-dependent cell penetration of N- and C-terminal truncated MCa$_{UF}$ peptides. Note the increase in scale for the penetration of these two peptides.

ity could reach 20% at 10 μM peptide concentration, and these effects had higher significance. Most peptides behaved equally well or better than MCa$_{UF1-33}$-C, indicating that truncation did not enhance cell toxicity of the peptides.

DISCUSSION

MCa$_F$ is a rather large and complex CPP with its three disulfide bridges which makes its use in *in vitro* and *in vivo* applications more delicate because of production yield (peptide with correct disulfide bridging) and cargo coupling (thiol groups are for the moment difficult to use). One may also argue that the size of the peptide introduces additional synthesis cost compared with other popular in use CPPs such as Tat and penetratin. Whereas size and folding most likely add a competitive advantage for *in vivo* applications because of peptide stability issues, it may be of interest to derive small CPPs from MCa that could have a broader use than MCa itself. The study we conducted not only aimed at defining these smaller MCa-derived CPP sequences, but also provided interesting clues on how MCa may have evolved for cell penetration. The most surprising finding from this study was therefore that all of the analogues we defined could be considered as CPPs, which suggests that MCa is a highly specialized sequence for the purpose of cell penetration. Although evidently none of the peptides could compete with MCa$_F$ itself for cell penetration, it is nevertheless obvious that many of the truncated MCa$_{UF}$ peptides are better CPPs than MCa$_{UF1-33}$ itself. These findings lead to two general conclusions. First, folding and disulfide bridging appear to be prerequisites to properly optimizing the CPP potential of all of the MCa domains. It is highly likely that the secondary structures triggered by disulfide bridging play a key role in that respect. We therefore believe that it would be worthwhile to design additional MCa analogues presenting both truncations (like in the present study) and 1 to 2 disulfide bridges to regain some of the secondary structures that confer a competitive advantage to MCa$_F$ for cell penetration. Second, the fact that all of the truncated sequences are CPPs that possess different properties and efficacies suggests that there is further room for MCa cell penetrating optimization. In this study, our data indicate that the amino acid region Lys^{11}-Ser^{18} would be an ideal target for mutagenesis. Glu^{12} mutation has already been shown to improve cell penetration on various analogues (11, 18). We now sense that Asp^{15} may also represent an excellent target for further optimization of MCa properties. Double mutagenesis may be an option. However, it will be essential to determine whether the disulfide bridging and folding ability of the native peptide is not affected by this procedure. Truncated MCa$_{UF}$

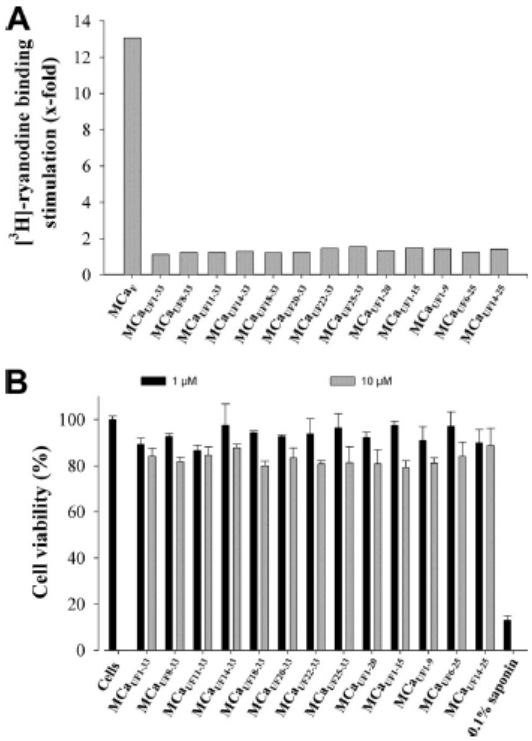

FIGURE 7. **Lack of pharmacological effects of the truncated peptides and reduced cell toxicity.** *A*, effect of MCa_F, MCa_{UF1-33}, and truncated MCa_{UF} peptides on [^{3}H]ryanodine binding. Data are expressed as -fold increase in binding induced by the peptides. *B*, effect of 1 and 10 μM MCa_{UF1-33} and truncated MCa_{UF} peptides on CHO cell viability. Peptides were incubated for 24 h with the cells *in vitro*.

peptides may also benefit from further mutagenesis of negatively charged residues, such as MCa_{UF1-20}. It is noteworthy that another well behaving truncated CPP, $MCa_{UF18-33}$, also contains a Glu residue at position 29 that could represent another target for mutagenesis and peptide optimization. This is also the case for MCa_{UF1-9} that contains an Asp residue at position 2.

Several other findings of this report merit some comments. First, we demonstrate that cargo coupling can occur at the N terminus as well as the C terminus of MCa, enhancing the flexibility of cargo coupling to our vectors. Second, although it is obvious that most of our truncated MCa_{UF} analogues remain heavily basic, we also found out that poorly charged MCa peptides could behave as efficient CPPs. This is the case for MCa_{UF1-9} which is one of our best performing CPPs, especially if one wishes to work with low CPP concentrations. Third, small size CPPs can be derived from MCa_{UF}, MCa_{UF1-9}, and $MCa_{UF25-33}$ being our smallest peptides. Although we did not test greater truncation, it is not impossible that still smaller CPPs might be designed on the basis of MCa sequence. Fourth, the truncated MCa_{UF} analogues differ somewhat in their mode of cell penetration, some being more prone to enter cells by macropinocytosis than others. Various peptides were even insensitive to amiloride application, suggesting that macropinocytosis did not contribute at all to their entry. We cannot exclude at this stage that these peptides rely on modes of endocytosis other than macropinocytosis. This is suggested by the punctuate nature of intracellular Cy5 fluorescence distribution. How reliably a punctuate distribution reveals endocytosis is however not known, and one cannot rule out also that this distribution is due to peptide aggregation with or without lipid components. When plasma membrane distribution could be observed, large diffuse staining was evident, indicating that when peptides encountered the membrane no such aggregation occurred. In any case, many of the peptides had distribution that mostly differed from plasma membrane labeling (including these membranes that had undergone endocytosis), indicating that peptide intracellular distribution may not necessarily colocalize with the plasma membrane components. Refined studies will be required, however, to define how much of the peptides enter cells by direct membrane translocation *versus* endocytosis.

In conclusion, we identified several interesting lead CPPs based on MCa_{UF} truncation strategy. This is the case for $MCa_{UF18-33}$ (macropinocytosis entry-independent), MCa_{UF1-9} (penetrates better at low concentration), and $MCa_{UF14-25}$ (yields the greatest cell entry of the dye). These peptides are easy to produce, yield good cell penetration, and we should be able to further improve their cell penetrating characteristics by mutagenesis or by reintroducing one disulfide bridge to restore some of the secondary structures. Although the scope of this study was not to compare our mini-MCa with other popular CPPs, we were surprised to find out that many of the MCa_{UF} vectors behaved far better than TAT for the transport of Cy5, both in CHO and F98 cells. It may be argued that the field does not require many more CPP sequences. However, a significant fraction of the ongoing research is based on the use of TAT, which no longer appears as the most competitive peptide. Also, increasing evidence suggests that CPP sequences differ in their cell type targeting properties, which will undoubtedly represent an important feature to exploit when it comes to developing *in vivo* applications. Other essential parameters for *in vivo* applications will be the peptide stability upon intravenous or intraperitoneal injection. In that respect, we found out that MCa is a particularly stable peptide with and without disulfide bridges.[4] These still "hidden" aspects of the CPP features may be advantageously exploited later on if the number of known CPPs is high. The advantages of using smaller CPPs over MCa_F remains to be investigated as one may of course argue also that they require higher concentrations and possibly longer incubation times for effectiveness, two factors that may lead to spurious signaling events *in vivo*.

REFERENCES

1. Fajloun, Z., Kharrat, R., Chen, L., Lecomte, C., Di Luccio, E., Bichet, D., El Ayeb, M., Rochat, H., Allen, P. D., Pessah, I. N., De Waard, M., and Sabatier, J. M. (2000) Chemical synthesis and characterization of maurocalcine, a scorpion toxin that activates Ca^{2+} release channel/ryanodine receptors. *FEBS Lett.* **469,** 179–185
2. Mosbah, A., Kharrat, R., Fajloun, Z., Renisio, J. G., Blanc, E., Sabatier, J. M., El Ayeb, M., and Darbon, H. (2000) A new fold in the scorpion toxin family, associated with an activity on a ryanodine-sensitive calcium channel. *Proteins* **40,** 436–442
3. Chen, L., Estève, E., Sabatier, J. M., Ronjat, M., De Waard, M., Allen, P. D., and Pessah, I. N. (2003) Maurocalcine and peptide A stabilize distinct

subconductance states of ryanodine receptor type 1, revealing a proportional gating mechanism. *J. Biol. Chem.* **278,** 16095–16106
4. Lukács, B., Sztretye, M., Almássy, J., Sárközi, S., Dienes, B., Mabrouk, K., Simut, C., Szabó, L., Szentesi, P., De Waard, M., Ronjat, M., Jóna, I., and Csernoch, L. (2008) Charged surface area of maurocalcine determines its interaction with the skeletal ryanodine receptor. *Biophys. J.* **95,** 3497–3509
5. Estève, E., Smida-Rezgui, S., Sarkozi, S., Szegedi, C., Regaya, I., Chen, L., Altafaj, X., Rochat, H., Allen, P., Pessah, I. N., Marty, I., Sabatier, J. M., Jona, I., De Waard, M., and Ronjat, M. (2003) Critical amino acid residues determine the binding affinity and the Ca^{2+} release efficacy of maurocalcine in skeletal muscle cells. *J. Biol. Chem.* **278,** 37822–37831
6. Altafaj, X., Cheng, W., Estève, E., Urbani, J., Grunwald, D., Sabatier, J. M., Coronado, R., De Waard, M., and Ronjat, M. (2005) Maurocalcine and domain A of the II–III loop of the dihydropyridine receptor Cav 1.1 subunit share common binding sites on the skeletal ryanodine receptor. *J. Biol. Chem.* **280,** 4013–4016
7. Gurrola, G. B., Arévalo, C., Sreekumar, R., Lokuta, A. J., Walker, J. W., and Valdivia, H. H. (1999) Activation of ryanodine receptors by imperatoxin A and a peptide segment of the II–III loop of the dihydropyridine receptor. *J. Biol. Chem.* **274,** 7879–7886
8. Szappanos, H., Smida-Rezgui, S., Cseri, J., Simut, C., Sabatier, J. M., De Waard, M., Kovács, L., Csernoch, L., and Ronjat, M. (2005) Differential effects of maurocalcine on Ca^{2+} release events and depolarization-induced Ca^{2+} release in rat skeletal muscle. *J. Physiol.* **565,** 843–853
9. Pouvreau, S., Csernoch, L., Allard, B., Sabatier, J. M., De Waard, M., Ronjat, M., and Jacquemond, V. (2006) Transient loss of voltage control of Ca^{2+} release in the presence of maurocalcine in skeletal muscle. *Biophys. J.* **91,** 2206–2215
10. Estève, E., Mabrouk, K., Dupuis, A., Smida-Rezgui, S., Altafaj, X., Grunwald, D., Platel, J. C., Andreotti, N., Marty, I., Sabatier, J. M., Ronjat, M., and De Waard, M. (2005) Transduction of the scorpion toxin maurocalcine into cells: evidence that the toxin crosses the plasma membrane. *J. Biol. Chem.* **280,** 12833–12839
11. Ram, N., Weiss, N., Texier-Nogues, I., Aroui, S., Andreotti, N., Pirollet, F., Ronjat, M., Sabatier, J. M., Darbon, H., Jacquemond, V., and De Waard, M. (2008) Design of a disulfide-less, pharmacologically inert, and chemically competent analog of maurocalcine for the efficient transport of impermeant compounds into cells. *J. Biol. Chem.* **283,** 27048–27056
12. Aroui, S., Brahim, S., De Waard, M., Bréard, J., and Kenani, A. (2009) Efficient induction of apoptosis by doxorubicin coupled to cell-penetrating peptides compared to unconjugated doxorubicin in the human breast cancer cell line MDA-MB 231. *Cancer Lett.* **285,** 28–38
13. Aroui, S., Brahim, S., Hamelin, J., De Waard, M., Bréard, J., and Kenani, A. (2009) Conjugation of doxorubicin to cell-penetrating peptides sensitizes human breast MDA-MB 231 cancer cells to endogenous TRAIL-induced apoptosis. *Apoptosis* **14,** 1352–1365
14. Aroui, S., Brahim, S., Waard, M. D., and Kenani, A. (2010) Cytotoxicity, intracellular distribution and uptake of doxorubicin and doxorubicin coupled to cell-penetrating peptides in different cell lines: a comparative study. *Biochem. Biophys. Res. Commun.* **391,** 419–425
15. Aroui, S., Ram, N., Appaix, F., Ronjat, M., Kenani, A., Pirollet, F., and De Waard, M. (2009) Maurocalcine as a nontoxic drug carrier overcomes doxorubicin resistance in the cancer cell line MDA-MB 231. *Pharm. Res.* **26,** 836–845
16. Boisseau, S., Mabrouk, K., Ram, N., Garmy, N., Collin, V., Tadmouri, A., Mikati, M., Sabatier, J. M., Ronjat, M., Fantini, J., and De Waard, M. (2006) Cell penetration properties of maurocalcine, a natural venom peptide active on the intracellular ryanodine receptor. *Biochim. Biophys. Acta* **1758,** 308–319
17. Ram, N., Aroui, S., Jaumain, E., Bichraoui, H., Mabrouk, K., Ronjat, M., Lortat-Jacob, H., and De Waard, M. (2008) Direct peptide interaction with surface glycosaminoglycans contributes to the cell penetration of maurocalcine. *J. Biol. Chem.* **283,** 24274–24284
18. Mabrouk, K., Ram, N., Boisseau, S., Strappazzon, F., Rehaim, A., Sadoul, R., Darbon, H., Ronjat, M., and De Waard, M. (2007) Critical amino acid residues of maurocalcine involved in pharmacology, lipid interaction and cell penetration. *Biochim. Biophys. Acta* **1768,** 2528–2540
19. Poillot, C., Dridi, K., Bichraoui, H., Pêcher, J., Alphonse, S., Douzi, B., Ronjat, M., Darbon, H., and De Waard, M. (2010) D-Maurocalcine, a pharmacologically inert efficient cell-penetrating peptide analogue. *J. Biol. Chem.* **285,** 34168–34180
20. Merrifield, R. B. (1969) Solid-phase peptide synthesis. *Adv. Enzymol. Relat. Areas Mol. Biol.* **32,** 221–296
21. Kim, D. H., Ohnishi, S. T., and Ikemoto, N. (1983) Kinetic studies of calcium release from sarcoplasmic reticulum *in vitro*. *J. Biol. Chem.* **258,** 9662–9668
22. West, M. A., Bretscher, M. S., and Watts, C. (1989) Distinct endocytotic pathways in epidermal growth factor-stimulated human carcinoma A431 cells. *J. Cell Biol.* **109,** 2731–2739
23. Veithen, A., Cupers, P., Baudhuin, P., and Courtoy, P. J. (1996) v-Src induces constitutive macropinocytosis in rat fibroblasts. *J. Cell Sci.* **109,** 2005–2012
24. Meier, O., Boucke, K., Hammer, S. V., Keller, S., Stidwill, R. P., Hemmi, S., and Greber, U. F. (2002) Adenovirus triggers macropinocytosis and endosomal leakage together with its clathrin-mediated uptake. *J. Cell Biol.* **158,** 1119–1131

3.1.3. Discussion

La MCa est un excellent CPP qui a montré l'efficacité de délivrance intracellulaire de produits d'intérêts divers, expérimentaux, diagnostiques, ou thérapeutiques. Cependant, pour son utilisation courante, surtout *in vivo*, des modifications ont été nécessaires. Les modifications ont porté notamment sur la suppression de l'activité pharmacologique native et des ponts disulfures. L'une des stratégies utilisées avec succès est le remplacement des résidus cystéines internes par l'Abu, ce qui a conduit à la MCa-Abu (*18*), l'analogue sans ponts disulfures ou linéaire, pharmacologiquement inerte, et efficace en pénétration cellulaire. Cependant, la MCa-Abu était toujours composée de 33 résidus, ce qui en faisait un peptide long comparativement aux CPPs usuels (Tableau 1). Dans ce travail, nous avons réduit la taille du CPP par la délétion de la MCa-Abu (ici appelée MCa_{UF1-33}). Nous avons obtenu douze nouveaux CPPs, analogues de la MCa de courte taille.

Nous avons conçu douze séquences par la délétion de la MCa_{UF1-33}, mais plusieurs autres séquences peuvent être obtenues par la même stratégie. Nous n'avons pas évalué toutes les séquences possibles car cela demanderait un travail énorme et coûteux. Toutes les séquences évaluées ont montré la propriété de pénétration cellulaire. La MCa ne possède donc pas de domaine minimal unique responsable de la pénétration cellulaire, contrairement aux protéines précurseuses des premiers CPPs connus, à savoir l'homéodomaine d'antennapedia, et la protéine Tat, dont la délétion a conduit à un domaine minimal responsable de leur pénétration cellulaire, la pénétratine (*9*) et la Tat_{48-60} (*59*), respectivement. Cela suggère que la MCa est une toxine hautement spécialisée en pénétration cellulaire, qui a la propriété de pénétration cellulaire distribuée tout le long de sa séquence. Plusieurs autres séquences susceptibles d'être dérivées de la MCa pourraient donc également avoir les propriétés de CPP. La MCa serait donc une source inépuisable de séquences de CPPs.

Quelques CPPs se sont démarqués par leur forte pénétration cellulaire. Il s'agit notamment de la MCa_{UF1-9}, la $MCa_{UF14-25}$, et la $MCa_{UF18-33}$. La MCa_{UF1-9} est la mieux indiquée pour de faibles concentrations intracellulaires; elle serait utilisée à des concentrations extracellulaires inférieures ou égales à 1 µM. Quant aux $MCa_{UF14-25}$ et $MCa_{UF18-33}$, elles sont mieux indiquées pour de fortes concentrations intracellulaires; elles seraient utilisées à des concentrations extracellulaires autour de 10 µM. Cependant, ces observations ont été faites seulement sur les cellules CHO; elles devraient être confirmées sur différents types cellulaires.

La plupart des analogues de la MCa_{UF1-33} délétés se sont avérés plus efficaces que la MCa_{UF1-33}. Ceci suggère que la délétion des CPPs pourrait être une stratégie pour l'optimisation de leur efficacité de pénétration cellulaire. Néanmoins, ces analogues délétés semblent toujours moins efficaces que la MCa native (MCa_F), suggérant une possible amélioration. L'avantage compétitif de la MCa_F serait le résultat du repliement et des structures secondaires associées. En effet, la MC_F est repliée par trois ponts disulfures, et de ce repliement résultent trois brins β. Le repliement et les structures secondaires associées seraient donc requis pour optimiser le potentiel de CPP des différents domaines de la MCa. Ainsi, nous croyons qu'il serait intéressant de concevoir d'autres analogues de la MCa délétés comportant 1 ou 2 ponts disulfures permettant leur repliement et l'acquisition des structures secondaires.

La troncation de la MCa a eu un impact sur la composition en résidus basiques et par conséquent, sur la charge nette des peptides. Curieusement, les analogues comportant une charge nette nulle (MCa_{UF1-15} et MCa_{UF1-9}) pénètrent efficacement dans les cellules CHO. Ceci constitue une exception au principe généralement admis selon lequel les CPPs comportent une charge nette positive (*11, 70*). Cependant, une observation minutieuse de ces peptides électriquement neutres montre que la charge positive de leurs résidus basiques jouerait toujours un rôle dans leur processus de pénétration cellulaire. En effet, ces analogues électriquement neutres comportent un résidu basique (la lysine en position 8) suffisamment éloigné du résidu chargé négativement (l'acide aspartique en position 2) pour ne pas être neutralisé (Fig.2.A-Chap.3.1.2). Ce résidu lysine non neutralisé pourrait interagir avec les protéoglycanes de la membrane plasmique et favoriser la pénétration cellulaire (*88*). La différence d'efficacité de pénétration cellulaire entre les deux peptides s'expliquerait par la différence de la proportion du résidu lysine non neutralisé. En effet, ce résidu représente 6 % (1 sur 15) et 11 % (1 sur 9), pour la MCa_{UF1-15} et la MCa_{UF1-9}, respectivement. La $MCa_{UF1-9,}$ qui a la proportion la plus élevée, a montré une meilleure efficacité de pénétration cellulaire (Fig.6.C-Chap. 3.1.2).

Nos peptides tronqués conservent la propriété de pénétration cellulaire par voie non endocytique (vraisemblablement la translocation directe), l'une des propriétés les plus recherchées en vectorisation par les CPPs. Cette propriété est suggérée par les résultats des expérimentations basées sur l'inhibition des différentes voies d'endocytose. Cependant, l'inhibition de certaines voies de la cellule peut en favoriser d'autres (*283*), d'où la

pénétration non endocytique observée aurait été favorisée par l'inhibition des voies d'endocytose. Pour confirmer ces observations, des expérimentations réalisées dans des conditions qui conservent la physiologie normale de la cellule sont nécessaires. Ces expérimentations pourraient utiliser des techniques de co-localisation du peptide et des endosomes ou lysosomes. Il s'agit de techniques de microscopie confocale qui permettent une visualisation à la fois, du peptide et des endosomes (*12*) ou des lysosomes (*85, 86*) grâce au marquage fluorescent.

3.1.4. Conclusion

La MCa est un excellent CPP issu du venin de scorpion. Afin de développer des applications *in vivo,* la MCa a subi des optimisations pour la suppression de son activité pharmacologique native et la simplification de sa synthèse et de son utilisation. Dans le présent travail, nous avons réduit la taille du peptide, pour le rendre plus simple et plus économique à produire.

Douze nouveaux CPPs de courte taille ont été obtenus par la délétion de l'analogue linéaire, la MCa_{UF1-33}. Tous ces nouveaux CPPs ont manifesté d'excellentes propriétés de pénétration cellulaire. Par ailleurs, ils ont une faible cytotoxicité; pénètrent dans la cellule essentiellement par une voie indépendante de la macropinocytose, vraisemblablement la translocation directe; et sont pharmacologiquement inertes. Quelques analogues, notamment la $MCa_{UF1-9,}$ la $MCa_{UF14-25,}$ et la $MCa_{UF18-33}$ se sont distingués par leur forte pénétration cellulaire; ils pourraient être exploités différemment selon les besoins spécifiques. La MCa_{UF1-9} est la mieux indiquée pour des concentrations intracellulaires relativement faibles; elle serait utilisée à des concentrations extracellulaires inférieures ou égales à 1 µM. Quant aux $MCa_{UF14-25}$ et $MCa_{UF18-33}$, elles sont mieux indiquées pour de fortes concentrations intracellulaires; elles seraient utilisées à des concentrations extracellulaires autour de 10 µM.

3.2. Propriétés de pénétration cellulaire d'un puissant CPP « mini-maurocalcine »

Résumé : La MCa est un puissant CPP issu du venin de scorpion *Scorpio maurus palmatus*. En vu des applications in vivo, la MCa a été optimisé ce qui a conduit à plusieurs analogues dont la MCa_{UF1-9} dont la séquence correspond à la face hydrophobe de la MCa repliée, et qui s'est avéré le mieux indiquée pour des applications nécessitant de faibles concentrations intracellulaires. Dans ce travail, nous avons approfondi la caractérisation de la MCa_{UF1-9}. La MCa_{UF1-9} a montré d'intéressantes caractéristiques la plaçant en bonne position au concert des CPPs. La MCa_{UF1-9} s'est avérée plus efficace que les CPPs usuels, la Tat, la pénétratine, et la polyarginine. Elle pénètre dans les cellules principalement par une voie non endocytique, vraisemblablement la translocation directe. La MCa_{UF1-9} a par ailleurs montré une augmentation de la pénétration cellulaire en milieu acide et une persistance intracellulaire. Les deux propriétés pourraient être exploitées, respectivement, pour la délivrance ciblée des anticancéreux dans les cellules cancéreuses et pour la rétention des médicaments dans les cellules résistantes au traitement par rejet de médicaments. La MCa_{UF1-9} paraît tellement optimisée pour la pénétration cellulaire qu'il est difficile de concevoir des mutations ponctuelles pouvant améliorer son efficacité. Curieusement, sa comparaison à des peptides da la même famille a conduit à la découverte d'un nouveau CPP plus performant, l'Had_{UF1-11}.

3.2.1. Introduction

La MCa (L-MCa) est une toxine issue du venin de scorpion, *Scorpio maurus palmatus*, et dotée d'excellentes propriétés de pénétration cellulaire. La MCa a d'abord été identifiée pour son activité pharmacologique sur les canaux RyRs situés à l'intérieur de la cellule, dans la membrane du RS (réticulum sarcoplasmique) (*60*). C'est l'observation de cette activité pharmacologique de la MCa qui a conduit à la découverte de ses propriétés de pénétration cellulaire (*277*).

La MCa est un peptide cationique composé de 33 résidus acides aminés. Onze (33%) de ses résidus sont des résidus basiques donc chargés positivement. Par ailleurs, le peptide comporte six résidus cystéines formant trois ponts disulfures : Cys^{3}-Cys^{17}, Cys^{10}-Cys^{21}, et Cys^{16}-Cys^{32} (*60*). Le peptide est replié et rigidement structurée par les trois ponts disulfures. Il comporte trois brins β s'étendant sur les résidus 9-11 (brin 1), 20-23 (brin 2), et 30-33 (brin 3).

La MCa a une activité pharmacologique qui consiste en l'activation des canaux RyR1 du RS des muscles squelettiques entrainant le relargage du Ca^{2+} (*273, 274*). La MCa active les canaux RyR1 par l'induction d'un état de sous-conductance de longue durée (*60, 274, 275*). La face de la MCa chargée positivement joue un rôle déterminant dans son activité pharmacologique; les principaux résidus impliqués sont des résidus basiques, notamment la Lys^{8}, la Lys^{20}, la Lys^{22}, l'Arg^{23}, et surtout l'Arg^{24} (*274*). Il a été montré que la MCa interagit également avec les canaux RyR2 des muscles cardiaques mais sans induire le relargage du Ca^{2+} (*276*). La propriété de la MCa d'activer les canaux RyR1 intracellulaires a conduit à la découverte de ses propriétés de pénétration cellulaire.

La MCa s'est avérée un CPP particulièrement intéressant. Sa pénétration cellulaire a lieu à de très faibles concentrations. Elle pénètre dans les cellules par une voie indépendante de l'endocytose, vraisemblablement la translocation directe, bien que la macropinocytose soit sa principale voie d'internalisation (*278*). La MCa a une faible cytotoxicité et une stabilité remarquable; elle n'est pas dénaturée par de hautes températures pouvant aller jusqu'à 100°C, ni par des conditions de pH extrêmes; elle peut donc être utilisée dans diverses conditions (*16, 279*). La MCa a par ailleurs montré une efficacité de délivrance intracellulaire de divers types de cargaisons: des protéines (*277*, *279*), des peptides (*18*), des fluorochromes (*16*), des médicaments (*61*), et des nanoparticules (*282*). Globalement, la MCa possède d'excellentes propriétés la disposant à être utilisée comme vecteur de délivrance intracellulaire des produits d'intérêts divers : expérimentaux, diagnostiques, ou thérapeutiques.

Cependant, dans son état natif, la MCa rencontrerait des obstacles qui limiteraient son utilisation en qualité de vecteur. Ces obstacles sont liés à l'activité pharmacologique indésirable dans la plupart des applications, surtout *in vivo*; à la présence des ponts disulfures qui compliquent la synthèse du peptide et le greffage de la cargaison; et à la taille du peptide relativement longue comparativement à des CPPs usuels. De ce fait, la MCa a subi des optimisations. Les optimisations ont consisté en la suppression de l'activité pharmacologique et à la suppression des ponts disulfures internes. L'activité pharmacologique a été supprimée par des mutations ponctuelles, notamment la mutation R24A (*17*), et par la synthèse d'un peptide diastéréoisomère, la D-MCa, composée essentiellement d'acides aminés énantiomères D (*16*). Les ponts disulfures ont été éliminés en remplaçant les résidus cystéines internes par l'Abu; l'analogue linéaire obtenu, la MCa_{Abu} ou $MCa_{UF1\text{-}33,}$ était en plus dépourvu de toute activité pharmacologique (*18*). La taille du peptide a été réduite par la délétion de l'analogue

linéaire (MCa_{UF1-33}), ce qui a conduit à 12 nouveaux CPPs de courte taille (*281*). Les CPPs de courte taille ont tous manifesté une excellente efficacité de pénétration cellulaire, mais quelques-uns, notamment la MCa_{UF1-9}, la $MCa_{UF14-25}$, et la $MCa_{UF18-33}$ se sont démarqués par leur forte pénétration cellulaire; ils pourraient être exploités différemment selon les concentrations intracellulaires recherchées. La MCa_{UF1-9} est la mieux indiquée pour de faibles concentrations intracellulaires; elle serait utilisée à des concentrations extracellulaires inférieures ou égales à 1 µM. Quant aux $MCa_{UF14-25}$ et $MCa_{UF18-33}$, elles sont mieux indiquées pour de fortes concentrations intracellulaires; elles seraient utilisées à des concentrations extracellulaires autour de 10 µM.

La MCa_{UF1-9} présente de meilleures perspectives d'avenir. Elle est efficace à de faibles concentrations. Ceci indique une utilisation en faible quantité, donc à moindre coût. Par ailleurs, composée de 9 résidus, la MCa_{UF1-9} est l'un des CPPs les plus courts connus à ce jour (Tableau 1). Sa courte taille signifie le moindre coût de synthèse. Globalement, la MCa_{UF1-9} représente un intérêt économique particulier. De ce fait, nous l'avons caractérisée de façon plus approfondie.

Le présent travail a porté sur la caractérisation approfondie de la MCa_{UF1-9}. La $MCa_{UF\ 1-9}$ a été comparée à des CPPs usuels, à savoir la Tat, la pénétratine, et la polyarginine, ainsi qu'à des domaines hydrophobes issus des peptides de la famille des calcines. Par ailleurs, le mode de pénétration cellulaire, la dépendance du pH du milieu, et la persistance intracellulaire du peptide ont été étudiés. La MC_{UF1-9} s'est avérée plus efficace que la Tat, la pénétratine, ou la polyarginine. Elle pénètre dans la cellule principalement par une voie indépendante de l'endocytose; sa pénétration cellulaire augmente en milieu acide; elle a une longue persistance intracellulaire. Sa comparaison à des domaines hydrophobes des peptides de la famille des calcines a conduit à la découverte de nouveaux CPPs, notamment l' Had_{UF1-11} qui s'est avéré le plus efficace.

3.2.2. Article publié

Pharmaceuticals **2013**, *6*, 320-339; doi:10.3390/ph6030320

OPEN ACCESS

pharmaceuticals

ISSN 1424-8247

www.mdpi.com/journal/pharmaceuticals

Article

Cell Penetration Properties of a Highly Efficient Mini Maurocalcine Peptide

Céline Tisseyre [1,2,3,†], Eloi Bahembera [1,2,3,†], Lucie Dardevet [1,2,3], Jean-Marc Sabatier [4], Michel Ronjat [1,2,3] and Michel De Waard [1,2,4,5,*]

1 Unité Inserm U836, Grenoble Institute of Neuroscience, Université Joseph Fourier, La Tronche, Chemin Fortuné Ferrini, Bâtiment Edmond Safra, 38042 Grenoble Cedex 09, France

2 Labex Ion Channel Science and Therapeutics, Nice, France

3 Université Joseph Fourier, Grenoble, France

4 Inserm U1097, Parc scientifique et technologique de Luminy, 163, avenue de Luminy, 13288 Marseille cedex 09, France

5 Smartox Biotechnology, Biopolis, 5 Avenue du Grand Sablon, 38700 La Tronche, France

† These authors contributed equally to this work.

* Author to whom correspondence should be addressed; E-Mail: michel.dewaard@ujf-grenoble.fr; Tel.: +33-4-56-52-05-63; Fax: +33-4-56-52-06-37.

Received: 23 February 2013; in revised form: 6 March 2013 / Accepted: 7 March 2013 / Published: 18 March 2013

Abstract: Maurocalcine is a highly potent cell-penetrating peptide isolated from the Tunisian scorpion *Maurus palmatus*. Many cell-penetrating peptide analogues have been derived from the full-length maurocalcine by internal cysteine substitutions and sequence truncation. Herein we have further characterized the cell-penetrating properties of one such peptide, MCa_{UF1-9}, whose sequence matches that of the hydrophobic face of maurocalcine. This peptide shows very favorable cell-penetration efficacy compared to Tat, penetratin or polyarginine. The peptide appears so specialized in cell penetration that it seems hard to improve by site directed mutagenesis. A comparative analysis of the efficacies of similar peptides isolated from other toxin members of the same family leads to the identification of hadrucalcin's hydrophobic face as an even better CPP. Protonation of the histidine residue at position 6 renders the cell penetration of MCa_{UF1-9} pH-sensitive. Greater cell penetration at acidic pH suggests that MCa_{UF1-9} can be used to specifically target cancer cells *in vivo* where tumor masses grow in more acidic environments.

Keywords: maurocalcine; hadrucalcin; toxin; cell penetrating peptide; F98 cells; glioma; analogs

1. Introduction

Maurocalcine (MCa) is a 33 amino acid residue peptide that was isolated in 2000 from the venom of the Tunisian chactid scorpion *Scorpio maurus palmatus* [1]. It folds according to an 'Inhibitor Cystine Knot' (ICK) motif [2] and contains three disulfide bridges connected by the following pattern: C_1-C_4, C_2-C_5 and C_3-C_6 [3]. Based on high amino acid sequence and pharmacological target similarities, MCa belongs to a larger family of scorpion toxins that also includes imperatoxin A (from *Pandinus imperator*) [4], opicalcine 1 and opicalcine 2 (from *Opistophthalmus carinatus*) [5], hemicalcin [6] and hadrucalcin [7]. All these peptides act on ryanodine receptors resulting in pharmacological activation. These receptors are calcium channels located in the membrane of the endoplasmic reticulum. They control Ca^{2+} release from internal stores and therefore a large number of cell functions [7–10]. Binding of MCa on the ryanodine receptor type 1 occurs on protein cytoplasmic domains. Because MCa acts within seconds, once applied to the extracellular medium, it was soon obvious that it had to cross the plasma membrane very efficiently in order to activate the ryanodine receptor [11]. An additional curiosity of MCa lies into the fact that there is an intriguing sequence homology with a domain of the L-type voltage-gated calcium channel from the skeletal muscle (domain A). This channel lies in the plasma membrane, while domain A is found underneath the membrane in the cytoplasm within a loop that has been recognized as extremely important for the process of excitation-contraction coupling [12,13]. While the role of domain A in excitation-contraction coupling is still unclear, it is however surprising and stimulating to observe that peptides containing domain A sequence act with quite a lot of similarities to MCa on the ryanodine receptor type 1 [14,15]. According to the ^{1}H-NMR solution structure, MCa is rigidly structured by the three disulfide bridges and contains three β-strands, comprising the following stretches of amino acid residues: 9–11 (strand 1), 20–23 (strand 2), and 30–33 (strand 3). MCa has an incredibly stable structure since it cannot be denatured, even at high temperatures up to 100 °C or extreme pH values [16]. Interestingly, the peptide is highly enriched in basic amino acid residues, more than a third of the amino acids being either lysine (seven out of 33) or arginine residues (four out of 33). The histidine residue at position 6 is susceptible, depending of the environmental pH, to introduce an additional positive charge to the peptide by protonation. Interestingly, stretches of positively charged residues seem to confound with the three MCa β-strands. The 3D structure of MCa also strikingly highlights the asymmetrical distribution of the positive charges at its surface: one face is highly basic, while the opposite face is rather hydrophobic. If, in addition, one depicts the amino acid residues important for the ryanodine receptor activation [17], then it appears that the peptide can be schematically represented with three domains: one hydrophobic head that tops the peptide, a larger second face, mainly basic, and a third side domain that contains the pharmacophore (Figure 1A).

Besides its Ca^{2+} channel activity, MCa is also used as a cell-penetrating peptide (CPP). Its properties have been investigated in detail. It was soon discovered that MCa could act as vector for the cell penetration of a variety of cargoes, including proteins [11], peptides [18], small dyes [16,19],

drugs [20–23] or nanoparticles [24,25]. The mechanism of cell penetration most likely includes a combination of membrane translocation (direct passage to the cytoplasm) and endocytosis, mostly macropinocytosis (indirect access to the cytoplasm through leakage from late endosomes) [16,19,26,27].

Figure 1. The hydrophobic domain of MCa is an efficient CPP. (**A**) Schematic representation of MCa 3D structure. The hydrophobic domain (from amino acid residue 1 to 9) is shown on top. Residues are in yellow. Shown also are the basic face (basic amino acid residues are in blue or in pink) and the pharmacophore (residues identified as interacting with the ryanodine receptor are in red or in pink). Pink residues belong both to the pharmacophore and the basic face. (**B**) Confocal microscopy images illustrating the penetration of four different peptides labeled with Cy5 at various concentrations into glioma F98 cells (blue color). Incubation times were 2 h for each peptide/concentration. Images were taken immediately after washout of the extracellular peptide. The plasma membrane is labeled with concanavalin-A-rhodamine (red color). (**C**) Dose-dependent penetration of each peptide-cargo complex in F98 cells as assessed by flow cytometry. A control Cys-Cy5 is also provided. (**D**) Absence of cell penetration of 33 µM Cys-Cy5 (a single Cys residue linked to Cy5—abbreviated C-Cy5) evaluated by confocal microscopy. (**E**) Lack of cell penetration of 3 µM $ChTx_{UF1-12}$-C-Cy5 as determined by confocal microscopy (right panel). Quantitative analysis of F98 $ChTx_{UF1-12}$-C-Cy5 fluorescence as determined by flow cytometry. Internalization of the $ChTx_{UF1-12}$-C-Cy5 peptide is lower than TAT-C-Cy5 but not negligible.

Figure 1

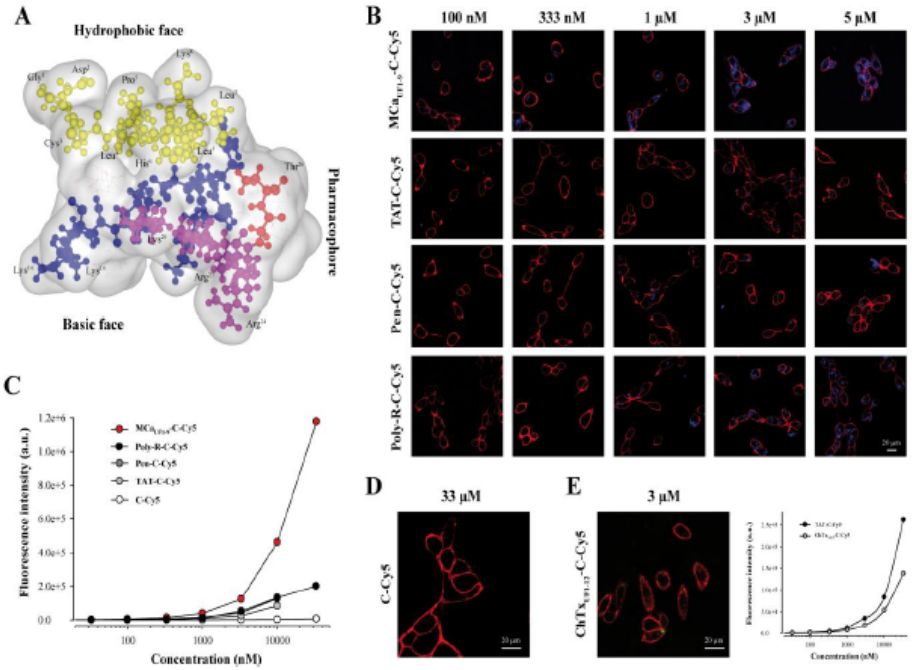

Even if the mechanism(s) of penetration of CPP are subject to debate [28,29], because of the rapidity of action of MCa on the ryanodine receptor, it appears clearly that one way of penetration of

MCa can be membrane translocation. Furthermore, MCa has the ability to bind onto glycosaminoglycans, including heparin and heparan sulfates, with micromolar affinity. However, cell penetration still occurs according to both mechanisms of penetration in cells devoid of glycosaminoglycans, suggesting that glycosaminoglycans do not preferentially direct MCa's cell penetration towards endocytosis [26]. In contrast, these cell surface receptors appear to be helpful as peptide sinks for increased peptide delivery into cells. More relevant to cell penetration is the fact that MCa binds to a number of membrane lipids, mostly negatively charged ones [26,27], as observed for other CPP [28]. Binding seems to occur with higher affinity (100 nM) in close agreement with the concentration of MCa required for cell penetration. In addition, MCa analogues that penetrate better than wild-type MCa also exhibit a greater affinity for membrane lipids and *vice versa*. Endocytosis becomes predominant with some large cargoes. Conversely, small cargoes seem to have less interference with a translocation mode of entry of CPP. These observations tend to indicate that endocytosis may become the preferential mode of cell entry of MCa if coupled to bulky cargoes that are expected to increase the duration of residency at the plasma membrane. However, although MCa is an extremely efficient vector for cell penetration of impermeable cargoes, it is of limited usefulness in its native conformation. Indeed, complex disulfide bridging may hamper the attachment of some cargoes. The size of the CPP is greater than those used in the literature. Finally, the native pharmacological activity is generally undesirable for most applications, so like other CPPs before, modification of the native MCa was made in order to ease its use *in vivo* as a new delivery system [30]. Canceling MCa's pharmacological activity turned out to be quite simple due to the fact that structural requirements involved in binding onto the ryanodine receptor are more stringent than for cell penetration. Several chemical strategies turned out to be successful including point mutations [17], blocking MCa's folding by preventing disulfide bridge formation [18], and producing a D-diastereomer MCa [16]. The second strategy had the advantage to produce a MCa analogue that was simpler to produce since the oxidation/folding step was no longer necessary. However, the resulting peptide turned out to be slightly less efficient in cell penetration than the folded/oxidized MCa, indicating that the correct positioning in space of the various structural determinants of MCa is important to optimize cell penetration. In addition, the unfolded MCa CPP was still thirty three amino acid residues in length. Quite recently, in an attempt to further delimitate the cell penetrating properties of MCa to smaller sequences, a number of unfolded truncated MCa-derived peptides were synthesized and assessed for cell penetration properties [19]. Surprisingly, all truncated peptides turned out to be more efficient than the unfolded full-length MCa for cell penetration, suggesting that each structured domain within the folded/oxidized MCa may provide a specific contribution to the cell penetration of the wild-type peptide. The shortest peptides were nine residues in length and included both the N-terminal and the C-terminal sequences. One of the peptides, $MCa_{UF1\text{-}9}$, stood out as atypical since the net charge of the peptide was 0 and its cell penetration properties differed to some extent from the significantly more basic other MCa-derived truncated peptides. Penetration of this peptide occurred at polarized ends of CHO cells. The peptide also showed greater residency times within the plasma membrane. Its penetration did not rely at all on macropinocytosis for cell entry (at least when coupled to a dye as cargo). Finally, penetration of this peptide occurs at lower extracellular concentrations than the more basic peptides derived from MCa [19]. Altogether the properties of $MCa_{UF1\text{-}9}$ seemed interesting enough to warrant a more in-depth investigation of its cell penetration properties. We therefore

compare herein the properties of this peptide to well-reputed CPP (Tat, penetratin and poly-R) or analogous peptides derived from other toxins of the calcin family. We investigated the properties of a number of point mutated MCa_{UF1-9} analogues, and more specifically the pH-sensitivity of its penetration in order to design pH-sensitive CPP. The data point to new very powerful CPP with unprecedented efficacies and demonstrate the pH-sensitivities of several of our analogues for cell penetration.

2. Results and Discussion

2.1. A Peptide Derived from the Hydrophobic Face of MCa Behaves as a Highly Competitive CPP

A schematic representation of MCa illustrates that the amino acid sequence 1 to 9 tops the rest of the peptide (yellow residues) and defines an independent more hydrophobic face (Figure 1A). The opposite side of the peptide is highly basic (blue and pink residues) and defines therefore a basic face. Some of the residues involved in binding onto the ryanodine receptor have been defined in the past [17]. They include important residues such as Arg^{23} and Arg^{24} and define the pharmacophore side (residues in red and in pink). Therefore the pharmacophore and basic regions overlap to some degree.

We compared the efficacy of MCa_{UF1-9} for cell penetration within the glioma rat cell line F98 to other very popular peptides, comprising TAT, penetratin (Pen) and poly-Arg (poly-R). All peptides included an additional C-terminal Cys residue that was labeled with the Cy5 fluorochrome which served the purpose of cargo in this study. Of note, the extra Cys residue in MCa_{UF1-9}-C-Cy5 is at its natural position as in the folded/oxidized MCa (Cys^{10}) where it is linked to Cys^{21} by a disulfide bridge. In contrast, Cys^{3} of MCa_{UF1-9} was replaced by an isosteric 2-aminobutyric acid (Abu) residue to avoid mislabeling by Cy5 in the middle of the sequence. A series of confocal microscopy images were taken immediately after a 2 h incubation of F98 cells with various concentrations of the four peptides tested (MCa_{UF1-9}-C-Cy5, TAT-C-Cy5, Pen-C-Cy5 and poly-R-C-Cy5). As shown, cell penetration of MCa_{UF1-9}-C-Cy5 is perceptible at concentrations as low as 100 nM, whereas none of the other peptides showed penetration at this concentration (Figure 1B). Penetration was then dose-dependent for all peptides. It was more marked at 333 nM for MCa_{UF1-9}-C-Cy5 and started to show up for Poly-R-C-Cy5, while still absent for TAT-C-Cy5 and Pen-C-Cy5. At 1 μM all peptides showed some degree of penetration, the least efficient peptide being TAT-C-Cy5. At 5 μM, F98 cells incubated with TAT-C-Cy5 showed levels of fluorescence that were more or less comparable to those obtained with MCa_{UF1-9}-C-Cy5 at 333 nM. These data qualitatively indicated that MCa_{UF1-9}-C-Cy5 behaved better than those three popular CPP as far as F98 cells are concerned. Similar results were obtained with CHO cells indicating that these differences in performances between the four peptides do not depend on the cell type studied (data not shown). With regard to cell distribution of the peptides, we did not notice any obvious differences in distribution suggesting that the peptides may all borrow the same mechanisms of cell penetration. However, a more complete investigation on this issue is needed before one comes to a firm conclusion. To more quantitatively compare the CPP, we investigated fluorescence levels by flow cytometry (Figure 1C). The data confirmed the confocal microscopy analyses showing that MCa_{UF1-9}-C-Cy5 behaves more potently than other CPP. The following order of penetration efficiency was observed: MCa_{UF1-9}-C-Cy5 >> Poly-R-C-Cy5 = Pen-C-Cy5 > TAT-C-Cy5. At 10 μM, MCa_{UF1-9}-C-Cy5

penetrates 5.5-fold better than TAT-C-Cy5, 3.6-fold better than Pen-C-Cy5, and 3.5-fold better than Poly-R-C-Cy5.

2.2. Randomly Defined Control Peptides Delimit the Threshold Level of an Acceptable Cell Penetration

Our data also illustrate that the control linker-cargo, a single Cys residue linked to Cy5 (C-Cy5), does not penetrate at all into F98 cells (at concentrations up to 33 μM), demonstrating the peptide specificity of cell entry (Figure 1C and D). Another control was also tested, based on a fragment of charybdotoxin (ChTx), a voltage-gated potassium channel blocker, not known previously for cell penetration aptitude. The peptide encompasses the 12 first amino acids of ChTx. Internal Cys residues were replaced by Abu, an additional Cys residue was added at the C-terminus and the resulting peptide labeled with Cy5 as well to yield $ChTx_{UF1\text{-}12}$-C-Cy5. Confocal microscopy images do not show any evidence of cell penetration if F98 cells are incubated 2 h with 3 μM $ChTx_{UF1\text{-}12}$-C-Cy5 (Figure 1E). However, if a more sensitive and quantitative approach is taken to examine the levels of fluorescence, it becomes obvious that F98 cells take up a defined amount of $ChTx_{UF1\text{-}12}$-C-Cy5. This is unlikely to represent the level of binding of this peptide to some cell-surface potassium channels as this fragment is not known to bind potassium channels. In contrast, it may indicate the propensity of some cell types to internalize peptides that present even low affinity for the plasma membrane. A comparison with our least-performing peptide TAT-C-Cy5 indicates that $ChTx_{UF1\text{-}12}$-C-Cy5 is less efficient than TAT-C-Cy5, although significant. At 10 μM, the cell entry of this non-conventional CPP is 1.57-fold less than TAT. These findings may question the relevance of some studies reporting the discovery of "new" CPP or alternatively may suggest that $ChTx_{UF1\text{-}12}$ can also be considered as a poorly performing CPP.

2.3. Pharmacological Blockade of Endocytosis in F98 Cells Affects Poorly $MCa_{UF1\text{-}9}$ Cell Entry

Punctiform distribution of $MCa_{UF1\text{-}9}$-C-Cy5 may be interpreted as a cell entry that is mainly based on a form of endocytosis. This point was assessed by FACS analyses using various drugs at the 2 h cell entry timepoint of 1 μM $MCa_{UF1\text{-}9}$-C-Cy5 in F98 cells. We tested amiloride, a macropinocytosis inhibitor, methyl-β-cyclodextrin to deplete membrane cholesterol and inhibit lipid raft-dependent pathways, nocodazole to prevent microtubule formation, and cytochalasin D to stop F-actin elongation, required for macropinocytosis and clathrin-dependent endocytosis [31]. Amiloride only affected $MCa_{UF1\text{-}9}$-C-Cy5 cell entry in F98 cells very mildly, with an average inhibition of 27% indicating an entry partly based on macropinocytosis (Figure 2).

The 18.5% inhibition observed by cytochalasin D, while being non-significant, was in agreement with the contribution of macropinocytosis to the cell entry of the peptide. Quite surprisingly, both methyl-β-cyclodextrin and nocodazole produced 24.7 and 48.9% increases in the cell entry of $MCa_{UF1\text{-}9}$-C-Cy5. The lack of inhibition by methyl-β-cyclodextrin indicates that caveolae-mediated endocytosis is not involved in the entry of this peptide. The observed increase in cell penetration may indicate on the contrary that one preferential route of cell entry by translocation may be in lipid rafts. Preventing the loss of lipid rafts by blocking endocytosis at this level would increase the surface area devoted to lipid rafts and hence peptide entry.

Figure 2. Effect of endocytosis inhibitors on MCa_{UF1-9} peptide penetration in F98 cells. (**A**) Representative FACS data showing the effect of amiloride (red curve), cytochalasine D (yellow curve), methyl-β-cyclodextrine (blue curve) and nocodazole (green curve) on 1 μM MCa_{UF1-9}-C-Cy5 cell entry (black curve). (**B**) Average fluorescence intensities for the cell entry of 1 μM MCa_{UF1-9}-C-Cy5 in F98 cells without and with endocytosis inhibitors. * $p \leq 0.1$.

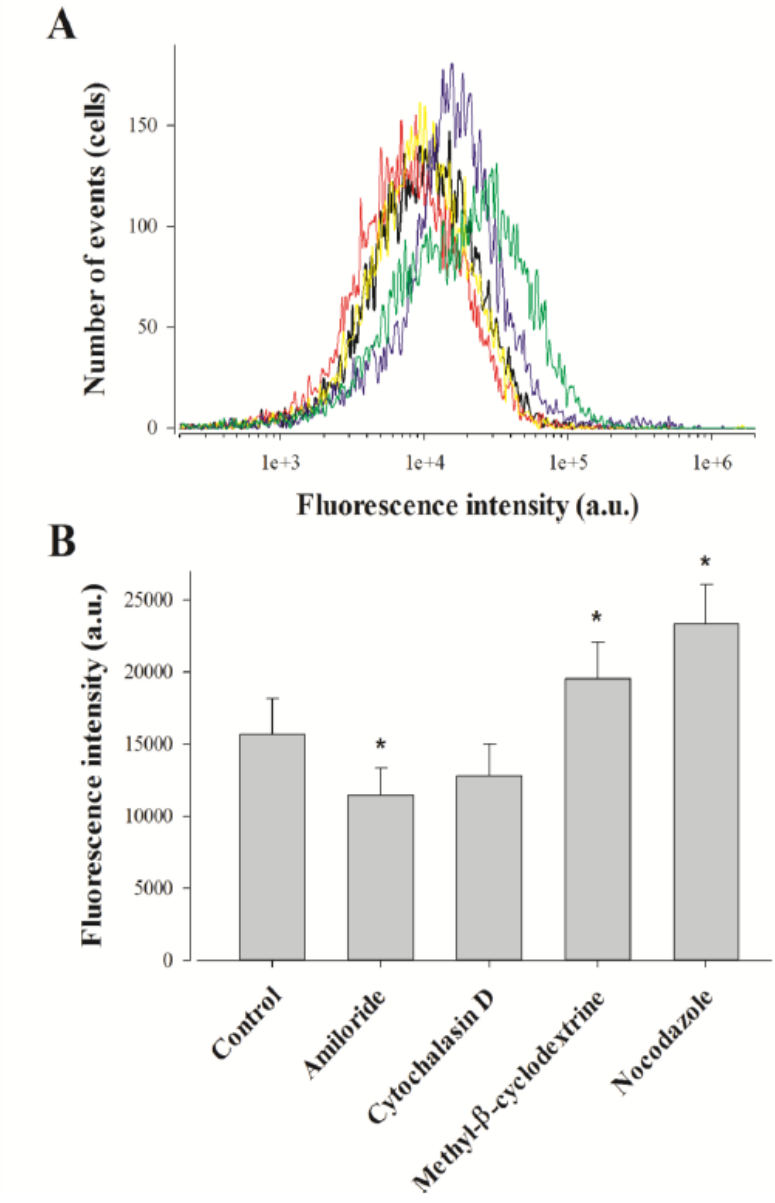

Similarly, it is possible that microtubules hinder cell penetration explaining why blocking their formation may help peptide entry to this large extent. These observations demonstrate that while the intracellular distribution of MCa_{UF1-9}-C-Cy5 in F98 cells looks punctiform, this is not necessarily the consequence of a cell entry by endocytosis.

2.4. Point Mutation of MCa$_{UF1-9}$ Fails to Optimize The Cell Penetrating Properties of This Peptide

Next, we attempted to design a number of MCa$_{UF1-9}$ peptide analogues in order to get some hints on what structural determinants may be important for the efficacy of this peptide in cell penetration. At the N-terminal side of Cys^3 (replaced by Abu) of MCa$_{UF1-9}$, there are two residues that appear of minor importance (Gly^1 and Asp^2). Removing these two residues yields MCa$_{UF3-9}$. As shown, MCa$_{UF3-9}$-C-Cy5 still accumulates very well in F98 cells (Figure 3A,B).

Figure 3. Structural determinants of MCa$_{UF1-9}$ peptide penetration. (**A**) Confocal images illustrating the penetration of 3 µM MCa$_{UF3-9}$-C-Cy5, MCa$_{UF1-9(W3)}$-C-Cy5, MCa$_{UF1-9(Q3)}$-C-Cy5 or MCa$_{UF1-9(A3)}$-C-Cy5 into F98 cells. 2 h incubation time before washout and imaging. (**B**) Effect of N-terminal peptide truncation on cell penetration efficacy of MCa$_{UF1-9}$-C-Cy5 as assessed by flow cytometry. (**C**) Effect of point mutation at position 3 on the cell penetration efficacy of MCa$_{UF1-9}$-C-Cy5. (**D**) Confocal images illustrating the penetration of 3 µM single or double point mutated MCa$_{UF1-9}$-C-Cy5 peptide into F98 cells. (E) Effect of single point mutations on the cell penetration efficacy of MCa$_{UF1-9}$-C-Cy5 as assessed by flow cytometry.

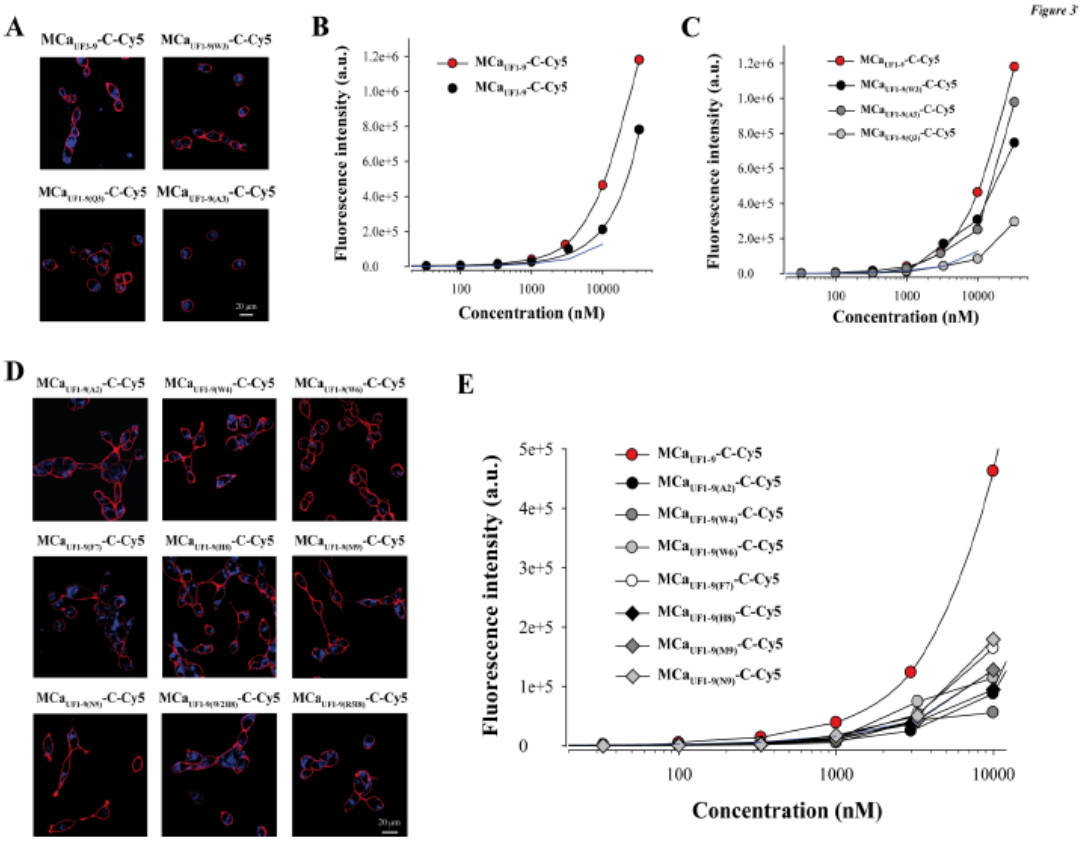

At the quantitative level, there was a 1.25-decrease in cell penetration efficacy at 3 µM, indicating that these two residues were most likely not essential for cell penetration. This deletion brings the size of this efficient CPP down to seven amino acid residues which is remarkably short. At position 3 of the

wild-type MCa there is normally a Cys residue that engages itself into a disulfide bridge. The lateral chain of this residue is therefore not exposed towards the outside face of the molecule and is unlikely to play a role in cell penetration. MCa_{UF1-9} contains an Abu residue instead of a Cys residue and the peptide is quite efficient for cell penetration. We nevertheless probed this position by replacing the Abu residue by Trp, Gln or Ala. As shown, none of these replacements at position 3 within MCa_{UF1-9}-C-Cy5 hindered the cell penetration of these analogues (Figure 3A). At 3 µM, $MCa_{UF1-9(W3)}$-C-Cy5 penetrated 1.36-fold better than MCa_{UF1-9}-C-Cy5, while $MCa_{UF1-9(A3)}$-C-Cy5 penetrated 1.08-fold less well, indicating little variations (Figure 3C). In contrast, when Gln was put at position 3 in the sequence, the resulting $MCa_{UF1-9(Q3)}$-C-Cy5 peptide behaved similarly to TAT but 2.94-fold less well than MCa_{UF1-9}-C-Cy5 suggesting that a Gln may hinder the cell penetration process. Next, we made a series of single (seven peptide) or double (two peptide) point mutated analogues to probe the functional importance of these MCa residues. As shown, all mutated MCa_{UF1-9}-C-Cy5 analogues produced evident cell penetration at 3 µM, indicating that none of the substitutions were powerful enough to fully prevent cell penetration (Figure 3D). However, according to flow cytometry analyses, none of the mutated peptides performed better than MCa_{UF1-9}-C-Cy5 (Figure 3E). Taking TAT-C-Cy5 as a standard, $MCa_{UF1-9(A2)}$-C-Cy5, $MCa_{UF1-9(W4)}$-C-Cy5 and $MCa_{UF1-9(H8)}$-C-Cy5 behaved slightly less well. In contrast, $MCa_{UF1-9(F7)}$-C-Cy5 and $MCa_{UF1-9(M9)}$-C-Cy5 still behaved better than TAT-C-Cy5. Double mutants ($MCa_{UF1-9(W2H8)}$-C-Cy5 and $MCa_{UF1-9(R5I8)}$-C-Cy5 were also closely similar to TAT-C-Cy5 (not shown). Overall, these data indicate that MCa_{UF1-9} peptide has been optimized for cell penetration with many amino acid residues playing an important role for cell entry. At this stage it would be difficult to point to one single residue as being more important than another one within the sequence.

2.5. Analogous Hydrophobic Domains of Other Toxin Members of the Calcin Family Are Also Excellent CPP

The inability to produce MCa_{UF1-9} peptides with greater cell penetration efficacies tends to indicate that sequence variation of this hydrophobic domain needs to be considered more cautiously to design optimized peptides. Interestingly, MCa belongs to a larger family of peptides that have, most of them, never been assessed for cell penetration. Results have been presented indicating that imperatoxin A also behaves as a CPP [32]. All these peptides are structured similarly to MCa, with a similar hydrophobic face topping a more basic face (Figure 4A). All peptides that have been tested are also active on the ryanodine receptor [6,7,33], indicating the presence of a similar pharmacophore. A close examination of the amino acid sequence of the hydrophobic domain reveals only minor sequence diversity among these peptides (Figure 4B). The nine first residues of hemicalcin are identical to MCa. Imperatoxin A, opicalcin 1 and opicalcin 2 differ from MCa only by residue 9 (an arginine instead of a leucine residue).

The most differing peptide sequence is the one derived from hadrucalcin with two extra N-terminal residues. Interestingly, the sequence SerGluLys replaces the Gly^1 residue of MCa, but Asp^2 of MCa is conserved. Also, four internal substitutions are noticeable. Leu^4, Pro^5, Lys^8 and Leu^9 of MCa are substituted by Iso, Lys, Gln and Arg, respectively. Finally, Had_{UF1-11} has an additional basic amino acid compared to MCa_{UF1-9}. We next evaluated the ability of these peptides to accumulate into F98 cells. At 1 µM, it was obvious, according to confocal imaging, that Imp_{UF1-9}-C-Cy5 (equivalent to

Opi1$_{UF1-9}$-C-Cy5 or Opi2$_{UF1-9}$-C-Cy5) is less efficient for cell penetration than MCa$_{UF1-9}$-C-Cy5 and Had$_{UF1-11}$-C-Cy5 (Figure 4D). Interestingly, a similar deletion of the two first amino terminal residues of Had$_{UF1-9}$-C-Cy5 yielded a peptide, MCa$_{UF3-11}$-C-Cy5 with excellent penetration capabilities. Evaluation of dose-dependent penetration by flow cytometry demonstrated that Imp$_{UF1-9}$-C-Cy5 penetrates quantitatively in a similar way than TAT-C-Cy5. For the first time, we also show that Had$_{UF1-11}$-C-Cy5 and Had$_{UF3-11}$-C-Cy5 both penetrate better than MCa$_{UF1-9}$-C-Cy5 (Figure 4C).

Figure 4. Cell penetration properties of the hydrophobic domains of toxins from the calcin family. (**A**) Real or modeled 3D structures of MCa (PDB access code 1C6W), imperatoxin A (access code 1IE6), hemicalcin (model), opicalcin 1 (model), opicalcin 2 (model) and hadrucalcin (model). Residues in blue describe the hydrophobic domain investigated in this study. Red residues are all amino acids that differ from MCa's amino acid sequence. Residues in green are cystine residues. (**B**) Amino acid sequences of the hydrophobic domains of each member of the calcin family. The third Cys residue is systematically replaced by Abu in our synthetic peptides and is represented in grey color. Residues in blue are those that differ from MCa$_{UF1-9}$ amino acid sequence. This sequence alignment defines three groups of peptides with similar N-terminal sequences. (**C**) Comparative cell penetration efficacies of the peptides derived from members of the calcin family as assessed by dose-response curves from flow cytometry data. TAT-C-Cy5 data are indicated by a blue dashed line for comparison. (**D**) Confocal images illustrating the cell penetration of each peptide of the calcin family after incubation of 1 µM of the peptides with F98 cells during 2 h. A significantly lower cell penetration is observed for Imp$_{UF1-9}$-C-Cy5 compared to the two hadrucalcin-derived peptides (Had$_{UF1-11}$-C-Cy5 and Had$_{UF3-11}$-C-Cy5).

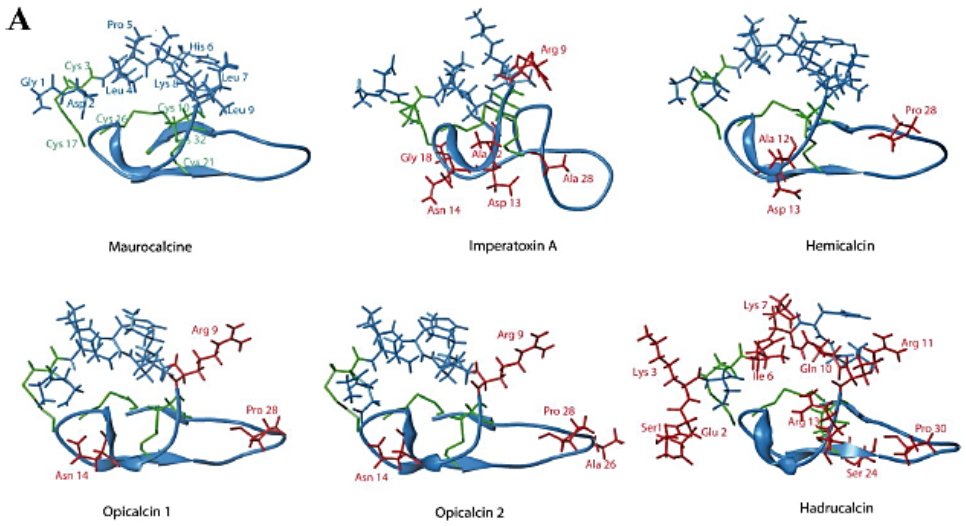

Figure 4. *Cont.*

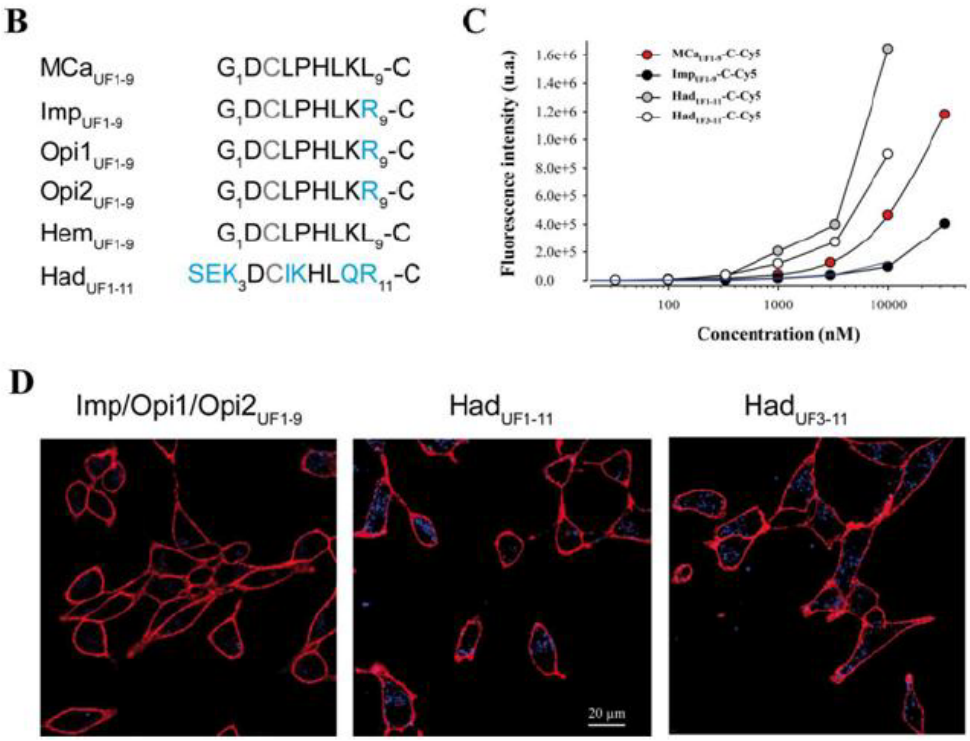

This indicates that a series of very selective set of amino acid substitutions are required to improve MCa$_{UF1-9}$ cell penetration properties. They also demonstrate that the calcin family can accommodate some variation in cell penetration efficacy for the activation of the ryanodine receptor. Nevertheless, it remains to be investigated whether the additional basic face and pharmacophore region are necessary to improve the characteristics of cell penetration of imperatoxin A, opicalcin 1 or opicalcin 2. In any case, it is obvious that Had$_{UF1-11}$ is a remarkable cell penetration peptide by the extent of its efficacy compared to the popular peptides challenged in Figure 1.

2.6. Cell Penetration of MCa$_{UF1-9}$ is pH-sensitive Owing to the Presence of an His Residue in its Amino Acid Sequence

Close examination of the amino acid sequence of MCa reveals that it contains a histidine residue at position 6. This residue is therefore also present in MCa$_{UF1-9}$. According to Figure 2 data, this histidine residue contributes to some extent to the cell penetration efficacy of MCa$_{UF1-9}$-C-Cy5. The imidazole sidechain of histidine has a pKa of approximately 6.0, while overall the pKa of the amino acid is 6.5. However, this value is susceptible to be influenced by the direct amino acid environment of this residue. In any case, it can be considered that at physiological conditions, relatively small changes in pH value is susceptible to alter the average charge of MCa$_{UF1-9}$. At a pH value lower than 6, the imidazole ring is essentially protonated. Protonation of the His residue at position 6 may affect the cell penetration efficacy of MCa$_{UF1-9}$-C-Cy5. To test this idea, the extracellular pH value was varied between 5.0 and 8.0 during the 2 h incubation of F98 cells with MCa$_{UF1-9}$-C-Cy5 and the total

accumulated fluorescence level evaluated by FACS. The data were normalized to the value at pH 5.0. As shown, decreasing pH values results in higher fluorescence values and therefore greater accumulation of the peptide in F98 cells (Figure 5A).

A fit of the data with a decreasing exponential suggests that the peptide enters into F98 cells with a 2.8-fold lower efficacy than at acidic pH values. Half of this decrease in efficacy occurs for a variation in pH from 5.0 to 5.7 indicating that the pKa value of this histidine residue within MCa_{UF1-9}-C-Cy5 may be close to 5.7. The involvement of His^6 in this pH-dependence of the cell penetration of the peptide is demonstrated by the lack of pH-dependence in cell penetration of the mutant peptide $MCa_{UF1-9(W6)}$-C-Cy5 in which His^6 is replaced by Trp^6 (Figure 5B). Overall, these data indicate that protonation of His^6, provided by acidic environments, results in improved MCa_{UF1-9}-C-Cy5 cell delivery. In that respect, it is important to note that F98 cells are from rat glioma and that the extracellular pH within the glioma tumors masses in the brain has been predicted to be acidic [34]. Our finding therefore suggests that the MCa_{UF1-9} peptide may be useful to more specifically deliver anti-tumor drugs within glioma.

2.7. Long-Lasting Cell Retention of MCa_{UF1-9}

One property of CPP is that they enter quite rapidly into cells. However, the persistence of their intracellular accumulation is seldom looked after. We investigated this question with three peptides. We used MCa_{UF1-9}-C-Cy5, a non or poorly charged peptide depending on the protonation level of His^6, $MCa_{UF11-33}$-C-Cy5, a highly charged peptide mainly encompassing the two C-terminal thirds of MCa, and Had_{UF3-11}-C-Cy5 which is less hydrophobic than MCa_{UF1-9}-C-Cy5. One could expect that hydrophobic peptides may more readily escape from the cell interior than charged peptides. To test this idea, F98 cells were loaded 2 h with 1 µM of each of these peptides, extensively washed, maintained in culture for a variable duration (between 0 and 34 h, washout time), treated with trypsin and the fluorescence level remaining in the cells estimated by FACS (Figure 5C).

As shown and quite remarkably, the fluorescence levels of the accumulated peptides fade away only slowly with time indicating that the cell entry of the peptides are faster than their cell exit (Figure 5C,D). Time constant of half exit were estimated to be 5 h for MCa_{UF1-9}-C-Cy5, 8 h and 20 min for $MCa_{UF11-33}$-C-Cy5 and 16 h and 40 min for Had_{UF3-11}-C-Cy5. After 34 h, cells still contained 27, 21 and 23% of MCa_{UF1-9}-C-Cy5, $MCa_{UF11-33}$-C-Cy5 and Had_{UF3-11}-C-Cy5 fluorescence, respectively. These values are suspected to be higher in fact since 34 h is enough to register at least one cell division cycle. This property of persistence indicates that MCa_{UF1-9}, but also $MCa_{UF11-33}$ and Had_{UF3-11}, can be used both as CPP and retention agents for drugs that may freely enter into cells but would also freely escape from them. We have previously used such a property to fight against chemo-resistance of the breast tumor cell line MDA-MB-231 by coupling doxorubicin to a non-folded version of MCa [20,22,23]. Confocal microscopy images of the cell distribution of both peptides tested indicate that the distribution of the peptides does not evolve with washout time (Figure 5D). The distribution remains mostly punctiform (with an evolution towards what may seem smaller dots), internal and hardly invades the nucleus.

Figure 5. pH-dependence and persistence of the cell penetration of MCa_{UF1-9}-C-Cy5. (**A**) Effect of extracellular pH variation on the cell penetration efficacy of 1 µM MCa_{UF1-9}-C-Cy5 in F98 cells (2 h incubation). Mean of n = 3 experiments ± S.D. Mean FACS results were normalized before averaging. Data were fitted by a decreasing exponential of the type $y = y_0 + a.e^{-bx}$ where $y_0 = 0.36 \pm 0.05$, $a = 0.64 \pm 0.09$ and $b = 1.76 \pm 0.61$. (**B**) Effect of extracellular pH variation on the cell penetration of 1 µM MCa_{UF1-9}(W6)-C-Cy5 in F98 cells (2 h incubation). The pH-insensitive Trp^6 replaces the pH-sensitive His^6 in this mutant peptide. (**C**) Persistence of the fluorescence signal in F98 cells preincubated 2 h with 1 µM MCa_{UF1-9}-C-Cy5 (net charge 0 if His^6 is unprotonated, black symbol), the positively charged $MCa_{UF11-33}$-C-Cy5 (net charge +7, red symbol) or the mildly charged Had_{UF3-11}-C-Cy5 peptide (net charge +2 if His^8 is unprotonated, white symbol). FACS results were normalized to 1 at t=0 min at the start of the washout of the CPP. Data were fitted with a decreasing exponential function with $1/\tau = 0.20 \pm 0.01$ h^{-1} (MCa_{UF1-9}-C-Cy5), 0.12 ± 0.03 h^{-1} ($MCa_{UF11-33}$-C-Cy5) et 0.06 ± 0.02 h^{-1} (Had_{UF3-11}-C-Cy5), where τ is the time constant of the decrease in the mean cell fluorescence level. The non-decreasing fraction of fluorescence was equal to 0.27 ± 0.14 (MCa_{UF1-9}-C-Cy5), 0.21 ± 0.07 ($MCa_{UF11-33}$-C-Cy5) and 0.23 ± 0.13 (Had_{UF3-11}-C-Cy5). (**D**) Corresponding confocal images illustrating that the intracellular distribution of the peptides did not change with time. The 2.5-fold image enhancement also shows a close to complete lack of nucleus invasion by the peptides. The images also show that the two peptides do not differ in the type of intracellular distribution 3.5 h after washout of the extracellular peptides.

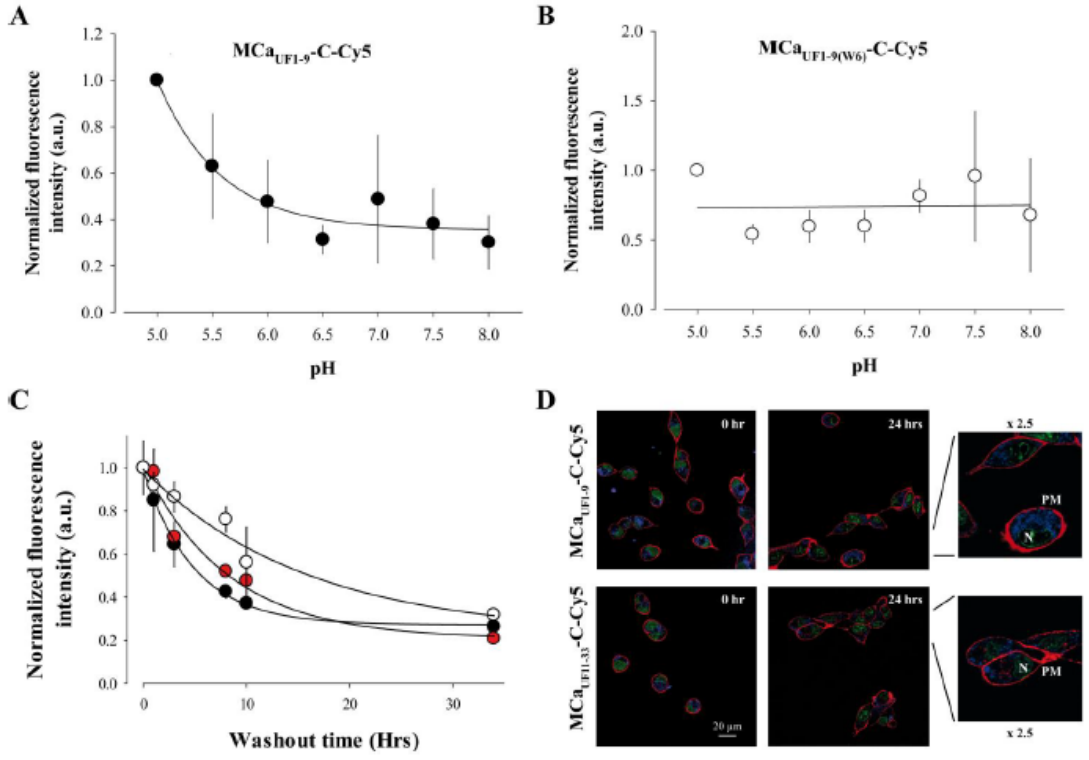

2.8. Discussion

While all MCa truncations and/or disruptions of disulfide bridges produce a loss of the 3D structure, MCa_{UF1-9} is more susceptible than other truncated peptides to preserve some of the structural characteristics that it may possess within the full-length MCa as it encloses by itself the entire hydrophobic face of MCa. At this stage, one may only speculate as to why MCa presents one hydrophobic face diametrically opposite to a highly charged basic face. It may present a strong advantage for the peptide if it has to deal with both a hydrophilic environment (extracellular space and cytoplasm) and a hydrophobic one (membrane lipids). Besides it may be essential to the mechanism of cell translocation if the peptide needs to cope with the amphiphilic nature of membrane lipids. The strong dipole moment of the peptide, resulting from the existence of these two different faces, probably orients the peptide in its interaction with the plasma membrane. The highly basic nature of MCa should also speed up the peptide entry through electrochemical attraction if one considers that it diffuses freely through the plasma membrane, in a similar way that Na^+ or Ca^{2+} ions would do when permeating through adequate ion channels while attracted by the inside negative membrane potential. Such a mechanism, if proven, would result in peptide accumulation against the concentration gradient. What the effect of a physical separation between these two peptide entities (hydrophobic face and basic face) might be on the cell penetration mechanism remains however unclear. One may notice at this point that MCa_{UF1-9}-C-Cy5 and $MCa_{UF11-33}$-C-Cy5 produce quite similar intracellular punctiform distributions in F98 cells arguing that they share nonetheless similar mechanisms of cell penetration. This was also the case for the other CPP investigated in this study (poly-R-C-Cy5, Tat-C-Cy5 and Pen-C-Cy5). It is of interest to note however that the cell distribution of fluorescent D-MCa, a full-length and well-structured analogue of MCa, is mostly diffuse [16] suggesting that combining the hydrophobic and basic faces of the molecule to shorten the residency time in the plasma membrane may represent a significant advantage in cell penetration.

The most interesting information that we could gather from our mutagenesis program of MCa_{UF1-9}-C-Cy5 was that the two first amino acid residues were the most dispensable for its penetration properties. This truncation approach led to the design of a 7-mer CPP that has greater potency than most popular CPPs on the market. Investigating the cell penetrating properties of peptides derived from the hydrophobic face of other peptides members of the calcin family turned out as a more interesting approach than mutagenesis. Most of these peptides differ by only a few amino acid residues, with the notable exception of hadrucalcin. Coherent with the mono-substitution we performed at amino acid 9 of MCa_{UF1-9}-C-Cy5, the cell penetration properties of Imp_{UF1-9}-C-Cy5, $Opi1_{UF1-9}$-C-Cy5 and $Opi2_{UF1-9}$-C-Cy5, all presenting Arg^9 instead of Leu^9, were reduced to some extent compared to MCa_{UF1-9}-C-Cy5. Remarkably, multiple amino acid substitution as demonstrated within Had_{UF1-11}-C-Cy5 resulted in an important and unexpected improvement of cell penetration. Similarly to MCa_{UF1-9}-C-Cy5, removing the two first N-terminal amino acid residues of Had_{UF1-11}-C-Cy5 produced a peptide with quite significant levels of cell penetration. The core of the sequence, the one we assume to be important for cell penetration (after Abu^3 in MCa_{UF1-9}), contains no less than 4 substitutions (Leu^4 by Ile, Pro^5 by Lys, Lys^8 by Gln, and Leu^9 by Arg). This indicates that quite elaborate alterations need to be done to MCa_{UF1-9} sequence to further improve it cell penetrating properties. In any case, these findings (i) define a novel CPP with unprecedented efficacy, and (ii)

open the door for the design of hadrucalcin/MCa chimeras 1 μM MCa_{UF1-9}-C-Cy5 fluorescence at any given concentration and never in terms of starting concentration at which cell entry was observed. These observations suggest that the affinity of these peptides for plasma membrane components remains unaltered.

Since we are interested in developing a number of applications in oncology for MCa analogues, we also investigated the role of His^6 in cell entry into the glioma F98 cells. Of great interest for future applications, we found that protonation of His^6, occurring at more acidic pH, but in a range compatible with pH values observed in glioma, produced a three-fold more potent peptide for cell penetration. We assume that protonated His^6 may form a salt bridge with Asp^2 in the non-structured MCa_{UF1-9}. It is likely that, without this salt bridge, the negative charge carried by Asp^2 may disfavor cell penetration of MCa_{UF1-9}. This observation on the importance of protonation in peptide cell penetration will be useful for the future design of new MCa analogues in which important basic amino acid residues may be substituted by His residues in order to further improve the tumor-selectivity of these potent CPP. Interesting positions will include Lys^{19}, Lys^{20}, Lys^{22} and Arg^{24} all shown to contribute to the cell penetration efficacy of the full length MCa [17].

3. Experimental

3.1. Reagents

N-α-Fmoc-L-aminoacids, Wang-Tentagel resin and reagents used for peptide syntheses were obtained from Iris Biotech (Marktredwitz, Germany). Solvents were analytical grade products from Acros Organics (Geel, Belgium). Cy5 maleimide mono-reactive dye was purchased from GE Healthcare (Saclay, France).

3.2. Peptide Syntheses

Chemical syntheses of truncated toxin peptides were performed as previously described [16]. Briefly, peptides were chemically synthesized by the solid-phase method [35] using an automated peptide synthesizer (CEM© Liberty 12, Matthews, NC, USA). Peptide chains were assembled stepwise on 0.24 meq of Fmoc-D-Arg-Pbf-Wang-Tentagel resin using 0.24 mmol of *N*-α-fluorenylmethyloxycarbonyl (Fmoc) L-amino-acid derivatives. The side-chain protecting groups were: trityl for Cys and Asn, *tert*-butyl for Ser, Thr, Glu and Asp, Pbf for Arg and *tert*-butylcarbonyl for Lys. Reagents were at the following concentrations: Fmoc-amino-acids [0.2 M Fmoc-AA-OH in dimethylformamide (DMF)], activator (0.5 M 2-(1H-benzotriazole-1-yl)-1,1,3,3-tetramethyluronium hexafluorophosphate in DMF), activator base [2 M diisopropylethylamine in N-methylpyrrolidone (NMP)] and deprotecting agent (5% piperazine/0.1 M 1-hydroxybenzotriazole in DMF), as advised by PepDriver (CEM©). After peptide chain assembly, resins were treated 4 h at room temperature with a mixture of trifluoroacetic acid/water/triisopropylsilane (TIS)/dithiothreitol (DTT) (92.5/2.5/2.5/2.5). The peptide mixtures were then filtered and the filtrates were precipitated by adding cold *tert*-butylmethyl ether. The crude peptides were pelleted by centrifugation (10,000 × *g*, 15 min) and the supernatants were discarded. Truncated toxin analogues were purified by HPLC using a Vydac C18 column (218TP1010, 25 × 10 cm). Elutions of the peptides were performed with a 10–60% acetonitrile

linear gradient containing 0.1% trifluoroacetic acid. The purified fractions were analyzed by analytical RP-HPLC (Vydac C18 column 218TP104, 25 × 4.6 cm). All analogues were characterized by MALDI-TOF mass spectrometry.

3.3. Peptide Labeling With Cy5

Each peptide was labeled with Cy5 according to the manufacturer's protocol (GE Healthcare). Peptides were dissolved at 200 µg/mL in 1 M $NaHCO_3$ buffer, pH 9.3. 500 µL of solubilized peptides were added to Cy5-maleimide containing tubes. The mixtures were incubated during 2 h at room temperature and then purified by HPLC using an analytical Vydac C18 column. Elution of the Cy5-labeled peptides was performed with a 5–90% acetonitrile linear gradient containing 0.1% trifluoroacetic acid. The pure peak fractions were lyophilized and peptides quantified by UV spectrophotometer at 650 nm.

3.4. Cell Culture

Undifferentiated malignant glioma rat (F98) cell line (from ATCC) was maintained at 37 °C in 5% CO_2 in DMEM/F-12 nutrient medium (Invitrogen, Cergy Pontoise, France) supplemented with 2% (v/v) heat-inactivated fetal bovine serum (Invitrogen) and 100 µg/mL streptomycine and 100 units/mL penicillin (Invitrogen).

3.5. Confocal Microscopy

For analysis of the cell entry of Cy5-labeled-truncated toxin peptides in living cells, cell cultures were incubated with the fluorescent peptides (in DMEM/F-12 nutrient medium only) for 2 h, and then washed twice with phosphate-buffered saline (PBS) alone. The plasma membrane was stained with 50 µg/mL rhodamine-conjugated concanavalin A (Invitrogen, Cergy Pontoise, France) for 5 min. Cells were washed once more. Live cells were then immediately analyzed by confocal laser scanning microscopy using a Zeiss LSM operating system. Rhodamine (561 nm) and Cy5 (633 nm) were sequentially excited and emission fluorescence were collected.

3.6. Fluorescence Activated Cell Sorting Analyses

F98 cells were incubated with various concentrations of Cy5-labeled peptides in DMEM/F-12 culture medium without serum at 37 °C for 2 h. The cells were then washed with PBS to remove excess extracellular peptide and treated with 0.48 mM versene (Invitrogen) for 5 min at 37 °C to detach cells from the surface, and centrifuged at 200 *g* in DMEM/F-12 culture medium before suspension in PBS. For experiments concerning endocytosis inhibitors, F98 cells were initially preincubated in DMEM/F-12 culture medium without serum for 30 min at 37 °C with different inhibitors of endocytosis: (i) 100 µM amiloride, (ii) 5 µg/mL cytochalasin D (10 µM), (iii) 20 µM nocodazole, or (iv) 5 mM methyl-β-cyclodextrin (all from Sigma, Lyon, France). The cells were then incubated for 2 h at 37 °C with 1 µM $MCa_{UF1\text{-}9}$-C-Cy5 in the presence of each drug. Flow cytometry analyses were performed with live cells using an Accuri C6 flow cytometer (BD Biosciences, Le Pont

de Claix, France). Data were obtained and analyzed using CFlow Sampler (BD Biosciences). Live cells were gated by forward/side scattering from a total of 10,000 events.

3.7. Molecular Modeling

Using Sybyl X 1.3 (Tripos Inc., St. Louis, MO, USA) and PDB structure of MCa (code 1C6W) and imperatoxin A (code 1IE6), we generated 3D models of opicalcin 1 and 2, hemicalcin and hadrucalcin. There is a sequence homology (76% up to 91%) between these proteins. Based on previous reports [6,7], we replaced some amino acid of MCa sequence to obtain the corresponding ones for the four different proteins. Several steps of minimization and control of the stereochemistry were performed to obtain a model for each molecule.

4. Conclusions

In this manuscript, we have demonstrated that $MCa_{UF1\text{-}9}$-C-Cy5 starts to show detectable penetration in glioma F98 cells at concentrations as low as 33 nM (5-fold increase over control) as detected by FACS. The process is visible at 100 nM by confocal microscopy and a comparative analysis reveals that it is highly competitive compared to TAT, penetratin or Poly-R CPP. One analogue turns out to be extremely competitive, $MCa_{UF3\text{-}9}$, owing to its performance, length and ease of synthesis. Nevertheless, we also demonstrate that engineered optimization of its cell penetrating properties is hard to achieve but that Mother Nature has provided an elegant solution to this problem by selecting itself the best amino acid substitutions under the form of new calcin analogues. In that respect, the hydrophobic domain of hadrucalcin outperforms that of MCa. We evidence for the first time the possibility to modulate peptide cell penetration by external pH provided that His residues are strategically incorporated within the amino acid sequence. This finding enlarges the potential application of these peptides to the treatment of glioma. Additionally, the observation that the residency time of these peptides in glioma F98 cells is quite long suggest that these peptides may be best used when injected once inside a solid tumor rather than by intravenous route.

Acknowledgements

We acknowledge financial support to MDW by Inserm and by the Nanofret grant and LabEx ICST of the Agence Nationale de la Recherche (ANR). MDW is a recipient of a contrat d'interface from Inserm and Grenoble Hospital. EB has a fellowship from ANR. We also thank the Région Rhône Alpes for the financial support of CT by an Emergence grant.

References

1. Fajloun, Z.; Kharrat, R.; Chen, L.; Lecomte, C.; di Luccio, E.; Bichet, D.; El Ayeb, M.; Rochat, H.; Allen, P.D.; Pessah, I.N.; *et al*. Chemical synthesis and characterization of maurocalcine, a scorpion toxin that activates Ca^{2+} release channel/ryanodine receptors. *FEBS Lett.* **2000**, *469*, 179–185.
2. Mouhat, S.; Jouirou, B.; Mosbah, A.; de Waard, M.; Sabatier, J.M. Diversity of folds in animal toxins acting on ion channels. *Biochem J.* **2004**, *378*, 717–726.

3. Mosbah, A.; Kharrat, R.; Fajloun, Z.; Renisio, J.G.; Blanc, E.; Sabatier, J.M.; El Ayeb, M.; Darbon, H. A new fold in the scorpion toxin family, associated with an activity on a ryanodine-sensitive calcium channel. *Proteins* **2000**, *40*, 436–442.
4. Zamudio, F.Z.; Gurrola, G.B.; Arevalo, C.; Sreekumar, R.; Walker, J.W.; Valdivia, H.H.; Possani, L.D. Primary structure and synthesis of imperatoxin A (iptx(a)), a peptide activator of Ca^{2+} release channels/ryanodine receptors. *FEBS Lett.* **1997**, *405*, 385–389.
5. Zhu, S.; Darbon, H.; Dyason, K.; Verdonck, F.; Tytgat, J. Evolutionary origin of inhibitor cystine knot peptides. *FASEB J.* **2003**, *17*, 1765–1767.
6. Shahbazzadeh, D.; Srairi-Abid, N.; Feng, W.; Ram, N.; Borchani, L.; Ronjat, M.; Akbari, A.; Pessah, I.N.; de Waard, M.; El Ayeb, M. Hemicalcin, a new toxin from the iranian scorpion hemiscorpius lepturus which is active on ryanodine-sensitive Ca^{2+} channels. *Biochem. J.* **2007**, *404*, 89–96.
7. Schwartz, E.F.; Capes, E.M.; Diego-Garcia, E.; Zamudio, F.Z.; Fuentes, O.; Possani, L.D.; Valdivia, H.H. Characterization of hadrucalcin, a peptide from hadrurus gertschi scorpion venom with pharmacological activity on ryanodine receptors. *Br. J. Pharmacol.* **2009**, *157*, 392–403.
8. Altafaj, X.; France, J.; Almassy, J.; Jona, I.; Rossi, D.; Sorrentino, V.; Mabrouk, K.; de Waard, M.; Ronjat, M. Maurocalcine interacts with the cardiac ryanodine receptor without inducing channel modification. *Biochem. J.* **2007**, *406*, 309–315.
9. Szappanos, H.; Smida-Rezgui, S.; Cseri, J.; Simut, C.; Sabatier, J.M.; de Waard, M.; Kovacs, L.; Csernoch, L.; Ronjat, M. Differential effects of maurocalcine on Ca^{2+} release events and depolarization-induced Ca^{2+} release in rat skeletal muscle. *J. Physiol.* **2005**, *565*, 843–853.
10. Gurrola, G.B.; Arevalo, C.; Sreekumar, R.; Lokuta, A.J.; Walker, J.W.; Valdivia, H.H. Activation of ryanodine receptors by imperatoxin A and a peptide segment of the II-III loop of the dihydropyridine receptor. *J. Biol. Chem.* **1999**, *274*, 7879–7886.
11. Esteve, E.; Mabrouk, K.; Dupuis, A.; Smida-Rezgui, S.; Altafaj, X.; Grunwald, D.; Platel, J.C.; Andreotti, N.; Marty, I.; Sabatier, J.M.; *et al.* Transduction of the scorpion toxin maurocalcine into cells. Evidence that the toxin crosses the plasma membrane. *J. Biol. Chem.* **2005**, *280*, 12833–12839.
12. Tanabe, T.; Beam, K.G.; Adams, B.A.; Niidome, T.; Numa, S. Regions of the skeletal muscle dihydropyridine receptor critical for excitation-contraction coupling. *Nature* **1990**, *346*, 567–569.
13. Tanabe, T.; Beam, K.G.; Powell, J.A.; Numa, S. Restoration of excitation-contraction coupling and slow calcium current in dysgenic muscle by dihydropyridine receptor complementary DNA. *Nature* **1988**, *336*, 134–139.
14. Altafaj, X.; Cheng, W.; Esteve, E.; Urbani, J.; Grunwald, D.; Sabatier, J.M.; Coronado, R.; de Waard, M.; Ronjat, M. Maurocalcine and domain a of the II-III loop of the dihydropyridine receptor $Ca_v1.1$ subunit share common binding sites on the skeletal ryanodine receptor. *J. Biol. Chem.* **2005**, *280*, 4013–4016.
15. Chen, L.; Esteve, E.; Sabatier, J.M.; Ronjat, M.; de Waard, M.; Allen, P.D.; Pessah, I.N. Maurocalcine and peptide a stabilize distinct subconductance states of ryanodine receptor type 1, revealing a proportional gating mechanism. *J. Biol. Chem.* **2003**, *278*, 16095–16106.

16. Poillot, C.; Dridi, K.; Bichraoui, H.; Pecher, J.; Alphonse, S.; Douzi, B.; Ronjat, M.; Darbon, H.; de Waard, M. D-maurocalcine, a pharmacologically inert efficient cell-penetrating peptide analogue. *J. Biol. Chem.* **2010**, *285*, 34168–34180.
17. Mabrouk, K.; Ram, N.; Boisseau, S.; Strappazzon, F.; Rehaim, A.; Sadoul, R.; Darbon, H.; Ronjat, M.; de Waard, M. Critical amino acid residues of maurocalcine involved in pharmacology, lipid interaction and cell penetration. *Biochim. Biophys. Acta* **2007**, *1768*, 2528–2540.
18. Ram, N.; Weiss, N.; Texier-Nogues, I.; Aroui, S.; Andreotti, N.; Pirollet, F.; Ronjat, M.; Sabatier, J.M.; Darbon, H.; Jacquemond, V.; *et al.* Design of a disulfide-less, pharmacologically-inert and chemically-competent analog of maurocalcine for the efficient transport of impermeant compounds into cells. *J. Biol. Chem.* **2008**, *283*, 27048–27056.
19. Poillot, C.; Bichraoui, H.; Tisseyre, C.; Bahemberae, E.; Andreotti, N.; Sabatier, J.M.; Ronjat, M.; de Waard, M. Small efficient cell-penetrating peptides derived from scorpion toxin maurocalcine. *J. Biol. Chem.* **2012**, *287*, 17331–17342.
20. Aroui, S.; Brahim, S.; de Waard, M.; Breard, J.; Kenani, A. Efficient induction of apoptosis by doxorubicin coupled to cell-penetrating peptides compared to unconjugated doxorubicin in the human breast cancer cell line MDA-MB 231. *Cancer Lett.* **2009**, *285*, 28–38.
21. Aroui, S.; Brahim, S.; de Waard, M.; Kenani, A. Cytotoxicity, intracellular distribution and uptake of doxorubicin and doxorubicin coupled to cell-penetrating peptides in different cell lines: A comparative study. *Biochem. Biophys. Res. Commun.* **2010**, *391*, 419–425.
22. Aroui, S.; Brahim, S.; Hamelin, J.; de Waard, M.; Breard, J.; Kenani, A. Conjugation of doxorubicin to cell penetrating peptides sensitizes human breast MDA-MB 231 cancer cells to endogenous trail-induced apoptosis. *Apoptosis* **2009**, *14*, 1352–1365.
23. Aroui, S.; Ram, N.; Appaix, F.; Ronjat, M.; Kenani, A.; Pirollet, F.; de Waard, M. Maurocalcine as a non-toxic drug carrier overcomes doxorubicin resistance in the cancer cell line MDA-MB 231. *Pharm. Res.* **2009**, *26*, 836–845.
24. Ram, N.; Texier-Nogues, I.; Pernet-Gallay, K.; Poillot, C.; Ronjat, M.; Andrieux, A.; Arnoult, C.; Daou, J.; de Waard, M. *In vitro* and *in vivo* cell delivery of quantum dots by the cell penetrating peptide maurocalcine. *Int. J. Biomed. Nanosci. Nanotechnol.* **2011**, *2*, 12–32.
25. Stasiuk, G.J.; Tamang, S.; Imbert, D.; Poillot, C.; Giardiello, M.; Tisseyre, C.; Barbider, E.L.; Fries, P.H.; de Waard, M.; Reiss, P.; Mazzanti, M. Cell-permeable ln(III) chelate-functionalized InP quantum dots as multimodal imaging agents. *ACS Nano* **2011**, *5*, 8193–8201.
26. Ram, N.; Aroui, S.; Jaumain, E.; Bichraoui, H.; Mabrouk, K.; Ronjat, M.; Lortat-Jacob, H.; de Waard, M. Direct peptide interaction with surface glycosaminoglycans contributes to the cell penetration of maurocalcine. *J. Biol. Chem.* **2008**, *283*, 24274–24284.
27. Boisseau, S.; Mabrouk, K.; Ram, N.; Garmy, N.; Collin, V.; Tadmouri, A.; Mikati, M.; Sabatier, J.M.; Ronjat, M.; Fantini, J.; *et al.* Cell penetration properties of maurocalcine, a natural venom peptide active on the intracellular ryanodine receptor. *Biochim. Biophys. Acta* **2006**, *1758*, 308–319.
28. Jones, A.T.; Sayers, E.J. Cell entry of cell penetrating peptides: Tales of tails wagging dogs. *J. Control. Release* **2012**, *161*, 582–591.
29. Lindgren, M.; Hallbrink, M.; Prochiantz, A.; Langel, U. Cell-penetrating peptides. *Trends Pharmacol. Sci.* **2000**, *21*, 99–103.

30. Lundberg, P.; Langel, U. A brief introduction to cell-penetrating peptides. *J. Mol. Recognit.* **2003**, *16*, 227–233.
31. Mano, M.; Teodosio, C.; Paiva, A.; Simoes, S.; Pedroso de Lima, M.C. On the mechanisms of the internalization of s4(13)-pv cell-penetrating peptide. *Biochem. J.* **2005**, *390*, 603–612.
32. Gurrola, G.B.; Capes, E.M.; Zamudio, F.Z.; Possani, L.D.; Valdivia, H.H. Imperatoxin A, a cell-penetrating peptide from scorpion venom, as a probe of Ca-release channels/ryanodine receptors. *Pharmaceuticals (Basel)* **2010**, *3*, 1093–1107.
33. El-Hayek, R.; Lokuta, A.J.; Arevalo, C.; Valdivia, H.H. Peptide probe of ryanodine receptor function. Imperatoxin A, a peptide from the venom of the scorpion pandinus imperator, selectively activates skeletal-type ryanodine receptor isoforms. *J. Biol. Chem.* **1995**, *270*, 28696–28704.
34. Garcia-Martin, M.L.; Herigault, G.; Remy, C.; Farion, R.; Ballesteros, P.; Coles, J.A.; Cerdan, S.; Ziegler, A. Mapping extracellular pH in rat brain gliomas *in vivo* by 1H magnetic resonance spectroscopic imaging: Comparison with maps of metabolites. *Cancer Res.* **2001**, *61*, 6524–6531.
35. Merrifield, R.B. Solid-phase peptide synthesis. *Adv. Enzymol. Relat. Areas Mol. Biol.* **1969**, *32*, 221–296.

3.2.3. Discussion

Dans l'étude précédente, la MCa_{UF1-9} s'est avérée la mieux indiquée des analogues de la MCa délétés pour des applications nécessitant de faibles concentrations intracellulaires. Composé de 9 résidus, la MCa_{UF1-9} est l'un des CPPs les plus courts connus à ce jour. Cette petitesse a pour avantage le moindre coût de synthèse. Par ailleurs, son efficacité à de faibles concentrations signifie une utilisation en faible quantité, donc un moindre coût d'utilisation. La MCa_{UF1-9} représente donc un intérêt économique particulier. En vue de son exploitation en termes d'applications, nous l'avons caractérisée de manière plus approfondie.

La MCa_{UF1-9} a montré une meilleure efficacité de pénétration cellulaire comparativement à des CPPs usuels, la Tat, la pénétratine, et la polyarginine. Ces observations remettent en question la place attribuée à la Tat et à la pénétratine dans le contexte des CPPs. Cependant, en plus des cellules F98, sur lesquelles a été réalisée la présente étude, la comparaison devrait être réalisée sur différents types cellulaires pour mieux positionner la MCa_{UF1-9} face à ces CPPs usuels.

Il a été surprenant de constater que le peptide $ChTx_{UF1-12}$ dérivé de la toxine Charybdotoxine (ChTx) normalement non reconnu comme un CPP, a montré une certaine pénétration cellulaire (Fig.1.E-Chap.3.2.2). Sur les cellules F98, la microscopie confocale n'a pas mis en évidence la pénétration cellulaire de la $ChTx_{UF1-12}$ à des concentrations extracellulaires allant jusqu'à 3 µM. En revanche, avec la cytométrie en flux, technique quantitative et plus sensible, une pénétration cellulaire de la $ChTx_{UF1-12}$ a été observée à des concentrations supérieures à 1 µM. Cependant, la pénétration cellulaire était plus faible que celle de la Tat, le moins efficace des CPPs déjà reconnus testés dans la présente étude. Il semble donc qu'à forte concentration tout peptide peut interagir avec la membrane plasmique ce qui conduit à son internalisation (*278*). Le fait que tous les peptides pourraient pénétrer dans la cellule à de fortes concentrations extracellulaires, soulèverait la question sur la vraie définition du CPP. En plus de la translocation directe, la caractéristique spéciale et fondatrice des CPPs, la concentration extracellulaire minimale efficace en pénétration cellulaire devrait être également prise en compte pour la définition des CPPs. Ainsi par exemple, tout peptide qui, dans au moins un type cellulaire, pénètre dans les cellules par la translocation directe (totalement ou partiellement) et qui, par la cytométrie en flux, manifeste une pénétration cellulaire à une concentration extracellulaire inférieure ou égale à 10 µM (simple exemple),

serait reconnu CPP. Evidemment, il faudrait y avoir un consensus sur la concentration de référence.

La MC_{UF1-9} pénètre dans la cellule essentiellement par une voie indépendante de l'endocytose. L'étude antérieure réalisée sur les cellules CHO avait montré une pénétration cellulaire de la MCa_{UF1-9} exclusivement indépendante de la macropinocytose (Fig.5.B-Chap.3.1.2). La présente étude qui a évalué la contribution de toutes les voies d'endocytose sur les cellules F98, a montré que la pénétration cellulaire de la MCa_{UF1-9} est principalement indépendante de l'endocytose (environ 75 %). Cependant, la macropinocytose contribue partiellement (environ 25 %) à la pénétration cellulaire du peptide (Fig.2-Chap.3.2.2). Ces résultats montrent que le mode de pénétration cellulaire des CPPs varie d'un type cellulaire à un autre.

La MCa_{UF1-9} a par ailleurs montré une augmentation de l'efficacité de pénétration cellulaire en milieu acide (Fig.5.A&B-Chap.3.2.2). Ceci s'expliquerait par la protonation de son résidu histidine (en position 6) en milieu acide conférant au peptide une charge positive supplémentaire qui améliore les interactions du peptide avec la surface de la membrane plasmique, indispensables dans le processus de pénétration cellulaire (*278*).
L'augmentation de l'efficacité de pénétration cellulaire en milieu acide pourrait être exploitée pour la délivrance ciblée des anticancéreux dans les cellules des tumeurs cancéreuses, notamment les gliomas. Dans le cadre du traitement anticancéreux, il est important de cibler les cellules cancéreuses qui seules doivent être éliminées, et préserver les cellules saines. Un tel ciblage est actuellement difficile à réaliser; le traitement élimine aussi bien des cellules malades que des cellules saines, ce qui est à l'origine de la plupart des effets indésirables observés au cours des thérapies anticancéreuses. Il a été montré que la plupart des tumeurs cancéreuses, particulièrement les gliomas évoluent dans un environnement acide (*284*, *285*). Cette caractéristique pourrait servir au ciblage des cellules des gliomas au moyen de la MCa_{UF1-9}. Etant plus efficace en milieu acide, *in vivo*, la MCa_{UF1-9} pénétrerait mieux dans les cellules des gliomas que dans les cellules normales évaluant, quant à elles, dans un environnement basique (pH 7,4 en moyenne) (*284*). Cependant, puisque la MCa_{UF1-9} pénètre également dans les cellules dans les conditions physiologiques normales, elle pénétrerait aussi dans les cellules des tissus sains, bien que moins efficacement. La MCa_{UF1-9} pourrait être optimisée pour un meilleur ciblage des gliomas. L'optimisation se ferait en réduisant au maximum (supprimer si possible) la pénétration cellulaire dans les conditions physiologiques

normales, tout en conservant ou améliorant la pénétration cellulaire en environnement tumoral (environnement acide). La stratégie consisterait à remplacer le résidu basique de la MCa_{UF1-9}, c'est-à-dire la lysine en position 8, par l'histidine, ce qui donnerait un peptide comportant 2 résidus histidines y compris celui en position 6; le peptide serait par exemple nommé, $MCa_{UF1-9}H(6,8)$. Dans les conditions physiologiques normales (pH 7,4), la $MCa_{UF1-9}H(6,8)$ n'aurait pas de résidu chargé positivement; elle aurait plutôt un résidu chargé négativement, l'aspartate en positon 2. Elle ne pourrait donc pas se fixer aux protéoglycanes de la surface cellulaire (*278*). Au contraire, elle serait repoussée loin de la surface cellulaire par répulsion des charges négatives des protéoglycanes de la surface cellulaire et du résidu aspartate du peptide. On remarque ici le rôle inhibiteur de la pénétration cellulaire qui serait joué par le résidu aspartate chargé négativement; sa présence dans la séquence du peptide serait donc importante. Le rôle inhibiteur de la pénétration cellulaire a déjà été observé dans la MCa native pour le glutamate en position 12, résidu acide également chargé négativement dans les conditions physiologiques normales (*17, 18*). En environnement des gliomas, donc en milieu acide, la $MCa_{UF1-9}H(6,8)$ retrouverait la propriété de pénétration cellulaire par la protonation des deux résidus histidines. Ainsi donc, la $MCa_{UF1-9}H(6,8)$ aurait une pénétration cellulaire très faible ou nulle en tissus sains et pénétrerait plus dans les cellules tumorales.

La comparaison de la MCa_{UF1-9} à des analogues issus des peptides de la même famille que la MCa (famille des calcines) a montré pour la première fois que tous ces peptides (du moins leur dérivés) sont dotés des propriétés de pénétration cellulaire. Curieusement, des analogues issus de l'hadrucalcine (Had_{UF1-11} et Had_{UF3-11}) se sont montrés plus efficaces que la MCa_{UF1-9} en pénétration cellulaire. L'Had_{UF1-11}, le plus efficace de tous apparait donc comme le CPP le plus puissant connu à ce jour. Cependant, pour confirmer sa supériorité, il devrait être davantage caractérisé, notamment pour élucider son mode de pénétration, évaluer sa toxicité et sa stabilité.

Finalement, vue la remarquable efficacité de l'$Had_{UF1-11,}$ nous l'avons retenu pour l'application de vectorisation des nanobiodétecteurs du Ca^{2+} cytosolique pour leur délivrance intracellulaire. Dans cette application, le CPP a été utilisé à une concentration de 1 µM; à cette concentration l'Had_{UF1-11} est manifestement plus efficace que les autres CPPs comparés (Fig.4.C-Chap.3.2.2).

3.2.4. Conclusion

La MCa_{UF1-9} est le mieux indiquée des analogues délétés de la MCa pour des applications nécessitant de faibles concentrations intracellulaires et représente un intérêt économique particulier. En vue d'en développer des applications, nous avons procédé à sa caractérisation de façon approfondie.

La MCa_{UF1-9} a montré d'intéressantes caractéristiques. Sa pénétration cellulaire se fait principalement par une voie non endocytique, vraisemblablement la translocation directe, le mode de pénétration précieuse, car il épargne le complexe CPP-cargaison de la séquestration et la dégradation endosomales. La MCa_{UF1-9} a par ailleurs montré une augmentation de l'efficacité de pénétration cellulaire en milieu acide. Ce caractère pourrait être exploité pour une délivrance ciblée des anticancéreux dans les cellules des gliomas. La MCa_{UF1-9} a également manifesté une longue persistance intracellulaire, ce qui suggère sa possible utilisation pour une rétention des médicaments dans des cellules résistantes par rejet de médicaments. En plus, la MCa_{UF1-9} s'est avérée plus efficace que les CPPs usuels, la Tat, la pénétratine, et la polyarginine.

D'autres observations importantes ont été faites. Des peptides normalement non reconnu comme des CPPs peuvent pénétrer dans les cellules lorsqu'ils sont utilisés à des concentrations extracellulaires relativement élevées. Cette observation suggère une révision des critères de définition des CPPs; ils devraient inclure la concentration extracellulaire minimale efficace, en plus du mode de pénétration cellulaire. Nous avons également remarqué que les propriétés de pénétration cellulaire des CPPs, notamment le mode de pénétration cellulaire, varient d'un type cellulaire à un autre.

Enfin, l'étude a conduit à la découverte de trois nouveaux CPPs dérivés des autres peptides de la famille des calcines : Imp_{UF1-9}, Had_{UF1-11} et Had_{UF3-11}. L'Had_{UF1-11} s'est avéré le meilleur en pénétration cellulaire; plus efficace que la MCa_{UF1-9}. Ceci justifie le choix de l'Had_{UF1-11} pour l'application de délivrance intracellulaire des nanobiodétecteurs du Ca^{2+} intracellulaire.

3.3. Adressage intracellulaire des nanobiodétecteurs des variations transitoires ponctuelles du Ca^{2+} intracellulaire

Résumé : La mesure des nanodomaines calciques intracellulaires par des indicateurs calciques conventionnels présente un défi expérimental majeur. La diffusion cytosolique et le photoblanchiement des indicateurs calciques conventionnels sont les principaux obstacles rencontrés. Pour concentrer localement et limiter la diffusion et le photoblanchiement des indicateurs calciques, nous avons mis au point des FRET-nanobiodétecteurs de Ca^{2+} dotés des propriétés de pénétration cellulaire. Les nanobiodétecteurs de Ca^{2+} ont été construits en attachant sur un QD plusieurs molécules de CaRuby et du CPP Had_{UF1-11}. Les tests réalisés sur les cellules BHK-21 vivantes par la microscopie confocale et par la cytométrie en flux ont montré l'efficacité de pénétration cellulaire des nanobiodétecteurs. Par ailleurs, les tests réalisés sur les cellules BHK-21 vivantes exprimant des canaux récepteurs du NMDA perméables au Ca^{2+} par la microscopie de fluorescence à réflexion totale interne (TIRF), ont montré l'efficacité des nanobiodétecteurs de Ca^{2+} à visualiser des variations locales et transitoires de la $[Ca^{2+}]$ cytosolique. Ces nanobiodétecteurs constituent une base pour la mise au point de nanobiodétecteurs d'autres ions tels que les protons H+.

3.3.1. Introduction

Le Ca^{2+} est un second messager intervenant dans diverses voies de signalisations cellulaires, dont le couplage d'excitation et contraction musculaire, le couplage d'excitation et excrétion de neurotransmetteurs, le couplage d'excitation et expression de gènes. La signalisation du calcique se fait sous forme des augmentations locales et transitoires de la $[Ca^{2+}]$ cytosolique formant des nanodomaines calciques. Ces augmentations résultent d'une entrée massive dans le cytosol, du Ca^{2+} suite à l'ouverture des canaux perméables au Ca^{2+} situés dans la membrane plasmique ou dans la membrane des stocks de Ca^{2+} intracellulaires (*268, 269*). Il est important de pouvoir mesurer les nanodomaines calciques pour mieux comprendre les différentes voies de signalisations dépendantes du Ca^{2+}.

Cependant, la mesure des nanodomaines calciques intracellulaires par des indicateurs calciques conventionnels présente un défi expérimental majeur. Les indicateurs calciques conventionnels, qui sont généralement de petites molécules organiques fluorescentes, diffusent dans le cytosol, ce qui rend difficile leur immobilisation en quantité suffisante sur de

petits volumes intracellulaires occupés par les nanodomaines calciques, ceci a pour conséquence un signal Ca^{2+} indétectable (*286*). Il est donc nécessaire de pouvoir concentrer et immobiliser les indicateurs calciques sur les sites des nanodomaines calciques. Par ailleurs les indicateurs calciques exposés aux rayons lasers excitants subissent rapidement le photoblanchiement. Le photoblanchiement pourrait être limité par une excitation moins forte et moins prolongée. L'utilisation des FRET-nanobiodétecteurs de Ca^{2+} permettrait de mieux mesurer les nanodomaines de Ca^{2+} en concentrant localement et en limitant la diffusion et le photoblanchiement des indicateurs calciques.

Les FRET-nanobiodétecteurs de Ca^{2+} sont composés d'une nanoparticule de type quantum dots (QDs) et des indicateurs de Ca^{2+}. Le QD sert de donneur d'énergie et les indicateurs de Ca^{2+} servent d'accepteurs d'énergie. En présence du Ca^{2+}, les indicateurs de Ca^{2+} émettent de la fluorescence excités par l'énergie transférée du QD (*287-289*).
Les QDs sont des nanocristaux inorganiques, semi-conductrices et fluorescentes. Les QDs sont constitués d'un noyau le plus souvent à base de Cadmium (Cd) et éventuellement d'une coque (simple ou double). Le diamètre moyen du noyau est de 2 à 10 nm. Les QDs ont d'extraordinaires propriétés optiques résultant essentiellement de leur confinement quantique. Les QDs ont un large spectre d'excitation et sont donc moins contraignants en matière de choix du laser d'excitation (*290*). Par contre, leur spectre d'émission est étroit et symétrique (*290*), ce qui garantit leur spécificité en qualité de marqueurs fluorescents. Par ailleurs, le spectre d'émission des QDs est modulable en fonction de leur taille, de leur composition, et de leur forme (*291*). De ce fait, les QDs peuvent émettre différentes longueurs d'onde de la gamme visible de la lumière, ce qui permet un marquage fluorescent multiplexe. Les QDs sont dotés d'une forte résistance au photoblanchiement permettant des analyses fluorescentes de façon plus prolongée comparativement aux fluorochromes organiques (*290*). Les QDs émettent une forte quantité de de fluorescence résultant à la fois de leur forte capacité d'absorption lumineuse et de leur grand rendement quantique. La forte fluorescence permet la visualisation même d'un seul QD, ce qui permet le marquage et la visualisation d'une seule molécule ou d'une organelle au sein d'une cellule vivante (*292-294*). Par ailleurs, la forte fluorescence fait des QDs de meilleurs donneurs FRET comparativement aux à fluorochromes organiques. Pour des applications in Vivo les QDs ont subi des optimisations. Ainsi par exemple, la couverture du noyau à base de Cd par une coque a base d'autres éléments, notamment le zinc (Zn) a réduit la cytotoxicité due au Cd (*295*). En plus, les QDs avec coque

ont manifesté de meilleures performances optiques comparativement aux QDs sans coque (*295*). Par ailleurs, les QDs ont été fonctionnalisés par des composés organiques permettant leur dispersion en milieu aqueux et le greffage de biomolécules (*295*).

L'un des indicateurs de Ca^{2+} utilisés comme accepteurs d'énergie est le Calcium Ruby (CaRuby). Le CaRuby est composé d'un fluorochrome organique (Rhodamine) couplé à un chélateur de Ca^{2+} (BAPTA) et d'une molécule de liaison (PEG). Les différents CaRuby disponibles ont une affinité pour la Ca^{2+} variable de 3 µM à 20 µM (*296*) et peuvent donc détecter différents niveaux de [Ca^{2+}] survenant dans la cellule (*268, 269*). La détection du Ca^{2+} se fait selon le principe : La Rhodamine couplé au BAPTA perd sa propriété de fluorescence par le mécanisme d'inhibition de transfert d'électrons. Mais, la propriété de fluorescence est rétablie lorsque le BAPTA fixe le Ca^{2+} (*288*).

Cependant, le nanobiodétecteur composé uniquement d'un QD et de CaRuby est incapable de pénétrer dans la cellule. Il a donc besoin d'une fonctionnalisation supplémentaire lui permettant de franchir la membrane cytoplasmique. Des études ont montré que les CPPs peuvent délivrer les QDs dans la cellule (*282*) suggérant une possible vectorisation des nananobiodétecteurs de Ca^{2+} par les CPPs.

Le présent travail a porté sur la conception des FRET-nanobiodétecteurs de Ca^{2+} dotés des propriétés de pénétration cellulaire pour la mesure dynamique des [Ca^{2+}] intracellulaires locales. Les nanobiodétecteurs ont été construits en attachant sur un QD plusieurs molécules de CaRuby et le CPP $Had_{UF1\text{-}11}$. Les tests réalisés par la microscopie confocale et par la cytométrie en flux sur les cellules BHK-21 vivantes, ont montré l'efficacité des nanobiodétecteurs à pénétrer dans les cellules. Les tests ont été également réalisés par la microscopie de fluorescence à réflexion totale interne (TIRF) sur les cellules BHK-21 vivantes et exprimant des canaux récepteurs du NMDA, perméables au Ca^{2+} après leur activation. Ces tests ont montré l'efficacité des nanobiodétecteurs à détecter des variations locales et transitoires de la [Ca^{2+}] cytosolique. Ces nanobiodétecteurs sont une base pour la mise au point de nanobiodétecteurs d'autres ions tels que les protons H^+.

3.3.2. Article publié

NANO LETTERS

Letter

pubs.acs.org/NanoLett

Cell-Penetrating Nanobiosensors for Pointillistic Intracellular Ca^{2+}-Transient Detection

Alsu I. Zamaleeva,[†,‡,§] Mayeul Collot,[∥,⊥,¶] Eloi Bahembera,[○,●] Céline Tisseyre,[○,●] Philippe Rostaing,[†,‡,§] Aleksey V. Yakovlev,[†,‡,§] Martin Oheim,[□,■] Michel de Waard,[○,●] Jean-Maurice Mallet,[∥,⊥,¶] and Anne Feltz*[,†,‡,§]

[†]Ecole Normale Supérieure, Institut de Biologie de l'ENS (IBENS), Paris F-75005, France

[‡]INSERM U1024, Paris F-75005, France

[§]CNRS UMR 8197, Paris F-75005, France

[∥]UPMC Université Paris 06, Ecole Normale Supérieure (ENS), Paris, F-75005 France

[⊥]CNRS UMR 7203, Paris F-75005, France

[¶]Laboratory of Biomolecules (LBM), Paris F-75005, France

[□]Brain Physiology Laboratory, Université Paris Descartes, PRES Sorbonne Paris Cité, Paris F-75006, France

[■]CNRS UMR 8118, Paris F-75006, France

[○]Inserm U836, Grenoble Neuroscience Institute, Research Group 3, LabEx Ion Channel Science and Therapeutics, BP170, 38042 Grenoble Cedex 09, France

[●]Université Joseph Fourier, Grenoble, France

Supporting Information

ABSTRACT: Small-molecule chemical calcium (Ca^{2+}) indicators are invaluable tools for studying intracellular signaling pathways but have severe shortcomings for detecting local Ca^{2+} entry. Nanobiosensors incorporating functionalized quantum dots (QDs) have emerged as promising alternatives but their intracellular use remains a major challenge. We designed cell-penetrating FRET-based Ca^{2+} nanobiosensors for the detection of local Ca^{2+} concentration transients, using commercially available CANdot565QD as a donor and CaRuby, a custom red-emitting Ca^{2+} indicator, as an acceptor. With Ca^{2+}-binding affinities covering the range of 3−20 μM, our CaRubies allow building sensors with a scalable affinity for detecting intracellular Ca^{2+} transients at various concentrations. To facilitate their cytoplasmic delivery, QDs were further functionalized with a small cell-penetrating peptide (CPP) derived from hadrucalcin (Had_{UF1-11}: H11), a ryanodine receptor-directed scorpion toxin identified within the venom of *Hadrurus gertschi*. Efficient internalization of QDs doubly functionalized with PEG5-CaRuby and H11 (in a molar ratio of 1:10:10, respectively) is demonstrated. In BHK cells expressing a *N*-methyl-D-aspartate receptor (NMDAR) construct, these nanobiosensors report rapid intracellular near-membrane Ca^{2+} transients following agonist application when imaged by TIRF microscopy. Our work presents the elaboration of cell-penetrating FRET-based nanobiosensors and validates their function for detection of intracellular Ca^{2+} transients.

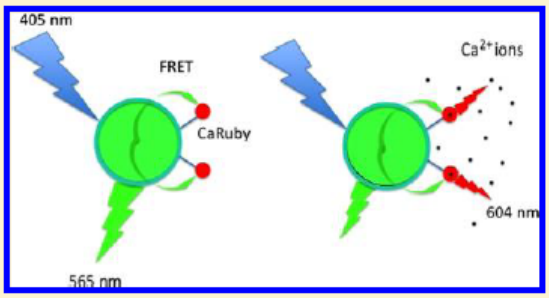

KEYWORDS: *Quantum dot biosensors, nanoparticle surface chemistry, FRET-based calcium probes, red-emitting calcium indicator, intracellular calcium fluorimetry, cell penetrating peptide*

Free calcium (Ca^{2+}) acts as a ubiquitous second messenger in numerous intracellular signaling pathways. Ca^{2+} controls cell metabolism, gene expression, vesicular trafficking and exocytosis to name a few functions. Ca^{2+} signals gain specificity by acting on different spatial and temporal scales. However, detecting fast and local Ca^{2+} concentration ($[Ca^{2+}]$) changes presents a major experimental challenge for microfluorimetric Ca^{2+} measurements with conventional Ca^{2+} indicators because only a few indicator molecules are localized in the small near-membrane volume invaded by local Ca^{2+} signaling events (see ref 1 for a measure of the external juxtacellular $[Ca^{2+}]$). Also, the intracellular diffusion of both the Ca^{2+} ions and the fluorescent Ca^{2+} indicator contributes to the rapid equilibration of Ca^{2+} gradients. Therefore, immobilizing and up-concentrat-

Received: November 12, 2013
Revised: April 16, 2014
Published: April 23, 2014

dx.doi.org/10.1021/nl500733g | Nano Lett. 2014, 14, 2994−3001

Nano Letters Letter

Table 1. Physical Parameters of QDs

QD donor	surface ligand	core/2 shells/surface ligand radius (nm)	QY %	ε^a (M^{-1} cm^{-1})	R_0 (Å) with CaRuby	r^e (Å) with PEG5 kDa
CANdot 565 organic	HDA/TOP/TOPO	~1.47[a] + 0.6[b] + ~1.2 = ~ 3.27	68	303764@405 nm 99040@543 nm		
CANdot 565-KC	50% pC/(pC + pK)	~1.8 ± 0.25[c]+	56	303764@405 nm	45	54
	85% pC/(pC + pK)	~2[d] = ~3.8	51	99040@543 nm		

[a]CdSe core estimated from the 543 nm first-exciton.[31] [b]CdS/ZnS shell.[32] [c]CdSe/CdS/ZnS by TEM (Supporting Information Figure S2). [d](pC+pK) from ref 29 [e]See Figure 2b.

ing the Ca^{2+} sensitive dye, for example, by binding several molecules to a slowly diffusing dextran or nanoparticle is expected to report local [Ca^{2+}] transients more accurately.

The development of fluorescent inorganic colloidal nanoparticles (quantum dots, QDs, with a core diameter of 2−10 nm) that combine high brightness, photostability, and narrow emission spectra has been a breakthrough for single-particle imaging.[2,3] QDs are being used as molecular beacons to monitor enzymatic reactions,[2,4,5] track single vesicles following their endocytic uptake,[6] or for studying membrane diffusion of individual QD-tagged receptors,[6−9] all of which are experiments in which QDs report molecular position. Adding a sensing functionality to this localization information, for example, via Förster resonance energy transfer (FRET) opens new tracks for developing powerful tools in the fields of toxin detection, cell physiology, and pathology.[10−12]

Despite the synthesis and characterization of several nanobiosensors in vitro, their intracellular use is still challenging. Two major obstacles have impeded cell studies with FRET-based QD sensors: (i) in our experience, Ca^{2+} indicators that display low basal fluorescence and high sensitivity alone often show a disappointing performance once linked to a QD donor, and (ii) getting across the plasma membrane in a noninvasive way is another difficult step. Cationic liposomes yield generally low transfection rates while further inducing damaging cellular stress. The demonstration that ferromagnetic beads linked to Tat-derived cell penetrating peptides (CPPs) enter cells points to a potentially more efficient delivery strategy.[13] Besides penetratin, a peptide from the insect homeotic protein Antennapedia,[14,15] natural CPPs have been derived from scorpion toxins targeted toward the ryanodine receptor.[16−18] In contrast to the widely used positively charged CPPs,[19−21] these latter peptides efficiently drive internalization at nanomolar concentrations even if they are not charged.[22]

QDs functionalized with these peptides enter cells, the most potent ones delivering them into the cytoplasm rather than getting stuck in the endosomal pathway.[2,3,23,24] To date, no ionic nanobiosensor having both sensing and cell-penetrating function has been reported. The synthesis of such a nanobiosensor is complicated by the fact that QDs must be rendered water-soluble in a first step, bound to the Ca^{2+} indicator in a controlled manner (stoichiometry, donor/acceptor distance), and the CPPs linked to the surface as well.

Here, we design and validate both in vitro and in situ, a FRET-based cell-penetrating Ca^{2+} nanobiosensor combining a green fluorescent CdSe/CdS/ZnS (core/2 shells) QD donor with a red-fluorescent Ca^{2+} indicator of 3 μM affinity for Ca^{2+} binding (CaRubyMe).[25]

Our sensor is also functionalized with a H11 CPP from a scorpion toxin to facilitate its cytoplasmic entry. By building on the recently developed toolbox[25−27] of CaRuby Ca^{2+} indicators with affinities for Ca^{2+} binding ranging from 3 to 20 μM, Ca^{2+} biosensors with a similar architecture can be generated that will cover the entire biologically relevant range of local Ca^{2+} signals.

Results and Discussion. *Preparation of Hydrophilic Peptide-coated Quantum Dots.* We worked with a single, large batch of CANdots that combine high quantum yield (QY: 68%) and narrow peak emission at 565 ± 8 nm with a fwhm of 50 nm, that is, small size variability. With the first exciton peak at 543 nm, their emission overlaps with the absorption spectrum of our CaRubies (Supporting Information Figure S1), yielding a calculated Förster radius of 4.5 nm. We used a single batch, kept in hexane at 4 °C, that was stable over two years of experimentation.

To obtain hydrophilic QDs we used ligand exchange of the passivating trioctylphosphine/trioctylphosphine oxide (TOP/TOPO) layer by short phytochelatin-related peptides that bind by metal-affinity of a cysteine-rich $(FCC)_3$ adhesive domain to the CdZnSe QD surface.[28] The number of peptides that can be accommodated on a ~600 nm emitting QD is ~25−30 for the phytochelatin-like peptides[29,30] ensuring valence control. This amphiphilic peptide coating provides small diameter, monodisperse, negatively charged, hydrophilic nanoparticles with a high colloidal stability. Using transmission electron microscopy, we estimated their size and obtained a mean radius of 1.8 ± 0.25 nm (Supporting Information Figure S2). We showed that the average size of the core/2 shells particles remained the same while the total size of QDs slightly increased after the ligand exchange (Table 1).

To facilitate binding of biomolecules to the QDs we first introduced mixed SH-terminated and NH_2-terminated phytochelatin-like peptides (pC and pK, respectively, see legend of Figure 1 and Supporting Information Material and Methods) in a 1:1 ratio, half of them, the pCs, to be engaged in a SH/

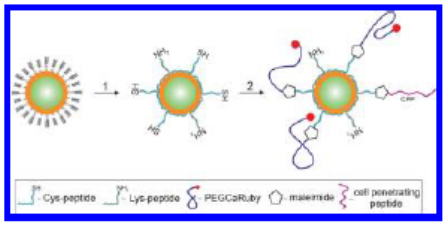

Figure 1. FRET-based Ca^{2+} biosensors. (Step 1) The QD TOP/TOPO passivating layer was replaced by a peptide coating made by mixing cysteine (SH function) and lysine (NH_2 function) terminated peptides (pC, Ac-CGSESGGSESG$(FCC)_3$F-amide; and pK, NH_2-KGSESGGSESG$(FCC)_3$F-amide respectively). Both components (hydrophobic QDs and peptides) were first dissolved in their respective solvents, pyridine and DMSO.[32] After mixing, surfactant exchange and peptide binding were initiated by raising the pH. (Step 2) Nanoparticles were further functionalized by adding CaRuby (red dots) and cell-penetrating peptides (CPP, purple wiggle) onto peptide-coated QDs using a SH/maleimide linking reaction.

dx.doi.org/10.1021/nl500733g | Nano Lett. 2014, 14, 2994−3001

maleimide linking reaction for further ligands conjugation[32] (Figure 1). The resulting constructs retained the photophysical properties of the original hydrophobic QDs (Table 1) with an only minor decrease of the fluorescence QY by ~12%. Because we aimed additionally at rendering the QDs membrane permeable by grafting CPPs, we considered increasing the relative number of pC peptides, but pC-only decorated QDs displayed a dramatically reduced QY. In contrast, by adding peptides in a 85:15% pC/pK ratio, some 25 SH sites are available for further conjugation[30] while keeping the QY at 51% (Table 1). We could thus investigate the properties of the FRET QDs-CaRuby pairs when varying acceptor to donor molar ratio (A/D).

Building of QD−CaRuby FRET pairs. CaRuby, the red-emitting Ca^{2+} indicator used here, is an extended rhodamine linked to a Ca^{2+}-chelating BAPTA moiety and having an additional linker arm (fluorescence excitation and emission peaks near 586 and 604 nm, respectively). Its Ca^{2+}-dependent fluorescence results from photoinduced electron transfer (PET) quenching. Ca^{2+} binding relieves PET and the fluorophore lights up.[26]

To functionalize QDs and avoid performing multiple reaction steps, we decided to synthesize a NH_2-terminated-PEG-CaRuby. The CaRuby PEGylation was efficiently performed with a commercially available NH_2-PEG-alkyne and CaRuby-N_3 by copper-catalyzed click chemistry. This compound was then transformed by a GMBS reaction into a maleimide-PEG-CaRuby for linkage. After binding maleimide-PEG-CaRuby to pC-sites of the QDs surface in a chosen QD/CaRuby stoichiometric ratio, the excess of unbound molecules of the dye was removed by dialysis (Supporting Information Figure S3).

Once assembled, we explored the spectral properties of the QD-CaRuby complexes in a 2 mM Ca^{2+} containing medium where FRET from the QD core to the rhodamine moiety is revealed. As illustrated in Figure 2 for QD-PEG5-CaRuby, FRET between the QD donor (D) and the CaRuby acceptor (A) increased with the number of CaRuby molecules, as expected for multiacceptor FRET.[33] We determined the A/D ratio by linear unmixing of the absorption spectra of the assembly using the pure A and D spectra. The A/D ratio was very close to the expected one, after correction for the fact that only 80% of the PEGs were labeled, implying an almost complete reaction. FRET efficiency ($E = 1 - F'_D/F_D$, where F'_D and F_D are the donor fluorescence intensities in the presence and absence of the acceptor, respectively) increased up to 80% while acceptor sensitization plateaued at 20% when the number of PEG5-CaRuby was increased up to 10. With a Förster radius of 4.5 nm, data of FRET efficiency (E) were well described by $E = nR_0^6/(nR_0^6 + r^6)$. Fit yielded a center-to-center distance r between donor and acceptor of 5.4 nm. This value results from the long 5 kDa PEG linker (black line in Figure 2b).

Ca^{2+} Sensing. Increasing the FRET efficiency should maximize the signal-to-noise ratio (SNR) for detecting Ca^{2+} transients. This can be achieved either by increasing A/D ratio (Figure 2a) or by reducing the D to A distance. To test the latter strategy, we prepared PEG-CaRubies of variable lengths: a custom-synthesized short <0.3 kDa NH_2-PEG-alkyne (see Supporting Information Materials and Methods, PEG0.3) and commercial 5 kDa (PEG5) and 10 kDa (PEG10) NH_2-PEG-alkyne. After coupling these CaRuby derivatives to the QDs, we systematically investigated the Ca^{2+}-sensitivity of the resulting FRET pairs with fluorimetric titrations in which we switched from a nominally Ca^{2+}-free solution (zero Ca^{2+} and 10 mM EGTA, peak photoluminescence, PL = F_0) to saturating (2 mM) Ca^{2+}: peak PL = F, and we used the relative increase in CaRuby fluorescence (dynamic range DR = $(F - F_0)/F_0$) as an index of sensitivity.

Although CaRuby retained a high Ca^{2+}-sensitivity after binding to PEG by click chemistry (DR = 60), unexpectedly, QD-CaRuby pairs built from short PEG0.3-CaRuby were largely Ca^{2+}-insensitive (DR = 0.5, n = 2). This was not due to the absence of FRET as evidenced by the donor quenching in the FRET pair (Figure 3b). Prasuhn et al.[34] obtained a Ca^{2+}-sensitive FRET signal when linking CaRuby to a QD through a short linker attached to a 6-His-terminated peptide composed of 2 α-helix turns. However, this signal was absent when a DHLA-PEG0.75 was intercalated instead of the peptide. This observation led us hypothesize that excessive proximity of the CaRuby to the QD surface perturbed Ca^{2+}-sensing. This should

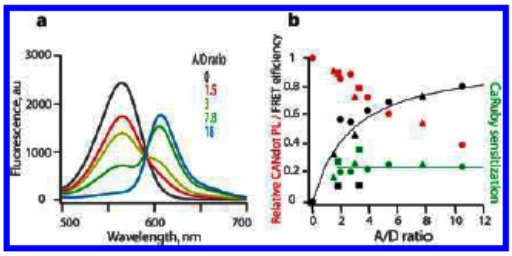

Figure 2. FRET upon 350 nm donor excitation, measured as donor quenching and acceptor sensitization, as a function of A/D ratio, at a constant [Ca^{2+}] of 2 mM. (a) Series of mixed spectra obtained by increasing the number of PEG5-CaRubyMe while keeping QD concentration constant. A/D ratio was measured by absorbance at 407 and 581 nm to evaluate QD and CaRuby concentrations, respectively. (b) Relative donor quenching (QD photoluminescence, red) and FRET efficiency (black) after linear unmixing. Acceptor sensitization (F_{CaRuby} (exc@350 nm) $-F_{QD}$ (exc@350 nm)/(F_{CaRuby} (exc@535 nm) is also reported (green). Symbols ▲, ●, ■ show results from 3 experiments; black line: fit with $E = nR_0^6/(nR_0^6 + r^6)$ with R_0 = 45.5 Å and variable r = 54.2 ± 1.6 Å. The line in green shows average acceptor sensitization for A/D ratio between 2 and 12 (~22%).

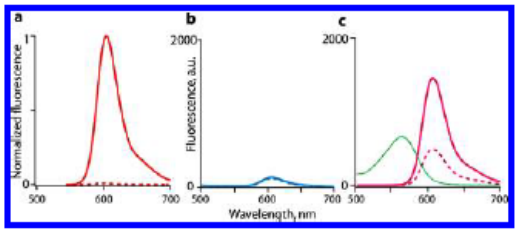

Figure 3. Emission spectra of FRET pairs in the presence (solid) and absence (dotted) of Ca^{2+}. (a) Normalized emission spectra of free PEG5-CaRuby. (b) Emission spectra of QD-PEG0.3-CaRuby with A/D = 18.8 (blue). (c) Spectra of QD-PEG5-CaRuby with A/D = 7.8. Acceptor and donor contribution to the spectra was separated by linear unmixing. FRET, estimated from QDs contribution to the spectrum, is unchanged (traces of QDs emission in 2 mM Ca^{2+} and 10 mM EGTA are superimposed). In panels b and c, QDs alone with no dye yielded a peak emission of about 2500 in both cases so allowing for direct comparison. In panel c, the same batch as in Figure 2 dark green trace.

dx.doi.org/10.1021/nl500733g | Nano Lett. 2014, 14, 2994−3001

not be the case when intercalating PEG5 or PEG10. However, even for these longer spacers the DR of the QD-CaRuby pair, while improving, remained quite low. At a 1:1 molar ratio, DR was ~1, as if CaRuby was still close to the QD surface, possibly due to the flexible PEG molecule backing upon itself. We therefore instead aimed at increasing the DR by systematically increasing the A/D ratio of PEG-CaRuby molecules bound onto a single QD, constructing stiffer "hairy ball" geometry.

Red fluorescence emission of QD-PEG5-CaRuby, either in response to direct excitation or via FRET, slowly but steadily increased with growing A/D ratio from 1 to 15 (Figure 4a; see

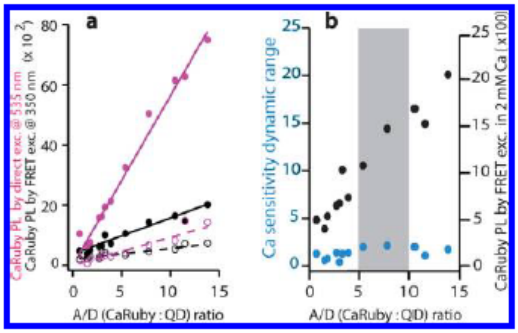

Figure 4. Ca^{2+} sensitivity of QD-PEG5-CaRuby as a function of A/D ratio. (a) CaRuby emission upon FRET excitation at 350 nm (in black) and direct excitation at 535 nm (in purple). Filled circles refer to measurements in a 2 mM Ca^{2+} and empty circles to measurements in 10 mM EGTA. FRET emission and PL obtained by direct excitation as well, linearly increase with an A/D ratio in the range 1–15 (PL by FRET in Ca^{2+} = 380 + 119 A/D ratio; FRET in EGTA = 200 + 36 A/D ratio). With CaRuby direct excitation, PL in Ca = 200 + 540 A/D ratio; in EGTA = 2 + 92 A/D ratio. (b) Summary graph displaying FRET absolute value increase (in 2 mM Ca^{2+}; black circles) whereas DR (blue dots) is constant when molar ratio was varied between 0 and 15. All data refer to the same QDs concentration. Data from 4 batches of QD-PEG5-CaRuby.

Supporting Information Figure S4 for QD-PEG10-CaRuby). In the same range, between 1 and 15 A/D, FRET efficiency (measured in 10 mM EGTA) also increased. As a result, the DR from the FRET-activated CaRuby was constant but low at ~2 (Figure 4b). With direct excitation, the DR was about twice as large but it never exceeded 5. Thus, while the DR of CaRuby is much reduced once linked to QDs, an A/D ratio in the range of 5–15 produces a Ca^{2+}-dependent fluorescence large enough to allow efficient Ca^{2+}-sensing (Figure 4b). As we aimed at visualizing and hence localize nanobiosensors inside the cell, even at resting intracellular $[Ca^{2+}]$, we finally retained an A/D ratio of 5–10 as a compromise for in situ experiments. Noticeably, these constructs proved to be stable over at least 2 months.

Next, we examined if the Ca^{2+}-binding affinity of CaRubyMe was changed by the nanosensor assembly. Samples of QD-PEG5-CaRubyMe (A/D ratio = 9) prepared at concentrations of 0.5 μM CaRuby were mixed with Ca^{2+} concentrations increasing from 0.1 up to 1000 μM (Figure 5a). Hill fit with fluorescence peaks from two separate experiments confirmed a K_d of 2.9 ± 0.3 μM (Figure 5b), not distinguishable from the 3.4 ± 0.5 μM, previously reported for CaRubyMe alone. Thus, despite its attachment in proximity of the highly charged QDs surface, CaRubyMe affinity for Ca^{2+} was unaltered. Furthermore, the k_{on} for Ca^{2+} binding to the nanobiosensors

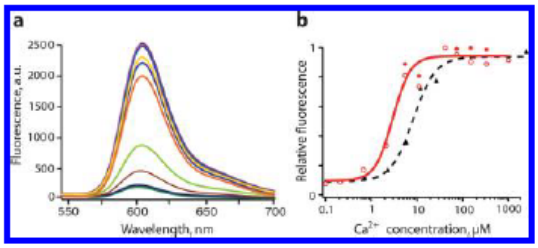

Figure 5. Fluorimetric titration against $[Ca^{2+}]$ of QD-PEG5-CaRubyMe complexes (A/D ratio = 9; buffer containing (in mM): 100 KCl and 30 MOPS, pH 7.2). (a) Superimposed fluorescence curves in the presence of increasing concentrations of Ca^{2+} as plotted in the dose–response curve on the right (red dots: direct excitation of CaRuby at 535 nm). (b) Peak fluorescence versus $[Ca^{2+}]$ for two independent titrations, filled and empty red dots, respectively. Red continuous line is Hill fit of all in cuvette data points, K_d = 2.9 ± 0.3 μM. Black triangles and dotted line show in cell-Ca2+ calibration using flow cytometry yielding a K_d of 7.6 ± 1.4 μM.

(calculated from the K_d and stopped-flow measurement of the k_{off}: ~150 s^{-1}) was of the order of 10^8 M^{-1} s^{-1}, as expected for BAPTA-based Ca^{2+} chelator.[35,36] This high k_{on} value makes our sensors an adequate tool for detecting fast $[Ca^{2+}]_i$ transients (Supporting Information Figure S5).

Internalization of Nanobiosensors. To promote the intracellular translocation of functionalized QDs, we used CPPs of specially high efficiency that we recently identified, derived from toxins targeted against the intracellular ryanodine receptor.[22] Uptake of H11 (Smartox Biotechnology, Saint Martin d'Hères, France), a CPP derived from the scorpion toxin hadrucalcin, was already significant at a concentration as low as 500 nM (Supporting Information Figure S6). Incubation of cells with 100 nM QDs functionalized with 5–10 CPPs brings CPP local concentration in this range. Baby hamster kidney cells (BHK-21) were incubated for 2 h with 100 nM QDs doubly functionalized with PEG5-CaRuby and H11 in the molar ratio 1:10:10 and the internalization efficiency was evaluated by live-cell confocal imaging. The nucleus and the plasma membrane were counterstained to better assess the cytoplasmic location of the QDs (Figure 6a).

As seen on the confocal section shown in Figure 6b, QD-CaRuby-H11 complexes penetrated inside the cells and were distributed throughout the cytoplasm. However, compared to conventional chemical Ca^{2+} indicators our sensors have a pointillistic distribution. This pointillistic distribution of our sensors provides a localized read-out of $[Ca^{2+}]$ at discrete points where the CaRuby has been up-concentrated. Internalization of functionalized QDs occurred without damaging side effects (Supporting Information Figure S7).

Because the number of internalized QDs varied from cell to cell, a first quantification of the internalized QDs was carried out using imaging flow cytometry. For the analysis QDs located in close vicinity to the plasma membrane were subtracted whether on its extracellular or intracellular sides. A number of QDs without CPPs were internalized; QDs internalization, however, as illustrated in Figure 6c, is almost doubled by CPPs addition, with no further improvement when going from 5 to 10 CPPs.

Electron micrographs of BHK cells loaded with QD-CaRuby-H11 complexes show groups of ~15–20 QDs dispersed over an area of ~500 nm diameter probably corresponding to the spots observed in confocal microscopy. Though at this point we

dx.doi.org/10.1021/nl500733g | Nano Lett. 2014, 14, 2994–3001

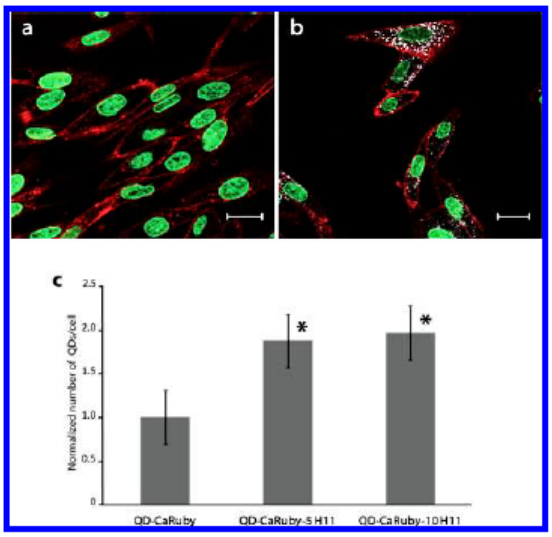

Figure 6. Cell penetration of QDs doubly functionalized with CaRuby and cell penetrating peptide H11. (a) Confocal microscopy section of live BHK-21 cells with Hoechst nuclear staining (green) and concanavalin-Alexa 647 membrane staining (red). (b) BHK-21 cells with internalized QDs. Gray dots show QDs-CaRuby-H11 emission upon direct excitation of CaRuby at 561 nm. Scale bar, 20 μm. (c) Imaging flow cytometry analysis of QDs penetration. Normalized average number of internalized QDs per cell for QD-CaRuby alone, QD-CaRuby-5H11, and QD-CaRuby-10H11 complexes, respectively. Measurements made upon CaRuby direct excitation at 561 nm. Data show mean ± s.e.m for 100 cells of each sample; *$-p$ < 0,05 compared to QD-CaRuby.

do not know their exact path for cell entry, we show QDs to be not enclosed in a membrane-delimited compartment (Figure 7). This is the conclusion attained with a TEM image poorly contrasted to better see the small size QDs (Figure 7) and as well of an TEM image where the contrast has been increased to the point when some uranyl acetate deposits are formed (Supporting Information Figure S8). Thus, our nanobiosensors are exposed to the intracellular medium and hence should be able to report the local cytoplasmic Ca^{2+} concentration.

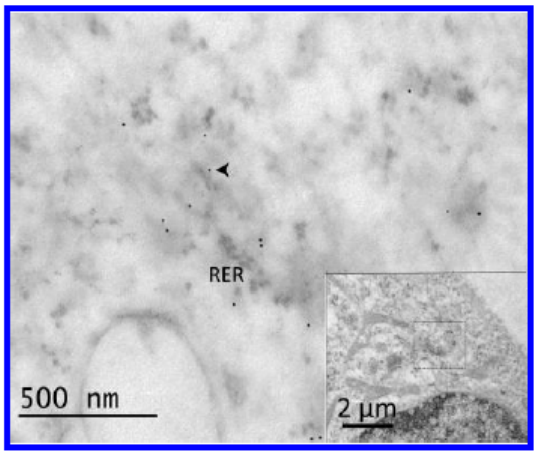

Figure 7. EM micrograph of QD-CaRuby-H11 complexes internalized in aBHK cell. Image shows zoom on the region of interest identified on the inset image. Individual QDs (arrow) appear as electron-dense spots of ~5 nm diameter, dispersed throughout the cytoplasm. Larger and less dense punctiform structures are the rough endoplasmic reticulum (RER) and ribosomes.

Intracellular Ca^{2+} Nanobiosensing. To demonstrate the Ca^{2+}-sensing ability of our sensors inside live cells we used HEK293 cells expressing *N*-methyl-D-aspartate receptors (NMDARs). These are plasma membrane cation-permeable channels mediating Ca^{2+} influx upon activation by agonist binding. Our nanobiosensors were loaded as described above, followed by the resuspension of the cells in a HEPES-buffered medium for time-lapse fluorescence measurements. External [Ca^{2+}] was raised to 10 mM to maximize Ca^{2+} entry upon receptors activation.

After loading of QD-CaRuby-H11 complexes, some QDs remained attached to the external side of plasma membrane, which resulted in a high background fluorescence. This background was efficiently reduced by adding to the extracellular saline 40 μM Cu^{2+}, an effective QDs and CaRuby quencher.[25,37] The Ca^{2+} binding affinity (K_d) to the nanosensor was slightly increased, an effect described for other Ca^{2+} indicators and possibly related to the higher viscosity of the intracellular medium (see Figure 5b dotted line).

Injection to the cell suspension of the NMDAR agonists glutamate and glycine in the presence of external Ca^{2+} produced an increase of the CaRuby fluorescence (Figure 8c, red trace), as expected from the NMDAR-mediated Ca^{2+} influx (Figure 8a), confirming the intracellular responsiveness of our Ca^{2+} nanobiosensors.

Preincubation of the cells with APV, a NMDAR antagonist, (Figure 8b) almost completely abolished the agonist-evoked

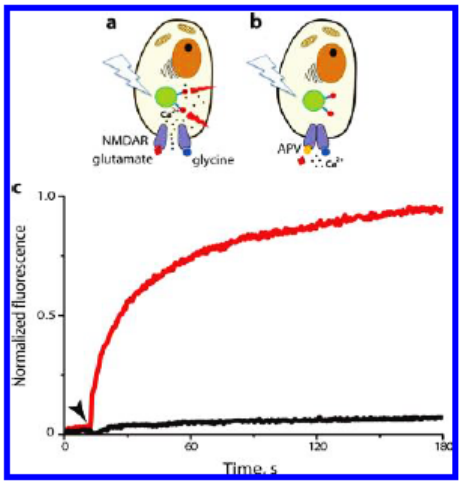

Figure 8. Intracellular [Ca^{2+}] measurement in a suspension of HEK293 cells transfected with NMDARs and incubated with 100 nM nanobiosensors. Schematic representation of (a) NMDAR activation by coapplication of agonists (100 μM glutamate and 20 μM glycine) followed by Ca^{2+} influx into the cell and (b) of the NMDAR blockade by an antagonist (100 μM APV) preventing Ca^{2+} influx upon application of the agonists. (c) Intracellular Ca^{2+}-dependent acceptor fluorescence as a function of time. Arrowhead marks application of agonists in absence of antagonist or after blocking NMDAR by APV, red and black traces, corresponding to conditions (a) and (b) respectively (2 replicates in 3 independent experiments).

dx.doi.org/10.1021/nl500733g | Nano Lett. 2014, 14, 2994−3001

Ca^{2+} response (Figure 8c, black trace). Likewise, no fluorescence increase was observed when applying agonists in Ca^{2+} free medium (data not shown). The Ca^{2+} response of our sensors is similar to that obtained using conventional dyes and cells, expressing the same subunits of NMDA receptor-channels.[38] We thus show that our QD-based Ca^{2+} nanobiosensors can specifically detect Ca^{2+} changes in a biologically relevant paradigm of receptor activation.

Finally, to demonstrate the ability of developed nanobiosensors to detect local subcellular Ca^{2+} signals in live cells, we loaded QD-CaRuby-H11 nanobiosensors into BHK cells stably expressing the NR1 and NR2 subunits of the NMDAR.[38] To visualize near-membrane QD sensors, we used total internal reflection fluorescence (TIRF) microscopy, simultaneously detecting in the green and red channel upon 405 and 568 nm evanescent-wave excitation on a custom prism-type VA TIRF microscope,[39] (Supporting Information Figure S9). To reduce noise caused by extracellularly attached QDs, QD-loaded cells were trypsinized and replated on quartz coverslips displaying a low autofluorescence. After trypsinization, transient $CuSO_4$ addition to BHK cells is not necessary unless an improved signal-to-noise ratio is sought (see Supporting Information Figure S10 illustrating the characteristics of the Cu^{2+} effect).

Evanescent-wave illumination allowed visualizing only those nanosensors close to the basal cell membrane with a high contrast, permitting readout of the fluorescence emitted by QD-sensors (Figure 9a,b). Ca^{2+} transients were evoked by NMDAR activation (100 μM glutamate, 20 μM glycine and 5 mM $CaCl_2$) and responses continuously recorded at 4 Hz during 3 min before and during agonists application. Figure 9c shows the Ca^{2+} transients detected at single sites, after background subtraction and correction for photobleaching, expressed as F/F_0, where F_0 is the (local) basal value before NMDAR activation. Our nanosensors read out local $[Ca^{2+}]$ transients that were distinct both, between cells (cell 1 and cell 2 in Figure 9c,d) and at the subcellular level, some displaying an F/F_0 up to 2.0 whereas some sensors nearby were silent and others show intermediary values.

Interestingly among the detected Ca^{2+} transients, the F/F_0 peak value read in a single cell at saturating concentration of agonists here applied was 2.2 $\pm$ 0.9 (ranging from 1.4 to 4.7, n = 14 cells, on 6 distinct coverslips from 4 distinct batches of cells). In cell 1, time constants at three regions of interest were 500, 700, and 900 ms, from top to bottom, respectively. In addition to variability in the agonist application, the distance from the biosensor to the Ca^{2+} source may account for such local variations. Along this line, the nonresponsiveness of red-emitting QDs is coherent with a localization in a cytoplasmic region ensuing no change in $[Ca^{2+}]$, but also alternatively with a localization in endosomes because this structure has a $[Ca^{2+}]$ saturating for the probe. Average kinetics of fluorescence transients recorded with QD-CaRuby-H11 were similar to those obtained with a conventional bulk-loaded small-molecule chemical Ca^{2+} indicator, X-rhod-1, AM, when the same cell was stimulated again following dye loading at the end of the experiment (Supporting Information Figure S10). Control applications in Ca^{2+}-free extracellular saline failed to produce measurable fluorescence changes.

Taken together, these experiments comfort our interpretation that QD-CaRuby-H11 sensors indeed detect cytoplasmic Ca^{2+} transients evoked by NMDAR-mediated Ca^{2+} influx across the plasma membrane. Furthermore, sequential applications of

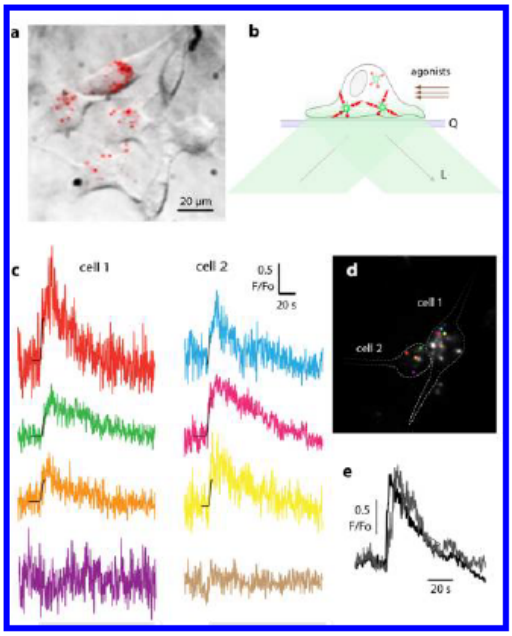

Figure 9. Read-out of local Ca^{2+} transients. (a) Localization of internalized biosensors (QD-CaRuby-H11 in a ratio 1:10:10) on the superimposed bright-field and time-averaged TIRF image of cultured BHK cells. (b) Schematic representation of the TIRF imaging of Ca^{2+} nanobiosensors. Confinement of excitation light (L) excites only fluorophores present in a ~100 nm layer above the quartz coverslip (Q). Among the three nanosensors schematized, only two are fluorescent while the third one is out-of-reach of the evanescent wave. (c) Local Ca^{2+} detection. Traces show simultaneously acquired transients in distinct spots in response to bath application of saturating concentrations of NMDAR agonists (during bottom black line) at various points in two neighboring cells "1" and "2" (left and right columns respectively); 700 images, t_{exp} = 250 ms. (d) Pseudocolor-overlay of spot positions on the cell outline. (e) Repetitive simulation evokes reversible Ca^{2+} transients. Superimposed traces, recorded at a same point, are responses to two successive bath applications of NMDAR agonists at a saturating concentration within between a 15 min long continuous bath perfusion of CTR saline for recovery from desensitization. Ca^{2+} signals were recorded with (c) and without (e) a previous transient application of Cu^{2+}.

NMADR agonists produced stereotyped reversible Ca^{2+} transients at the same site as expected (Figure 9e).

Compared to classical chemical Ca^{2+} indicators, FRET-based nanobiosensors are attractive for probing microdomain Ca^{2+} signals because, (i) QD-based, they combine high brightness with low cytoplasmic mobility[40−43] and low photobleaching compared to organic Ca^{2+} probes. (ii) They further allow localizing by green fluorescence candidate sites even at resting Ca^{2+}. (iii) With conventional chemical small-molecule Ca^{2+} indicators and genetically encoded Ca^{2+} indicators (GECIs), only a few indicator molecules are localized in the small near-membrane volume invaded by local Ca^{2+} signaling events.[44] Here, covalently linking the Ca^{2+} sensor to the QD surface locally up-concentrates the indicator up to the approximately millimolar range, a concentration that cannot be attained by simple aqueous dilution, thus (iv) permitting to attain signal-to-noise ratios favorable for the detection of fast and local Ca^{2+} transients. (v) Average cytoplasmic concentrations is maintained low, and hence exogenous Ca^{2+} buffer capacity. (vi)

dx.doi.org/10.1021/nl500733g | Nano Lett. 2014, 14, 2994−3001

Compared to other red-emitting low-affinity Ca^{2+} probes like Xrhod-5F or CaRuby-Cl alone, their large molecular weight prevents mitochondrial internalization and light-induced cytotoxicity.

Here, using a commercial QD donor, our CaRuby as a red-emitting Ca^{2+}-sensitive acceptor and a cell-penetrating peptide-derived cytoplasmically active toxin to facilitate cell entry, our Ca^{2+} nanobiosensors combine ease of synthesis, controlled stoichiometric assembly, high colloidal stability and efficient cytoplasmic delivery. Added to the extracellular saline, these Ca^{2+} nanobiosensors are internalized within 2 h to display a punctate cytoplasmic distribution when imaged with TIRF microscopy on the day thereafter, after replating. In a cell line stably expressing the Ca^{2+}-permeable NMDA receptor channel, we detected heterogeneous intracellular Ca^{2+} transients following receptor-activation with specific agonists, thus providing the first validation of Ca^{2+} nanobiosensors for subcellular biological Ca^{2+} imaging in live cells.

The next logical step is the targeting of our sensor by its further functionalization with specific antibodies to a high-conductivity Ca^{2+} channel such as the RyRs (400 pS) or NMDARs (50 pS) and perform optical single-channel recording.

■ ASSOCIATED CONTENT

Supporting Information

Eleven supplementary figures and their legends, detailed materials and methods, and abbreviations. This material is available free of charge via the Internet at http://pubs.acs.org.

■ AUTHOR INFORMATION

Corresponding Author

*E-mail: anne.feltz@ens.fr.

Present Addresses

(M.C.) UMR 7213 CNRS, Laboratoire de Biophotonique et Pharmacologie 74 route du Rhin, CS 60024, F - 67401 Illkirch 67400, France.

(A.V.Y) Biology Faculty, Kazan Federal University, Kazan, Russia

(A.I.Z., secondary address) Biomaterials and Nanomaterials Group, Department of Microbiology, Kazan Federal University, Kazan, Republic of Tatarstan, RF, 420008.

Author Contributions

The manuscript was written through contributions of all authors. All authors have given approval to the final version of the manuscript.

A.I.Z. and M.C. contributed equally to the work.

Notes

The authors declare no competing financial interest.

■ ACKNOWLEDGMENTS

We want to thank Institut Curie for giving us access to its Flow Cytometry platform, and especially to Mrs. Z. Maciorowski for her help in initiating us to this technique. O. Hernandez-Cubero helped us in the analysis of the TEM images. Christian Boudier (UMR7213 Laboratoire de Biophotonique et Pharmacologie, Strasbourg) a permis les expériences de "stopped flow". We thank Pierre Paoletti's group (IBENS, Paris) for providing the NMDAR (NR1 and NR2B) plasmids. We specially thank Dr. H. Bräuner-Osborne and J. Egebjerg (University of Copenhagen) for providing the BHK cell line stably expressing NR1 and NR2 subunits of the NMDA receptor that also proved to be strongly adherent to quartz coverslips making possible the present TIRF experiments. This work has received support under the program "Investissements d'Avenir" launched by the French government and implemented by the ANR (ANR-10-LABX-54 MEMO LIFE, ANR-11-IDEX-001-02-PSL). This work was supported by the French Agence National de la Recherche (ANR P3N, nanoFRET^2 grant, to A.F., J.M.M., M.d.W., M.O.) and the European Union (FP6 STRP AUTOSCREEN grant and FP7 ERA-NET NeuronNANOSYN grant to M.O.). M.O. is supported by the FranceBioImaging initiative (FBI).

■ REFERENCES

(1) Etter, E. F.; Kuhn, M. A.; Fay, F. S. *J. Biol. Chem.* **1994**, *269*, 10141−9.

(2) Alivisatos, A. P.; Gu, W.; Larabell, C. *Annu. Rev. Biomed Eng.* **2005**, *7*, 55−76.

(3) Michalet, X.; Pinaud, F. F.; Bentolila, L. A.; Tsay, J. M.; Doose, S.; Li, J. J.; Sundaresan, G.; Wu, A. M.; Gambhir, S. S.; Weiss, S. *Science* **2005**, *307*, 538−44.

(4) Biebricher, A.; Wende, W.; Escude, C.; Pingoud, A.; Desbiolles, P. *Biophys. J.* **2009**, *96*, L50−2.

(5) Lidke, D. S.; Nagy, P.; Heintzmann, R.; Arndt-Jovin, D. J.; Post, J. N.; Grecco, H. E.; Jares-Erijman, E. A.; Jovin, T. M. *Nat. Biotechnol.* **2004**, *22*, 198−203.

(6) Zhang, Q.; Li, Y.; Tsien, R. W. *Science* **2009**, *323*, 1448−53.

(7) Dahan, M.; Levi, S.; Luccardini, C.; Rostaing, P.; Riveau, B.; Triller, A. *Science* **2003**, *302*, 442−5.

(8) Saint-Michel, E.; Giannone, G.; Choquet, D.; Thoumine, O. *Biophys. J.* **2009**, *97*, 480−9.

(9) Triller, A.; Choquet, D. *Neuron* **2008**, *59*, 359−74.

(10) Delehanty, J. B.; Susumu, K.; Manthe, R. L.; Algar, W. R.; Medintz, I. L. *Anal. Chim. Acta* **2012**, *750*, 63−81.

(11) Sapsford, K. E.; Berti, L.; Medintz, I. L. *Angew. Chem., Int. Ed.* **2006**, *45*, 4562−89.

(12) Wang, Y.; Chen, L. *Nanomedicine* **2011**, *7*, 385−402.

(13) Josephson, L.; Tung, C. H.; Moore, A.; Weissleder, R. *Bioconjugate Chem.* **1999**, *10*, 186−191.

(14) Derossi, D.; Joliot, A. H.; Chassaing, G.; Prochiantz, A. *J. Biol. Chem.* **1994**, *269*, 10444−50.

(15) Joliot, A.; Pernelle, C.; Deagostini-Bazin, H.; Prochiantz, A. *Proc. Natl. Acad. Sci. U.S.A.* **1991**, *88*, 1864−8.

(16) Esteve, E.; Smida-Rezgui, S.; Sarkozi, S.; Szegedi, C.; Regaya, I.; Chen, L.; Altafaj, X.; Rochat, H.; Allen, P.; Pessah, I. N.; Marty, I.; Sabatier, J. M.; Jona, I.; De Waard, M.; Ronjat, M. *J. Biol. Chem.* **2003**, *278*, 37822−31.

(17) Poillot, C.; Bichraoui, H.; Tisseyre, C.; Bahembera, E.; Andreotti, N.; Sabatier, J. M.; Ronjat, M.; De Waard, M. *J. Biol. Chem.* **2012**, *287*, 17331−17342.

(18) Poillot, C.; Dridi, K.; Bichraoui, H.; Pecher, J.; Alphonse, S.; Douzi, B.; Ronjat, M.; Darbon, H.; De Waard, M. *J. Biol. Chem.* **2010**, *285*, 34168−80.

(19) Derossi, D.; Chassaing, G.; Prochiantz, A. *Trends Cell Biol.* **1998**, *8*, 84−7.

(20) Boeneman, K.; Delehanty, J. B.; Blanco-Canosa, J. B.; Susumu, K.; Stewart, M. H.; Oh, E.; Huston, A. L.; Dawson, G.; Ingale, S.; Walters, R.; Domowicz, M.; Deschamps, J. R.; Algar, W. R.; Dimaggio, S.; Manono, J.; Spillmann, C. M.; Thompson, D.; Jennings, T. L.; Dawson, P. E.; Medintz, I. L. *ACS Nano* **2013**, *7*, 3778−96.

(21) Walrant, A.; Vogel, A.; Correia, I.; Lequin, O.; Olausson, B. E.; Desbat, B.; Sagan, S.; Alves, I. D. *Biochim. Biophys. Acta* **2012**, *1818*, 1755−63.

(22) Tisseyre, C.; Bahembera, E.; Dardevet, L.; Sabatier, J. M.; Ronjat, M.; De Waard, M. *Pharmaceuticals* **2013**, *6*, 320−339.

(23) Ram, N.; Texier-Nogues, I.; Pernet-Gallay, K.; Poillot, C.; Ronjat, M.; Andrieux, A.; Arnoult, C.; Daou, J.; De Waard, M. *Int. J. Biomed. Nanosci. Nanotechnol.* **2011**, *2*, 12−32.

(24) Ram, N.; Weiss, N.; Texier-Nogues, I.; Aroui, S.; Andreotti, N.; Pirollet, F.; Ronjat, M.; Sabatier, J. M.; Darbon, H.; Jacquemond, V.; De Waard, M. *J. Biol. Chem.* **2008**, *283*, 27048−56.
(25) Collot, M.; Loukou, C.; Yakovlev, A. V.; Wilms, C. D.; Li, D.; Evrard, A.; Zamaleeva, A.; Bourdieu, L.; Leger, J. F.; Ropert, N.; Eilers, J.; Oheim, M.; Feltz, A.; Mallet, J. M. *J. Am. Chem. Soc.* **2012**, *134*, 14923−31.
(26) Gaillard, S.; Yakovlev, A.; Luccardini, C.; Oheim, M.; Feltz, A.; Mallet, J. M. *Org. Lett.* **2007**, *9*, 2629−32.
(27) Luccardini, C.; Yakovlev, A. V.; Pasche, M.; Gaillard, S.; Li, D.; Rousseau, F.; Ly, R.; Becherer, U.; Mallet, J. M.; Feltz, A.; Oheim, M. *Cell Calcium* **2009**, *45*, 275−83.
(28) Pinaud, F.; Michalet, X.; Bentolila, L. A.; Tsay, J. M.; Doose, S.; Li, J. J.; Iyer, G.; Weiss, S. *Biomaterials* **2006**, *27*, 1679−87.
(29) Clarke, S.; Pinaud, F.; Beutel, O.; You, C.; Piehler, J.; Dahan, M. *Nano Lett.* **2010**, *10*, 2147−54.
(30) Iyer, G.; Pinaud, F.; Tsay, J.; Weiss, S. *Small* **2007**, *3*, 793−8.
(31) Yu, W. W.; Qu, L.; Guo, W.; Peng, X. *Chem. Mater.* **2003**, *15*, 2854−2860.
(32) Pinaud, F.; King, D.; Moore, H. P.; Weiss, S. *J. Am. Chem. Soc.* **2004**, *126*, 6115−23.
(33) Yakovlev, A. V.; Zhang, F.; Zulqurnain, A.; Azhar-Zahoor, A.; Luccardini, C.; Gaillard, S.; Mallet, J. M.; Tauc, P.; Bro chon, J. C.; Parak, W. J.; Feltz, A.; Oheim, M. *Langmuir* **2009**, *25*, 3232−9.
(34) Prasuhn, D. E.; Feltz, A.; Blanco-Canosa, J. B.; Susumu, K.; Stewart, M. H.; Mei, B. C.; Yakovlev, A. V.; Loukov, C.; Mallet, J. M.; Oheim, M.; Dawson, P. E.; Medintz, I. L. *ACS Nano* **2010**, *4*, 5487−97.
(35) Kao, J. P.; Tsien, R. Y. *Biophys. J.* **1988**, *53*, 635−9.
(36) Jackson, A. P.; Timmerman, M. P.; Bagshaw, C. R.; Ashley, C. C. *FEBS Lett.* **1987**, *216*, 35−9.
(37) Xie, H.-Y.; Liang, J.-G.; Zhang, Z.-L.; Liu, Y.; He, Z.-K.; Pang, D.-W. *Spectrochim. Acta, Part A* **2004**, *60*, 2527−2530.
(38) Hansen, K. B.; Brauner-Osborne, H.; Egebjerg, J. *Comb Chem. High Throughput Screening* **2008**, *11*, 304−15.
(39) van't Hoff, M.; Reuter, M.; Dryden, D. T.; Oheim, M. *Phys. Chem. Chem. Phys.* **2009**, *11*, 7713−7720.
(40) Courty, S.; Luccardini, C.; Bellaiche, Y.; Cappello, G.; Dahan, M. *Nano Lett.* **2006**, *6*, 1491−5.
(41) Grünwald, D.; Hoekstra, A.; Dange, T.; Buschmann, V.; Kubitscheck, U. *ChemPhysChem* **2006**, *7*, 812−815.
(42) Yum, K.; Na, S.; Xiang, Y.; Wang, N.; Yu, M. F. *Nano Lett.* **2009**, *9*, 2193−2198.
(43) Delehanty, J. B.; Bradburne, C. E.; Susumu, K.; Boeneman, K.; Mei, B. C.; Farrell, D.; Blanco-Canosa, J. B.; Dawson, P. E.; Mattoussi, H.; Medintz, I. L. *J. Am. Chem. Soc.* **2011**, *133*, 10482−10489.
(44) Oheim, M.; van't Hoff, M.; Feltz, A.; Zamaleeva, A.; Mallet, J. M.; Collot, M. *Biochim. Biophys. Acta* **2014**.

SUPPORTING INFORMATION

Cell-penetrating nanobiosensors for pointillistic intracellular Ca^{2+}-transient detection

Alsu I. Zamaleeva*, Mayeul Collot*, Eloi Bahembera, Céline Tisseyre, Philippe Rostaing, Aleksey V. Yakovlev, Martin Oheim, Michel De Waard, Jean-Maurice Mallet, Anne Feltz * *

* Both authors contributed equally
** **Corresponding author:** anne.feltz@ens.fr

TABLE OF CONTENTS

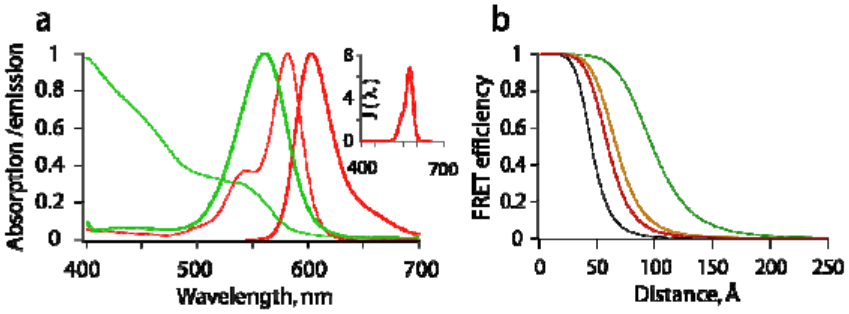

Fig. S1: **FRET characteristics of the donor and acceptor pair formed by CANdots and PEG5-CaRubyMe**. (a) Traces show normalized absorbance and emission spectra (thin and thick lines respectively) of QDs 565 (in red) and PEG5CaRubyMe (in green). QDs excitation between 407-450 nm will yield FRET emission of CaRubyMe due to overlap of the donor emission and acceptor excitation spectra (Inset shows the energy, J *vs* wavelength which peaks at $6.8e^{-13}$ M^{-1} cm^3 yielding a R_0 Förster radius of 45 Å). (b) FRET efficiency is here expressed as a function of the distance r donor to acceptor when the number n (or A/D) of CaRuby molecules attached per QD is varied. FRET efficacy, $E= nR_0^6 / (nR_0^6 + r^6)$, is given with A/D ratio equals from 1, 2, 5, 100 from left to right.

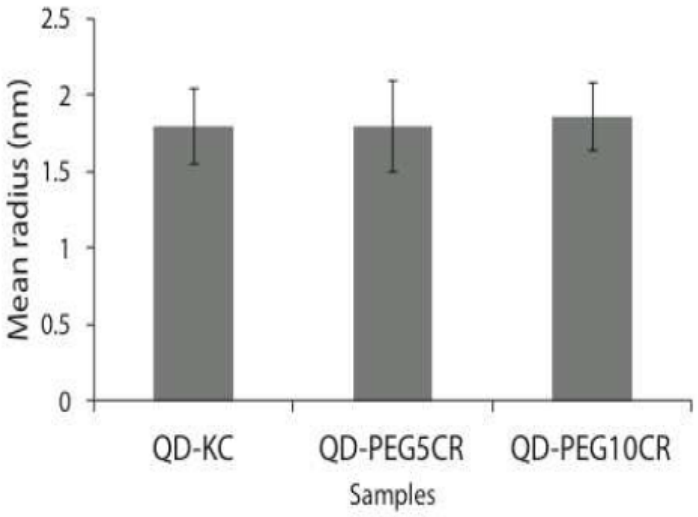

Fig. S2: Determination of the QDs core/2 shells radius by transmission electron microscopy. Statistical measurements yielded radius sizes of 1.8 ± 0.25 nm for QD-KC, 1.8 ± 0.3 nm for QD-PEG5CaRuby (CR) and 1.86 ± 0.22 nm for QD-PEG10CaRuby (CR) respectively (mean ± SD, 15-20 dots each).

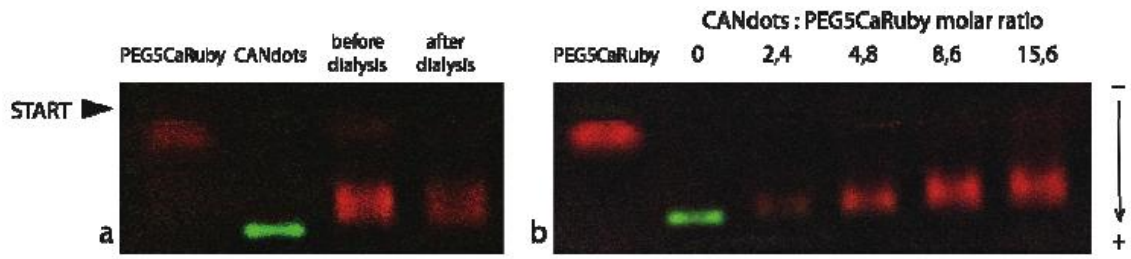

Fig. S3: Electrophoretic mobility of QD-PEG5CaRubyMe complexes in 0.5% agarose gel. (a) Gel electrophoresis of free PEG5-CaRuby, CANdots after ligand exchange, CANdots-PEG5-CaRuby complexes in ratio 1:12, illustrating efficiency of 48 hours dialysis purification. (b) Gel electrophoresis of free PEG5-CaRuby, and CANdots-PEG5-CaRuby complexes in different molar (A/D) ratios, as indicated at top of each lane. Samples show decrease of electrophoretic mobility with increased number of fixed dye molecules on the quantum dots.

S6

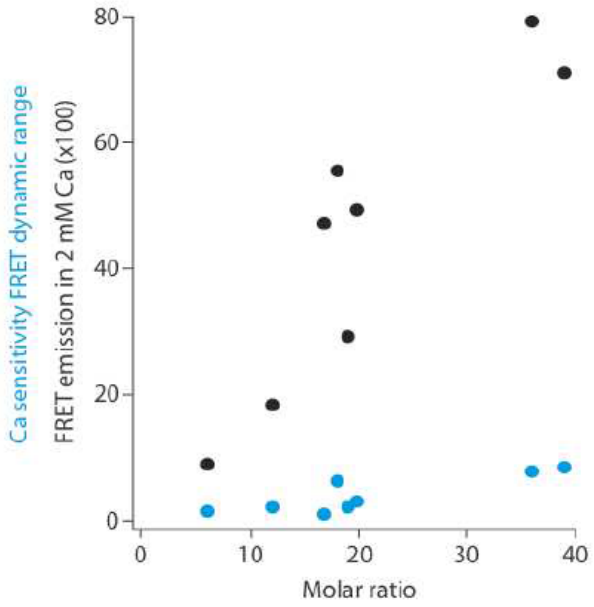

Fig. S4: Ca^{2+} sensitivity of QD-PEG10CaRuby. Graph displaying FRET absolute value increase (in 2 mM Ca^{2+}; black circles) whereas DR (blue dots) is constant when A/D is varied between 0 and 40. All data refer to the same QDs concentration.

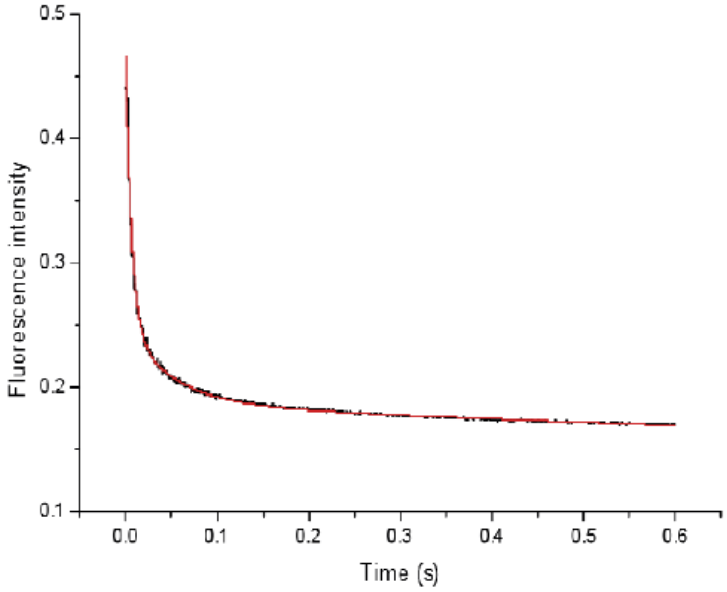

Fig. S5: Kinetics of Ca^{2+} binding to the QD-PEG5-CaRubyMe complexes. Addition of 5 mM EGTA displaced Ca^{2+} from saturated 0.5 µM CaRubyMe complexes. Emission was observed using an OG 590 nm long pass filter (excitation at 546 nm). A bi-exponential function (red line) fitted to the average (black line) of 4 experiments yielded two dissociation constants of 155 s-1 and 19.4 s-1 (and respective amplitudes 0.227 and 0.064). Similar experiments with 0.5 µM CaRubyMe yielded a koff of 300s-1 and 9.3 s-1 (of respective amplitudes 0.262 and 0.0528). From their respective K_D (2.9 and 3. 4 µM), estimated Ca^{2+} binding kon to the the nanoprobe and free CaRubyMe were 0.5 10^8 and 10^8 M^{-1} s^{-1}.

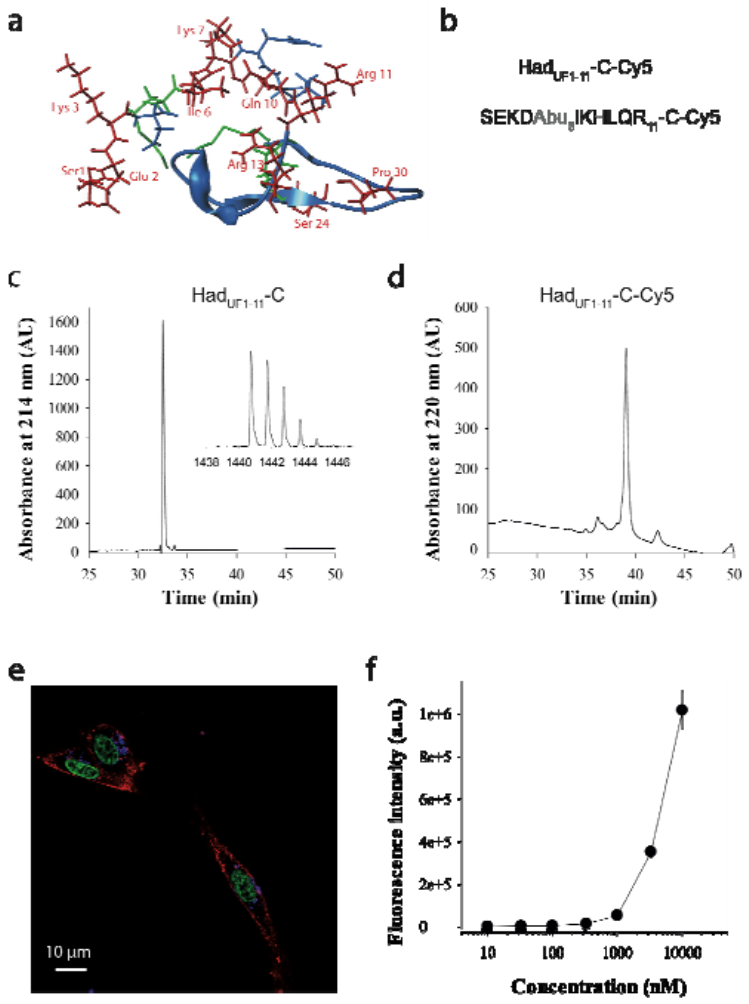

Fig. S6: Characterization of the cell penetration properties of HadUF1-11-C-Cy5 in cultured BHK cells. (a) Modeled 3D structure hadrucalcin (based on maurocalcine 3D structure, PDB access code 1C6W). Red residues are amino acids that differ from the amino acid sequence of maurocalcine. Residues in green are cystine residues. The peptide used for cell penetration Had$_{UF1-11}$ goes from Ser^{1} to Arg^{11} and forms one upper face of hadrucalcin. (b) Single letter code amino acid sequence of Had$_{UF1-11}$-C-Cy5. The fifth Cys residue is replaced by Abu in our synthetic peptide and is represented in grey color. (c) Analytical C18 reversed phase HPLC profile of purified Had$_{UF\ 1-11}$-C peptide. Insert: mass spectra of Had$_{UF1-11}$-C. (d) Analytical C18 reversed phase HPLC profile of purified Cy5-labeled Had$_{UF\ 1-11}$-C-Cy5 peptide. Note the shift in elution time indicating greater hydrophobicity of the conjugate. (e) Confocal microscopy image of 1 µM Had$_{UF1-11}$-Cy5 (blue) penetration in BHK cells. Cell membranes are labelled with concanavalin A-rhodamin (red), while nuclei are stained with Hoechst (green). (f) Quantitative assessment of cell penetration of Had$_{UF1-11}$-C-Cy5 by flow cytometry.

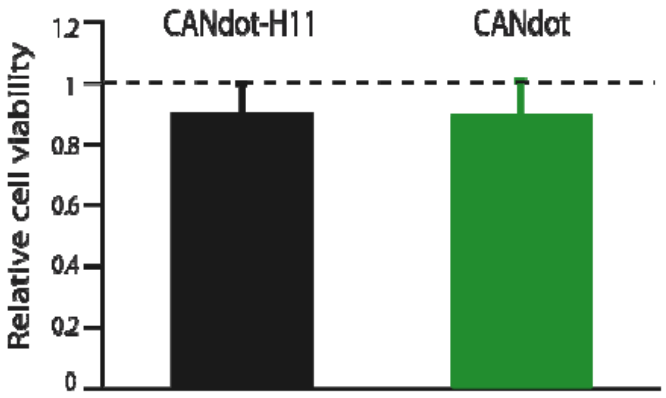

Fig. S7: Cell viability upon addition of QD functionalized with CPPs as assessed by the MTT toxicity test. 0.25 µM QDs without and with liganded CPPs (molar ratio 1:5) were incubated for 24 hours on BHK cells in culture at 80% confluence. Values are relative to control values (wells with solution exchange but no addition of QDs), 3 experiments, 4-6 wells each. Independent experiments with addition of 10 µM $Had_{UF1\text{-}11}$ did not reveal any toxicity of the CPPs.

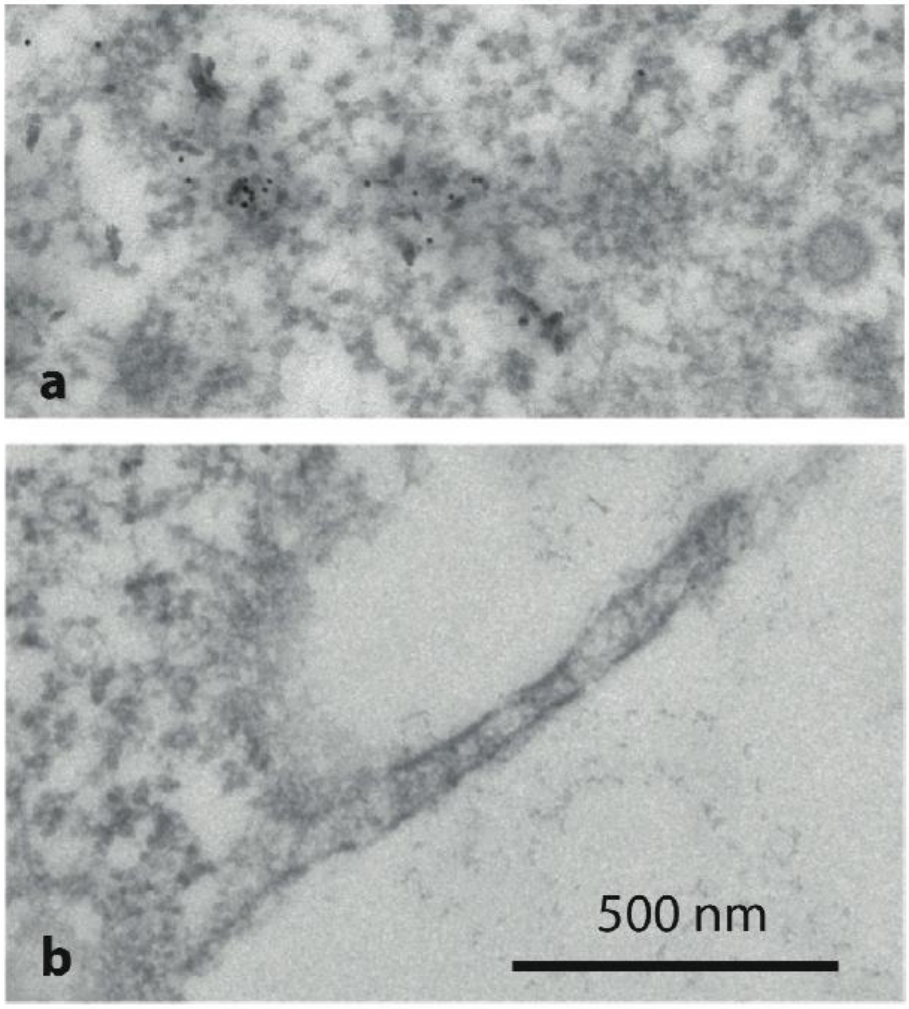

Fig. S8: EM micrograph of internalized QD-CaRuby-H11 complexes applying strong staining. A reinforced staining (with 5% uranyl acetate in 70 % methanol) was used for improved membrane visualization. In this condition, membranes are well preserved, see a likely coated-vesicule at bottom right in (a) and a filopode of the same cell in (b). However, importantly in (a) no membrane can be detected in a region where grouped QDs can be observed constituting a figure similar to that seen in Figure 7. Note the presence of deposits characteristic of uranyl acetate in the regions where QDs are present.

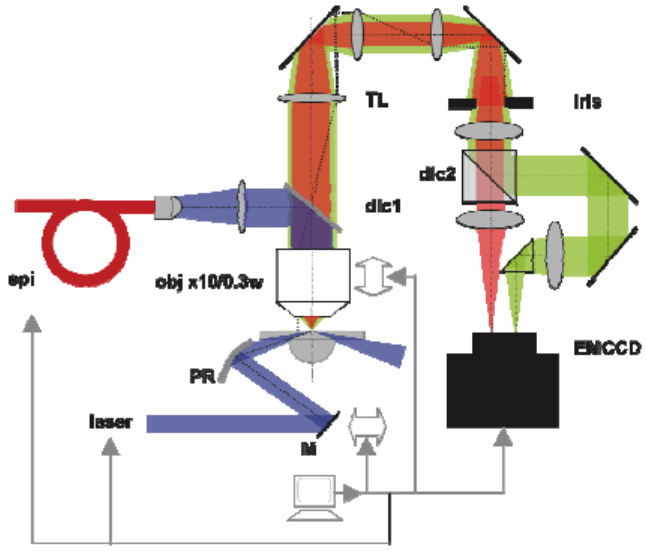

Fig. S9: Schematic optical layout of the variable-angle prism-based TIRF microscope used for imaging individual nanobiosensors in live cells. Obj: objective lens, TL: tube lens, dic: dichroic mirror, EMCCD: electron-multiplying charge-coupled device. Depending on the excitaton wavelength (shown here: 405 nm, blue) the beam angle of the totally reflected light was adjusted by sliding a small mirror (M). The parabolic reflector (PR) guaranteed that the beam always hit the same excitation spot. Fluorescence was extracted by a first dichroic (dic 1) that also permitting epifluorescence excitation. A custom dual viewer device separated red (CaRuby) and green (QD) emissions with a secondary dichroic (dic2) and appropriate emission filters (not shown). A green-light emitting LED below the quartz prism permitted bright field imaging (not shown).

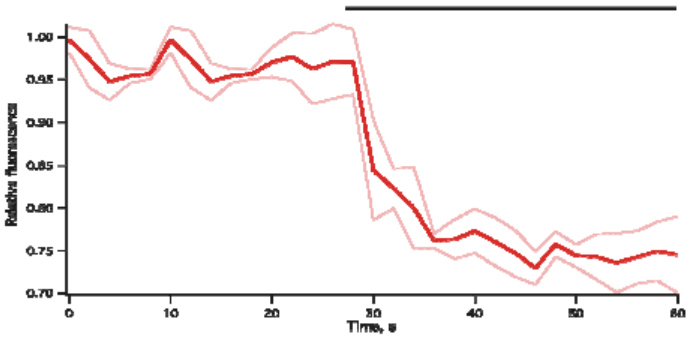

Fig S10: TIRF imaging of copper quenching of the extracellular nanobiosensors. A 40 µM CuSO4 bath solution quenches both QDs and CaRuby (see main text). Here with a preparation of QD-CaRuby loaded cells, then trypsinized and replated, copper application - horizontal black line - reduces basal cell fluorescence by 24% (average normalized fluorescence of 3 cells ± S.D., in red and light red respectively). Effect ranged from 10% to 25%, which implies that after trypsinization most imaged QDs were intracellular. After a first copper application, absolute remaining fluorescence did not change after wash nor upon a second CuSO4 application (not shown). 250 ms long TIRF frames taken for one minute at 0.5 Hz to minimize photobleaching.

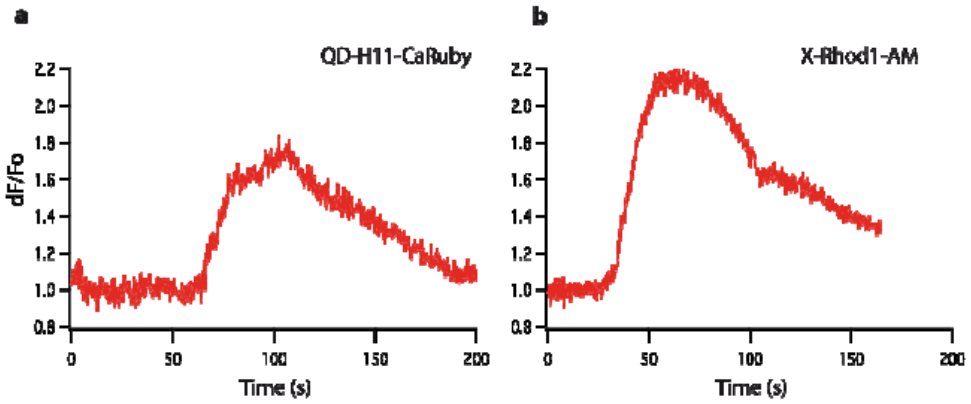

Fig. S11: Averaged Ca2+ transient recorded with QD-H11-CaRuby loaded cell (a) and X-Rhod1 loaded cell (b) have similar kinetics. (a) is the average of the signals evoked at 12 red-emitting points from top cell presented in Fig. 8a. In (b), cells were loaded by 5 min exposure to 1 µM X-Rhod1-AM (+ pluronic acid) before recording the response to bath applied NMDAR agonists at the same saturating concentration as in (a).

MATERIAL and METHODS

Drugs and chemicals:
ACN (Sigma-Aldrich, 271004); APV (Tocris, 0106); 1M CaCl2 (Fluka, 21115); Blasticidine S hydrochloride (Sigma-Aldrich, 15205); Coumarin 314 (Sigma-Aldrich, 392995); DIEA (Sigma-Aldrich, 387649); DMEM (Invitrogen, 31885); Ethanol (Merck, 100983); HEPES (Sigma-Aldrich, H3375); geneticine (Gibco, 10131); glycine (Tocris, 0219); glutamate (Tocris, 0218); HOBt (Iris-Biotech, RL-1035); Methanol (Merck, 106009); MOPS (Sigma-Aldrich, M-1254); MTT (Sigma-Aldrich, M-5655); NTA (Sigma-Aldrich, N-9877); TFA (Sigma-Aldrich, T6508); water (Fluka, Cat No. 95305).

Quantum dots (QDs): Hydrophobic TOP/TOPO coated CdSe/CdS/ZnS QDs (CANdots, Hamburg, Germany ; λEm=565 nm) sold in hexane were transferred to a toluene medium by slowly evaporating hexane under reduced pressure and kept as a µM stock solution at 4°C.

Synthesis of peptide-coated QDs: Hydrophobic QDs were coated with peptides as previously described.[1] Briefly, 1 nmole of the QDs stock solution in toluene was heated to 120°C to remove the solvent and redispersed in 450 µL of pyridine. Separately, 2 mg of each following peptides (New England Peptide, USA) were dissolved in 25 µL dimethyl sulfoxide (DMSO) before mixing at the indicated ratio: Ac-CGSESGGSESG$(FCC)_3$F-amide and NH2-KGSESGGSESG$(FCC)_3$F-amide. The QDs in pyridine and peptides in DMSO were mixed. Surfactant exchange and peptide binding was initiated by rising pH by addition of 12 µL of tetramethylammonium hydroxide (25% w/v in methanol). Following centrifugation, the QDs formed a pellet that was redissolved in 100 µL of DMSO. Next, the resulting peptide-coated QDs (pQDs) in DMSO were eluted through G25 Sephadex column equilibrated with twice its volume with a HEPES-buffered solution (HBS, in mM: 140 NaCl, 2.5 KCl, 10 HEPES, pH 7.2). To remove excess of peptides, the pQDs were purified using desalting column (Macrospin™, Harvard Apparatus). The pQDs were stored in HBS at 4°C until further use. Quantum yields (QYs) for hydrophobic QDs (λEm =563 nm, QY= 68 %) and the pQDs (λEm =563 nm, QY= 56%) were determined by standard procedures using coumarin 314 in ethanol (λEm =477 nm, QY=68%) as a reference as used by CAN Gmbh.

Preparation of the ligands:

CPPs were prepared as maleimide compounds by N-[g-maleimidobutyryloxy]succinimide ester (GMBS) addition at a molar ratio of 1:10 and stored dessicated after HPLC purification. For use, they were dissolved in HBS.

CaRubies PEGylation: CaRubies have been PEGylated using NH_2-PEG-alkyne of variable length (10 kDa, 5 kDa, 3 kDa, Iris Biotech and synthesised 0.3 kDa PEG) taking advantage of their side chain for click chemistry. Details of the Cu-catalyzed azide/alkyne cycloaddition (CuAAC) click conjugation has been already reported.[2] Briefly, alkyne-PEG-NH_2 and CaRuby were added in a 1(2 µmol): 2 molar ratio in 2 ml of methanol. A heterogeneous solution of $CuSO_4 \cdot 5H_2O$ (20 eq.) and of sodium ascorbate (25 eq.) in 500 µl of water was then added. The mixture was stirred overnight in the dark. The product was extracted with dichloromethane (DCM) and washed with a 0.1M solution of EDTA. The organic phase was evaporated and the crude purified through a LH-60 column (DCM/MeOH : 1/1). The first colored fraction was evaporated, taken up in distilled water and lyophilized to give the clicked product as a purple solid (yield ~80% for PEG10-CaRuby). Ca^{2+} sensitivity of CaRubies was unaltered by the click reaction.

0.3 kDa PEG synthesis:

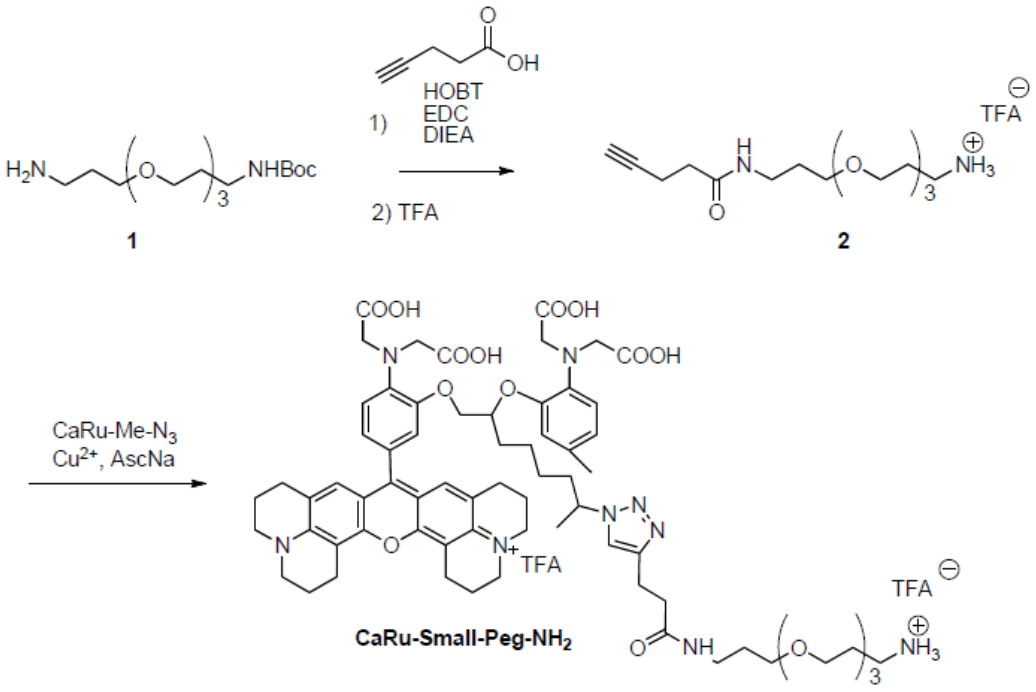

1 was synthesized following a published protocol [3] To a solution of **1** (1.00 g, 3.125 mmol, 1 eq) in DCM (15 mL) were added 4-pentynoic acid (0.367 g, 3.75 mmol, 1.2 eq), HOBt (0.506 g, 3.750 mmol, 1.2 eq) DIEA (1.620 mL, 9.375 mmol, 3 eq) and EDC (0.900 g, 4.687 mmol, 1.5 eq). The solution was allowed to stir overnight. The solution was washed with HCl (1M) neutralized with a saturated $NaHCO_3$ solution before being dried over $MgSO_4$, filtered and evaporated. The crude product was purified by column chromatography on silica gel (7/3 DCM/Acetone) to obtain 1.00 g of the desired product (80%) as a yellowish syrup. Rf = 0.45 (7/3 DCM/Acetone). This product was solubilized in DCM (8 mL) and TFA was added (3 mL). The reaction was sonicated for 1 hour. The solvents were then evaporated and the product was washed by addition of ether, sonication and removal of the supernatant (repeated 2 times). The remaining ether was evaporated and the product was dried under vacuum to give **2** in a quantitative manner as a yellowish oil. ^{1}H-NMR (300 MHz, D2O): δ 3.57 (s, 10H), 3.48 (t, *J* = 6.2 Hz, 2H), 3.17 (t, *J* = 6.5 Hz, 2H), 3.00 (t, *J* = 6.8 Hz, 2H), 2.38-2.26 (m, 5H), 1.84 (t, *J* = 6.3 Hz, 2H), 1.69 (t, *J* = 6.5 Hz, 2H).

To a solution of **CaRuby-Me-N_3** (10 mg, 0.01 mmol, 1 eq) and the **2** (15 mg, 0.037 mmol, 3.7 eq) in methanol (4 mL) was added a heterogeneous solution of $CuSO_4 \cdot 5H_2O$ (10 mg, 0.04 mmol, 4 eq) and sodium ascorbate (10 mg, 0.05 mmol, 5 eq) in water (500 µL). The mixture was stirred at room temperature for 3 days in the dark before being evaporated, the crude was purified by reverse phase chromatography on a C-18 column (ACN (0.1% TFA)/Water (0.1% TFA), 20/80 to 100/0) to obtain 10 mg of **CaRuby-small PEG-NH_2** (75%) as a purple solid after lyophilization.

Assembling functionalized QDs and purification: Prior to conjugation, the QDs were diluted to ~ 1 µM. All products to be conjugated at the desired molar ratio were prepared separately in a x5 GMBS (Thermo Scientific, USA) solution and left to react 1 hour at room temperature. Then, they were purified on G-10

Macro SpinColumn (Harvard Apparatus, USA) to remove excess of GMBS product. Finally, maleimide activated products and QDs were allowed to react overnight.
Dialysis was applied to remove excess of unbound molecules of PEGX-CaRuby. The samples were dialyzed in tubes with MWCO 50 kDa (Spectra/Por) against HBS buffer for 48 hours. In order to find optimal conditions for dialysis and to check its efficiency we used agarose gel electrophoresis. Gel electrophoresis was performed in 0.5% low electroendosmosis agarose (Ambion, USA) gels in 0.5X TAE buffer applying a 10 V/cm electric field for 20 minutes. The fluorescence of the complexes was detected and imaged directly on gels using ultraviolet excitation and a digital camera.

Electron microscopy:
Estimation of QDs diameter: For observation of QD at electronic level, formwar coated 400 mesh nickel grids are floated with the support film side facing up inside a few drops of the different specimens solutions for 30 mimutes. After washing in distilled water, grids are treated with 2 % of uranyl acetate in water, drained off after 15 minutes and dried before observation (Philips Tecnaï 12 at 80 kV).
The core/shell diameter was extracted from EM micrographs. Using MATLAB® we obtain radial profiles of the QD. Higher SNR (Signal to Noise Ratio) was achieved by subtracting background noise. Estimate radius corresponding to half width half maximum (HWHM) after denoising was (in nm): 1.8 ± 0.25 (mean ± SD), 1.8 ± 0.3 and 1.86 ± 0.22 for QD-KC, QD-PEG5CaRuby and QD-PEG10CaRuby respectively.

Cell EM: After loading with QDots-CPPs-CaRuby at the concentration of 150 nM, cells culture were prepared on ACLAR film (0,2 mm thick , Agar scientific UK), and fixed with 4 % paraformaldehyde and 0.1 % glutaraldehyde in PBS for 30 minutes at room temperature. They were then rinsed 3 times 10 minutes in the same buffer and postfixed in 1 % OsO4 in PBS for 15 minutes at 4 °C. After wash in water, cells were dehydrated in ethanol graded series of concentrations to 90 %, then in hydroxy propyl methacrylate (90, 95, 97 %) and finally embedded in Epon. Ultrathin sections (70 nm) were contrasted as previously, or for better visualization of the membranes they were stained with 5 % uranyl acetate prepared in 70% methanol.

Fluorimetry: Methods used have been published previously.[2,4] Briefly, CaRuby dynamic range for Ca2+ sensing was estimated from peak PL of CaRuby measured in a solution containing (in mM): 100 KCl , 30 MOPS, and pH was adjusted at 7.2 by KOH addition. KD was evaluated similarly adjusting the Ca2+ concentration as previously described using NTA for adjusting the Ca2+ concentration in the low micromolar range.[5] FRET fluorescence spectra (500-700 nm) were obtained by excitation light at 350 nm, and direct emission spectra (545-700 nm) were obtained by excitation at 535 nm. All values for FRET pairs were calculated, after spectral linear unmixing, by fit to the QD and CaRuby spectra (MatLab curve fitting tool).
Kinetics of the Ca^{2+} binding reaction to free CaRuby-Me and to QD-CPP-PEG5CaRubyMe was performed with a stopped flow apparatus (SFM-3, Bio-Logic, Claix, France). The reaction was carried out in 100 mM KCl, 30 mM MOPS and 10 mM NTA to adjust free Ca^{2+} concentration in the µmolar range around CaRuby-Me KD in the µmolar range, pH 7.4, 20°C. For koff evaluation, no NTA was added. The excitation and emission wavelengths were 450 and 514 nm (Melles-Griot interferential filter) respectively. Data acquisition and processing were done with the Biokine software from the instrument manufacturer.

CPP labeling with Cy5: The $Had_{UF1.11}$-C peptide was labeled with Cy5 according to the manufacturer's protocol (GE Healthcare). The peptide was dissolved at a concentration of 200 µg/ml in 1 M $NaHCO_3$ buffer, pH 9.3. 500 µl of the solubilized peptide was added to a Cy5-maleimide containing tube. The mixture was incubated during 2 hours at room temperature and then purified by HPLC using an analytical Vydac C18 column. Elution of the Cy5-labeled peptide was performed using a 10-60% acetonitrile linear gradient containing 0.1% trifluoroacetic acid. The pure peak fraction was lyophilized and the peptide quantified by UV spectrophotometer at 650 nm.

Cell culture and transfection for experiments on cells suspension: BHK-21 (clone 13) (baby hamster kidney) cell line was obtained from European Collection of Cell Cultures. Cells were cultured in a flask in DMEM medium (Gibco, Grand Island, NY) supplemented with 10% fetal calf serum (FCS, Sigma), Pen Strep (100 g/mL), pyruvate (110 mg/L) and glutamate (100 mg/L) and incubated in 5% CO_2 at 37˚C. The cells were collected from 90% confluent cell culture flasks by aspirating off the media and incubating with trypsin-EDTA (Gibco) for 2 min. DMEM medium, containing 10% FCS was added to stop trypsinization. Then, this solution was separated from the medium by centrifugation at 800 rpm for 3 min. The cells pellet was suspended in DMEM to obtain a homogeneous cell suspension at the desired final concentration for the toxicity assay or for investigation of QD-CaRuby-CPP penetration. For the intracellular Ca^{2+} measurements, HEK293 cells, transfected with NR1/NR2B NMDA receptors, were used. Cells were cultured in a flask in the same way as BHK-21 cells. Transfection was carried out on 80% confluent cells and nucleic acid-jet PRIME® complexes, containing 5 µg NR1 and 5 µg NR2B DNA plasmid, were added. After 4 hours incubation, the medium was replaced for fresh medium containing 200 µM APV and cells were left for 48 hours in the incubator to allow the expression.

Cell culture of a BHK cell line stably expressing NR2-NMDAR: Baby Hamster Kidney (BHK) cells stably expressing the NR1 and NR2 subunits of the N-methyl-D-aspartate receptor (NMDAR)[6] were grown in presence of two selection antibiotics (geneticine and blasticidine for each plasmid respectively). Further cells were maintained in presence of the two competitive antagonists of the glycine and glutamate binding sites, 5,7 dichlorokynurate (DCKA, 200 µM) and amino- 5, phosphonovalerate (APV, 200 µM) respectively. To reduce intracellular autofluorescence cells were cultured in phenol-red free DMEM.
For imaging, cells were transferred onto the stage of a custom microscope[7] (see below) and were continuously perfused at 3 ml/min with extracellular HEPES buffered saline containing (in mM): 140 NaCl, 2 KCl, 1.3 CaCl2 and 1.1 MgCl2, 10 Hepes and pH was adjusted to 7.4 (NaOH). 'Zero Ca^{2+}' solution contained was nominally Ca^{2+} free and containted 1.1 mM $MgCl_2$. 1 day before imaging, cells were loaded by exposure for 2 hours to 100 nM QD-CaRuby-CPP, trypsinized and re-plated on uncoated 25-mm ∅ #1.5 quartz coverslips (Technical Glass Products, Painesville, OH) that had previously been cleaned by successive baths in acetone, ethanol, water and were finally exposed to UV light for one hour.

Toxicity assay (3-(4,5-Dimethylthiazol-2-yl)-2,5-diphenyltetrazolium bromide, MTT, assay): Cells were plated into 96-well microplates and grown until reaching 75% confluence. After 2 days of culture, the cells were incubated for 24 hours at 37 °C with CPPs at a concentration of 10 µM. Control wells containing cell culture medium alone or with cells, both without peptide addition, were included in each experiment. 2% SDS was used as a toxic agent for comparison. The cells were then incubated with MTT added at 1.5 mM for 30 min (stock at 15 mM (25 mg/5 ml in HBS; MW 335). Conversion of MTT into purple-colored MTT formazan by the living cells indicates the extent of cell viability. The crystals were dissolved with 100 µl DMSO, and the optical density was measured at 490 nm using a microplate reader (Biotek ELx-800, Mandel Scientific Inc.) for quantification of cell viability. All assays were run in triplicates.

Confocal microscopy: BHK-21 cells were plated into 8-well Lab-Tek plates (at 10% confluence). Before incubation with quantum dots, cells were washed twice with DMEM/F-12 medium without serum and antibiotics (assuming that the serum could prevent the CPP penetration into the cell). The complexes at the concentration of 100 nM QD were added to a final volume of 150 µl per each well and were incubated for 2 hours at 37° C and 5% CO_2. Then, nuclei were stained by adding Hoechst 34580 (Invitrogen) at a final concentration 1 µl/ml and cells were further incubated for 10 minutes. Afterwards

cells were washed twice with DPB to remove free Hoechst and free QDs. Finally, after addition of 150 µl of DMEM/F-12 (without serum and pH indicator), plates were left in the incubator.
Just before imaging, plasma membranes were labeled by adding Concanavalin A-Alexa Fluor 647 (Invitrogen) to a final concentration of 25 µg/ml (150 µl final volume) and incubating for a 1 minute at room temperature. Cells were then washed 2 times with DPBS and finally kept in 250 µl of DMEM/F-12 (without serum and pH indicator). Live cells were immediately visualized by confocal microscope.

For analysis of the cell entry of Cy5-labeled-$Had_{UF1\text{-}11}$-C peptide in living cells, cell cultures were incubated with the fluorescent peptide (in DMEM/F-12 nutrient medium only) for 2 hours, and then washed twice with phosphate-buffered saline (PBS) alone. For analysis of cell entry of a dye, just before imaging, the plasma membrane was labeled with 5 (25) µg/ml rhodamine-conjugated concanavalin A (Invitrogen) for 5 (1, respectively) min at room temperature. Cells were washed twice DPBS and finally kept in DMEM/F-12 (without serum and pH indicator). Live cells were then immediately analyzed by confocal laser scanning microscopy using a Zeiss LSM operating system. Rhodamine (580 nm) and Cy5 (670 nm) were sequentially excited and emission fluorescence was collected.

Fluorescence imaging was carried out with a confocal microscope (LSM 710, Zeiss, Germany). The QDs-CaRuby-H11 were excited with 561 nm laser line and detected with 550-610 nm band-pass filter, Hoechst 34580 was excited with 405 nm laser line and detected with 389-500 nm band-pass filter and Concanavalin A-Alexa Fluor 647 was excited with 633 nm laser line and detected with 620-740 nm band-pass filter. The total acquisition time was 3min. Images were collected by the microscope software (ZEN 2011).

Flow cytometry analysis: BHK cells were incubated with various concentrations of Cy5-labeled peptide in DMEM-F12 culture medium without serum at 37°C for 2 hours. The cells were then washed with PBS to remove excess extracellular peptide and treated with 1 mg/ml trypsin-EDTA (Invitrogen) for 5 min at 37°C to detach cells from the surface, and centrifuged at 200 g before suspension in PBS. Flow cytometry analyses were performed with live cells using an Accuri C6 flow cytometer (BD Biosciences). Data were obtained and analyzed using CFlow Sampler (BD Biosciences). Live cells were gated by forward/side scattering from a total of 10,000 events.

Intracellular Ca calibration experiments were performed using a BD LSR Fortessa (BD Biosciences) flow cytometer. After QDs loading (as above), BHK cells were resuspended in a 30 mM MOPS and 10 mM NTA- buffered solutions at variable free [Ca2+] concentrations Slight cell membranes permeabilization was achieved by 0.06% Tritonx100 addition just before flow cytometer analysis. Live cells were gated by forward/side scattering from a total of 10,000 events and mean fluorescence intensity (MFI; 561 nm and 610 ± 20 nm for excitation and emission respectively) was determined for every condition.

Imaging cytometry: For imaging flow cytometry analysis, the same procedure of plating and incubation with QDs as for confocal microscopy was applied with the difference that after incubation the cells were trypsinized and resuspended in DPBS. DAPI staining (at a final concentration of 2.5 µg/ml) was used to reject dead cells. Cell images were acquired using multispectral imaging flow cytometer (Image Stream 100 with 12 channels and 2 cameras, Amnis Corporation), collecting 500 events per sample at 60 x magnification. A 561 nm wavelength laser was used to excite QD-CaRuby complexes and the emission fluorescence was collected using the 595-660 spectral detection channel. Cell images were analyzed using IDEAS image-analysis software (Amnis). Three main criteria were used to select cells for analysis. Starting from the "Begin analysis" wizard, firstly cells within the focal plane were selected using a histogram of the root-mean-squared gradient of the bright field image. Secondly, a gating based on a two-dimensional plot of area versus aspect ratio was used to isolate a population of single cells. A third step was to eliminate dead cells using a histogram of the fluorescence intensity in the DAPI channel. After that, "Masks" feature was applied to determine the cytoplasmic part of the cell. For this purpose an "Object" mask was created on the bright field image and it was eroded by 8 pixels to separate cell

membrane and cytoplasm of the cells. Finally, complex masking schemes as described in the "Spot Counting" protocol (Amnis) were used to identify and calculate the number of particles inside the cells. More precisely, after a "Spot" mask was applied, an "Intensity" threshold was determined. Then a "Peak" mask was used to separate two close spots with one mask into two and a "Range" mask was applied to limit the mask to spots of a certain size in order to eliminate the noise. Final counting was carried out in the CaRuby channel.

Intracellular Ca^{2+} measurements on cells suspension: Plated 80% confluent HEK293 cells expressing NR1 and NR2B subunits of the NMDA receptor were exposed for 4 hours to 100 nM QDs in the medium without antibiotics nor foetal calf serum; after cells scraping, they were centrifuge to remove excess of QD, and then they were suspended in HEPES buffered extracellular medium, containing 1.3 mM Ca^{2+}.
Just before the measurement 10 mM Ca^{2+} final concentration was added to cells suspension and they were allowed to rest for 5 minutes. In order to reduce the basal fluorescence introduced by quantum dots attached to the external membrane and exposed to the high extracellular Ca^{2+} concentration 40 µM final concentration $CuSO_4$ was applied. The minimal concentration quenching both CaRuby emission and QDs was found experimentally.
Intracellular Ca^{2+} flux was measured using a JASCO FP-8300 spectrofluorometer (Japan) equipped with a CSP-829 sample compartment lid with syringe port for drug injection. A time-course measurement mode was performed with excitation at 545 nm (bandwith 5 nm) and a 606 nm (bandwith 5 nm) filter. A baseline fluorescence (F_{basal} signal) was recorded over 10 seconds, after which agonists of NMDA receptors (100 µM glutamate + 20 µM glycine final concentration) or antagonist of NMDA receptors (100 µM APV final concentration) were injected with a Hamilton micro syringe to the cuvette containing a 450 µl suspension of approximately 2 $x10^5$ cells and fluorescence (F) in response to the application was measured for 3 min.

The results are presented as $F- F_{basal}/ F_{basal}$. All measurements were performed using 2 replicates and in 3 independent experiments.

In cell imaging of single nanoparticules using TIRF microscopy: For single-nanobiosensor imaging we used a prism-type variable-angle total internal reflection fluorescence microscope (VA-TIRFM) described earlier[7] and modified for the experiments, Fig. S7. The beams of a 405-nm solid state laser (LasNova20, Lasos, Jena, Germany) and the 568-nm line of an Ar^+/Kr^+ mixed-gas laser (35 KAP 431, CVI MellesGriot, Carlsbad, CA) were combined (zt405RDC, AHF Analysentechnik, Tübingen, Germany), directed via all-mirror optics and a precision quartz prism (Bernhard Halle Nachf., Berlin, Germany) at a supercritical angle (q = 65.5 ± 0.5° [q_c=60.9°] to the cell/substrate interface. The calculated penetration depths of the evanescent fields set up by total internal reflection (TIR) were (1/e-intensity decay) ~75 nm (110 nm) at 405 (568) nm, respectively. Fluorescence was collected through a ×10/NA 0.3w (UMPlanFl) or a ×60/NA1.1w objective (LUMFl, both from Olympus-Europe, Hamburg, Germany), filtered with a HQ490DCXR primary dichroic and BA520IF long-pass filter, split up with a HQ590DCXR secondary dichroic into a green (BL562/40) and red (BP620/60) colour channel. Scattered laser light was rejected with two stacked 488/568-nm holographic rugate notch filters (Barr Precision Optics, Westford, MA) and the red and green component images projected via an achromatic telescope (f_1 = 50 mm, f_2 = 40 mm) side-by-side onto an electron-multiplying CCD detector (QuantEM512SC, Photometrics, Tucson, AZ). A wavelength-tunable Xe-arc monochromator (Polychrome II, TILL Photonics, Gräfelfing, Germany) provided whole-field epifluorescence (EPI) excitation. A green-light emitting diode (LED) mounted underneath the prism provided bright-field (BF) illumination. All shutters, light sources, acquisition and the piezo-focus drive (PIFOC, Physik Instrumente, Karlsruhe, Germany) were controlled with METAMORPH (MDS Analytical Technol., Sunnyvale, CA). Typical laser powers in the sample plane were ~1 mW for 405- and 300 µW for 568-nm excitation, with exposure times of 125 ms. Final magnifications were 508 ± 20 nm/px at ×10 with an extra magnification of ×2.

Small islets of flat, elongated BHK cells were imaged consecutively in bright field (BF) and upon 405-nm and 568-nm evanescent-wave (EW) excitation. Cells outside the excitation spot were not exposed to light, thereby minimizing photobleaching and allowing imaging several cells on the same coverslip. Glutamate, glycine and high Ca^{2+} (at 100 µM, 20 µM and 5 mM final concentration, respectively) were applied locally whilst the bath perfusion with standard extracellular saline was kept running to speed up solution exchange. 300 control and stimulation images were continuously acquired at 4Hz at 250-ms long exposure in the "stream" mode and processed using Metamorph (Molecular Devices).

We subtracted a dark image from each fluorescence image, extracted the average signal from 2-µm diameter circular regions of interest and corrected the resulting trace for photobleaching (fit of a single exponential). Ca^{2+} transients are shown as F/F_0, where F_0 is the average basal fluorescence before NMDAR activation. Absolute signals emitted by a nanobiosensor were small and noisy as expected from the roughly 10 CaRuby molecules per QD. We therefore measured the mean peak F/F_0 amplitude over 6 frames around the peak location determined from the 9-point box-filtered trace. Similarly, fluorescence risetimes were determined by a sigmoid fit to the rising phase of the F/F_0 transient, again on the 9-points box-filtered trace.

ABBREVIATIONS

A, acceptor in a FRET pair; ACN, acetonitrile; APV, (2R)-amino-5-phosphonovaleric acid NMDAR antagonist; BAPTA,1,2-bis(o-aminophenoxy)ethane-N,N,N',N'-tetra-acetic acid; BHK, baby hamster kidney cell line; Ca^{2+}, calcium (ion); CPP, cell penetrating peptide; CuAAC, Copper-Catalyzed Azide-Alkyne Cycloaddition; DCM, dichloro-methene; DMEM, Dulbecco's minimal essential medium; D, donor in a FRET pair; DHLA, dihydrolipoic acid; DIEA, N,N-Diisopropylethylamine; DPBS, Dulbecco's Phosphate-Buffered Saline ;E, FRET efficacy estimated on the donor; EDC, N-(3-Dimethylaminopropyl)-N'-ethylcarbonate; EDTA, Ethylenediaminetetraacetic acid; EGTA, ethylene glycol tetraacetic acid; F, fluorescence intensity; FP, fluorescent protein; FRET, Förster resonance energy transfer; GMBS, N-[γ-maleimidobutyryloxy]succinimide ester; H11, 11 aminoacids long peptide, $Had_{UF1\text{-}11}$, prepared from Hadrucalcin toxin; HEK: human kidney cells; HEPES, 4-(2-hydroxyethyl)-1-piperazineethanesulfonic acid; HWHM, Half Width at Half Maximum; MeOH, methanol; HOBt, hydroxybenzotriazole; MOPS, 3-(N-morpholino) propanesulfonic acid; MTT, 3-(4,5-Dimethylthiazol-2-yl)-2,5-diphenyltetrazolium bromide ; NMDA, N-methyl-D-aspartate; NMDAR, NMDA-sensitive glutamate receptor type; NTA, nitrilotriacetic acid; pC, Ac-CGSESGGSESG(FCC)3F-amide peptide ; pK, NH_2-KGSESGGSESG(FCC)3F-amide peptide ; PEG, poly-ethylene glycol; PET, photoinduced electron transfer; PL, photoluminescence; QD, quantum dot, or fluorescent colloidal nanoparticle; SNR, signal to noise ratio; TAE, Tris-acetate-EDTA buffer; TEM, transmission electron microscopy; TFA, trifluoroacetic acid; TOP/TOP, Tri-n-octylphosphine/Tri-n-octylphosphine oxide.

REFERENCES

(1) Pinaud, F.; King, D.; Moore, H. P.; Weiss, S. *J Am Chem Soc* **2004**, *126*, 6115-23.

(2) Collot, M.; Loukou, C.; Yakovlev, A. V.; Wilms, C. D.; Li, D.; Evrard, A.; Zamaleeva, A.; Bourdieu, L.; Leger, J. F.; Ropert, N.; Eilers, J.; Oheim, M.; Feltz, A.; Mallet, J. M. *J Am Chem Soc* **2012**, *134*, 14923-31.

(3) Zhang, L.; Wu, L.; Brunsveld, L. *Angewandte Chemie* **2007**, 1798-1802.

(4) Yakovlev, A. V.; Zhang, F.; Zulqurnain, A.; Azhar-Zahoor, A.; Luccardini, C.; Gaillard, S.; Mallet, J. M.; Tauc, P.; Brochon, J. C.; Parak, W. J.; Feltz, A.; Oheim, M. *Langmuir* **2009**, *25*, 3232-9.

(5) Gaillard, S.; Yakovlev, A.; Luccardini, C.; Oheim, M.; Feltz, A.; Mallet, J. M. *Org Lett* **2007**, *9*, 2629-32.

(6) Hansen, K.B.; Brauner-Osborne, H.; Egebjerg, J. *Comb Chem High Throughput Screen*, **2008**, 11, 304-15.

(7) van 't Hoff M, Reuter M, Dryden DT, Oheim M. *Phys Chem Chem Phys*, **2009**, 11, 7713-20.

3.3.3. Discussion

Pour la mesure efficace des nanodomaines calciques intracellulaires, nous avons mis au point des FRET-nanobiodétecteurs de Ca^{2+} dotés des propriétés de pénétration cellulaire. Les nanobiodétecteurs sont composés d'un QD portant à sa surface plusieurs molécules de l'indicateur calcique (CaRuby) et du CPP (Had_{UF1-11}).

Le CPP Had_{UF1-11} a permis une pénétration cellulaire significative des nanobiodétecteurs de Ca^{2+}. Cependant, nous avons remarqué une certaine pénétration cellulaire des nanobiodétecteurs sans CPP (Fig.6.C- Chap.3.3.2). Ces nanobiodétecteurs sans CPP auraient été internalisés par l'endocytose grâce à la présence des peptides hydrophiles à la surface des QDs; 15 % de ces peptides contenaient le résidu lysine, résidu basique chargé positivement pouvant donc se fixer aux protéoglycanes de la surface cellulaire et déclencher l'endocytose (*278*). Une analyse du rôle de l'endocytose par les inhibiteurs des différentes voies d'endocytose ou par l'analyse de la co-localisation des nanobiodétecteurs et des endosomes / lysosomes (*12, 85, 86*) pourrait confirmer ou infirmer cette hypothèse. Il serait également intéressant d'étudier l'efficacité de détection du Ca^{2+} intracellulaire par ces nanobiodétecteurs internalisés sans CPP. Les nanobiodétecteurs séquestrés dans les endosomes ne pourraient pas détecter le Ca^{2+} cytosolique.

Les nanobiodétecteurs de Ca^{2+} ont été conçus pour la détection des nanodomaines du Ca^{2+} cytosolique. Pour détecter la présence ou pas d'un nanodomaine calcique dans une région intracellulaire donnée, il faut d'abord se rassurer de la présence du détecteur dans cette région avant l'entrée du flux calcique générant les nanodomaines. En principe, la technologie FRET permet de répondre à cette exigence. Avant l'apparition des nanodomaines, le QD (donneur) émet de la fluorescence qui permet de localiser le nanobiodétecteur. A l'apparition d'un nanodomaine calcique, le CaRuby (accepteur) reçoit de l'énergie du QD et émet de la fluorescence qui révèle la présence du nanodomaine calcique. Il est important de noter que l'excitation du CaRuby par l'énergie émanant du QD et non directement par les rayons lasers limiterait le photoblanchiement du CaRuby.

Cependant, l'efficacité de nos nanobiodétecteurs a été finalement validée *in situ* en excitation directe. Un FRET-nanodétecteur est principalement caractérisé par l'efficacité FRET et la sensibilisation de l'accepteur. L'efficacité FRET peut se définir comme « le taux de transfert de l'énergie du donneur à l'accepteur ou le taux d'absorption de la fluorescence

du donneur par l'accepteur ». Quant à la sensibilisation de l'accepteur, elle peut se définir comme le « rapport de la quantité de fluorescence de l'accepteur excité par le donneur (mode FRET), sur sa quantité de fluorescence émise dans les mêmes conditions sous l'excitation directe par les rayons lasers ».

In vitro, nos nanobiodétecteurs ont pu atteindre une efficacité FRET de 80% (absorption de 80% de la fluorescence du QD par le CaRuby). Par contre, la sensibilisation du CaRuby par FRET n'a pas pu dépasser 20%. Cette faible sensibilisation s'expliquerait par une faible quantité de photons transférés du QD au CaRuby par FRET comparativement à la quantité de photons fournie au CaRuby par les faisceaux lasers en excitation directe. Ceci serait la conséquence, du moins partiellement, du transfert d'énergie partiel du QD au CaRuby (transfert de seulement 80 %). La sensibilisation de CaRuby pourrait être améliorée par l'utilisation des QDs émettant une quantité de fluorescence plus intense; c'est-à-dire des QDs ayant une plus grande capacité d'absorption (un plus grand coefficient d'extinction) et un plus grand rendement quantique.

In situ, le signal du CaRuby en mode FRET était trop faible pour être détecté. Cela aurait été la conséquence de la faible sensibilisation du CaRuby. De ce fait, le CaRuby a été excité directement par les rayons lasers. Ainsi donc, l'imagerie des nanodomaines calciques a nécessité deux lasers, l'un pour l'excitation du QD afin de localiser le nanobiodétecteur, et l'autre pour exciter le CaRuby afin de visualiser le signal calcique; en mode FRET un seul laser aurait suffi. Par ailleurs l'excitation directe du CaRuby par les rayons laser de façon relativement prolongée comportait le risque de photoblanchiement. Curieusement, le CaRuby a manifesté de la fluorescence en présence de la [Ca^{2+}] intracellulaire de repos (Fig.6.b-Chap.3.3.2). Ceci a pour inconvénient un faible rapport signal/bruit de fond. Le photoblanchiement et le faible rapport signal/bruit de fond expliqueraient le faible signal avec lequel les nanodomaines calciques ont été observés. L'utilisation de CaRuby de faible affinité, qui ne fixe le Ca^{2+} que lors des augmentations transitoires de la [Ca^{2+}], augmenterait le rapport signal/bruit de fond. Il existe déjà plusieurs variétés de CaRuby ayant une affinité pour le Ca^{2+} de 3 µM à 22 µM (*296*) qui pourraient faciliter cette optimisation.

Il convient de remarquer que les variations de la [Ca^{2+}] cytosolique observées au cours de nos expérimentations pourraient correspondre à la diffusion du Ca^{2+} après l'entrée du flux calcique, et non aux centres même des nanodomaines calciques qui généralement ont de fortes concentrations (*269*). Ceci expliquerait en partie les faibles signaux calciques observés.

Une visualisation plus précise des nanodomaines avec un signal plus fort pourrait être réalisée en positionnant les nanobiodétecteurs dans des sites sièges des nanodomaines calciques. Cela pourrait se faire par une fonctionnalisation supplémentaire des nanobiodétecteurs au moyen des anticorps spécifiques des canaux calciques d'intérêt.

Le présent travail a montré l'efficacité des nanobiodétecteurs de visualiser les nanodomaines calciques en utilisant la microscopie TIRF. La microscopie TIRF permet une imagerie à très forte résolution en limitant le champ d'observation dans un rayon d'environ 100 nm à partir du point d'impact des rayons incidents. Cela nécessite que le signal produit dans cet espace nanométrique soit suffisamment intense pour être détecté. La visualisation des événements calciques par nos nanobiodétecteurs au moyen de la microscopie TIRF donne la certitude que ces nanobiodétecteurs rendent compte des événements nanométriques, donc visualisent effectivement des nanodomaines calciques. Par ailleurs, ça montre que les nanobiodétecteurs produisent une fluorescence suffisamment intense pour être détecté à l'échelle nanométrique. Ils pourraient être efficacement utilisés avec n'importe quelle autre technologie d'imagerie à forte résolution, notamment la microscopie confocale (*292*).

3.3.4. Conclusion

La détection de nanodomaines calciques intracellulaires présente un défi expérimental. Cette détection nécessite une concentration et une immobilisation de l'indicateur de Ca^{2+} aux sites des nanodomaines calciques. Avec les indicateurs de Ca^{2+} conventionnels, il est difficile de remplir ces conditions.

Nous avons mis au point des FRET-nanobiodétecteurs de Ca^{2+} dotés des propriétés de pénétrer dans la cellule et de concentrer localement l'indicateur de Ca^{2+}. Les nanobiodétecteurs sont constitués d'un QD recouvert de molécules de l'indicateur de Ca^{2+} (CaRuby) et du CPP ($Had_{UF1\text{-}11)}$, dans un rapport de 1 : 10 : 10, respectivement. Les nanobiodétecteurs ont montré leur efficacité de détecter les nanodomaines du Ca^{2+} cytosolique. Cependant, le signal était faible. Le signal pourrait être amélioré en utilisant une variété de CaRuby de faible affinité, ce qui augmenterait le rapport signal/bruit de fond.
Par ailleurs, une fonctionnalisation supplémentaire, notamment par des anticorps spécifiques des canaux Ca^{2+}, permettrait leur immobilisation aux sites de nanodomines de Ca^{2+} d'intérêt.

4. DISCUSSION GENERALE

La MCa est le premier exemple d'une toxine animale repliée / oxydée doté d'excellentes propriétés de CPP. Elle délivre dans les cellules divers types de cargaisons (*16, 18, 61, 279, 280*); elle pénètre dans les cellules à de très faibles concentrations; elle est peu toxique; elle a une remarquable stabilité (*16*). Toutes ces propriétés font de la MCa un CPP prometteur pour des applications de délivrance intracellulaire de macromolécules ou nanoparticules d'intérêts expérimentaux, diagnostiques, ou thérapeutiques. Cependant, l'activité pharmacologique de la MCa sur les canaux RyRs entrainant le relargage du Ca^{2+} stocké dans le RS (réticulum sarcoplasmique) vers le cytosol, est indésirable dans la plupart d'applications envisageables, particulièrement *in vivo*. Même si les différentes évaluations de la cytotoxicité de la MCa réalisées sur des cultures cellulaires n'ont pas jusqu'à présent montré de cytotoxicité signifie de la MCa, fort probablement du fait de la faible expression des canaux RyRs par les cellules utilisées, son utilisation *in vivo*, occasionnerait des effets indésirables importants (*60*). Pour une utilisation *in vivo*, la MCa a donc été débarrassée de son activité pharmacologique. Différentes stratégies ont été utilisées avec succès : des mutations ponctuelles, notamment la mutation R24A (*273, 274*); la synthèse du peptide au moyen des acides aminés énantiomères D (*16*); et la suppression des ponts disulfures intramoléculaires par le remplacement des résidus cystéines par l'acides 2-amino butyrique (Abu) conduisant à un peptide linéaire (*18*). La suppression des ponts disulfures fut en plus une stratégie d'optimisation de la MCa en rapport avec sa production et utilisation. La présence de trois ponts disulfures dans la molécule nécessite des étapes de repliement/oxydation du peptide au cours de la synthèse. Il est difficile de réussir un repliement correct, c'est-à-dire identique à celui de la MCa native, surtout en présence d'une cystéine supplémentaire réservée au greffage de la cargaison. Le rendement du processus est donc faible, ce qui se traduit par un coup de production élevé. Par ailleurs, la présence de six résidus cystéines intramoléculaires complique le greffage de la cargaison, si le greffage est envisagé d'être réalisé au moyen d'une cystéine supplémentaire (une $7^{ème}$ cystéine). En effet, la cargaison pouvant bien se greffer aussi bien à la cystéine supplémentaire qu'aux cystéines intramoléculaires, il est difficile de contrôler le site de fixation da la cargaison. Or il a été montré que le site de greffage d'une cargaison sur un CPP influe sur l'efficacité de pénétration cellulaire (*297*). Nos travaux ont montré une légère différence de pénétration cellulaire entre la MCa portant la cargaison (Cy5-C) en N-ter (Cy5-C-MCa_{UF1-33}) et celle

portant la cargaison en C-Ter (MCa_{UF1-33}-C-Cy5) (Fig.1.D-Chap. 3.1.2), mais la différence pourrait être très significative avec la cargaison en position latérale du peptide, c'est à dire greffée sur une cystéine au milieu de la chaîne peptidique (*297*). Le remplacement des cystéines internes par l'Abu a permis d'éliminer ces obstacles.
Le coup de production de la MCa est également exacerbé par la taille du peptide. Composée de 33 résidus acides aminés, la MCa native est relativement plus longue que les CPPs couramment utilisés tels que la TAT composé de 13 résidus ou la pénétratine composé de 16 résidus. Il s'est donc avéré nécessaire de réduire la taille du peptide.

Dans ce travail, nous avons poursuivi l'optimisation du vecteur MCa pour le rendre plus simple plus économique à produire par la réduction de sa taille et améliorer ses performances. Par la délétion de la MCa linéaire complète (MCa_{UF1-33}), nous avons obtenus 12 nouveaux excellents CPPs plus courts et plus efficaces en pénétration cellulaire que la MCa_{UF1-33}. Cependant, ces observations ont été faites seulement sur les cellules CHO. Pour une meilleure appréciation, l'évaluation devrait être étendue sur plusieurs types cellulaires. Les analogues MCa_{UF1-9}, $MCa_{UF14-25}$, $MCa_{UF18-33}$-C, et MCa_{UF1-20}-C se sont démarqués par leur remarquable efficacité. Cependant, l'accumulation en forte quantité de la $MCa_{UF14-25}$, la $MCa_{UF18-33}$, et la MCa_{UF1-20} est observée lorsque les peptides sont utilisés à de fortes concentrations, $\geq$ 10 µM. Même si à 10 µM ces peptides n'ont pas montré de forte cytotoxicité sur les cellules CHO (environ 20 % de cytotoxicité), ils pourraient être toxiques sur d'autres types cellulaires. La MCa_{UF1-9} présente de meilleures perspectives en termes d'applications. Elle est la plus efficace en pénétration cellulaire à des concentrations extracellulaires $\leq$ 1 µM, concentrations présentant moins de risque de cytotoxicité et évidemment plus économiques.

Cependant, il serait intéressant de savoir si les quantités de peptides internalisés observées sont suffisantes pour des applications envisageables, avant de procéder à cette application. Pour ce faire, il faudrait au moins déterminer la quantité ou la concentration intracellulaire du peptide internalisé afin de la comparer à la quantité intracellulaire nécessaire pour cette application (estimable connaissant la quantité nécessaire de la cargaison). Les techniques de mesures utilisées au cours des présents travaux ne permettent pas de faire une telle quantification. Nous avons marqué les peptides par un fluorochrome organique, la Cy5, et par la microscopie confocale et le FACS nous avons mesuré la fluorescence intracellulaire que nous avons exprimée en unité arbitraire (non standard). De telles mesures sont adaptées à

des évaluations qualitatives et comparatives, mais ne donnent pas de quantité absolue (ou concentration) du peptide internalisé. Contrairement à l'absorbance des fluorochromes qui se convertit en concentration du peptide marqué (dans ces travaux la concentration des peptides marqués par la Cy5 a été déterminée par la mesure de l'absorbance de la Cy5 par spectrophotométrie), la fluorescence ne permettrait pas une estimation correcte de la concentration du peptide car la fluorescence des fluorochromes se dissipent au cours du temps par photoblanchiement. L'estimation de la concentration intracellulaire des CPP-cargaisons nécessite donc le marquage des peptides par un marqueur stable rendant fidèlement compte des quantités internalisées. Le radiomarquage est une technique stable qui répond à cette exigence. Une technique efficace de mono-radiomarquage des CPPs par iode 125 a été récemment décrite; elle permet désormais de réaliser des analyses quantitatives précises de la distribution intracellulaire des CPPs (*298*).

Les analogues de la MCa délétés pénètrent dans les cellules principalement de façon indépendante de l'endocytose, vraisemblablement par la translocation directe (Fig.5-Chap.3.1.2, Fig.2-Chap.3.2.2). L'endocytose est la voie principale d'internalisation de la plupart des CPPs connus à ce jour (*12*). Cette voie de pénétration cause des problèmes de séquestration et dégradation des CPPs et leurs cargaisons dans les endosomes, ce qui rend difficile leur accès à des cibles cytoplasmiques ou nucléaires. Ce problème n'est pas rencontré si la pénétration cellulaire se fait par la translocation directe qui consiste à traverser la membrane plasmique directement sans passer par les endosomes.

Cependant, la macropinocytose contribue partiellement à la pénétration cellulaire de la plupart de ces analogues délétés (Fig.5-Chap.3.1.2, Fig.2-Chap.3.2.2). Ceci a été également observé avec la MCa native et ses analogues non délétés (*16*, *278*). I apparaît donc qu'en règle générale, les CPPs pénètrent dans la cellule de façon concomitante par la translocation directe et par l'endocytose. Il semble que tout peptide qui se fixe sur la surface cellulaire à travers, notamment, des interactions avec les protéoglycanes ou les phospholipides, entre dans le processus d'internalisation par endocytose. Si en plus, le peptide est un CPP, il s'engage également dans un processus d'internalisation par la translocation directe. L'aboutissement de chaque processus, et donc sa contribution dans l'internalisation du peptide, dépendrait des propriétés intrinsèques du CPP et des conditions expérimentales.

Parmi les propriétés intrinsèques du CPP, figurerait la taille de la chaîne peptidique. Les CPPs courts entreraient plus facilement par la translocation directe, et par conséquent auraient les

meilleures performances en pénétration cellulaire que les CPPs longs. Cela expliquerait les meilleures performances des analogues de la MCa délétés comparativement à la MCa linéaire non délétée (MCa_{UF1-33}) (Fig.2.B & C-Chap.3.1.2). Par ailleurs, une étude antérieure avait montré une meilleure efficacité de la MCa native comparativement à la MCa linéaire non délétée (*18*). Cela s'expliquerait, du moins partiellement, par le repliement de la MCa native qui la rend plus compacte (donc plus courte) que la MCa linéaire non délétée. Ceci suggère que le repliement des analogues de la MCa délétés pourrait améliorer leur efficacité de pénétration cellulaire.

Pour les conditions expérimentales, on note notamment, l'impact du type cellulaire. Par exemple, les présents travaux ont montré que la MCa_{UF1-9}-Cy5 pénètre dans les cellules CHO par une voie complètement indépendante de la macropinocyotose (Fig.5-Chap.3.1.2); et dans les cellules F98, la macropinocytose contribue à sa pénétration à hauteur d'environ 25 % (Fig.2-Chap.3.2.2).

La $MCa_{UF1-9,}$ mais également la $MCa_{UF11-33}$ et l' Had_{UF3-11} ont montré la propriété de persistance intracellulaire. Au bout de 34 heures, plus de 20 % de leur quantité initialement internalisée sont toujours observés dans les cellules F98 (Fig.5.C&D-Chap.3.2.2). Il serait intéressant d'évaluer cette propriété également chez les autres analogues délétés, notamment ceux les plus prometteurs, notamment la $MCa_{UF14-25}$, la $MCa_{UF18-33}$, et la MCa_{UF1-20}. Cette propriété de persistance intracellulaire pourrait être exploitée pour la rétention intracellulaire des médicaments dans les cellules qui ont développé une résistance par le rejet de médicaments. Cette propriété a déjà été démontrée avec les analogues non délétés de la MCa qui, couplés à des anticancéreux, ont permis leur rétention dans des cellules cancéreuses résistantes et de vaincre la résistance (*61, 299*). Par ailleurs, nos résultats montrent une accumulation intracellulaire sans saturation des analogues délétés de la MCa (Fig.6-Chap.3.1.2). Cela suggère que des molécules thérapeutiques transportées par ces analogues pourraient s'accumuler dans la cellule jusqu'à atteindre des concentrations nécessaires pour leur efficacité.

Cependant, les résultats obtenus *in vitro* (ou *in situ*) ne sont pas directement transposables *in vivo*. L'utilisation *in vivo* nécessiterait d'autres optimisations.

L'un des problèmes qui se poseraient *in vivo* est la stabilité des CPPs. *In vivo* les CPPs seraient plus en contact avec les enzymes et peuvent donc être plus facilement digérés, ce qui limiterait leur durée de circulation dans l'organisme. Dans les travaux antérieurs, il a été

conçu un analogue de la MCa, la D-MCa totalement insensible à la digestion enzymatique (*16*). L'analogue est composé d'acides aminés énantiomères D, méconnus par les organismes vivants; les organismes vivants ne contiennent et ne reconnaissent naturellement que des acides aminés énantiomères L. De la même manière, il serait intéressant de concevoir des isomères D des analogues de la MCa délétés pour optimiser leur stabilité *in vivo*.

Un autre problème pouvant être rencontré spécialement pour des applications de délivrance de médicaments dans les cellules cérébrales, notamment les cellules gliales, est la difficulté de franchir la barrière hémato-encéphalique (BHE). La BHE est le principal obstacle au développement de médicaments agissant sur le cerveau. En effet, la plupart de molécules sont incapables de traverser cette barrière et accéder au cerveau. L'utilisation des QDs pourrait permettre au complexe CPP-médicament de traverser la BHE. Il a été montré que les QDs fonctionnalisés par la transferrine traversent la BHE par le mécanisme de transcytose après s'être liés aux récepteurs de la transferrine abondamment présents à la surface des cellules endothéliales de la BHE (*300*). Le complexe CPP-médicament serait greffé, de préférence par pont disulfure, au QD fonctionnalisé par la transferrine. Le QD transporterait le CPP-cargaison à travers la BHE, et ensuite, grâce au CPP tout le complexe (QD-CPP-médicament) pénétrerait dans les cellules gliales. Dans les cellules gliales, l'environnement réducteur du cytosol romprait le pont disulfure, dissociant ainsi le QD et le complexe CPP-médicament. Ceci préviendrait l'encombrement stérique par le QD qui pourrait gêner l'activité du médicament.

5. CONCLUSION GENERALE

La MCa est une toxine issue du venin de scorpion, dotée d'excellentes propriétés de pénétration cellulaire. Pour son utilisation en qualité de vecteur, surtout *in vivo*, la MCa a subi des optimisations. Pour ce faire, l'activité pharmacologique et les ponts disulfures du peptide ont été supprimés au cours des travaux antérieurs à notre thèse. Au cours de notre thèse, nous avons d'une part, poursuivi les optimisations en réduisant la taille du peptide, et d'autre part, dans le cadre du développement des applications, nous avons démontré l'efficacité d'un CPP analogue de la MCa à délivrer des nanobiodétecteurs dans les cellules.

Douze nouveaux CPPs, analogues de la MCa de courte taille ont été obtenus. Ils ont tous manifesté d'excellentes propriétés de pénétration cellulaire. En plus, ils ont une faible

cytotoxicité; ils pénètrent dans la cellule essentiellement par une voie indépendante de la macropinocytose, vraisemblablement la translocation directe; ils sont pharmacologiquement inertes. Ils pourraient servir pour différentes applications selon des besoins spécifiques.

Parmi les douze analogues, la MCa_{UF1-9} présente de meilleures perspectives d'avenir. Elle est la plus efficace à de faibles concentrations extracellulaires; elle a la taille la plus courte. Par ailleurs, elle est plus efficace que les CPPs usuels, la Tat, la pénétratine, et la polyarginine. En plus, sa pénétration cellulaire est meilleure en milieu acide; de ce fait, elle pourrait être utilisée pour un ciblage des cellules cancéreuses, notamment celles des gliomas, qui évoluent dans un environnement acide. La MCa_{UF1-9} a également montré une longue persistance intracellulaire qui pourrait être exploitée pour la rétention des médicaments dans les cellules qui ont développé une résistance par rejet de médicaments.

Les domaines hydrophobes des autres peptides de la famille des calcines se sont également révélés d'excellents CPPs. Parmi eux, l'Had_{UF1-11} s'est avéré le plus efficace; meilleur que la $MCa_{UF1-9.}$ Cependant, sa supériorité devrait être confirmée ou infirmée par une caractérisation approfondie prenant en compte différents critères d'évaluation des CPPs, notamment le mode de pénétration cellulaire et la cytotoxicité.
Compte tenu de son excellente efficacité, l'Had_{UF1-11} a été utilisé dans l'application de vectorisation des nanobiodétecteurs du Ca^{2+} cytosolique. L'Had_{UF1-11} a efficacement délivré les nanobiodétecteurs dans les cellules, et les nanobiodétecteurs délivrés ont montré l'efficacité de visualiser les nanodomaines du Ca^{2+} cytosolique.

Globalement, les peptides de la famille des calcines apparaissent spécialisés pour la pénétration cellulaire ; ils constituent une source quasi inépuisable de CPPs. Cela a particulièrement été démontré par la MCa qui, ayant la propriété de pénétration cellulaire distribuée tout le long de sa séquence, a généré plusieurs CPPs par délétion. Les analogues de la MCa (tous les CPPs de la famille des calcines) promettent un bon avenir. En effet, beaucoup de phénomènes intracellulaires restent à être élucidés, et ceux qui l'ont déjà été montrent la possibilité du développement des stratégies thérapeutiques ou diagnostiques ayant des cibles intracellulaires. L'étude de ces phénomènes et le développement de ces stratégies auront besoin des CPPs pour accéder au milieu intracellulaire. Les CPPs analogues de la MCa qui à ce jour apparaissent les plus efficaces, seront sans doute les mieux indiqués pour les différentes applications.

ANNEXE

En plus des travaux sur la MCa, j'ai été également impliqué dans les travaux sur la sous-unité β4 du canal calcique qui ont abouti à la présente publication.

The EMBO Journal (2012) 31, 3730–3744 | © 2012 European Molecular Biology Organization | All Rights Reserved 0261-4189/12
www.embojournal.org

THE EMBO JOURNAL

Cacnb4 directly couples electrical activity to gene expression, a process defective in juvenile epilepsy

Abir Tadmouri[1,10], Shigeki Kiyonaka[2,10], Maud Barbado[1,3,10], Matthieu Rousset[4,5,10], Katell Fablet[1,10], Seishiro Sawamura[2], Eloi Bahembera[1,3], Karin Pernet-Gallay[1], Christophe Arnoult[1], Takafumi Miki[2], Karin Sadoul[6], Sylvie Gory-Faure[1], Caroline Lambrecht[7], Florian Lesage[3,8], Satoshi Akiyama[2], Saadi Khochbin[6], Sylvain Baulande[9], Veerle Janssens[7], Annie Andrieux[1], Ricardo Dolmetsch[4], Michel Ronjat[1,3,*], Yasuo Mori[2] and Michel De Waard[1,3,*]

[1]Unité Inserm U836, Grenoble Institute of Neuroscience, Université Joseph Fourier, La Tronche, France, [2]Laboratory of Molecular Biology, Department of Synthetic Chemistry and Biological Chemistry, Graduate School of Engineering, Kyoto University, Kyoto, Japan, [3]LabEx ICST 'Ion Channel Science and Therapeutics', Nice, France, [4]Department of Neurobiology, Stanford University School of Medicine, Stanford, CA, USA, [5]CRBM, CNRS UMR5237, Montpellier, France, [6]Inserm U823, Institut Albert Bonniot, Grenoble, France, [7]Laboratory of Protein Phosphorylation and Proteomics, University of Leuven, Leuven, Belgium, [8]Institut de Pharmacologie Moléculaire et Cellulaire, CNRS UMR 7275, Sophia Antipolis, Valbonne, France and [9]PartnerChip, Bat. G2, Evry, France

Calcium current through voltage-gated calcium channels (VGCC) controls gene expression. Here, we describe a novel signalling pathway in which the VGCC Cacnb4 subunit directly couples neuronal excitability to transcription. Electrical activity induces Cacnb4 association to Ppp2r5d, a regulatory subunit of PP2A phosphatase, followed by (i) nuclear translocation of Cacnb4/Ppp2r5d/PP2A, (ii) association with the tyrosine hydroxylase (TH) gene promoter through the nuclear transcription factor thyroid hormone receptor alpha (TRα), and (iii) histone binding through association of Cacnb4 with HP1γ concomitantly with Ser[10] histone H3 dephosphorylation by PP2A. This signalling cascade leads to TH gene repression by Cacnb4 and is controlled by the state of interaction between the SH3 and guanylate kinase (GK) modules of Cacnb4. The human R482X CACNB4 mutation, responsible for a form of juvenile myoclonic epilepsy, prevents association with Ppp2r5 and nuclear targeting of the complex by altering Cacnb4 conformation. These findings demonstrate that an intact VGCC subunit acts as a repressor recruiting platform to control neuronal gene expression.

The EMBO Journal (2012) **31**, 3730–3744. doi:10.1038/emboj.2012.226; Published online 14 August 2012

*Corresponding authors. M Ronjat or M De Waard, Unité Inserm U836, Grenoble Institute of Neuroscience, Université Joseph Fourier, Site Santé, La Tronche 38700, France. Tel.: +33 4 56 52 05 63; Fax: +33 4 56 52 06 37; E-mail: michel.ronjat@ujf-grenoble.fr or Tel.: +33 4 56 52 05 65; Fax: +33 4 56 52 06 37; E-mail: michel.dewaard@ujf-grenoble.fr
[10]These authors contributed equally to this work

Received: 21 December 2011; accepted: 17 July 2012; published online: 14 August 2012

Subject Categories: signal transduction; chromatin & transcription; neuroscience
Keywords: β_4 subunit; gene regulation; HP1γ; phosphatase 2A; thyroid receptor alpha

Introduction

Voltage-gated calcium channels (VGCC) are heteromultimeric complexes that translate electric signals into calcium influx (Catterall *et al*, 2005), thereby controlling synaptic vesicle exocytosis, neuronal excitability and gene expression (Deisseroth *et al*, 2003; Flavell and Greenberg, 2008; Greer and Greenberg, 2008). In VGCC, the pore-forming subunit is associated to auxiliary subunits, among which the cytoplasmic Cacnb4 (β_4) plays an essential function in channel expression level at the plasma membrane and biophysical properties (Arikkath and Campbell, 2003). Mutations in the genes encoding VGCC induce diverse neuronal pathologies, such as epilepsy, ataxia, autism and migraine (Bidaud *et al*, 2006). In humans, a mutation of *CACNB4*, leading to a 38 amino acid truncation of β_4 C-terminus, has been associated to juvenile myoclonic epilepsy (Escayg *et al*, 2000). In mice, a four-nucleotide insertion into a splice donor site of *Cacnb4* results in a truncation of 60% of the protein sequence and a *lethargic* (*lh*) phenotype (Burgess *et al*, 1997). How these mutations may affect VGCC-mediated function still remains an open question. Calcium entering through VGCC has been implicated in gene regulation by activating calcium-binding proteins that propagate the signal to the nucleus (Rosen *et al*, 1994; Graef *et al*, 1999; Dolmetsch *et al*, 2001; Oliveria *et al*, 2007) or by diffusing to the nucleus with or without signal amplification by intracellular stores (Hardingham *et al*, 1997; Carrion *et al*, 1999; Hardingham *et al*, 2001). Evidence for alternative pathways have been reported. First, an atypical short β_4 splice variant, β_{4c}, was shown to interact with heterochromatin protein 1 gamma (HP1γ), a nuclear protein involved in gene silencing and transcription regulation (Hibino *et al*, 2003; Xu *et al*, 2011). However, β_{4c} lacks the domain required for association with the pore subunit (Chen *et al*, 2004) and therefore cannot couple neuronal activity to gene regulation. A second pathway implicates CCAT, a C-terminal fragment of Cacna1c VGCC, as a calcium-regulated transcription factor (Gomez-Ospina *et al*, 2006). In this case, calcium influx triggers CCAT nuclear export providing a calcium-dependent link between neuronal activity and transcription. The origin of this fragment (channel proteolysis or alternative splicing) remains unknown.

Here, we show that β_4 directly couples neuronal excitability to gene expression along a signalling pathway that is disrupted by the human R482X mutation. We found that electrical activity promotes the formation of a new nuclear complex in which β_4 plays the role of an organizing platform that brings together a transcription factor for DNA binding, a phosphatase for

histone dephosphorylation and HP1γ for nucleosome association. Formation of this complex controls gene activity as witnessed by the case of tyrosine hydroxylase (TH) gene.

Results

β_4 nuclear localization

β_4 is highly expressed in the hippocampal dentate gyrus of adult wild-type (wt) C57Bl/6 mice brain but not in *lh* mice brain (Figure 1A). β_4 labelling is strongest in soma and coincides with NeuN nuclear labelling, suggesting that a fraction of β_4 protein may be localized in cell nuclei, in agreement with previous observations (Subramanyam *et al*, 2009). Western blot analyses of wt brain lysates show a unique 58 kDa band, corresponding to β_4, absent in *lh* (Figure 1B). Western blot analyses of cytoplasmic versus nuclear fractions of wt brain lysates show the presence of β_4 in the nucleus (Figure 1C). Electron microscopy (EM)

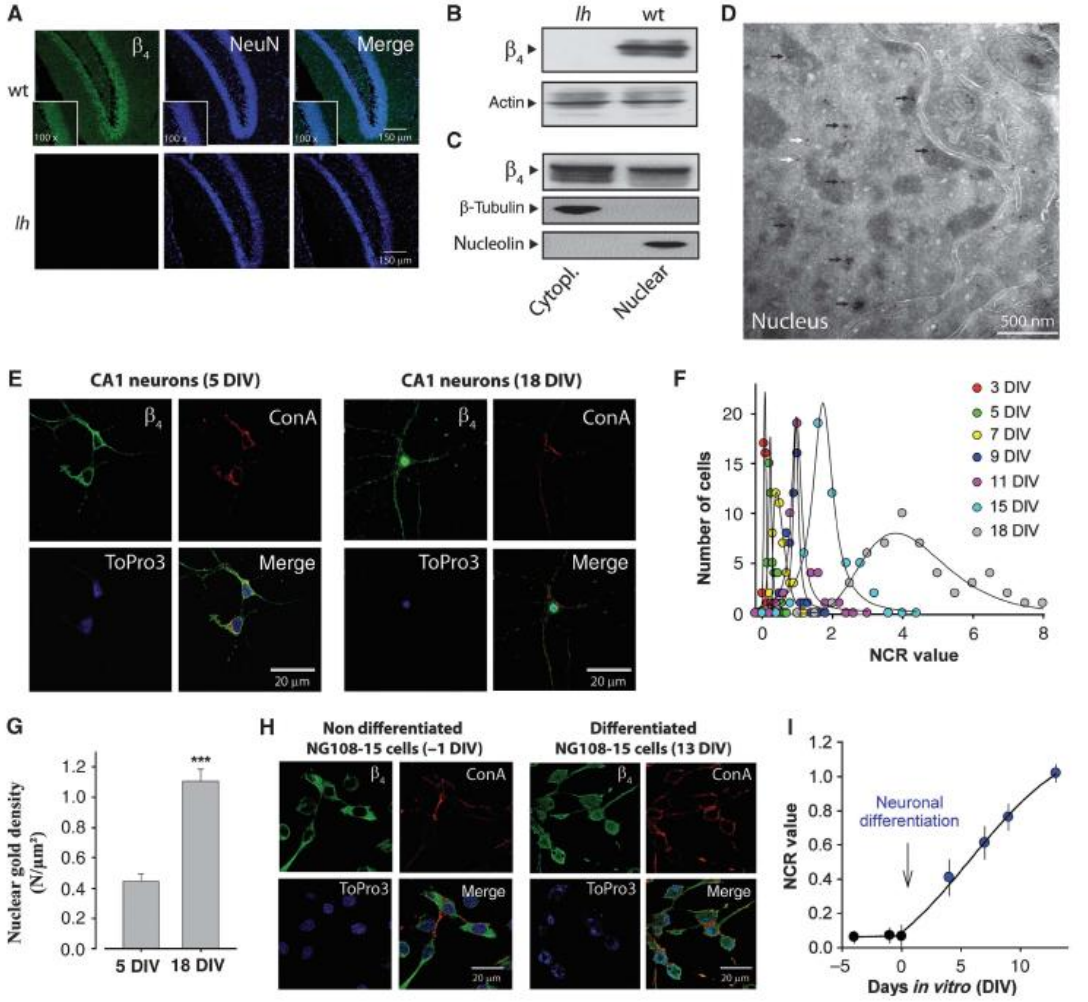

Figure 1 Presence of β_4 in the nucleus of neurons. (**A**) Immunohistochemical confocal images of 20 µm coronal sections of adult wt (upper panels) or *lh* (lower panels) mice brains showing the distribution of endogenous β_4 in the dentate gyrus (green, left panels). Neuronal nuclei were labelled with NeuN (blue, middle panels). Right panels illustrate merged images. The inserts show × 5 images of the CA3 region (initially × 20). (**B**) Western blots of adult wt and *lh* mice brain lysates indicating the presence of β_4 only in wt mice. Actin staining was used as an internal control. (**C**) β_4 immunoblotting from cytoplasmic and nuclear fractions of adult wt mice brain. β-Tubulin and nucleolin are used as indicators of nuclear and cytoplasmic fraction purities, respectively. (**D**) EM image of an ultrathin cryosection of the CA1 hippocampal region showing the intranuclear presence of β_4 labelled with antibody-coated 15 nm gold particles. Black and white arrows indicate the position of gold particles associated to heterochromatin and euchromatin, respectively. (**E**) Confocal images of hippocampal neurons from embryonic E18 mice brains in primary culture at 5 DIV (left panels) and 18 DIV (right panels). Green: immunocytochemical staining of β_4; red: membrane staining with concanavalin A (ConA) conjugated to rhodamine; blue: nuclear staining with ToPro3. (**F**) DIV-dependent evolution of β_4 NCR values in neurons ($n = 50$ cells for each data point). (**G**) Nuclear density of β_4 in hippocampal neurons at 5 and 18 DIV as assessed by EM ($n = 28$ and 20 nuclei, respectively). (**H**) Confocal images of NG108.15 cells 1 day before (−1 DIV) and 13 days (13 DIV) after induction of neuronal differentiation with 1 mM cAMP and serum reduction. Colour code is as in (**E**). Differentiated NG108-15 cells have larger nuclei than non-differentiated cells. (**I**) Mean NCR values expressed in percent as a function of culture time *in vitro*. DIV 0 represents the induction time of neuronal differentiation.

demonstrates the presence of β_4 in the nucleus of CA1 hippocampal neurons (Figure 1D; Supplementary Figure 1). In primary cultures of hippocampal neurons, β_4 is predominantly expressed within the cytoplasm/plasma membrane at 5 DIV (Figure 1E, left panels). In contrast, the protein is densely located in the nucleus at 18 DIV (Figure 1E, right panels). The nuclear to cytoplasmic density ratios (NCR values) of β_4 increase as a function of time from 0.07 (3 DIV) to 3.81 (18 DIV) on average indicating the differentiation-dependent progressive targeting of β_4 to neuronal nuclei (Figure 1F). NCR value increase is accompanied by a histogram broadening witnessing higher β_4 subcellular distribution variability among neurons. β_4 nuclear appearance coincides with that of VGCC currents and electrical activity at 5 DIV (unpublished observation). EM analysis of hippocampal neurons at 5 and 18 DIV also illustrate the increase of β_4 nuclear density at 18 DIV (Figure 1G). Synchronized neuronal differentiation of NG108-15 cells, induced by serum deprivation and 1 mM cAMP, is accompanied by VGCC expression (Chemin *et al*, 2002). In undifferentiated NG108.15 cells, β_4 is exclusively cytoplasmic, while present in nuclei after 13 days of differentiation (Figure 1H). Mean NCR values illustrate that nuclear β_4 expression is triggered by neuronal differentiation (Figure 1I).

β_4 epilepsy mutation alters nuclear targeting

To search for a β_4 nuclear targeting domain, truncated β_4-EGFP constructs were expressed in CHO cells (Figure 2A). In CHO and HEK293 cells, β_4-EGFP spontaneously locates in the nucleus (NCR = 10.1 ± 3.3 for CHO cells). In contrast,

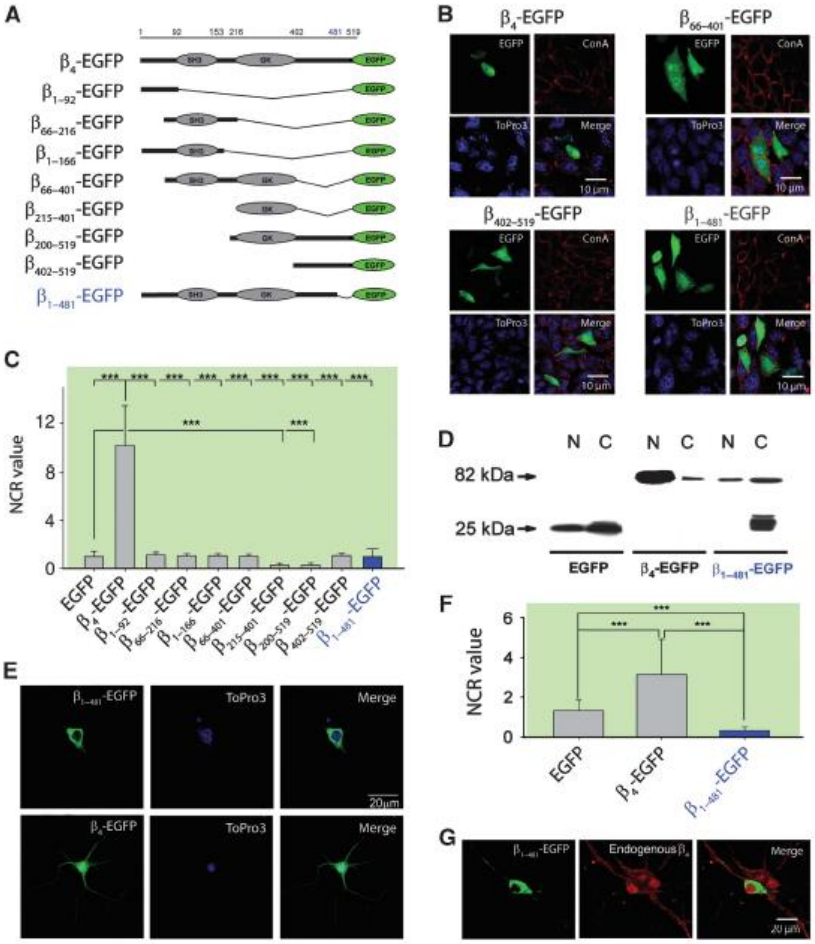

Figure 2 Nuclear targeting and structural integrity of β_4 are disrupted by the human juvenile epilepsy mutation. (**A**) Schematic representation of different truncated β_4 constructs in pEGFP-C1. The β_{1-481}-EGFP mutant is also shown. (**B**) Confocal images of CHO cells expressing some representative constructs, including β_4-EGFP and mutant β_{1-481}-EGFP. Expression time is 24 h after transfection. (**C**) Mean NCR values of EGFP fluorescence for each condition in transfected CHO cells. ***$P \leqslant 0.01$. (**D**) Western blot detecting EGFP in nuclear and cytoplasmic fractions of CHO cells after 2 days of transfection with EGFP, β_4-EGFP or β_{1-481}-EGFP. Cytoplasmic β_{1-481}-EGFP is less stable than cytoplasmic β_4-EGFP, as witnessed by the presence of lower molecular weight bands. These truncated constructs are deficient in nuclear accumulation as shown in (**C**), possibly because containing GK domains. (**E**) Confocal images of hippocampal neurones transfected at 7 DIV with β_{1-481}-EGFP (upper panels) or β_4-EGFP (lower panels). Images were acquired at 9 DIV on β-tubulin III-positive cells. (**F**) NCR values for each construct. ***$P \leqslant 0.01$. (**G**) Confocal images of hippocampal neurons transfected with β_{1-481}-EGFP showing the comparative distribution of endogenous β_4 (red) and exogenous β_{1-481}-EGFP (green).

truncated constructs are deficient in nuclear targeting suggesting that β_4 has no nuclear localization sequence (NLS) or that the NLS depends on β_4 structure integrity (Figure 2B and C). Indeed, five constructs display a distribution similar to EGFP alone (NCR ~1). Two constructs, that contain β_4 guanylate kinase (GK) domain, show preferential cytoplasm distribution (NCR = 0.27 ± 0.2 and 0.26 ± 0.2 for $\beta_{216-402}$-EGFP and $\beta_{216-519}$-EGFP, respectively). β_4-EGFP truncation therefore results in 10- to 40-fold decrease of nuclear targeting efficiency. These data were confirmed for two truncated β_4 constructs by western blot analyses of nuclear and cytoplasmic fractions of transfected HEK293 cells (Supplementary Figure 2a). An earlier report mentioned the importance of a restricted N-terminal domain for β_4 nuclear accumulation (Subramanyam *et al*, 2009). As observed in this study, mutation of this domain significantly reduced nuclear accumulation albeit by a limited extent (by 1.41-fold, from a mean NCR value of 11.4 ± 0.7 to 8.1 ± 0.7). However, $\beta_{R28A-R29A-S30A}$-EGFP still significantly accumulates into the nucleus in contrast to the constructs presented in this manuscript.

We engineered a β_{1-481}-EGFP mutant (Figure 2A) corresponding to the human juvenile myoclonic epilepsy mutation (Escayg *et al*, 2000) and assessed its cellular distribution in CHO cells (Figure 2B and C). Nuclear accumulation of β_{1-481}-EGFP mutant is strongly reduced (NCR = 0.98 ± 0.62; 10.3-fold lower than β_4-EGFP NCR). This mutation induces a loss in nuclear targeting as shown by western blot analyses of nuclear and cytoplasmic fractions of CHO cells (Figure 2D). Finally, β_{1-481}-EGFP mutant is completely excluded from hippocampal neuron nuclei at 7 DIV (NCR = 0.32 ± 0.18; Figure 2E and F). This corresponds to a 9.5-fold decrease in NCR value compared to β_4-EGFP (3.15 ± 1.76), a reduction similar to that measured in CHO cells. Double imaging of immunolabelled endogenous β_4 and β_{1-481}-EGFP indicates the extent of nuclear exclusion of the mutant (Figure 2G). In conclusion, the nuclear targeting of β_4 requires the preservation of its structural integrity. The human epilepsy mutation alters this structural integrity and hinders nuclear targeting.

The SH3/GK interaction controls β_4 nuclear targeting

Interaction between β SH3 and GK domains regulates channel activity (McGee *et al*, 2004; Takahashi *et al*, 2005). Its role was therefore investigated on β_4 nuclear targeting. Three constructs were designed: β_{1-166}-EGFP, $\beta_{200-519}$-myc and $\beta_{200-481}$-myc (corresponding to the juvenile epilepsy deletion) (Figure 3A). In agreement with Figure 2C, none of these constructs show a specific nuclear targeting in CHO cells (Figure 3B). Expressed together, β_{1-166}-EGFP and $\beta_{200-519}$-myc reconstitute a nuclear-targeting-competent complex (Figure 3C; NCR = 6.9 ± 1.6 for β_{1-166}-EGFP and 7.1 ± 1.1 for $\beta_{200-519}$-myc). In contrast, expression of β_{1-166}-EGFP with $\beta_{200-481}$-myc fails to form a nuclear complex (Figure 3C, right panels). Co-immunoprecipitation experiments show that $\beta_{200-481}$-myc no longer interacts with β_{1-166}-EGFP contrary to $\beta_{200-519}$-myc (Figure 3D). These data suggest that the human mutation prevents β_4 nuclear targeting by modulating the SH3/GK interaction. This issue was further addressed by investigating the effect of two mutations (SH3 L125P or GK P225R) known to disrupt the SH3/GK interaction (McGee *et al*, 2004; Takahashi *et al*, 2004; Figure 3E). As shown, $\beta_{1-166\text{-}L125P}$-EGFP no longer interacts with $\beta_{200-519}$-myc (Figure 3F). Also, both β_{L125P}-EGFP and β_{P225R}-EGFP are completely excluded from hippocampal neuron nuclei (Figure 3G). NCR values, 0.43 ± 0.15 (L125P) and 0.43 ± 0.11 (P225R), correspond to a 7.3-fold decrease in mutant β_4 nuclear localization (Figure 3H). These results demonstrate that β_4 nuclear targeting requires the internal SH3/GK and reveal a previously unrecognized structural role of the last C-terminal 38 amino-acid sequence in modulating the interaction between the C-terminal containing hemi-β_4 subunit and the SH3-containing β_4 fragment.

The phosphatase 2A Ppp2r5d (B56δ) subunit contributes to β_4 nuclear localization

Absence of a clear molecular determinant for β_4 nuclear targeting suggests that this process requires at least one protein partner, whereas defective β_{1-481}, β_{L125P} and β_{P225R} nuclear localization indicates that interaction with this (these) partners depends on SH3/GK interaction state. Yeast two-hybrid screenings were performed with a mouse brain complementary DNA library using β_4 as bait. The 62 positive clones were subjected to two-hybrid β-galactosidase assays using β_4 and β_{1-481} as baits. B56δ, a 594 amino-acid protein containing a poorly defined NLS at its C-terminus, was revealed to interact with β_4 but not with β_{1-481} (Figure 4A). B56δ is one of the two regulatory subunits of phosphatase 2A (PP2A), along with B56γ, known to target PP2A to the nucleus (McCright *et al*, 1996). Co-immunoprecipitation confirms that β_4-EGFP, but not β_{1-481}-EGFP, interacts with B56δ-myc expressed in HEK293 cells (Figure 4B). As expected, Cacna1e and RIM1 were also identified as β_4 partners (Kiyonaka *et al*, 2007). In contrast to B56δ, both proteins interact equally well with β_4 and β_{1-481}. These yeast two-hybrid assays also reveal that Cacnb3 (β_3), another β isoform, also interacts with B56δ suggesting the existence of redundant signalling pathways (Figure 4C). β_{4c}, a short β_4 splice variant, known to interact with the HP1γ chromo shadow domain (Hibino *et al*, 2003), does not interact with B56δ. Conversely, β_4 does not interact with HP1γ in these conditions (Figure 4C). Truncated β_4 constructs were analysed for B56δ interaction by yeast two-hybrid assays (Figure 4D). β_{49-519} is the only truncated construct interacting with B56δ indicating that the N-terminus is not essential for this interaction. B56δ does not interact with β_{L125P} confirming that binding to β_4 requires an intact SH3/GK interaction (Figure 4D). Endogenous B56δ is expressed in both HEK293 and CHO cells in agreement with spontaneous nuclear targeting of β_4 (Supplementary Figure 3a and b). Exogenous B56δ-myc co-localizes with nuclear β_4-EGFP and further increases β_4-EGFP nuclear targeting in CHO cells (Supplementary Figure 3c). Conversely, expression of a B56δ shRNA, reducing the level of endogenous B56δ in CHO cells (Supplementary Figure 3b), leads to a reduction of β_4-EGFP nuclear targeting (NCR value dropping from 11.5 ± 0.7 to 7.3 ± 0.5 or average 4.3-fold redistribution between nuclear and cytoplasmic pools by WB) (Figure 4E and F). In agreement with binding data, B56δ-myc expression has no effect on β_{1-481}-EGFP distribution in CHO cells (Supplementary Figure 3d). Expression of B56δ-myc in non-differentiated NG108-15 cells produces a marked nuclear re-localization of endogenous β_4 (Figure 4G; 11.8-fold increase in NCR). The influence of B56δ on endogenous β_4 nuclear localization was further

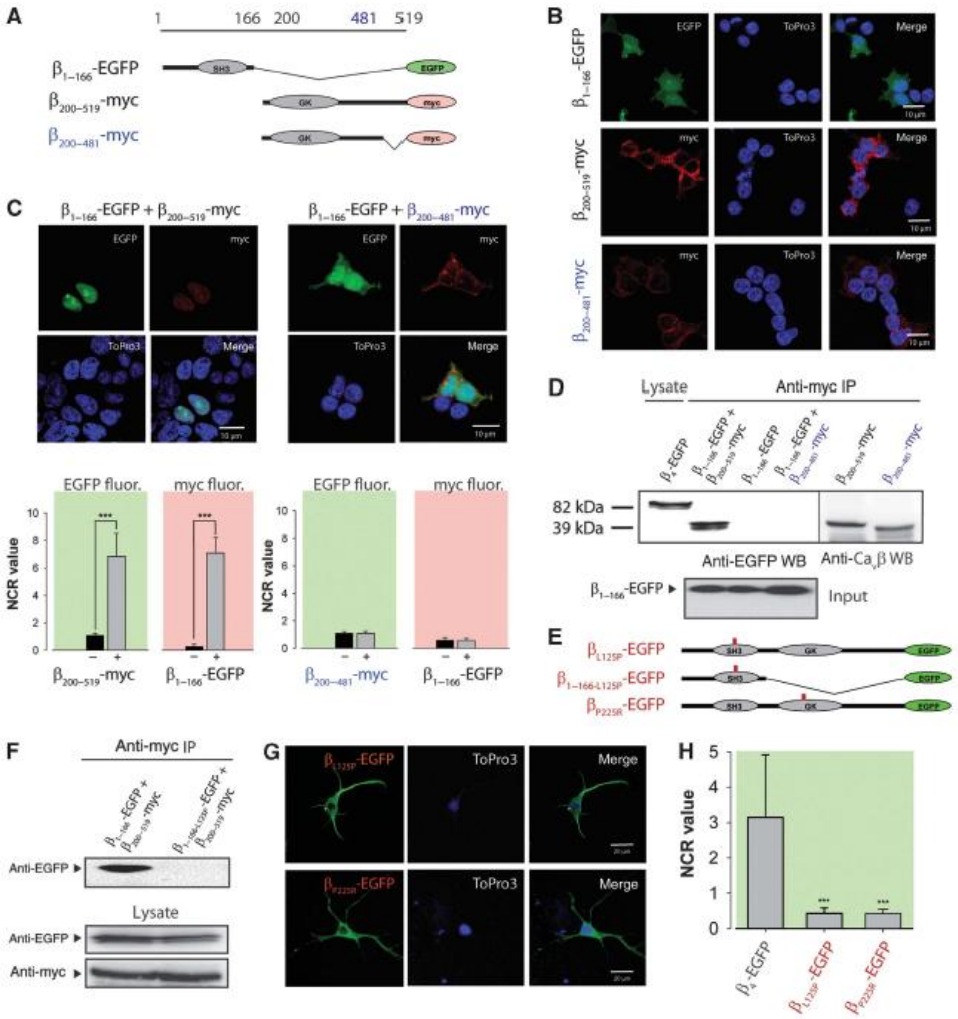

Figure 3 The SH3/GK interaction is required for β_4 nuclear localization. (**A**) EGFP- or myc-tagged β_4-truncated constructs used for confocal microscopy and co-immunoprecipitation experiments. (**B**) Confocal images of CHO cells transfected with individual constructs. (**C**) Confocal images of CHO cells expressing β_{1-166}-EGFP with $\beta_{200-519}$-myc, or β_{1-166}-EGFP with $\beta_{200-481}$-myc (upper panels). Mean NCR values of EGFP or anti-myc fluorescence summarizing the effect of the co-expressions on nuclear localization (lower panels). $***P \leqslant 0.001$. (**D**) Immunoprecipitation experiments in CHO cells investigating the association of β_{1-166}-EGFP with $\beta_{200-519}$-myc or $\beta_{200-481}$-myc. Left panel: immunoprecipitation via anti-myc antibodies and western blot of EGFP, except first lane showing β_4-EGFP expression level in cell lysates. Right panel: western blot with polyclonal anti-β antibody (Bichet *et al*, 2000) indicating equivalent $\beta_{200-519}$-myc and $\beta_{200-481}$-myc immunoprecipitation levels. β_{1-166}-EGFP expression confirmed by cell EGFP fluorescence. (**E**) Schematic representation of β_{L125P}-EGFP, $\beta_{1-166\text{-}L125P}$-EGFP and β_{P225R}-EGFP mutants. (**F**) Lack of co-immunoprecipitation shows the absence of $\beta_{200-519}$-myc/$\beta_{1-166\text{-}L125P}$-EGFP interaction. Expression of β_{1-166}-EGFP and $\beta_{200-519}$-myc was verified by the cell fluorescence and western blot as in (**D**). (**G**) Confocal images of hippocampal neurons showing the cytoplasmic localization of β_{L125P}-EGFP and β_{P225R}-EGFP. Cells were transfected for 48 h at 6 DIV. (**H**) Mean NCR values for β_4-EGFP, β_{L125P}-EGFP and β_{P225R}-EGFP fluorescence in hippocampal neurons. $***P \leqslant 0.001$.

investigated using B56δ$^{-/-}$ mice (Louis *et al*, 2011). Hippocampal neurons from B56δ$^{-/-}$ mice show a significant 1.65-fold decrease in NCR value at 11 DIV (Figure 4H). Similarly, the density of immunogold-labelled endogenous β_4 is significantly decreased by 1.61-fold in B56δ$^{-/-}$ adult hippocampal neurons compared to wt hippocampal neurons (Figure 4I). In conclusion, B56δ is an SH3/GK conformation-sensitive β_4 partner that contributes to nuclear distribution of β_4. Since a fraction of β_4 is still nuclear in the absence B56δ, we conclude that other B56 isoforms and/or nuclear partners also help β_4 accumulation in neuronal nuclei. β_{1-481}-deficient nuclear targeting originates from its inability to interact with B56δ.

β_4 forms a complex with B56δ and active PP2A

Immunoprecipitation of endogenous β_4 from wt mice brain results in co-precipitation of B56δ and PP2A (Figure 5A). As expected, neither B56δ nor PP2A are immunoprecipitated

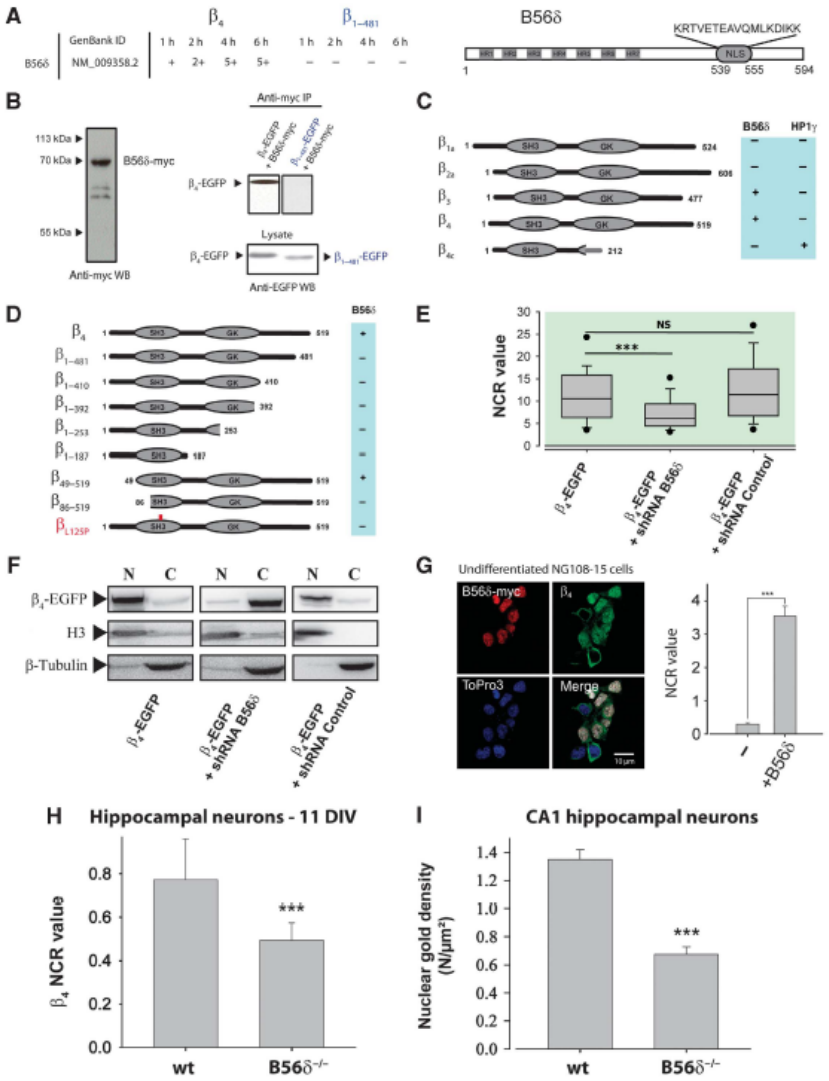

Figure 4 B56δ/β_4 interaction contributes to β_4 nuclear localization. (**A**) Yeast two-hybrid results indicating the interaction level of β_4 and β_{1-481} with B56δ as a function of time (left). The interactions were scored as the ratio of β-galactosidase activity to His prototrophy. Schematic representation of mouse B56δ showing the NLS amino-acid sequence (right). The position of seven HEAT repeats is shown by homology with B56γ (Magnusdottir *et al*, 2009). (**B**) Co-immunoprecipitation experiments determining the interaction between β_4-EGFP or β_{1-481}-EGFP with B56δ-myc in HEK293 cells. Left panel: expression of B56δ-myc was confirmed by western blot (Mr 69 kDa). Right panel: pull-down with anti-myc antibody, and western blot with anti-EGFP antibody. (**C**) Interactions of β isoforms with B56δ and HP1γ in yeast two-hybrid assay. (**D**) Interactions of truncated and mutated β_4 constructs with B56δ using yeast two-hybrid assay. (**E**) Effect of B56δ shRNA and control shRNA on the NCR value of β_4-EGFP in CHO cells. $^{***}P \leqslant 0.001$; NS, $P \geqslant 0.1$. (**F**) Effect of B56δ shRNA and control shRNA on the nuclear/cytoplasmic distribution of β_4-EGFP in CHO cells, as assessed by WB. Histone H3 and β-tubulin are used as markers of the nucleus (N) and cytoplasm (C), respectively. Performed in duplicate. Average ratios of 4.2 ± 0.32 (β_4-EGFP) and 0.97 ± 0.81 (β_4-EGFP + shRNA B56δ). (**G**) Confocal images showing the cell distribution of endogenous β_4 in undifferentiated NG108.15 cells in the absence or presence of B56δ-myc (left panels). B56δ-myc was transfected 24 h before confocal imaging. Panels in green present the endogenous β_4 detected with an anti-β_4. Mean NCR values showing that B56δ-myc induces the redistribution of endogenous β_4 to the nucleus (right panel). $^{***}P \leqslant 0.001$. (**H**) Mean NCR values of endogenous β_4 from wt and B56δ$^{-/-}$ hippocampal neurons at 11 DIV. $^{***}P \leqslant 0.001$. (**I**) Average immunogold-labelled endogenous β_4 in nuclei from pyramidal neurons from wt and B56δ$^{-/-}$ mice hippocampus measured by EM ($n = 36$ and 51 nuclei, respectively). $^{***}P \leqslant 0.001$. Control counts in *lh* hippocampus were 0.51 ± 0.36 gold particles/μm^2.

from *lh* mice brain by β_4 antibodies. Similarly, PP2A is not precipitated by β_4 antibodies using B56δ$^{-/-}$ mice brain indicating that PP2A/β_4 association requires B56δ. In HEK293 cells, overexpression of B56δ-EGFP with β_4-myc strongly enhances endogenous PP2A immunoprecipitation through β_4-myc (Figure 5B). Restricted immunoprecipitation of endogenous PP2A by antibodies against β_4-myc suggests that not all endogenous B56δ (Supplementary Figure 3a)

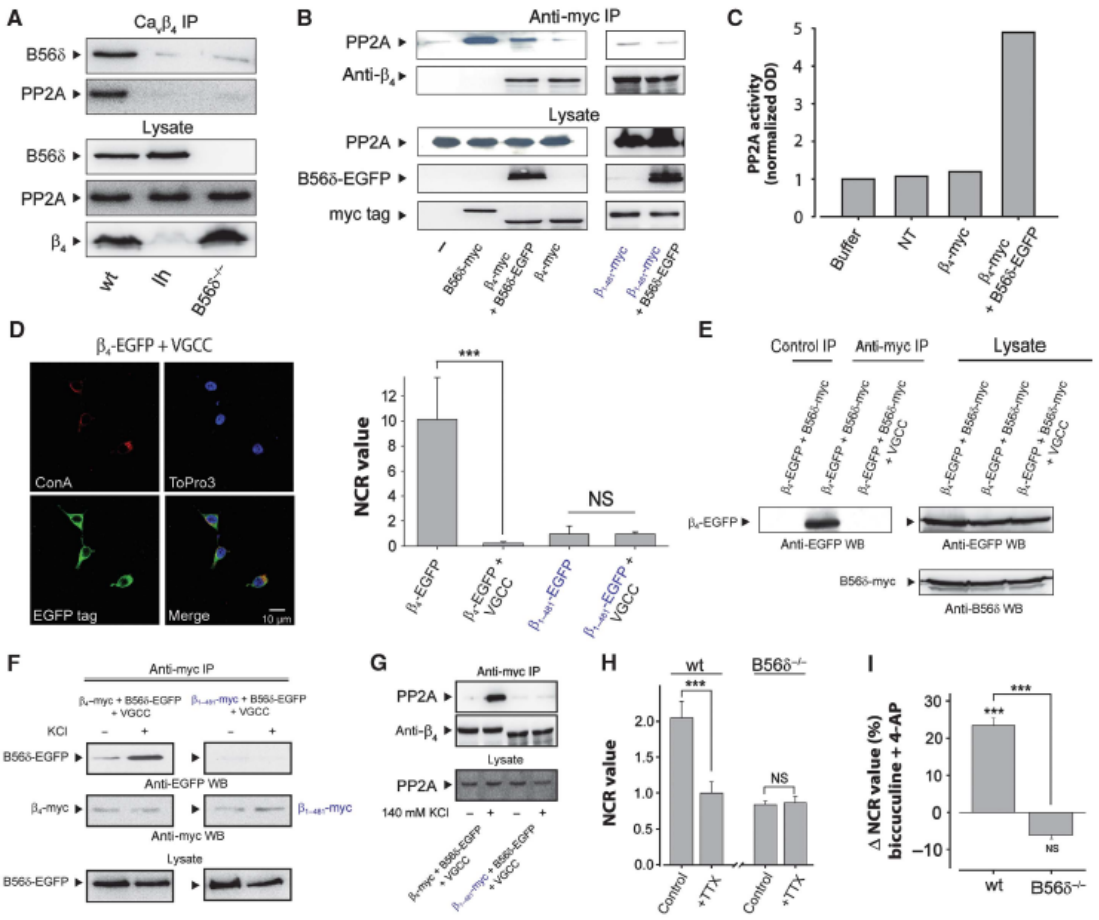

Figure 5 β$_4$ association to B56δ/PP2A is inhibited by channel expression and activated by membrane depolarization. (**A**) β$_4$ immunoprecipitates B56δ and PP2A from wt mice brain but not from *lh* or B56δ$^{-/-}$ mice as shown by western blots. (**B**) Left panel: immunoprecipitation of endogenous PP2A by B56δ-myc or β$_4$-myc ± B56δ-EGFP expressed in HEK293 cells. Right panel: similar experiments using β$_{1-481}$-myc ± B56δ-EGFP. (**C**) Endogenous PP2A phosphatase activity associated to immunoprecipitated β$_4$-myc ± B56δ-EGFP expressed in HEK293 cells. Dephosphorylation of *p*-nitrophenyl phosphate (*p*NPP), a generic phosphatase substrate, was measured by absorbance of the metabolite at 405 nm. Experiment in duplicate. (**D**) Confocal images of HEK293 cells 2 days after transfection with β$_4$-EGFP together with Cacna1a and Cacna2d2 subunits (VGCC) (left panel). Mean NCR values of EGFP fluorescence in various transfection conditions ($n = 50$ for each condition, right panel). (**E**) Western blot analysis of β$_4$-EGFP subunit immunoprecipitated by B56δ-myc ± VGCC expressed in HEK293 cells. Control IP represents precipitation in absence of anti-myc antibodies. (**F**) Western blot analysis of B56δ-EGFP immunoprecipitated by β$_4$-myc (left panels) or β$_{1-481}$-myc (right panels) expressed in HEK293 cells together with VGCC, without or with a 30-min depolarization by 140 mM KCl. (**G**) Effect of HEK293 membrane depolarization (140 mM KCl, 30 min) on β$_4$-myc or β$_{1-481}$-myc complex formation with PP2A in the presence of B56δ-EGFP and VGCC. (**H**) Mean NCR values of β$_4$ immunofluorescence in wt or B56δ$^{-/-}$ hippocampal neurons at 18 DIV (control or 1 μM TTX). TTX was added at 11 DIV in the culture media ($n = 50$ for each condition). (**I**) Effect of a 1-h application of 40 μM biccuculine and 400 μM 4-AP on average β$_4$ NCR value in wt and B56δ$^{-/-}$ hippocampal neurons. NS, non significant; ***$P < 0.001$.

is associated to PP2A in these cells, possibly due to a competition with other B regulatory isoforms unable to associate to β$_4$-myc. As expected, β$_{1-481}$-myc mutant does not precipitate endogenous PP2A in the presence of B56δ-EGFP (Figure 5B). β$_4$-myc/B56δ-EGFP complex immunoprecipitated from HEK293 cells shows PP2A phosphatase activity (Figure 5C).

Membrane depolarization triggers β$_4$ association to B56δ

β$_4$-EGFP, expressed together with Cacna1a and Cacna2d2, pore-forming and auxiliary subunits of VGCC, loses its nuclear distribution in HEK293 cells (Figure 5D, NCR = 0.25 ± 0.1, i.e., 40-fold reduction). Part of β$_4$-EGFP staining is cytoplasmic instead of at the plasma membrane, possibly by interaction with Cacna1a stuck in the endoplasmic reticulum. As expected, β$_{1-481}$-EGFP mutant distribution remains cytoplasmic in the presence of VGCC (Figure 5D, right panel). In the presence of Cacna1a and Cacna2d2, B56δ-myc no longer interacts with β$_4$-EGFP (Figure 5E). These data indicate that (i) B56δ does not form a higher order molecular complex with the channel and (ii) β$_4$ association to Cacna1a overrides its interaction with B56δ. In addition, B56δ-EGFP does not affect VGCC kinetics and current densities in HEK293 cells

(Supplementary Figure 4a and b). Also, Ca^{2+} currents were not modified in hippocampal neurons from B56δ$^{-/-}$ mice (Supplementary Figure 4c and d), confirming that B56δ does not associate to the channel complex. Previous reports evidenced that β/channel interaction is reversible (Restituito *et al*, 2001; Sandoz *et al*, 2004; Spafford *et al*, 2004), but the impact of membrane depolarization on this interaction has not been studied. Membrane depolarization of HEK293 cells enhances β_4-myc interaction with B56δ-EGFP, while it does not promote any interaction between β_{1-481}-myc and B56δ-EGFP (Figure 5F). In the presence of VGCC, the depolarization-induced B56δ-myc/β_4-EGFP interaction requires external Ca^{2+} (Supplementary Figure 5). In these conditions, β_4-myc precipitates endogenous PP2A only upon membrane depolarization (Figure 5G). In contrast, β_{1-481}-myc does not precipitate PP2A upon depolarization. Finally, blocking electrical activity of 11 DIV hippocampal neurons by 1 μM tetrodotoxin (TTX) produces a significant 2.1-fold reduction of β_4 NCR value measured at 18 DIV (Figure 5H). This TTX effect is not observed in B56δ$^{-/-}$ hippocampal neurons, demonstrating that β_4 nuclear accumulation induced by electrical activity relies on B56δ. Note the 2.45-fold reduction in NCR value between wt and B56δ$^{-/-}$ control neurons at 18 DIV in agreement with B56δ role in β_4 nuclear accumulation. Conversely, a 1-h stimulation of neuronal electric activity by a biccuculine/4-AP cocktail produces a significant 23.5 ± 1.9% increase in NCR value that is not observed in B56δ$^{-/-}$ hippocampal neurons (Figure 5I). Depolarization of the plasma membrane therefore represents an important signalling event that allows β_4/B56δ interaction and favours β_4 nuclear accumulation.

β_4 represses TH gene expression by interacting with the thyroid hormone receptor alpha

To determine whether β_4 regulates transcription of endogenous genes, we analysed a publicly available microarray data set comparing gene expression in wt and *lh* mice cerebellum (data set GSE6275 from Gene Expression Omnibus; http://www.ncbi.nlm.nih.gov/geo). A volcano plot representation of our statistical analysis identifies 56 upregulated and 38 downregulated genes (over two-fold expression change, $P<0.05$) in *lh* mice cerebellum (Supplementary Figure 6). Based on gene ontology annotations, clustering of regulated transcripts in functional groups illustrate that many encode proteins with functions related to signalling and ion transport (Supplementary Figure 6). Among these genes, those coding for TH and for BC031748 cDNA sequence are the most upregulated and downregulated, respectively (Figure 6A). The effect of β_4 on gene expression was confirmed on a set of genes by qRT–PCR experiments using purified mRNA from wt and *lh* mice cerebellum (Figure 6B). From both approaches, TH gene shows the greatest variation in expression level; an interesting observation considering its relevance in epilepsy (Hess and Wilson, 1991; Bengzon *et al*, 1999; Donato *et al*, 2006). The upregulation of TH expression in *lh* mice cerebellum indicates that β_4 acts as a repressor on this gene. Transcripts upregulation or downregulation is lost in the hippocampus and in the cortex indicating the existence of compensatory mechanisms to the lack of β_4. Interaction of β_4 with the promoter region of TH gene was investigated by chromatin immunoprecipitation (ChIP) experiments. ChIP of the TH gene promoter from hippocampal neurons in culture, using antibodies against β_4, shows specific precipitation at 18 DIV but not at 1 DIV (Figure 6C). As a control, ChIP of the 3′-UTR region of TH gene was negative at 18 DIV. Similar results were obtained for ChIP experiments of the transmembrane protein 100 gene promoter (Supplementary Figure 7), suggesting that the TH promoter is not an isolated case. In wt mice brain, β_4 antibodies immunoprecipitate 1.89 ± 0.42% of TH promoter input, corresponding to a 6.3-fold enrichment over control (Figure 6D). In contrast, no specific TH promoter immunoprecipitation is observed using *lh* mice brain (Figure 6D). β_4 antibodies also immunoprecipitate 1.37 ± 0.06% of TH promoter from B56δ$^{-/-}$ mice, indicating that β_4 association with the promoter does not necessarily require the B56δ partner (3.3-fold enrichment; Supplementary Figure 8a). Yeast two-hybrid screening, using β_4 as bait, was used to identify a transcription factor that targets β_4 to the TH gene. The thyroid hormone receptor alpha (TRα) came out as a positive candidate (Figure 6E). TRα is a nuclear receptor that contains a T3 hormone binding domain and a DNA binding domain interacting with Thyroid Receptor Elements (TRE). Interaction of TRα with β_4 was confirmed by co-immunoprecipitation experiments in HEK293 cells (Figure 6F). However, this interaction is barely detectable in wt brain lysates probably because it constitutes a minor interacting fraction of total brain β_4 (not shown). ChIP using TRα antibodies shows that TRα can interact with the TH gene promoter regardless of the presence of β_4 or B56δ (Figure 6G). Enrichments of the TH gene promoter were 4.92-, 4.77- and 4.27-fold for wt, *lh* and B56δ KO brains, respectively. This result is in agreement with the presence of putative TRE in the promoter region and in the coding sequence of the TH gene. The effect of TRα on TH gene promoter was tested using a luciferase reporter (Figure 6H). TRα has little effect on its own on the expression of luciferase, while its activation by the T3 hormone leads to a 4.4-fold repression of luciferase expression (Figure 6H). Interestingly, β_4, like T3, activates the repressing function of TRα (4.8-fold repression). The effect of β_4 on TRα activity may therefore constitute a first step of TH gene repression in agreement with the upregulation of this gene in the cerebellum in the absence of β_4.

B56δ induces the recruitment of HP1γ by β_4 and contributes to association of the signalling complex with histones

ChIP experiments using B56δ antibodies reveal the presence of B56δ within the β_4 complex associated to the promoter of the TH gene (Figure 7A). Control experiments using B56δ KO mice brain demonstrate the specificity of the signal, while the absence of TH precipitation in *lh* brain denotes a key role of β_4 in targeting B56δ to the TH promoter. The presence of PP2A in the complex associated to the TH promoter was also confirmed by using PP2A antibodies (Figure 7B). TH promoter precipitation by PP2A antibodies was diminished in *lh* brain indicating the importance of β_4 in recruiting PP2A to the TH gene (Supplementary Figure 8b). Next, we questioned the role of B56δ and PP2A in TH gene regulation. Phosphorylation of histones regulates chromatin state and gene transcription (Jenuwein and Allis, 2001). Within the nucleus of wt CA1 hippocampal neurons, 45% of β_4 gold-labelled is associated to heterochromatin (black arrows; $n = 195/440$, Figure 1D), whereas the remaining fraction is

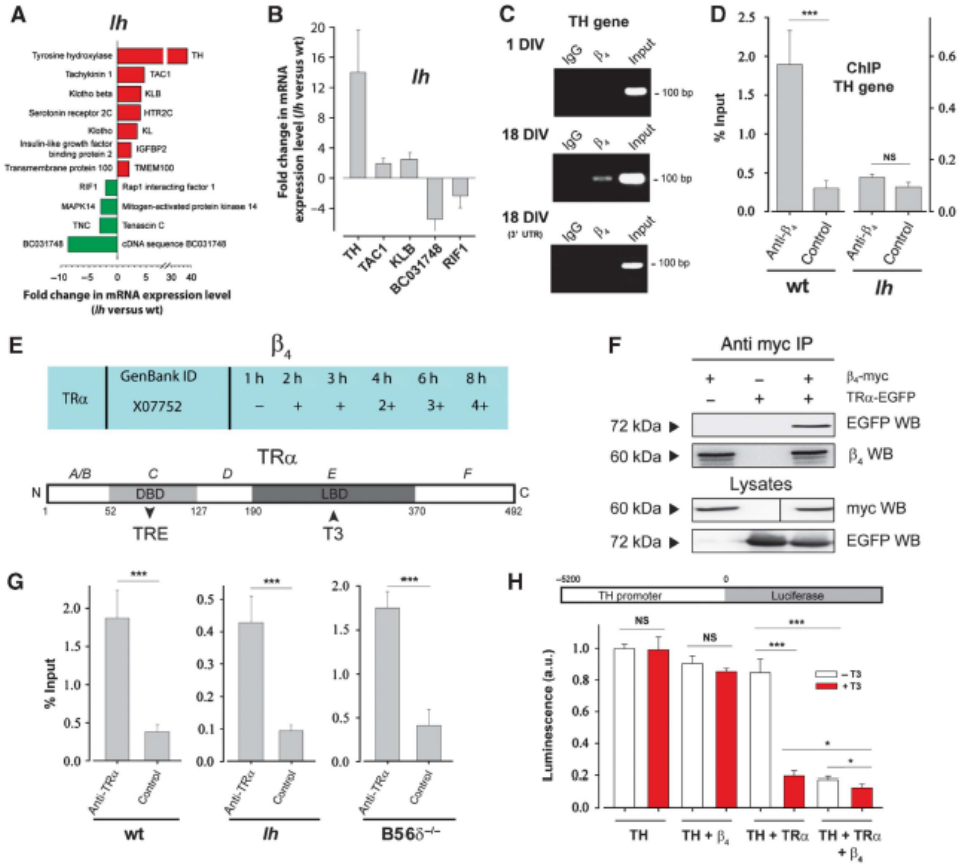

Figure 6 β_4 regulates gene expression by interacting with a transcription factor. (**A**) Histogram showing upregulated (in red) and downregulated (in green) genes displaying a >2-fold change in *lh* versus wt cerebellum mRNA levels as detected with transcriptomic probe sets. (**B**) qRT–PCR experiments showing upregulation of TH, TAC1, KLB and downregulation of BC031748 and RIF1 in *lh* versus wt cerebellum. Mean ± s.d. of three experiments performed in triplicate. Data were normalized using three housekeeping genes (glyceraldehyde 3-phosphate dehydrogenase, transferin receptor and peptidylprolyl isomerase A). (**C**) Agarose gel of representative ChIP assay on hippocampal neurons at 1 or 18 DIV with anti-β_4 antibodies. (**D**) TH promoter immunoprecipitation in presence or absence (control) of anti-β_4 antibodies, expressed as percentage of input, from wt or *lh* mice brain ($n = 4–22$, left panel). $^{***}P < 0.001$. (**E**) Yeast two-hybrid results indicating the interaction level of β_4 with TRα as a function of time (upper panel). The interactions were scored as the ratio of β-galactosidase activity to His prototrophy. Schematic representation of mouse TRα showing the localization of the DNA Binding Domain (DBD) and the Ligand Binding Domain (LBD) (lower panel). (**F**) Western blot analysis of TRα-EGFP immunoprecipitated by β_4-myc expressed in HEK293 cells. (**G**) TH promoter immunoprecipitation by anti-TRα antibodies, expressed as percentage of input, from wt, *lh* or B56δ$^{-/-}$ mice brain ($n = 4–20$, left panel). $^{***}P < 0.001$. (**H**) Schematic representation of the luciferase reporter system under the control of TH promoter (upper panel). Luciferase expression measured in the absence and presence of T3 in HEK293 cells transfected with the luciferase reporter alone or together with TRα ± β_4 (lower panel). An everted repeat type 6 TRE is present in the promoter region of TH gene (TGGCCTTGCCTGAGGCCA) at position −341 to −323.

associated to euchromatin. Expression of B56δ-EGFP together with β_4-myc in HEK293 cells leads to a genome-wide dephosphorylation of Ser^{10} of histone H3 (Figure 7C), in agreement with earlier findings that PP2A dephosphorylates histone H3 (Nowak *et al*, 2003). This effect cannot be attributed to an increased population of transfected cells in G2/M phases of the cell cycle (Supplementary Figure 8c). In addition, immunoprecipitated β_4-myc/B56δ-EGFP/PP2A-HA complex allows dephosphorylation of a Ser^{10} phosphorylated histone H3 N-terminal peptide (Figure 7D). Finally, ChIP experiments using anti-histone H3 and anti-phosphorylated H3 Ser^{10} antibodies show that the absence of β_4 in *lh* brain is accompanied by an increase of histone H3 Ser^{10} phosphorylation at the TH promoter (Figure 7E). Ser^{10} dephosphorylation of histone H3 has been associated to recruitment of HP1γ (Fischle *et al*, 2005). Interestingly, HP1γ has been shown to interact with a PXVXV motif on β_{4c} (Xu *et al*, 2011), a short splice variant of β_4. Although this motif is also found in full-length β_4 (Figure 7F), no interaction with HP1γ has been detected by yeast two hybrid (Figure 4C; Hibino *et al*, 2003). Nevertheless, we questioned whether the interaction of β_4 with B56δ could control its interaction with HP1γ. Indeed, expression of B56δ-EGFP strongly enhances immunoprecipitation of HP1γ-EGFP by β_4-myc (Figure 7G). The basal level of precipitation of HP1γ-EGFP by β_4-myc is due to the presence of endogenous B56δ in HEK293 cells

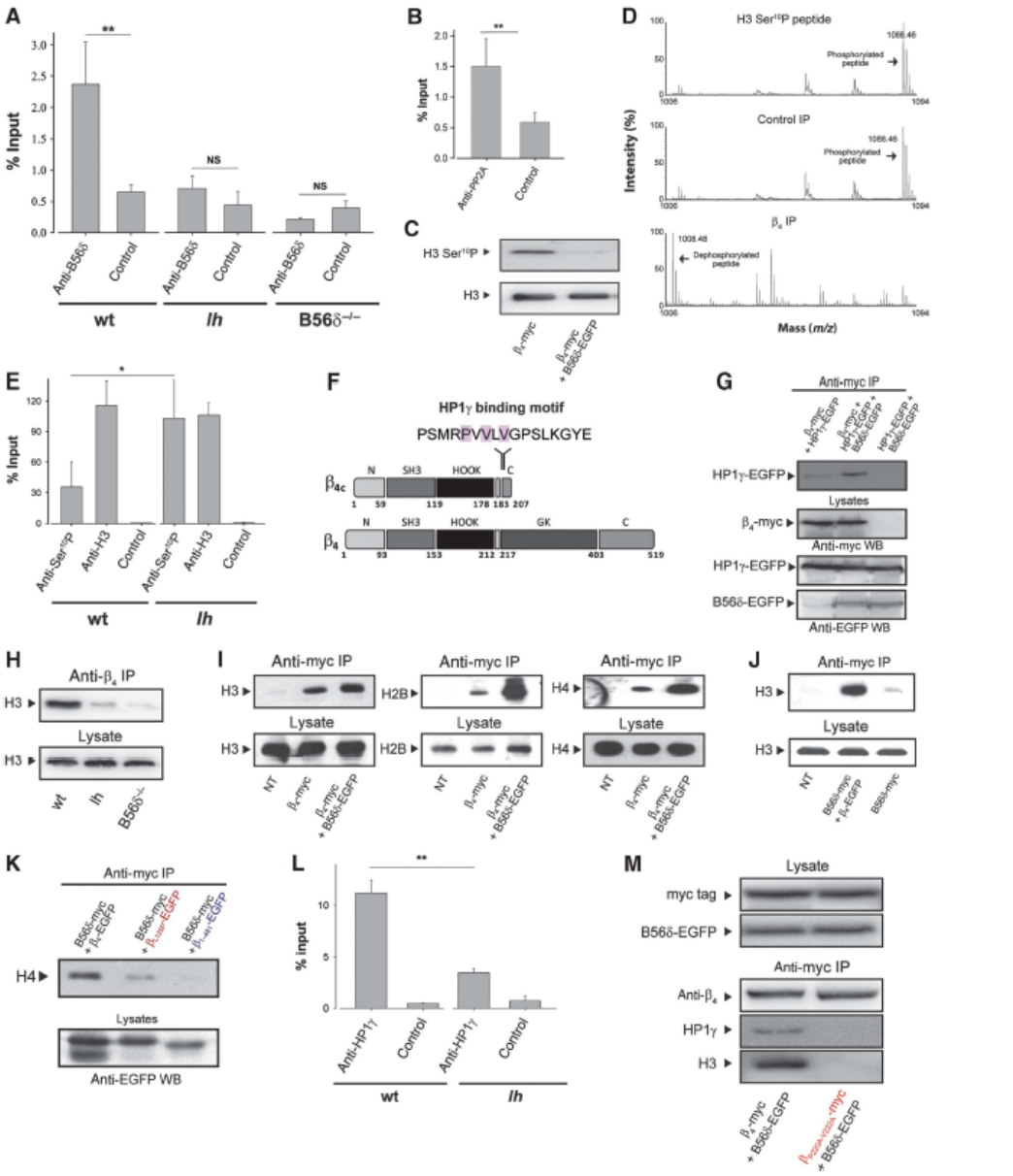

Figure 7 Association of β_4 to HP1γ and histones requires B56δ. (**A**) TH promoter immunoprecipitation by anti-B56δ antibodies, expressed as percentage of input, from wt, *lh* or B56δ$^{-/-}$ mice brain ($n=2$–8). $^{**}P<0.05$. (**B**) TH promoter immunoprecipitation by anti-PP2A antibodies, expressed as percentage of input, from wt mice brain ($n=12$). $^{**}P<0.05$. (**C**) Western blot of H3 and H3 Ser^{10}P in HEK293 cells expressing β_4-myc alone or with B56δ-EGFP. (**D**) Mass spectrometry data showing dephosphorylation of the phosphorylated N-terminal histone H3 peptide (amino acids 5–13 phosphorylated on Ser^{10}) by β_4-myc immunoprecipitated from HEK293 cells, co-transfected with B56δ-EGFP and PP2A-HA. (**E**) TH promoter immunoprecipitation by anti-Ser^{10}P H3 or anti-H3 antibodies, expressed as percentage of input, from wt or *lh* mice brain ($n=3$–22). $^{*}P<0.1$. (**F**) Schematic representation of β_{4c} and β_4 illustrating the localization of the HP1γ binding motif (critical residues are shadowed). (**G**) Western blot of HP1γ-EGFP following immunoprecipitation by anti-myc antibodies from HEK293 cells expressing various combinations of HP1γ-EGFP, B56δ-EGFP and β_4-myc. (**H**) Immunoprecipitation of histone H3 from wt, *lh* or B56δ$^{-/-}$ brain by anti-β_4 antibodies. (**I**) Immunoprecipitation of H3, H2B and H4 histones from HEK293 cells by β_4-myc in the absence or presence of B56δ-EGFP. Control: immunoprecipitation in non-transfected cells (NT). (**J**) Immunoprecipitation of histone H3 in HEK293 cells by B56δ-myc in the absence or presence of β_4-EGFP. (**K**) Lack of co-immunoprecipitation of histone H4 and B56δ-myc in HEK293 cells in the presence of β_{L125P}-EGFP or β_{1-481}-EGFP mutants. (**L**) TH promoter immunoprecipitation by anti-HP1γ antibodies, expressed as percentage of input, from wt or *lh* mice brain ($n=4$–14). $^{**}P<0.05$. (**M**) Mutation of the HP1γ binding motif prevents β_4-myc association to histone H3 in the presence of B56δ-EGFP.

(Supplementary Figure 3a). The B56δ dependence of HP1γ/β_4 interaction, together with the PP2A-induced dephosphorylation of histone H3 Ser[10], prompted us to investigate the interaction of this complex with histones. Immunoprecipitation of mice brain β_4 leads to the precipitation of histone H3 (Figure 7H). The specificity of this association is witnessed by the lack of histone H3 precipitation from *lh* brain. Importantly, β_4 association with histone H3 is lost in B56δ$^{-/-}$ mice brain, in agreement with the specific role of B56δ in β_4/HP1γ interaction. In HEK293 cells, immunoprecipitation of β_4-myc leads to the co-precipitation of all histones (H2B, H3 and H4) (Figure 7I), constitutive of nucleosomes. This is in agreement with the endogenous expression of B56δ (Supplementary Figure 3a) and HP1γ (Supplementary Figure 3d) in these cells. Expression of B56δ further enhances β_4-myc/histone interaction (Figure 7I). Similarly, B56δ-myc requires the expression of β_4-EGFP to precipitate histone H3, in agreement with the fact that HP1γ binds β_4 and not B56δ (Figure 7J). B56δ-myc expressed together with β_{L125P}-EGFP or β_{1-481}-EGFP mutants, deficient for B56δ association, no longer precipitate histone H4 further supporting the B56δ dependence of β_4/HP1γ interaction (Figure 7K). Neuronal differentiation strongly increases the association of endogenous β_4 with histone H3 in NG108-15 (Supplementary Figure 9a), which correlates with the differentiation-dependent β_4 nuclear targeting (Figure 1H and I). In the presence of B56δ-EGFP and channel subunits, membrane depolarization increases β_4-myc, but not β_{1-481}-myc, association to histone H3 (Supplementary Figure 9b). Coherent with its role as PP2A regulatory subunit and its genome-wide effect observed in Figure 7C, B56δ-EGFP expression in HEK293 cells also results in dephosphorylation of Ser[10] of β_4-myc-associated histone H3 (Supplementary Figure 9c). ChIP experiments using anti-HP1γ antibodies demonstrate the association of HP1γ to the TH promoter (Figure 7L). The strong decrease of this association in *lh* brain illustrates the role of β_4 in recruiting HP1γ to the TH gene. Finally, double mutation of the HP1γ binding motif of β_4 precludes the B56δ-dependent interaction of β_4 with histone H3 demonstrating that HP1γ or HP1γ-like proteins are required for β_4 association to histones (Figure 7M).

β_4-dependent TH gene repression is mediated by electrical activity

Our results indicate that in neurons there should be a β_4-dependent coupling between electrical activity and TH gene repression. To validate this conclusion, the electrical activity dependence of TH mRNA levels was investigated using cerebellar granule neurons from wt and *lh* mice. Because these cells required depolarizing conditions to survive (25 mM KCl), which promotes basal level electrical activity, our control condition was defined as TH mRNA level after 2 days of TTX treatment (from 8 DIV to 10 DIV). Promoting electrical activity for 1 day, by removing TTX from 9 DIV to 10 DIV, induces strong TH mRNA level repression in wt (50%) but not in *lh* neurons (Figure 8A).

Discussion

Here, we characterized a novel signalling pathway in which, under membrane depolarization, the VGCC β_4 subunit accumulates in the nucleus and acquires a gene regulatory function by successively recruiting the B56δ/PP2A complex, a transcription factor and the heterochromatin protein, HP1γ. Nuclear localization of β_4 was previously shown in mice brain by Subramanyam *et al* (2009). In contrast to what we observe with endogenous β_4, these authors show that depolarization of cultured neurons expressing V5-tagged β_4 promotes nuclear export of the tagged protein. Besides the possibility that the V5 tag may interfere with the β_4/ B56δ interaction we describe and thus modify β_4 nuclear targeting pathways, these results may highlight an active equilibrium between different pathways of β_4 nuclear import and export.

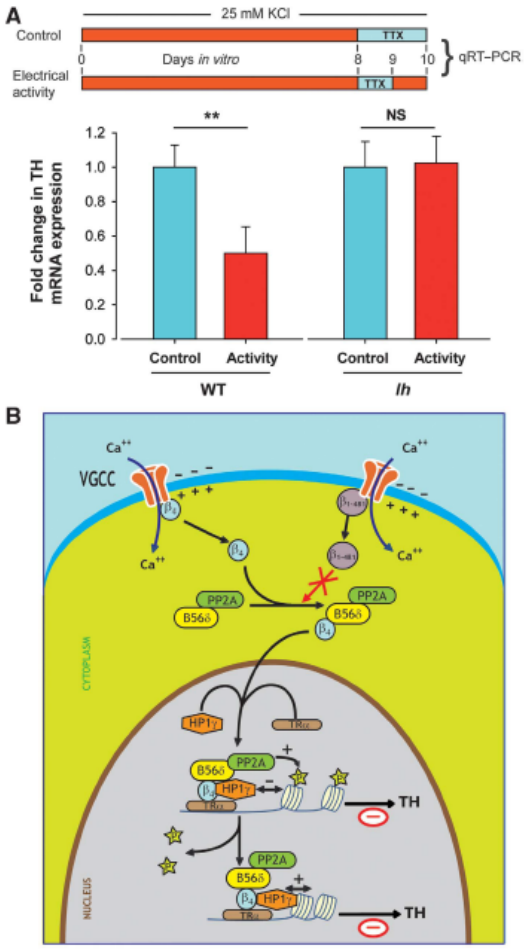

Figure 8 Experimental validation and schematic illustration of the novel excitation-transcription pathway mediated by β_4. (**A**) Electrical activity reduces TH mRNA levels in primary cultures of cerebellar granule neuronal from wt mice but not from *lh* mice. Upper panel represents the experimental protocol. First condition in which TTX is added for 2 days (8–10 DIV) is used as control condition without electrical activity (blue colour), whereas second condition in which TTX is washed out at 9 DIV is used as the condition in which electrical activity is restored (red colour). Lower panel illustrates the fold-change in TH mRNA level induced by electrical activity using rpl27 as housekeeping gene and normalization to control condition. $^{**}P<0.05$. (**B**) Schematic representation of the new signalling pathway and of the defective steps produced by the epileptic truncation of β_4.

This group identified the N-terminus of β_4 as a possible determinant of nuclear accumulation. In support with the previous hypothesis, our own results show that this domain only partially interferes with β_4 nuclear accumulation suggesting the existence of different pathways controlling β_4 subcellular localization involving different β_4 protein partners. We demonstrate here that the N-terminus of β_4 is not important for its interaction with B56δ suggesting that its contribution to nuclear accumulation occurs through a B56δ-independent pathway. In our work, we focused on the β_4 nuclear pathway that involves B56δ and that is disrupted by the human epileptic mutation of β_4. We show that *in-vitro* TRα acts as a transcription factor capable to interact with β_4 and repress TH gene expression. The *in-vivo* implication of TRα in controlling TH gene expression remains to be deciphered. The resulting nuclear platform, structured by β_4, binds to specific gene promoters, dephosphorylates histones associated to these promoters and orients HP1γ interaction with the dephosphorylated histones. The formation of this complex allows gene repression, first by a direct effect of β_4 on TRα, and second by HP1γ recruitment known to promote heterochromatin formation (Figure 8B). This later step may lead to long-term gene repression, while the first step is conceptually more dynamic. In *lh* brain, a complete disorganization of this signalling pathway is observed in the absence of β_4. The combined reduction in HP1γ levels and greater phosphorylation level of histone H3 Ser^{10} are two events that conceptually may favour the upregulation of TH expression. In that respect, further studies on the ability of nuclear β_4 complex to induce other histone post-translational modifications, such as methylation or acetylation, will complete the characterization of the role of this complex in gene regulation. While our data demonstrate the key role of β_4 in organizing TH gene repression, TH expression is not uniformly upregulated in all *lh* brain areas indicating the existence of compensatory mechanisms. In that respect, B56γ, that also targets PP2A to the nucleus (McCright *et al*, 1996), and β_3, another VGCC subunit, that is also addressed to the nucleus (Beguin *et al*, 2006) and binds B56δ (Figure 4C) and TRα (unpublished observation), might participate to this compensation process. The juvenile epilepsy mutant that normally associates with VGCC (Escayg *et al*, 2000) is defective for B56δ association. This mutant no longer forms a complex with PP2A, and is unable to translocate to the nucleus and to interact with HP1γ and histones (Figure 8B). Therefore, this mutation induces a full destabilization of the β_4 signalling pathway. At the structural level, formation of the B56δ/β_4 complex requires the interaction between the β_4 SH3 and GK modules. The nuclear targeting defect induced by the human mutation resides in the loss of this interaction highlighting an unexpected role of β_4 C-terminal domain in controlling β_4 conformation state. Association of B56δ with β_4 promotes β_4/HP1γ interaction further indicating the exquisite modularity of β_4 as an adaptor protein.

In earlier reports, B56δ/PP2A was shown to regulate gene expression through a complex interplay between DARPP-32 phosphorylation state (Ahn *et al*, 2007), phosphatase 1 (PP1) activity and histone H3 phosphorylation level (Stipanovich *et al*, 2008). PP1 complexes have been associated to other histone-modifying enzymes, such as histone deacetylases or kinases, with chromatin remodelling capabilities (Hsu *et al*, 2000; Murnion *et al*, 2001) and with transcription repressors or activators (Canettieri *et al*, 2003; Jin *et al*, 2003). Here, we illustrate that, like PP1, PP2A belongs to a signalling macromolecular complex which ultimately regulates gene expression by modulating the histone code. This complex is organized by the VGCC β_4 subunit that plays the role of a platform that, besides PP2A, also recruits a nuclear receptor and a heterochromatin protein, HP1γ. By homology with PP1, this protein complex is likely to be enriched by other nucleosome-modifying enzymes in the near future. It should be emphasized that long-term modifications accompanying epileptic disorders have previously been associated to changes in post-translational state of histones and to alterations in transcriptional programs (Huang *et al*, 2002; Sng *et al*, 2006). This work thus opens exciting perspectives for understanding the underlying molecular causes of epilepsy in which VGCC subunits have been implicated.

Materials and methods

Mice lines

Lethargic (B6EiC3H-a/A-*lh*) and wild-type mice (strain B6EiC3H) were obtained from Jackson Labs and genotyped as previously described (Burgess *et al*, 1997). B56δ$^{-/-}$ mice were generated by exchanging 146 bp of exon 3, exons 4–14, and 45 bp of exon 15 of the *Ppp2r5d* gene with a neomycine cassette through homologous recombination (Louis *et al*, 2011). Animal procedures were run with the approval of the local ethical committee and all efforts were made to minimize both the suffering and number of animal used. Also, the experiments were carried out in accordance with the International Ethical Committee Guidelines (EEC Council Directive 86/609, OJ L 358, 1, December 12, 1987; Guide for the Care and Use of Laboratory Animals, US National Research Council, 1996) for the care and use of laboratory animals.

Electron microscopy

Mice were fixed by intracardiac perfusion during 10 min with 50 ml of fixation buffer (2% paraformaldehyde, 0.2% glutaraldehyde in 0.1 M phosphate buffer pH 7.3). The hippocampus was then isolated and kept in fixation buffer during 2 days. A transversal slice was made in the mid third of the hippocampus and dissection of the CA1/CA3 area in this slice was performed under a binocular magnifier. Hippocampal neurons were cultured in B100 plates during 5 or 18 days and fixed 2 h with fixation buffer. Cells were gently detached with a cell scraper, centrifuged and embedded in 10% gelatine. The cell pellet was then cut in small pieces. In all, 1 mm^3 cell or tissue samples were then incubated during 4 h in 2.3 M sucrose and frozen in liquid nitrogen. Cryosections were made at −120°C using a cryo-ultramicrotome (Leica-Reichert) and retrieved with a 1:1 solution of 2.3 M sucrose and 2% methylcellulose (Liou *et al*, 1996). Cryosections were first incubated with primary anti-β_4 (Everest Biotech, 1:100), then incubated with rabbit anti-goat antibodies (Jackson, 1:400) and revealed with protein A-gold conjugated (CMC, Utrecht). Labelled cryosections were viewed at 80 kV with a 1200EX JEOL TEM microscope and images were acquired with a digital camera (Veleta, SIS, Olympus). Gold particles were counted and surface area measured with iTEM software (analySIS).

Hippocampal neurons, NG108-15 cell cultures and cerebellar granule neurons

Primary cultures of hippocampal neurons were prepared as previously described (Peris *et al*, 2009). Astrocyte proliferation was blocked by 10 μM arabinoside cytosine (AraC) 4 days after plating. Predominance of neurons was witnessed by Tuj1 labelling and lack of GFAP staining. NG108.15 cells were differentiated 2 days after plating by decreasing fetal calf serum to 1% and addition of 1 mM dibutyryl cAMP. Cell lines were transfected using jetPEI and neurons at 9 DIV using calcium phosphate. Dissociated cerebellar granule neurons were prepared as previously described (Kiyonaka *et al*, 2007) except that 0.02% (w/v) trypsin (Difco) was used for dissociation of cerebellar tissues. Three hours after cell plating, culture medium was replaced with Neurobasal (Invitrogen) with 2% B-27 (GIBCO), 26 mM KCl, 60 U/ml penicillin, and 60 μg/ml

streptomycin, and renewed every 3 days. At 8 DIV, 0.1 μM TTX was added in the culture medium to block electrical activity. At 9 DIV, the TTX was washed out to promote electrical activity or maintained for continued electrical activity block. At 10 DIV, total RNA was isolated using NucleoSpin RNA XS (Macherey-Nagel) according to manufacturer's instructions.

Plasmid constructions

cDNA constructs coding for EGFP-tagged β_4 fragments were generated by PCR amplification using rat β_4-EGFP plasmid as template (GenBank accession code L02315) and subcloned into pEGFP-C1 using *Hind*III and *Kpn*I sites. Myc-tagged β_4 fragments were subcloned into pcDNA3.1(+) using *Hind*III and *Xba*I sites. For yeast two-hybrid assays, rat β_1, β_2, β_3, β_4 and β_4 mutants were subcloned into pGBK-T7 vector (Kiyonaka *et al*, 2007). QuikChange® Site-Directed Mutagenesis Kit (Stratagene) or overlap extension method was used to produce β_{L125P}-EGFP, β_{P225R}-EGFP, $\beta_{1\text{-}166\text{-}L125P}$-EGFP, $\beta_{P220A\text{-}V222A}$-myc and $\beta_{R28A\text{-}R29A\text{-}S30A}$-EGFP. Mouse B56δ (GenBank accession code NM009358), HP1γ (NM_007624) and TRα (NM_178060) were cloned from mouse brain Marathon-Ready cDNA (Clontech) using PCR and inserted into pCMV-tag3 vector and pEGFP-C2 vector using *Eco*RI and *Sal*I site. The B56δ and control shRNAs (sense strand sequences: 5′-CATCGCATCTATGGC AAGTTT-3′ and 5′-CAACAAGATGAAGAGCACCAA-3′, respectively) were subcloned into TRC1.5 vector (Sigma). All constructs were sequenced. Human Cacna1a (GenBank accession code AF004883) and rat Cacna1a (code NM012919) were also used for expression experiments. The TH-luciferase reporter gene was as previously described (Robert *et al*, 1997) and contains 5200 bps of the TH promoter upstream of the *Firefly* luciferase coding region.

Cytochemical stainings

Cells were fixed with 4% paraformaldehyde in PBS for 15 min. After PBS washing, plasma membranes were stained 5 min with 5 μg/ml concanavalin A-rhodamine. Cells were permeabilized with 0.1% Triton X-100. Myc-tagged constructs were visualized using biotinylated anti-myc antibodies (1:600, Santa Cruz) and Cy3-Streptavidin (1:300, Amersham). Endogenous β_4 was labelled for 1–2 h with a goat antibody directed against its carboxyl-terminus (1/1000 dilution, Everest Biotech), followed by Alexa488 conjugated anti-goat (1:500, Molecular Probes). Cell nuclei were visualized using ToPro3 dye (T3605; Molecular Probes Inc). Images were obtained with a confocal microscope (Leica SP2). NCR values correspond to the average measure of 50 cells. In each cell, fluorescence intensities were measured in 40 different ROI (20 for the cytoplasm and 20 for the nucleus). Merged pictures were obtained by using Adobe Photoshop software.

Yeast two-hybrid assays

Rat β_4, subcloned into pGBK-T7, was used as bait to screen a mouse brain pACT2 library expressed in the yeast strain AH109 (Clontech) (Kiyonaka *et al*, 2007). In all, 5.0×10^6 transformants were cultured with synthetic medium lacking adenine, histidine, leucine and tryptophan. His^+ colonies were assayed in yeast cells for β-galactosidase activity by a filter assay. Signal strengths of interactions were evaluated visually after every 1 h of colour development. For mapping of the β_4 region that interacts with B56δ or HP1γ, yeast strain Y187 was co-transformed with each β bait vector and the B56δ or HP1γ prey vector. The interactions were evaluated by β-galactosidase activity on a filter.

Subcellular fractionation and western blotting

Transfected HEK293 cells were lysed with 10 mM Tris pH 7.5, 10 mM KCl, 1.5 mM $MgCl_2$, 0.5% Triton X-100 and protease inhibitor cocktail (Roche). Nuclei and cytoplasm were separated by 5 min centrifugation at 2000 r.p.m. Pellets corresponding to nuclei were sonicated in lysis buffer. For mice brain subcellular fractionation, brains were homogenized in 0.32 M sucrose, 20 mM HEPES, pH 7.4, 1 mM DTT, 1 mM PMSF and protease inhibitor cocktail (Roche). The homogenate was centrifuged 10 min at 800 *g*. The resulting crude nuclear pellet was washed twice with homogenization buffer, resuspended in a volume equivalent to the cytoplasmic fraction, and sonicated. Nuclear and cytoplasmic (supernatant) proteins, from equal volumes, were separated by SDS–PAGE and analysed by western blot. EGFP-tagged proteins were visualized using anti-EGFP antibodies (1:300, Santa Cruz or 1:5000 Rockland) and anti-β_4 as described (Kiyonaka *et al*, 2007).

Immunoprecipitation experiments

Transfected cells were lysed 30 min in 10 mM Tris pH 7.4, 1.5 mM $MgCl_2$, 60 mM KCl, 15 mM NaCl, 0.5% Triton X-100 supplemented with protease inhibitor cocktail (Roche), sonicated and centrifuged 5 min at 1500 *g*. Similar procedure applies for mice brain, except that they were homogenized first in lysis buffer. Protein extracts were incubated with streptavidin beads (Dynabeads® Streptavidin M-280; Dynal) precoated with 3 μg of biotinylated anti-myc antibody (Santa Cruz Biotechnology Inc.). For immunoprecipitation of endogenous β_4, protein extracts were incubated with 40 μl of Dynabeads protein G (Dynal) precoated with anti-β_4 antibodies (Everest Biotech). Beads were washed with PBS/0.1% Tween-20. Immunoprecipitated proteins were eluted with denaturating buffer and analysed by western blot. For immunoprecipitation of phosphorylated histones, lysis buffer was supplemented with 50 mM NaF phosphatase inhibitor. For immunoprecipitation and ChIP, primary antibodies were used at 10 μg: anti-β_4 from Everest or as described (Kiyonaka *et al*, 2007), anti-histone H2B from Upstate, anti-histone H3, anti-phosphorylated Ser^{10} histone H3, anti-histone H4, anti-HP1γ, and anti-TRα from Abcam, anti-B56δ as described in Martens *et al* (2004), anti-PP2A from Bethyl Laboratories Inc., and anti-actin from Sigma-Aldrich.

PP2A activity

PP2A activity of immunoprecipitates was measured using SensoLyte™*p*NPP protein phosphatase kit from AnaSpec. Incubation lasted 1 h at 37°C in assay buffer in the presence of *p*-nitrophenyl phosphate (*p*NPP). OD was measured at 405 nm.

Quantitative RT–PCR

Total RNAs were extracted from wt, *lh* or B56δ$^{-/-}$ cerebellum using the RNeasy kit, supplemented with DNase I (Qiagen). cDNAs were synthesized from 1 μg total RNA using random hexamer primers (Promega) and Superscript II (Invitrogen). Primers recognizing mice sequences were designed with the Primer 3 software (http://frodo.wi.mit.edu/) or by Sigma service (Supplementary Figure 10). Real-time PCR was performed with a light cycler 480 instrument using the Lightcycler LC480 SYBR green I master (Roche) according to manufacturer's instructions. The cycling protocol was 10 min at 95°C followed by 40 cycles of 3 steps each (10 s at 95°C, 5 s at 60°C and 10 s at 72°C). The specificity of the amplification was check by generating a melting curve ranging from 65 to 95°C. Multiple normalization of gene expression (Vandesompele *et al*, 2002) was performed using three housekeeping genes (glyceraldehyde 3-phosphate dehydrogenase, transferin receptor and peptidylprolyl isomerase A).

For TH expression levels in cerebellar granule neurons, cDNAs were synthesized using AMV reverse transcriptase XL and an oligo dT-adaptor primer (TaKaRa). Real-time PCR and cycling protocol were performed as above, except for the number of cycles (50). TH gene expression was normalized relative to rpl27 (de Jonge *et al*, 2007). Values were expressed relative to wt treated with TTX, which was given the arbitrary value of 1.

Chromatin immunoprecipitation

Frozen adult mice brain (wt, *lh* or B56δ$^{-/-}$) was first crunched into powder in a mortar filled with liquid nitrogen. This powder was resuspended in 1% formaldehyde (in PBS) and incubated for 20 min at RT. Crosslinking was stopped by addition of glycine (125 mM final concentration) and incubation 5 min. Fixed tissues were thus washed with (i) cold PBS (5 min), (ii) 10 mM HEPES, 0.5 mM EGTA, 10 mM EDTA and Triton X-100 0.25%, pH 7.4 (10 min) and (iii) 10 mM HEPES, 0.5 mM EGTA, 1 mM EDTA and 200 mM NaCl, pH 7.4 (10 min). Samples were then solubilized in 1 ml of buffer containing 50 mM Tris, pH 7.4, 10 mM EDTA, 1% SDS for 2 h at 4°C, sonicated until reaching an average 500–1000 bps DNA fragment size, and centrifuged 5 min at 20 000 *g*. In all, 100 μl of lysate ($OD_{280} = 0.266$) was incubated overnight at 4°C in 1 ml of 0.01% SDS, 1.1% Triton X-100, 1.2 mM EDTA, 16 mM Tris pH 8.0 and 170 mM NaCl, 1 mM PMSF, and protease inhibitor cocktail, with or without 10 μg antibodies. Immunoprecipitation was performed by adding Dynabeads protein G (Invitrogen). Different washing steps and elution were performed as described (Dahl and Collas, 2008). Crosslinks were reversed overnight at 65°C. DNA samples were sequentially treated with RNAse A and proteinase K. DNA was extracted by phenol/chloroform and ethanol precipitated with glycogen as a carrier. DNA pellet was dissolved in

water and real-time quantitative PCR analyses were performed on 25 ng of DNA in duplicate with selected primers (Supplementary Figure 10). On cultured hippocampal neurons, ChIP experiments were conducted on 5×10^6 cells using the Magna ChIP™ (MILLIPORE) according to manufacturer's protocol. The PCR cycling protocol was 10 min at 94°C followed by 38 cycles of 3 steps each (30 s at 94°C, 30 s at 55°C or 61°C, and 30 s at 72°C), and 7 min at 72°C. Annealing temperature for the promoter region of TH was 55°C and for the 3′UTR of TH was 61°C.

Mass spectrometry

The histone H3 peptide phosphorylated at Ser^{10} $QTARKS_pTGGC$ was obtained from Smartox Biotechnologies (Grenoble, France). Immunoprecipitates were washed with (in mM) 40 Tris pH 8.4, 34 $MgCl_2$, 4 EDTA, 4 DTT, and incubated overnight at 37°C with 1 mM peptide. Dephosphorylation was evaluated by MALDI-TOF (Applied 4800) mass spectrometry. Briefly, 1 µl of peptide solution was spotted directly onto the MALDI target, dried and 1 µl of 20% α-Cyano-4-hydroxy-cinnamic acid (Sigma) was added in 50% acetonitrile, 0.1% trifluoroacetic acid.

Supplementary data

Supplementary data are available at *The EMBO Journal* Online (http://www.embojournal.org).

Acknowledgements

We are indebted to Dr Hiroshi Hibino (Osaka University, Japan) for providing HP1γ constructs used for co-immunoprecipitation, confocal imaging and yeast two-hybrid assays. We thank Dr Rosalie Sears (Oregon Health & Sciences University, Portland, USA) for the pD30-PP2A-HA-C clone. MB is a postdoctoral fellow of Association Française contre les Myopathies.

Author contributions: AT and KF studied the nuclear localization of β_4 and its structural determinants. ShK, TM and SA made several cDNA constructs and performed yeast two-hybrid and ChIP experiments. MB, KF and MiR performed RT–PCR, immunoprecipitation and ChIP experiments. CA did electrophysiological recordings. SG-F and AA provided their expertise with hippocampal neuron cultures. KS performed mass spectrometry experiments and SaK contributed to discussion, design and interpretation of data regarding nuclear function of β_4 complex. FL performed CHCB2 experiments. KP-G did EM experiments. SB performed transcriptomic analyses. CL and VJ provided the $B56\delta^{-/-}$ mice line and analytical tools. RD, MiR, YM and MDW coordinated the study. MiR and MDW wrote the manuscript.

Conflict of interest

The authors declare that they have no conflict of interest.

References

Ahn JH, McAvoy T, Rakhilin SV, Nishi A, Greengard P, Nairn AC (2007) Protein kinase A activates protein phosphatase 2A by phosphorylation of the B56delta subunit. *Proc Natl Acad Sci USA* **104:** 2979–2984

Arikkath J, Campbell KP (2003) Auxiliary subunits: essential components of the voltage-gated calcium channel complex. *Curr Opin Neurobiol* **13:** 298–307

Beguin P, Mahalakshmi RN, Nagashima K, Cher DH, Ikeda H, Yamada Y, Seino Y, Hunziker W (2006) Nuclear sequestration of beta-subunits by Rad and Rem is controlled by 14-3-3 and calmodulin and reveals a novel mechanism for Ca2+ channel regulation. *J Mol Biol* **355:** 34–46

Bengzon J, Hansson SR, Hoffman BJ, Lindvall O (1999) Regulation of norepinephrine transporter and tyrosine hydroxylase mRNAs after kainic acid-induced seizures. *Brain Res* **842:** 239–242

Bichet D, Cornet V, Geib S, Carlier E, Volsen S, Hoshi T, Mori Y, De Waard M (2000) The I-II loop of the Ca2+ channel alpha1 subunit contains an endoplasmic reticulum retention signal antagonized by the beta subunit. *Neuron* **25:** 177–190

Bidaud I, Mezghrani A, Swayne LA, Monteil A, Lory P (2006) Voltage-gated calcium channels in genetic diseases. *Biochim Biophys Acta* **1763:** 1169–1174

Burgess DL, Jones JM, Meisler MH, Noebels JL (1997) Mutation of the Ca2+ channel beta subunit gene Cchb4 is associated with ataxia and seizures in the lethargic (lh) mouse. *Cell* **88:** 385–392

Canettieri G, Morantte I, Guzman E, Asahara H, Herzig S, Anderson SD, Yates III JR, Montminy M (2003) Attenuation of a phosphorylation-dependent activator by an HDAC-PP1 complex. *Nat Struct Biol* **10:** 175–181

Carrion AM, Link WA, Ledo F, Mellstrom B, Naranjo JR (1999) DREAM is a Ca2+-regulated transcriptional repressor. *Nature* **398:** 80–84

Catterall WA, Perez-Reyes E, Snutch TP, Striessnig J (2005) International Union of Pharmacology. XLVIII. Nomenclature and structure-function relationships of voltage-gated calcium channels. *Pharmacol Rev* **57:** 411–425

Chemin J, Nargeot J, Lory P (2002) Neuronal T-type alpha 1H calcium channels induce neuritogenesis and expression of high-voltage-activated calcium channels in the NG108-15 cell line. *J Neurosci* **22:** 6856–6862

Chen YH, Li MH, Zhang Y, He LL, Yamada Y, Fitzmaurice A, Shen Y, Zhang H, Tong L, Yang J (2004) Structural basis of the alpha(1)-beta subunit interaction of voltage-gated Ca(2+) channels. *Nature* **429:** 675–680

Dahl JA, Collas P (2008) A rapid micro chromatin immunoprecipitation assay (microChIP). *Nat Protoc* **3:** 1032–1045

de Jonge HJ, Fehrmann RS, de Bont ES, Hofstra RM, Gerbens F, Kamps WA, de Vries EG, van der Zee AG, te Meerman GJ, ter Elst A (2007) Evidence based selection of housekeeping genes. *PLoS ONE* **2:** e898

Deisseroth K, Mermelstein PG, Xia H, Tsien RW (2003) Signaling from synapse to nucleus: the logic behind the mechanisms. *Curr Opin Neurobiol* **13:** 354–365

Dolmetsch RE, Pajvani U, Fife K, Spotts JM, Greenberg ME (2001) Signaling to the nucleus by an L-type calcium channel-calmodulin complex through the MAP kinase pathway. *Science* **294:** 333–339

Donato R, Page KM, Koch D, Nieto-Rostro M, Foucault I, Davies A, Wilkinson T, Rees M, Edwards FA, Dolphin AC (2006) The ducky(2J) mutation in Cacna2d2 results in reduced spontaneous Purkinje cell activity and altered gene expression. *J Neurosci* **26:** 12576–12586

Escayg A, De Waard M, Lee DD, Bichet D, Wolf P, Mayer T, Johnston J, Baloh R, Sander T, Meisler MH (2000) Coding and noncoding variation of the human calcium-channel beta4-subunit gene CACNB4 in patients with idiopathic generalized epilepsy and episodic ataxia. *Am J Hum Genet* **66:** 1531–1539

Fischle W, Tseng BS, Dormann HL, Ueberheide BM, Garcia BA, Shabanowitz J, Hunt DF, Funabiki H, Allis CD (2005) Regulation of HP1-chromatin binding by histone H3 methylation and phosphorylation. *Nature* **438:** 1116–1122

Flavell SW, Greenberg ME (2008) Signaling mechanisms linking neuronal activity to gene expression and plasticity of the nervous system. *Annu Rev Neurosci* **31:** 563–590

Gomez-Ospina N, Tsuruta F, Barreto-Chang O, Hu L, Dolmetsch R (2006) The C terminus of the L-type voltage-gated calcium channel Ca(V)1.2 encodes a transcription factor. *Cell* **127:** 591–606

Graef IA, Mermelstein PG, Stankunas K, Neilson JR, Deisseroth K, Tsien RW, Crabtree GR (1999) L-type calcium channels and GSK-3 regulate the activity of NF-ATc4 in hippocampal neurons. *Nature* **401:** 703–708

Greer PL, Greenberg ME (2008) From synapse to nucleus: calcium-dependent gene transcription in the control of synapse development and function. *Neuron* **59:** 846–860

Hardingham GE, Arnold FJ, Bading H (2001) Nuclear calcium signaling controls CREB-mediated gene expression triggered by synaptic activity. *Nat Neurosci* **4:** 261–267

Hardingham GE, Chawla S, Johnson CM, Bading H (1997) Distinct functions of nuclear and cytoplasmic calcium in the control of gene expression. *Nature* **385:** 260–265

Hess EJ, Wilson MC (1991) Tottering and leaner mutations perturb transient developmental expression of tyrosine hydroxylase in embryologically distinct Purkinje cells. *Neuron* **6:** 123–132

Hibino H, Pironkova R, Onwumere O, Rousset M, Charnet P, Hudspeth AJ, Lesage F (2003) Direct interaction with a nuclear protein and regulation of gene silencing by a variant of the Ca2+-channel beta 4 subunit. *Proc Natl Acad Sci USA* **100:** 307–312

Hsu JY, Sun ZW, Li X, Reuben M, Tatchell K, Bishop DK, Grushcow JM, Brame CJ, Caldwell JA, Hunt DF, Lin R, Smith MM, Allis CD (2000) Mitotic phosphorylation of histone H3 is governed by Ipl1/aurora kinase and Glc7/PP1 phosphatase in budding yeast and nematodes. *Cell* **102:** 279–291

Huang Y, Doherty JJ, Dingledine R (2002) Altered histone acetylation at glutamate receptor 2 and brain-derived neurotrophic factor genes is an early event triggered by status epilepticus. *J Neurosci* **22:** 8422–8428

Jenuwein T, Allis CD (2001) Translating the histone code. *Science* **293:** 1074–1080

Jin Q, van Eynde A, Beullens M, Roy N, Thiel G, Stalmans W, Bollen M (2003) The protein phosphatase-1 (PP1) regulator, nuclear inhibitor of PP1 (NIPP1), interacts with the polycomb group protein, embryonic ectoderm development (EED), and functions as a transcriptional repressor. *J Biol Chem* **278:** 30677–30685

Kiyonaka S, Wakamori M, Miki T, Uriu Y, Nonaka M, Bito H, Beedle AM, Mori E, Hara Y, De Waard M, Kanagawa M, Itakura M, Takahashi M, Campbell KP, Mori Y (2007) RIM1 confers sustained activity and neurotransmitter vesicle anchoring to presynaptic Ca2+ channels. *Nat Neurosci* **10:** 691–701

Liou W, Geuze HJ, Slot JW (1996) Improving structural integrity of cryosections for immunogold labeling. *Histochem Cell Biol* **106:** 41–58

Louis JV, Martens E, Borghgraef P, Lambrecht C, Sents W, Longin S, Zwaenepoel K, Pijnenborg R, Landrieu I, Lippens G, Ledermann B, Gotz J, Van Leuven F, Goris J, Janssens V (2011) Mice lacking phosphatase PP2A subunit PR61/B'delta (Ppp2r5d) develop spatially restricted tauopathy by deregulation of CDK5 and GSK3beta. *Proc Natl Acad Sci USA* **108:** 6957–6962

Magnusdottir A, Stenmark P, Flodin S, Nyman T, Kotenyova T, Graslund S, Ogg D, Nordlund P (2009) The structure of the PP2A regulatory subunit B56 gamma: the remaining piece of the PP2A jigsaw puzzle. *Proteins* **74:** 212–221

Martens E, Stevens I, Janssens V, Vermeesch J, Gotz J, Goris J, Van Hoof C (2004) Genomic organisation, chromosomal localisation tissue distribution and developmental regulation of the PR61/B' regulatory subunits of protein phosphatase 2A in mice. *J Mol Biol* **336:** 971–986

McCright B, Rivers AM, Audlin S, Virshup DM (1996) The B56 family of protein phosphatase 2A (PP2A) regulatory subunits encodes differentiation-induced phosphoproteins that target PP2A to both nucleus and cytoplasm. *J Biol Chem* **271:** 22081–22089

McGee AW, Nunziato DA, Maltez JM, Prehoda KE, Pitt GS, Bredt DS (2004) Calcium channel function regulated by the SH3-GK module in beta subunits. *Neuron* **42:** 89–99

Murnion ME, Adams RR, Callister DM, Allis CD, Earnshaw WC, Swedlow JR (2001) Chromatin-associated protein phosphatase 1 regulates aurora-B and histone H3 phosphorylation. *J Biol Chem* **276:** 26656–26665

Nowak SJ, Pai CY, Corces VG (2003) Protein phosphatase 2A activity affects histone H3 phosphorylation and transcription in Drosophila melanogaster. *Mol Cell Biol* **23:** 6129–6138

Oliveria SF, Dell'Acqua ML, Sather WA (2007) AKAP79/150 anchoring of calcineurin controls neuronal L-type Ca2+ channel activity and nuclear signaling. *Neuron* **55:** 261–275

Peris L, Wagenbach M, Lafanechere L, Brocard J, Moore AT, Kozielski F, Job D, Wordeman L, Andrieux A (2009) Motor-dependent microtubule disassembly driven by tubulin tyrosination. *J Cell Biol* **185:** 1159–1166

Restituito S, Cens T, Rousset M, Charnet P (2001) Ca(2+) channel inactivation heterogeneity reveals physiological unbinding of auxiliary beta subunits. *Biophys J* **81:** 89–96

Robert JJ, Geoffroy MC, Finiels F, Mallet J (1997) An adenoviral vector-based system to study neuronal gene expression: analysis of the rat tyrosine hydroxylase promoter in cultured neurons. *J Neurochem* **68:** 2152–2160

Rosen LB, Ginty DD, Weber MJ, Greenberg ME (1994) Membrane depolarization and calcium influx stimulate MEK and MAP kinase via activation of Ras. *Neuron* **12:** 1207–1221

Sandoz G, Lopez-Gonzalez I, Grunwald D, Bichet D, Altafaj X, Weiss N, Ronjat M, Dupuis A, De Waard M (2004) Cavbeta-subunit displacement is a key step to induce the reluctant state of P/Q calcium channels by direct G protein regulation. *Proc Natl Acad Sci USA* **101:** 6267–6272

Sng JC, Taniura H, Yoneda Y (2006) Histone modifications in kainate-induced status epilepticus. *Eur J Neurosci* **23:** 1269–1282

Spafford JD, Van Minnen J, Larsen P, Smit AB, Syed NI, Zamponi GW (2004) Uncoupling of calcium channel alpha1 and beta subunits in developing neurons. *J Biol Chem* **279:** 41157–41167

Stipanovich A, Valjent E, Matamales M, Nishi A, Ahn JH, Maroteaux M, Bertran-Gonzalez J, Brami-Cherrier K, Enslen H, Corbille AG, Filhol O, Nairn AC, Greengard P, Herve D, Girault JA (2008) A phosphatase cascade by which rewarding stimuli control nucleosomal response. *Nature* **453:** 879–884

Subramanyam P, Obermair GJ, Baumgartner S, Gebhart M, Striessnig J, Kaufmann WA, Geley S, Flucher BE (2009) Activity and calcium regulate nuclear targeting of the calcium channel beta(4b) subunit in nerve and muscle cells. *Channels (Austin)* **3:** 343–355

Takahashi SX, Miriyala J, Colecraft HM (2004) Membrane-associated guanylate kinase-like properties of beta-subunits required for modulation of voltage-dependent Ca2+ channels. *Proc Natl Acad Sci USA* **101:** 7193–7198

Takahashi SX, Miriyala J, Tay LH, Yue DT, Colecraft HM (2005) A CaVbeta SH3/guanylate kinase domain interaction regulates multiple properties of voltage-gated Ca2+ channels. *J Gen Physiol* **126:** 365–377

Vandesompele J, De Preter K, Pattyn F, Poppe B, Van Roy N, De Paepe A, Speleman F (2002) Accurate normalization of real-time quantitative RT-PCR data by geometric averaging of multiple internal control genes. *Genome Biol* **3:** 34

Xu X, Lee YJ, Holm JB, Terry MD, Oswald RE, Horne WA (2011) The Ca2+ channel beta4c subunit interacts with heterochromatin protein 1 via a PXVXL binding motif. *J Biol Chem* **286:** 9677–9687

REFERENCES

1. Opalinska, J. B., and Gewirtz, A. M. (2002) Nucleic-acid therapeutics: basic principles and recent applications, *Nat Rev Drug Discov 1*, 503-514.
2. Jarver, P., and Langel, U. (2004) The use of cell-penetrating peptides as a tool for gene regulation, *Drug Discov Today 9*, 395-402.
3. Glover, D. J., Lipps, H. J., and Jans, D. A. (2005) Towards safe, non-viral therapeutic gene expression in humans, *Nat Rev Genet 6*, 299-310.
4. Torchilin, V. P. (2005) Recent advances with liposomes as pharmaceutical carriers, *Nat Rev Drug Discov 4*, 145-160.
5. de Fougerolles, A., Vornlocher, H. P., Maraganore, J., and Lieberman, J. (2007) Interfering with disease: a progress report on siRNA-based therapeutics, *Nat Rev Drug Discov 6*, 443-453.
6. Kong, H. J., and Mooney, D. J. (2007) Microenvironmental regulation of biomacromolecular therapies, *Nat Rev Drug Discov 6*, 455-463.
7. Joliot, A., and Prochiantz, A. (2004) Transduction peptides: from technology to physiology, *Nat Cell Biol 6*, 189-196.
8. Green, M., and Loewenstein, P. M. (1988) Autonomous functional domains of chemically synthesized human immunodeficiency virus tat trans-activator protein, *Cell 55*, 1179-1188.
9. Derossi, D., Joliot, A. H., Chassaing, G., and Prochiantz, A. (1994) The third helix of the Antennapedia homeodomain translocates through biological membranes, *J Biol Chem 269*, 10444-10450.
10. Elliott, G., and O'Hare, P. (1999) Intercellular trafficking of VP22-GFP fusion proteins, *Gene Ther 6*, 149-151.
11. Tilstra, J., Rehman, K. K., Hennon, T., Plevy, S. E., Clemens, P., and Robbins, P. D. (2007) Protein transduction: identification, characterization and optimization, *Biochem Soc Trans 35*, 811-815.
12. Richard, J. P., Melikov, K., Vives, E., Ramos, C., Verbeure, B., Gait, M. J., Chernomordik, L. V., and Lebleu, B. (2003) Cell-penetrating peptides. A reevaluation of the mechanism of cellular uptake, *J Biol Chem 278*, 585-590.
13. Wadia, J. S., Stan, R. V., and Dowdy, S. F. (2004) Transducible TAT-HA fusogenic peptide enhances escape of TAT-fusion proteins after lipid raft macropinocytosis, *Nat Med 10*, 310-315.
14. Veach, R. A., Liu, D., Yao, S., Chen, Y., Liu, X. Y., Downs, S., and Hawiger, J. (2004) Receptor/transporter-independent targeting of functional peptides across the plasma membrane, *J Biol Chem 279*, 11425-11431.
15. Rothe, R., Liguori, L., Villegas-Mendez, A., Marques, B., Grunwald, D., Drouet, E., and Lenormand, J. L. (2010) Characterization of the cell-penetrating properties of the Epstein-Barr virus ZEBRA trans-activator, *J Biol Chem 285*, 20224-20233.
16. Poillot, C., Dridi, K., Bichraoui, H., Pecher, J., Alphonse, S., Douzi, B., Ronjat, M., Darbon, H., and De Waard, M. (2010) D-Maurocalcine, a pharmacologically inert efficient cell-penetrating peptide analogue, *J Biol Chem 285*, 34168-34180.
17. Mabrouk, K., Ram, N., Boisseau, S., Strappazzon, F., Rehaim, A., Sadoul, R., Darbon, H., Ronjat, M., and De Waard, M. (2007) Critical amino acid residues of maurocalcine involved in pharmacology, lipid interaction and cell penetration, *Biochim Biophys Acta 1768*, 2528-2540.
18. Ram, N., Weiss, N., Texier-Nogues, I., Aroui, S., Andreotti, N., Pirollet, F., Ronjat, M., Sabatier, J. M., Darbon, H., Jacquemond, V., and De Waard, M. (2008) Design of a disulfide-less, pharmacologically inert, and chemically competent analog of maurocalcine for the efficient transport of impermeant compounds into cells, *J Biol Chem 283*, 27048-27056.
19. Gorter, E., and Grendel, F. (1925) On Bimolecular Layers of Lipoids on the Chromocytes of the Blood, *J Exp Med 41*, 439-443.

20. Cooper, G. (2000) *The Cell: A Molecular Approach. 2nd edition*, Sunderland, MA.
21. Heitz, F., Morris, M. C., and Divita, G. (2009) Twenty years of cell-penetrating peptides: from molecular mechanisms to therapeutics, *Br J Pharmacol 157*, 195-206.
22. Wilson, R. (2010) The extracellular matrix: an underexplored but important proteome, *Expert Rev Proteomics 7*, 803-806.
23. Yanagishita, M., Podyma-Inoue, K. A., and Yokoyama, M. (2009) Extraction and separation of proteoglycans, *Glycoconj J 26*, 953-959.
24. Charnaux, N. Fonctions des protéoglycanes à héparane sulfate.
25. Slepnev, V. I., and De Camilli, P. (2000) Accessory factors in clathrin-dependent synaptic vesicle endocytosis, *Nat Rev Neurosci 1*, 161-172.
26. Conner, S. D., and Schmid, S. L. (2003) Regulated portals of entry into the cell, *Nature 422*, 37-44.
27. Bashkirov, P. V., Akimov, S. A., Evseev, A. I., Schmid, S. L., Zimmerberg, J., and Frolov, V. A. (2008) GTPase cycle of dynamin is coupled to membrane squeeze and release, leading to spontaneous fission, *Cell 135*, 1276-1286.
28. Pucadyil, T. J., and Schmid, S. L. (2008) Real-time visualization of dynamin-catalyzed membrane fission and vesicle release, *Cell 135*, 1263-1275.
29. Roux, A., and Antonny, B. (2008) The long and short of membrane fission, *Cell 135*, 1163-1165.
30. Stan, R. V. (2002) Structure and function of endothelial caveolae, *Microsc Res Tech 57*, 350-364.
31. Rothberg, K. G., Heuser, J. E., Donzell, W. C., Ying, Y. S., Glenney, J. R., and Anderson, R. G. (1992) Caveolin, a protein component of caveolae membrane coats, *Cell 68*, 673-682.
32. Thomsen, P., Roepstorff, K., Stahlhut, M., and van Deurs, B. (2002) Caveolae are highly immobile plasma membrane microdomains, which are not involved in constitutive endocytic trafficking, *Mol Biol Cell 13*, 238-250.
33. Pelkmans, L., Burli, T., Zerial, M., and Helenius, A. (2004) Caveolin-stabilized membrane domains as multifunctional transport and sorting devices in endocytic membrane traffic, *Cell 118*, 767-780.
34. Hommelgaard, A. M., Roepstorff, K., Vilhardt, F., Torgersen, M. L., Sandvig, K., and van Deurs, B. (2005) Caveolae: stable membrane domains with a potential for internalization, *Traffic 6*, 720-724.
35. Parton, R. G., Hanzal-Bayer, M., and Hancock, J. F. (2006) Biogenesis of caveolae: a structural model for caveolin-induced domain formation, *J Cell Sci 119*, 787-796.
36. Kirkham, M., Fujita, A., Chadda, R., Nixon, S. J., Kurzchalia, T. V., Sharma, D. K., Pagano, R. E., Hancock, J. F., Mayor, S., and Parton, R. G. (2005) Ultrastructural identification of uncoated caveolin-independent early endocytic vehicles, *J Cell Biol 168*, 465-476.
37. Lajoie, P., and Nabi, I. R. (2007) Regulation of raft-dependent endocytosis, *J Cell Mol Med 11*, 644-653.
38. Le, P. U., Guay, G., Altschuler, Y., and Nabi, I. R. (2002) Caveolin-1 is a negative regulator of caveolae-mediated endocytosis to the endoplasmic reticulum, *J Biol Chem 277*, 3371-3379.
39. Damm, E. M., Pelkmans, L., Kartenbeck, J., Mezzacasa, A., Kurzchalia, T., and Helenius, A. (2005) Clathrin- and caveolin-1-independent endocytosis: entry of simian virus 40 into cells devoid of caveolae, *J Cell Biol 168*, 477-488.
40. Parton, R. G., Joggerst, B., and Simons, K. (1994) Regulated internalization of caveolae, *J Cell Biol 127*, 1199-1215.
41. Sverdlov, M., Shajahan, A. N., and Minshall, R. D. (2007) Tyrosine phosphorylation-dependence of caveolae-mediated endocytosis, *J Cell Mol Med 11*, 1239-1250.

42. Blanchet, M. H., Le Good, J. A., Mesnard, D., Oorschot, V., Baflast, S., Minchiotti, G., Klumperman, J., and Constam, D. B. (2008) Cripto recruits Furin and PACE4 and controls Nodal trafficking during proteolytic maturation, *EMBO J 27*, 2580-2591.
43. Sabharanjak, S., Sharma, P., Parton, R. G., and Mayor, S. (2002) GPI-anchored proteins are delivered to recycling endosomes via a distinct cdc42-regulated, clathrin-independent pinocytic pathway, *Dev Cell 2*, 411-423.
44. Frick, M., Bright, N. A., Riento, K., Bray, A., Merrified, C., and Nichols, B. J. (2007) Coassembly of flotillins induces formation of membrane microdomains, membrane curvature, and vesicle budding, *Curr Biol 17*, 1151-1156.
45. Glebov, O. O., Bright, N. A., and Nichols, B. J. (2006) Flotillin-1 defines a clathrin-independent endocytic pathway in mammalian cells, *Nat Cell Biol 8*, 46-54.
46. Swanson, J. A., and Watts, C. (1995) Macropinocytosis, *Trends Cell Biol 5*, 424-428.
47. Nichols, B. (2003) Caveosomes and endocytosis of lipid rafts, *J Cell Sci 116*, 4707-4714.
48. Pooga, M., Hallbrink, M., Zorko, M., and Langel, U. (1998) Cell penetration by transportan, *FASEB J 12*, 67-77.
49. Yeaman, M. R., and Yount, N. Y. (2003) Mechanisms of antimicrobial peptide action and resistance, *Pharmacol Rev 55*, 27-55.
50. Herbig, M. E., Weller, K., Krauss, U., Beck-Sickinger, A. G., Merkle, H. P., and Zerbe, O. (2005) Membrane surface-associated helices promote lipid interactions and cellular uptake of human calcitonin-derived cell penetrating peptides, *Biophys J 89*, 4056-4066.
51. Derossi, D., Calvet, S., Trembleau, A., Brunissen, A., Chassaing, G., and Prochiantz, A. (1996) Cell internalization of the third helix of the Antennapedia homeodomain is receptor-independent, *J Biol Chem 271*, 18188-18193.
52. Shai, Y., and Oren, Z. (2001) From "carpet" mechanism to de-novo designed diastereomeric cell-selective antimicrobial peptides, *Peptides 22*, 1629-1641.
53. Lundberg, P., and Langel, U. (2003) A brief introduction to cell-penetrating peptides, *J Mol Recognit 16*, 227-233.
54. Ehrenstein, G., and Lecar, H. (1977) Electrically gated ionic channels in lipid bilayers, *Q Rev Biophys 10*, 1-34.
55. Breukink, E., and de Kruijff, B. (1999) The lantibiotic nisin, a special case or not?, *Biochim Biophys Acta 1462*, 223-234.
56. Murriel, C. L., and Dowdy, S. F. (2006) Influence of protein transduction domains on intracellular delivery of macromolecules, *Expert Opin Drug Deliv 3*, 739-746.
57. Frankel, A. D., and Pabo, C. O. (1988) Cellular uptake of the tat protein from human immunodeficiency virus, *Cell 55*, 1189-1193.
58. Joliot, A., Pernelle, C., Deagostini-Bazin, H., and Prochiantz, A. (1991) Antennapedia homeobox peptide regulates neural morphogenesis, *Proc Natl Acad Sci U S A 88*, 1864-1868.
59. Vives, E., Brodin, P., and Lebleu, B. (1997) A truncated HIV-1 Tat protein basic domain rapidly translocates through the plasma membrane and accumulates in the cell nucleus, *J Biol Chem 272*, 16010-16017.
60. Fajloun, Z., Kharrat, R., Chen, L., Lecomte, C., Di Luccio, E., Bichet, D., El Ayeb, M., Rochat, H., Allen, P. D., Pessah, I. N., De Waard, M., and Sabatier, J. M. (2000) Chemical synthesis and characterization of maurocalcine, a scorpion toxin that activates Ca(2+) release channel/ryanodine receptors, *FEBS Lett 469*, 179-185.
61. Aroui, S., Ram, N., Appaix, F., Ronjat, M., Kenani, A., Pirollet, F., and De Waard, M. (2009) Maurocalcine as a non toxic drug carrier overcomes doxorubicin resistance in the cancer cell line MDA-MB 231, *Pharm Res 26*, 836-845.
62. Johnson, J. L., Lowell, B. C., Ryabinina, O. P., Lloyd, R. S., and McCullough, A. K. (2010) TAT-mediated delivery of a DNA repair enzyme to skin cells rapidly initiates repair of UV-induced DNA damage, *J Invest Dermatol 131*, 753-761.

63. Pooga, M., Kut, C., Kihlmark, M., Hallbrink, M., Fernaeus, S., Raid, R., Land, T., Hallberg, E., Bartfai, T., and Langel, U. (2001) Cellular translocation of proteins by transportan, *FASEB J 15*, 1451-1453.
64. Chaubey, B., Tripathi, S., Ganguly, S., Harris, D., Casale, R. A., and Pandey, V. N. (2005) A PNA-transportan conjugate targeted to the TAR region of the HIV-1 genome exhibits both antiviral and virucidal properties, *Virology 331*, 418-428.
65. Morris, M. C., Depollier, J., Mery, J., Heitz, F., and Divita, G. (2001) A peptide carrier for the delivery of biologically active proteins into mammalian cells, *Nat Biotechnol 19*, 1173-1176.
66. Kim, D. W., Jeong, H. J., Kang, H. W., Shin, M. J., Sohn, E. J., Kim, M. J., Ahn, E. H., An, J. J., Jang, S. H., Yoo, K. Y., Won, M. H., Kang, T. C., Hwang, I. K., Kwon, O. S., Cho, S. W., Park, J., Eum, W. S., and Choi, S. Y. (2009) Transduced human PEP-1-catalase fusion protein attenuates ischemic neuronal damage, *Free Radic Biol Med 47*, 941-952.
67. Morris, M. C., Vidal, P., Chaloin, L., Heitz, F., and Divita, G. (1997) A new peptide vector for efficient delivery of oligonucleotides into mammalian cells, *Nucleic Acids Res 25*, 2730-2736.
68. Crombez, L., Charnet, A., Morris, M. C., Aldrian-Herrada, G., Heitz, F., and Divita, G. (2007) A non-covalent peptide-based strategy for siRNA delivery, *Biochem Soc Trans 35*, 44-46.
69. Zhang, C., Tang, N., Liu, X., Liang, W., Xu, W., and Torchilin, V. P. (2006) siRNA-containing liposomes modified with polyarginine effectively silence the targeted gene, *J Control Release 112*, 229-239.
70. Futaki, S., Suzuki, T., Ohashi, W., Yagami, T., Tanaka, S., Ueda, K., and Sugiura, Y. (2001) Arginine-rich peptides. An abundant source of membrane-permeable peptides having potential as carriers for intracellular protein delivery, *J Biol Chem 276*, 5836-5840.
71. Wender, P. A., Mitchell, D. J., Pattabiraman, K., Pelkey, E. T., Steinman, L., and Rothbard, J. B. (2000) The design, synthesis, and evaluation of molecules that enable or enhance cellular uptake: peptoid molecular transporters, *Proc Natl Acad Sci U S A 97*, 13003-13008.
72. Schwarze, S. R., Ho, A., Vocero-Akbani, A., and Dowdy, S. F. (1999) In vivo protein transduction: delivery of a biologically active protein into the mouse, *Science 285*, 1569-1572.
73. Deshayes, S., Morris, M. C., Divita, G., and Heitz, F. (2005) Cell-penetrating peptides: tools for intracellular delivery of therapeutics, *Cell Mol Life Sci 62*, 1839-1849.
74. Snyder, E. L., and Dowdy, S. F. (2005) Recent advances in the use of protein transduction domains for the delivery of peptides, proteins and nucleic acids in vivo, *Expert Opin Drug Deliv 2*, 43-51.
75. Ziegler, A. (2008) Thermodynamic studies and binding mechanisms of cell-penetrating peptides with lipids and glycosaminoglycans, *Adv Drug Deliv Rev 60*, 580-597.
76. Soomets, U., Lindgren, M., Gallet, X., Hallbrink, M., Elmquist, A., Balaspiri, L., Zorko, M., Pooga, M., Brasseur, R., and Langel, U. (2000) Deletion analogues of transportan, *Biochim Biophys Acta 1467*, 165-176.
77. Elmquist, A., Lindgren, M., Bartfai, T., and Langel, U. (2001) VE-cadherin-derived cell-penetrating peptide, pVEC, with carrier functions, *Exp Cell Res 269*, 237-244.
78. El-Andaloussi, S., Johansson, H. J., Holm, T., and Langel, U. (2007) A novel cell-penetrating peptide, M918, for efficient delivery of proteins and peptide nucleic acids, *Mol Ther 15*, 1820-1826.
79. Lundberg, M., and Johansson, M. (2002) Positively charged DNA-binding proteins cause apparent cell membrane translocation, *Biochem Biophys Res Commun 291*, 367-371.
80. Lundberg, M., and Johansson, M. (2001) Is VP22 nuclear homing an artifact?, *Nat Biotechnol 19*, 713-714.
81. Drin, G., Mazel, M., Clair, P., Mathieu, D., Kaczorek, M., and Temsamani, J. (2001) Physico-chemical requirements for cellular uptake of pAntp peptide. Role of lipid-binding affinity, *Eur J Biochem 268*, 1304-1314.

82. Hallbrink, M., Floren, A., Elmquist, A., Pooga, M., Bartfai, T., and Langel, U. (2001) Cargo delivery kinetics of cell-penetrating peptides, *Biochim Biophys Acta 1515*, 101-109.
83. Kaplan, I. M., Wadia, J. S., and Dowdy, S. F. (2005) Cationic TAT peptide transduction domain enters cells by macropinocytosis, *J Control Release 102*, 247-253.
84. Mano, M., Teodosio, C., Paiva, A., Simoes, S., and Pedroso de Lima, M. C. (2005) On the mechanisms of the internalization of S4(13)-PV cell-penetrating peptide, *Biochem J 390*, 603-612.
85. Sandgren, S., Cheng, F., and Belting, M. (2002) Nuclear targeting of macromolecular polyanions by an HIV-Tat derived peptide. Role for cell-surface proteoglycans, *J Biol Chem 277*, 38877-38883.
86. Sieczkarski, S. B., and Whittaker, G. R. (2002) Dissecting virus entry via endocytosis, *J Gen Virol 83*, 1535-1545.
87. Magzoub, M., and Graslund, A. (2004) Cell-penetrating peptides: [corrected] from inception to application, *Q Rev Biophys 37*, 147-195.
88. Rusnati, M., Coltrini, D., Oreste, P., Zoppetti, G., Albini, A., Noonan, D., d'Adda di Fagagna, F., Giacca, M., and Presta, M. (1997) Interaction of HIV-1 Tat protein with heparin. Role of the backbone structure, sulfation, and size, *J Biol Chem 272*, 11313-11320.
89. Thoren, P. E., Persson, D., Lincoln, P., and Norden, B. (2005) Membrane destabilizing properties of cell-penetrating peptides, *Biophys Chem 114*, 169-179.
90. Patel, L. N., Zaro, J. L., and Shen, W. C. (2007) Cell penetrating peptides: intracellular pathways and pharmaceutical perspectives, *Pharm Res 24*, 1977-1992.
91. Nakase, I., Niwa, M., Takeuchi, T., Sonomura, K., Kawabata, N., Koike, Y., Takehashi, M., Tanaka, S., Ueda, K., Simpson, J. C., Jones, A. T., Sugiura, Y., and Futaki, S. (2004) Cellular uptake of arginine-rich peptides: roles for macropinocytosis and actin rearrangement, *Mol Ther 10*, 1011-1022.
92. Fischer, R., Fotin-Mleczek, M., Hufnagel, H., and Brock, R. (2005) Break on through to the other side-biophysics and cell biology shed light on cell-penetrating peptides, *Chembiochem 6*, 2126-2142.
93. Richard, J. P., Melikov, K., Brooks, H., Prevot, P., Lebleu, B., and Chernomordik, L. V. (2005) Cellular uptake of unconjugated TAT peptide involves clathrin-dependent endocytosis and heparan sulfate receptors, *J Biol Chem 280*, 15300-15306.
94. Ziegler, A., Nervi, P., Durrenberger, M., and Seelig, J. (2005) The cationic cell-penetrating peptide CPP(TAT) derived from the HIV-1 protein TAT is rapidly transported into living fibroblasts: optical, biophysical, and metabolic evidence, *Biochemistry 44*, 138-148.
95. Tunnemann, G., Martin, R. M., Haupt, S., Patsch, C., Edenhofer, F., and Cardoso, M. C. (2006) Cargo-dependent mode of uptake and bioavailability of TAT-containing proteins and peptides in living cells, *FASEB J 20*, 1775-1784.
96. Fretz, M. M., Penning, N. A., Al-Taei, S., Futaki, S., Takeuchi, T., Nakase, I., Storm, G., and Jones, A. T. (2007) Temperature-, concentration- and cholesterol-dependent translocation of L- and D-octa-arginine across the plasma and nuclear membrane of CD34+ leukaemia cells, *Biochem J 403*, 335-342.
97. Terrone, D., Sang, S. L., Roudaia, L., and Silvius, J. R. (2003) Penetratin and related cell-penetrating cationic peptides can translocate across lipid bilayers in the presence of a transbilayer potential, *Biochemistry 42*, 13787-13799.
98. Thoren, P. E., Persson, D., Isakson, P., Goksor, M., Onfelt, A., and Norden, B. (2003) Uptake of analogs of penetratin, Tat(48-60) and oligoarginine in live cells, *Biochem Biophys Res Commun 307*, 100-107.
99. Rothbard, J. B., Jessop, T. C., Lewis, R. S., Murray, B. A., and Wender, P. A. (2004) Role of membrane potential and hydrogen bonding in the mechanism of translocation of guanidinium-rich peptides into cells, *J Am Chem Soc 126*, 9506-9507.

100. Deshayes, S., Heitz, A., Morris, M. C., Charnet, P., Divita, G., and Heitz, F. (2004) Insight into the mechanism of internalization of the cell-penetrating carrier peptide Pep-1 through conformational analysis, *Biochemistry 43*, 1449-1457.
101. Guterstam, P., Madani, F., Hirose, H., Takeuchi, T., Futaki, S., El Andaloussi, S., Graslund, A., and Langel, U. (2009) Elucidating cell-penetrating peptide mechanisms of action for membrane interaction, cellular uptake, and translocation utilizing the hydrophobic counter-anion pyrenebutyrate, *Biochim Biophys Acta 1788*, 2509-2517.
102. Derossi, D., Chassaing, G., and Prochiantz, A. (1998) Trojan peptides: the penetratin system for intracellular delivery, *Trends Cell Biol 8*, 84-87.
103. Oehlke, J., Scheller, A., Wiesner, B., Krause, E., Beyermann, M., Klauschenz, E., Melzig, M., and Bienert, M. (1998) Cellular uptake of an alpha-helical amphipathic model peptide with the potential to deliver polar compounds into the cell interior non-endocytically, *Biochim Biophys Acta 1414*, 127-139.
104. Cartier, R., and Reszka, R. (2002) Utilization of synthetic peptides containing nuclear localization signals for nonviral gene transfer systems, *Gene Ther 9*, 157-167.
105. Simeoni, F., Morris, M. C., Heitz, F., and Divita, G. (2003) Insight into the mechanism of the peptide-based gene delivery system MPG: implications for delivery of siRNA into mammalian cells, *Nucleic Acids Res 31*, 2717-2724.
106. Nagahara, H., Vocero-Akbani, A. M., Snyder, E. L., Ho, A., Latham, D. G., Lissy, N. A., Becker-Hapak, M., Ezhevsky, S. A., and Dowdy, S. F. (1998) Transduction of full-length TAT fusion proteins into mammalian cells: TAT-p27Kip1 induces cell migration, *Nat Med 4*, 1449-1452.
107. Gait, M. J. (2003) Peptide-mediated cellular delivery of antisense oligonucleotides and their analogues, *Cell Mol Life Sci 60*, 844-853.
108. Moulton, H. M., and Moulton, J. D. (2004) Arginine-rich cell-penetrating peptides with uncharged antisense oligomers, *Drug Discov Today 9*, 870.
109. Zatsepin, T. S., Turner, J. J., Oretskaya, T. S., and Gait, M. J. (2005) Conjugates of oligonucleotides and analogues with cell penetrating peptides as gene silencing agents, *Curr Pharm Des 11*, 3639-3654.
110. Koppelhus, U., Awasthi, S. K., Zachar, V., Holst, H. U., Ebbesen, P., and Nielsen, P. E. (2002) Cell-dependent differential cellular uptake of PNA, peptides, and PNA-peptide conjugates, *Antisense Nucleic Acid Drug Dev 12*, 51-63.
111. Abes, S., Moulton, H. M., Clair, P., Prevot, P., Youngblood, D. S., Wu, R. P., Iversen, P. L., and Lebleu, B. (2006) Vectorization of morpholino oligomers by the (R-Ahx-R)4 peptide allows efficient splicing correction in the absence of endosomolytic agents, *J Control Release 116*, 304-313.
112. Lebleu, B., Moulton, H. M., Abes, R., Ivanova, G. D., Abes, S., Stein, D. A., Iversen, P. L., Arzumanov, A. A., and Gait, M. J. (2008) Cell penetrating peptide conjugates of steric block oligonucleotides, *Adv Drug Deliv Rev 60*, 517-529.
113. Juliano, R., Alam, M. R., Dixit, V., and Kang, H. (2008) Mechanisms and strategies for effective delivery of antisense and siRNA oligonucleotides, *Nucleic Acids Res 36*, 4158-4171.
114. Morris, M. C., Deshayes, S., Heitz, F., and Divita, G. (2008) Cell-penetrating peptides: from molecular mechanisms to therapeutics, *Biol Cell 100*, 201-217.
115. Lear, J. D., and DeGrado, W. F. (1987) Membrane binding and conformational properties of peptides representing the NH2 terminus of influenza HA-2, *J Biol Chem 262*, 6500-6505.
116. Parente, R. A., Nadasdi, L., Subbarao, N. K., and Szoka, F. C., Jr. (1990) Association of a pH-sensitive peptide with membrane vesicles: role of amino acid sequence, *Biochemistry 29*, 8713-8719.
117. Dietz, G. P., and Bahr, M. (2004) Delivery of bioactive molecules into the cell: the Trojan horse approach, *Mol Cell Neurosci 27*, 85-131.

118. Gros, E., Deshayes, S., Morris, M. C., Aldrian-Herrada, G., Depollier, J., Heitz, F., and Divita, G. (2006) A non-covalent peptide-based strategy for protein and peptide nucleic acid transduction, *Biochim Biophys Acta 1758*, 384-393.
119. Foerg, C., and Merkle, H. P. (2008) On the biomedical promise of cell penetrating peptides: limits versus prospects, *J Pharm Sci 97*, 144-162.
120. Tung, C. H., Mueller, S., and Weissleder, R. (2002) Novel branching membrane translocational peptide as gene delivery vector, *Bioorg Med Chem 10*, 3609-3614.
121. Ignatovich, I. A., Dizhe, E. B., Pavlotskaya, A. V., Akifiev, B. N., Burov, S. V., Orlov, S. V., and Perevozchikov, A. P. (2003) Complexes of plasmid DNA with basic domain 47-57 of the HIV-1 Tat protein are transferred to mammalian cells by endocytosis-mediated pathways, *J Biol Chem 278*, 42625-42636.
122. Rudolph, C., Plank, C., Lausier, J., Schillinger, U., Muller, R. H., and Rosenecker, J. (2003) Oligomers of the arginine-rich motif of the HIV-1 TAT protein are capable of transferring plasmid DNA into cells, *J Biol Chem 278*, 11411-11418.
123. Kogure, K., Moriguchi, R., Sasaki, K., Ueno, M., Futaki, S., and Harashima, H. (2004) Development of a non-viral multifunctional envelope-type nano device by a novel lipid film hydration method, *J Control Release 98*, 317-323.
124. MacKay, J. A., Li, W., Huang, Z., Dy, E. E., Huynh, G., Tihan, T., Collins, R., Deen, D. F., and Szoka, F. C., Jr. (2008) HIV TAT peptide modifies the distribution of DNA nanolipoparticles following convection-enhanced delivery, *Mol Ther 16*, 893-900.
125. Rittner, K., Benavente, A., Bompard-Sorlet, A., Heitz, F., Divita, G., Brasseur, R., and Jacobs, E. (2002) New basic membrane-destabilizing peptides for plasmid-based gene delivery in vitro and in vivo, *Mol Ther 5*, 104-114.
126. Morris, M. C., Chaloin, L., Mery, J., Heitz, F., and Divita, G. (1999) A novel potent strategy for gene delivery using a single peptide vector as a carrier, *Nucleic Acids Res 27*, 3510-3517.
127. Escriou, V., Carriere, M., Scherman, D., and Wils, P. (2003) NLS bioconjugates for targeting therapeutic genes to the nucleus, *Adv Drug Deliv Rev 55*, 295-306.
128. Morris, M. C., Gros, E., Aldrian-Herrada, G., Choob, M., Archdeacon, J., Heitz, F., and Divita, G. (2007) A non-covalent peptide-based carrier for in vivo delivery of DNA mimics, *Nucleic Acids Res 35*, e49.
129. Koppelhus, U., and Nielsen, P. E. (2003) Cellular delivery of peptide nucleic acid (PNA), *Adv Drug Deliv Rev 55*, 267-280.
130. Abes, S., Turner, J. J., Ivanova, G. D., Owen, D., Williams, D., Arzumanov, A., Clair, P., Gait, M. J., and Lebleu, B. (2007) Efficient splicing correction by PNA conjugation to an R6-Penetratin delivery peptide, *Nucleic Acids Res 35*, 4495-4502.
131. Elbashir, S. M., Harborth, J., Lendeckel, W., Yalcin, A., Weber, K., and Tuschl, T. (2001) Duplexes of 21-nucleotide RNAs mediate RNA interference in cultured mammalian cells, *Nature 411*, 494-498.
132. Hannon, G. J. (2002) RNA interference, *Nature 418*, 244-251.
133. Fisher, L., Soomets, U., Cortes Toro, V., Chilton, L., Jiang, Y., Langel, U., and Iverfeldt, K. (2004) Cellular delivery of a double-stranded oligonucleotide NFkappaB decoy by hybridization to complementary PNA linked to a cell-penetrating peptide, *Gene Ther 11*, 1264-1272.
134. El-Andaloussi, S., Holm, T., and Langel, U. (2005) Cell-penetrating peptides: mechanisms and applications, *Curr Pharm Des 11*, 3597-3611.
135. Marthinet, E., Divita, G., Bernaud, J., Rigal, D., and Baggetto, L. G. (2000) Modulation of the typical multidrug resistance phenotype by targeting the MED-1 region of human MDR1 promoter, *Gene Ther 7*, 1224-1233.
136. Asai, A., Oshima, Y., Yamamoto, Y., Uochi, T. A., Kusaka, H., Akinaga, S., Yamashita, Y., Pongracz, K., Pruzan, R., Wunder, E., Piatyszek, M., Li, S., Chin, A. C., Harley, C. B., and

Gryaznov, S. (2003) A novel telomerase template antagonist (GRN163) as a potential anticancer agent, *Cancer Res 63*, 3931-3939.

137. Gryaznov, S., Asai, A., Oshima, Y., Yamamoto, Y., Pongracz, K., Pruzan, R., Wunder, E., Piatyszek, M., Li, S., Chin, A., Harley, C., Akinaga, S., and Yamashita, Y. (2003) Oligonucleotide N3' --> P5' thio-phosphoramidate telomerase template antagonists as potential anticancer agents, *Nucleosides Nucleotides Nucleic Acids 22*, 577-581.
138. Rousselle, C., Smirnova, M., Clair, P., Lefauconnier, J. M., Chavanieu, A., Calas, B., Scherrmann, J. M., and Temsamani, J. (2001) Enhanced delivery of doxorubicin into the brain via a peptide-vector-mediated strategy: saturation kinetics and specificity, *J Pharmacol Exp Ther 296*, 124-131.
139. Hosotani, R., Miyamoto, Y., Fujimoto, K., Doi, R., Otaka, A., Fujii, N., and Imamura, M. (2002) Trojan p16 peptide suppresses pancreatic cancer growth and prolongs survival in mice, *Clin Cancer Res 8*, 1271-1276.
140. Snyder, E. L., Meade, B. R., Saenz, C. C., and Dowdy, S. F. (2004) Treatment of terminal peritoneal carcinomatosis by a transducible p53-activating peptide, *PLoS Biol 2*, E36.
141. Gondeau, C., Gerbal-Chaloin, S., Bello, P., Aldrian-Herrada, G., Morris, M. C., and Divita, G. (2005) Design of a novel class of peptide inhibitors of cyclin-dependent kinase/cyclin activation, *J Biol Chem 280*, 13793-13800.
142. Michl, J., Scharf, B., Schmidt, A., Huynh, C., Hannan, R., von Gizycki, H., Friedman, F. K., Brandt-Rauf, P., Fine, R. L., and Pincus, M. R. (2006) PNC-28, a p53-derived peptide that is cytotoxic to cancer cells, blocks pancreatic cancer cell growth in vivo, *Int J Cancer 119*, 1577-1585.
143. Knight, J. S., Lan, K., Bajaj, B., Sharma, N., Tsai, D. E., and Robertson, E. S. (2006) A peptide-based inhibitor for prevention of B cell hyperproliferation induced by Epstein-Barr virus, *Virology 354*, 207-214.
144. Tang, X., Molina, M., and Amar, S. (2007) p53 short peptide (p53pep164) regulates lipopolysaccharide-induced tumor necrosis factor-alpha factor/cytokine expression, *Cancer Res 67*, 1308-1316.
145. Bowne, W. B., Michl, J., Bluth, M. H., Zenilman, M. E., and Pincus, M. R. (2007) Novel peptides from the RAS-p21 and p53 proteins for the treatment of cancer, *Cancer Ther 5B*, 331-344.
146. Myou, S., Leff, A. R., Myo, S., Boetticher, E., Meliton, A. Y., Lambertino, A. T., Liu, J., Xu, C., Munoz, N. M., and Zhu, X. (2003) Activation of group IV cytosolic phospholipase A2 in human eosinophils by phosphoinositide 3-kinase through a mitogen-activated protein kinase-independent pathway, *J Immunol 171*, 4399-4405.
147. Cao, G., Pei, W., Ge, H., Liang, Q., Luo, Y., Sharp, F. R., Lu, A., Ran, R., Graham, S. H., and Chen, J. (2002) In Vivo Delivery of a Bcl-xL Fusion Protein Containing the TAT Protein Transduction Domain Protects against Ischemic Brain Injury and Neuronal Apoptosis, *J Neurosci 22*, 5423-5431.
148. Bright, R., Raval, A. P., Dembner, J. M., Perez-Pinzon, M. A., Steinberg, G. K., Yenari, M. A., and Mochly-Rosen, D. (2004) Protein kinase C delta mediates cerebral reperfusion injury in vivo, *J Neurosci 24*, 6880-6888.
149. Rhyner, C., Kundig, T., Akdis, C. A., and Crameri, R. (2007) Targeting the MHC II presentation pathway in allergy vaccine development, *Biochem Soc Trans 35*, 833-834.
150. Muller, G. J. (1993) Scorpionism in South Africa. A report of 42 serious scorpion envenomations, *S Afr Med J 83*, 405-411.
151. Gwee, M. C., Nirthanan, S., Khoo, H. E., Gopalakrishnakone, P., Kini, R. M., and Cheah, L. S. (2002) Autonomic effects of some scorpion venoms and toxins, *Clin Exp Pharmacol Physiol 29*, 795-801.

152. Catterall, W. A. (1980) Neurotoxins that act on voltage-sensitive sodium channels in excitable membranes, *Annu Rev Pharmacol Toxicol 20*, 15-43.
153. Valdivia, H. H., Kirby, M. S., Lederer, W. J., and Coronado, R. (1992) Scorpion toxins targeted against the sarcoplasmic reticulum Ca(2+)-release channel of skeletal and cardiac muscle, *Proc Natl Acad Sci U S A 89*, 12185-12189.
154. Garcia, M. L., Hanner, M., Knaus, H. G., Koch, R., Schmalhofer, W., Slaughter, R. S., and Kaczorowski, G. J. (1997) Pharmacology of potassium channels, *Adv Pharmacol 39*, 425-471.
155. Miranda, F., Kupeyan, C., Rochat, H., Rochat, C., and Lissitzky, S. (1970) Purification of animal neurotoxins. Isolation and characterization of eleven neurotoxins from the venoms of the scorpions Androctonus australis hector, Buthus occitanus tunetanus and Leiurus quinquestriatus quinquestriatus, *Eur J Biochem 16*, 514-523.
156. Rochat, H., Bernard, P., and Couraud, F. (1979) Scorpion toxins: chemistry and mode of action, *Adv Cytopharmacol 3*, 325-334.
157. Kobayashi, Y., Takashima, H., Tamaoki, H., Kyogoku, Y., Lambert, P., Kuroda, H., Chino, N., Watanabe, T. X., Kimura, T., Sakakibara, S., and et al. (1991) The cystine-stabilized alpha-helix: a common structural motif of ion-channel blocking neurotoxic peptides, *Biopolymers 31*, 1213-1220.
158. Fontecilla-Camps, J. C., Almassy, R. J., Suddath, F. L., Watt, D. D., and Bugg, C. E. (1980) Three-dimensional structure of a protein from scorpion venom: a new structural class of neurotoxins, *Proc Natl Acad Sci U S A 77*, 6496-6500.
159. Lebreton, F., Delepierre, M., Ramirez, A. N., Balderas, C., and Possani, L. D. (1994) Primary and NMR three-dimensional structure determination of a novel crustacean toxin from the venom of the scorpion Centruroides limpidus limpidus Karsch, *Biochemistry 33*, 11135-11149.
160. Oren, D. A., Froy, O., Amit, E., Kleinberger-Doron, N., Gurevitz, M., and Shaanan, B. (1998) An excitatory scorpion toxin with a distinctive feature: an additional alpha helix at the C terminus and its implications for interaction with insect sodium channels, *Structure 6*, 1095-1103.
161. Legros, C., and Martin-Eauclaire, M. F. (1997) [Scorpion toxins], *C R Seances Soc Biol Fil 191*, 345-380.
162. Inceoglu, B., Lango, J., Wu, J., Hawkins, P., Southern, J., and Hammock, B. D. (2001) Isolation and characterization of a novel type of neurotoxic peptide from the venom of the South African scorpion Parabuthus transvaalicus (Buthidae), *Eur J Biochem 268*, 5407-5413.
163. Srairi-Abid, N., Guijarro, J. I., Benkhalifa, R., Mantegazza, M., Cheikh, A., Ben Aissa, M., Haumont, P. Y., Delepierre, M., and El Ayeb, M. (2005) A new type of scorpion Na+-channel-toxin-like polypeptide active on K+ channels, *Biochem J 388*, 455-464.
164. Inceoglu, B., Lango, J., Pessah, I. N., and Hammock, B. D. (2005) Three structurally related, highly potent, peptides from the venom of Parabuthus transvaalicus possess divergent biological activity, *Toxicon 45*, 727-733.
165. Carbone, E., Wanke, E., Prestipino, G., Possani, L. D., and Maelicke, A. (1982) Selective blockage of voltage-dependent K+ channels by a novel scorpion toxin, *Nature 296*, 90-91.
166. Miller, C., Moczydlowski, E., Latorre, R., and Phillips, M. (1985) Charybdotoxin, a protein inhibitor of single Ca2+-activated K+ channels from mammalian skeletal muscle, *Nature 313*, 316-318.
167. DeBin, J. A., Maggio, J. E., and Strichartz, G. R. (1993) Purification and characterization of chlorotoxin, a chloride channel ligand from the venom of the scorpion, *Am J Physiol 264*, C361-369.
168. Valdivia, H. H., and Possani, L. D. (1998) Peptide toxins as probes of ryanodine receptor structure and function, *Trends Cardiovasc Med 8*, 111-118.

169. Catterall, W. A. (1992) Cellular and molecular biology of voltage-gated sodium channels, *Physiol Rev 72*, S15-48.
170. Jover, E., Couraud, F., and Rochat, H. (1980) Two types of scorpion neurotoxins characterized by their binding to two separate receptor sites on rat brain synaptosomes, *Biochem Biophys Res Commun 95*, 1607-1614.
171. Wheeler, K. P., Watt, D. D., and Lazdunski, M. (1983) Classification of Na channel receptors specific for various scorpion toxins, *Pflugers Arch 397*, 164-165.
172. Gimenez-Gallego, G., Navia, M. A., Reuben, J. P., Katz, G. M., Kaczorowski, G. J., and Garcia, M. L. (1988) Purification, sequence, and model structure of charybdotoxin, a potent selective inhibitor of calcium-activated potassium channels, *Proc Natl Acad Sci U S A 85*, 3329-3333.
173. Crest, M., Jacquet, G., Gola, M., Zerrouk, H., Benslimane, A., Rochat, H., Mansuelle, P., and Martin-Eauclaire, M. F. (1992) Kaliotoxin, a novel peptidyl inhibitor of neuronal BK-type Ca(2+)-activated K+ channels characterized from Androctonus mauretanicus mauretanicus venom, *J Biol Chem 267*, 1640-1647.
174. Castle, N. A., and Strong, P. N. (1986) Identification of two toxins from scorpion (Leiurus quinquestriatus) venom which block distinct classes of calcium-activated potassium channel, *FEBS Lett 209*, 117-121.
175. Peter, M., Jr., Hajdu, P., Varga, Z., Damjanovich, S., Possani, L. D., Panyi, G., and Gaspar, R., Jr. (2000) Blockage of human T lymphocyte Kv1.3 channels by Pi1, a novel class of scorpion toxin, *Biochem Biophys Res Commun 278*, 34-37.
176. Goldstein, S. A., and Miller, C. (1993) Mechanism of charybdotoxin block of a voltage-gated K+ channel, *Biophys J 65*, 1613-1619.
177. DeBin, J. A., and Strichartz, G. R. (1991) Chloride channel inhibition by the venom of the scorpion Leiurus quinquestriatus, *Toxicon 29*, 1403-1408.
178. Lippens, G., Najib, J., Wodak, S. J., and Tartar, A. (1995) NMR sequential assignments and solution structure of chlorotoxin, a small scorpion toxin that blocks chloride channels, *Biochemistry 34*, 13-21.
179. Adjadj, E., Naudat, V., Quiniou, E., Wouters, D., Sautiere, P., and Craescu, C. T. (1997) Solution structure of Lqh-8/6, a toxin-like peptide from a scorpion venom--structural heterogeneity induced by proline cis/trans isomerization, *Eur J Biochem 246*, 218-227.
180. Ali, S. A., Stoeva, S., Schutz, J., Kayed, R., Abassi, A., Zaidi, Z. H., and Voelter, W. (1998) Purification and primary structure of low molecular mass peptides from scorpion (Buthus sindicus) venom, *Comp Biochem Physiol A Mol Integr Physiol 121*, 323-332.
181. Zamudio, F. Z., Gurrola, G. B., Arevalo, C., Sreekumar, R., Walker, J. W., Valdivia, H. H., and Possani, L. D. (1997) Primary structure and synthesis of Imperatoxin A (IpTx(a)), a peptide activator of Ca2+ release channels/ryanodine receptors, *FEBS Lett 405*, 385-389.
182. Shahbazzadeh, D., Srairi-Abid, N., Feng, W., Ram, N., Borchani, L., Ronjat, M., Akbari, A., Pessah, I. N., De Waard, M., and El Ayeb, M. (2007) Hemicalcin, a new toxin from the Iranian scorpion Hemiscorpius lepturus which is active on ryanodine-sensitive Ca2+ channels, *Biochem J 404*, 89-96.
183. Zhu, S., Darbon, H., Dyason, K., Verdonck, F., and Tytgat, J. (2003) Evolutionary origin of inhibitor cystine knot peptides, *FASEB J 17*, 1765-1767.
184. Schwartz, E. F., Capes, E. M., Diego-Garcia, E., Zamudio, F. Z., Fuentes, O., Possani, L. D., and Valdivia, H. H. (2009) Characterization of hadrucalcin, a peptide from Hadrurus gertschi scorpion venom with pharmacological activity on ryanodine receptors, *Br J Pharmacol 157*, 392-403.
185. Curtis, B. M., and Catterall, W. A. (1986) Reconstitution of the voltage-sensitive calcium channel purified from skeletal muscle transverse tubules, *Biochemistry 25*, 3077-3083.

186. Flockerzi, V., Oeken, H. J., Hofmann, F., Pelzer, D., Cavalie, A., and Trautwein, W. (1986) Purified dihydropyridine-binding site from skeletal muscle t-tubules is a functional calcium channel, *Nature 323*, 66-68.
187. Hosey, M. M., Barhanin, J., Schmid, A., Vandaele, S., Ptasienski, J., O'Callahan, C., Cooper, C., and Lazdunski, M. (1987) Photoaffinity labelling and phosphorylation of a 165 kilodalton peptide associated with dihydropyridine and phenylalkylamine-sensitive calcium channels, *Biochem Biophys Res Commun 147*, 1137-1145.
188. Leung, A. T., Imagawa, T., and Campbell, K. P. (1987) Structural characterization of the 1,4-dihydropyridine receptor of the voltage-dependent Ca2+ channel from rabbit skeletal muscle. Evidence for two distinct high molecular weight subunits, *J Biol Chem 262*, 7943-7946.
189. Striessnig, J., Knaus, H. G., Grabner, M., Moosburger, K., Seitz, W., Lietz, H., and Glossmann, H. (1987) Photoaffinity labelling of the phenylalkylamine receptor of the skeletal muscle transverse-tubule calcium channel, *FEBS Lett 212*, 247-253.
190. Takahashi, M., Seagar, M. J., Jones, J. F., Reber, B. F., and Catterall, W. A. (1987) Subunit structure of dihydropyridine-sensitive calcium channels from skeletal muscle, *Proc Natl Acad Sci U S A 84*, 5478-5482.
191. Perez-Reyes, E., Kim, H. S., Lacerda, A. E., Horne, W., Wei, X. Y., Rampe, D., Campbell, K. P., Brown, A. M., and Birnbaumer, L. (1989) Induction of calcium currents by the expression of the alpha 1-subunit of the dihydropyridine receptor from skeletal muscle, *Nature 340*, 233-236.
192. Lacerda, A. E., Kim, H. S., Ruth, P., Perez-Reyes, E., Flockerzi, V., Hofmann, F., Birnbaumer, L., and Brown, A. M. (1991) Normalization of current kinetics by interaction between the alpha 1 and beta subunits of the skeletal muscle dihydropyridine-sensitive Ca2+ channel, *Nature 352*, 527-530.
193. Singer, D., Biel, M., Lotan, I., Flockerzi, V., Hofmann, F., and Dascal, N. (1991) The roles of the subunits in the function of the calcium channel, *Science 253*, 1553-1557.
194. Arikkath, J., and Campbell, K. P. (2003) Auxiliary subunits: essential components of the voltage-gated calcium channel complex, *Curr Opin Neurobiol 13*, 298-307.
195. Davies, A., Hendrich, J., Van Minh, A. T., Wratten, J., Douglas, L., and Dolphin, A. C. (2007) Functional biology of the alpha(2)delta subunits of voltage-gated calcium channels, *Trends Pharmacol Sci 28*, 220-228.
196. Tsien, R. W., Lipscombe, D., Madison, D. V., Bley, K. R., and Fox, A. P. (1988) Multiple types of neuronal calcium channels and their selective modulation, *Trends Neurosci 11*, 431-438.
197. Reuter, H. (1979) Properties of two inward membrane currents in the heart, *Annu Rev Physiol 41*, 413-424.
198. Nowycky, M. C., Fox, A. P., and Tsien, R. W. (1985) Three types of neuronal calcium channel with different calcium agonist sensitivity, *Nature 316*, 440-443.
199. Olivera, B. M., Miljanich, G. P., Ramachandran, J., and Adams, M. E. (1994) Calcium channel diversity and neurotransmitter release: the omega-conotoxins and omega-agatoxins, *Annu Rev Biochem 63*, 823-867.
200. Grigoriadis, D. E., Hoare, S. R., Lechner, S. M., Slee, D. H., and Williams, J. A. (2009) Drugability of extracellular targets: discovery of small molecule drugs targeting allosteric, functional, and subunit-selective sites on GPCRs and ion channels, *Neuropsychopharmacology 34*, 106-125.
201. Llinas, R., and Yarom, Y. (1981) Electrophysiology of mammalian inferior olivary neurones in vitro. Different types of voltage-dependent ionic conductances, *J Physiol 315*, 549-567.
202. Llinas, R. R., Sugimori, M., and Cherksey, B. (1989) Voltage-dependent calcium conductances in mammalian neurons. The P channel, *Ann N Y Acad Sci 560*, 103-111.

203. Mintz, I. M., Adams, M. E., and Bean, B. P. (1992) P-type calcium channels in rat central and peripheral neurons, *Neuron 9*, 85-95.
204. Randall, A., and Tsien, R. W. (1995) Pharmacological dissection of multiple types of Ca2+ channel currents in rat cerebellar granule neurons, *J Neurosci 15*, 2995-3012.
205. Newcomb, R., Szoke, B., Palma, A., Wang, G., Chen, X., Hopkins, W., Cong, R., Miller, J., Urge, L., Tarczy-Hornoch, K., Loo, J. A., Dooley, D. J., Nadasdi, L., Tsien, R. W., Lemos, J., and Miljanich, G. (1998) Selective peptide antagonist of the class E calcium channel from the venom of the tarantula Hysterocrates gigas, *Biochemistry 37*, 15353-15362.
206. Tottene, A., Moretti, A., and Pietrobon, D. (1996) Functional diversity of P-type and R-type calcium channels in rat cerebellar neurons, *J Neurosci 16*, 6353-6363.
207. Hoth, M., and Penner, R. (1992) Depletion of intracellular calcium stores activates a calcium current in mast cells, *Nature 355*, 353-356.
208. Parekh, A. B., and Penner, R. (1997) Store depletion and calcium influx, *Physiol Rev 77*, 901-930.
209. Zweifach, A., and Lewis, R. S. (1993) Mitogen-regulated Ca2+ current of T lymphocytes is activated by depletion of intracellular Ca2+ stores, *Proc Natl Acad Sci U S A 90*, 6295-6299.
210. Gilabert, J. A., and Parekh, A. B. (2000) Respiring mitochondria determine the pattern of activation and inactivation of the store-operated Ca(2+) current I(CRAC), *EMBO J 19*, 6401-6407.
211. Hoth, M., Button, D. C., and Lewis, R. S. (2000) Mitochondrial control of calcium-channel gating: a mechanism for sustained signaling and transcriptional activation in T lymphocytes, *Proc Natl Acad Sci U S A 97*, 10607-10612.
212. Fierro, L., and Parekh, A. B. (1999) Fast calcium-dependent inactivation of calcium release-activated calcium current (CRAC) in RBL-1 cells, *J Membr Biol 168*, 9-17.
213. Hoth, M., and Penner, R. (1993) Calcium release-activated calcium current in rat mast cells, *J Physiol 465*, 359-386.
214. Zweifach, A., and Lewis, R. S. (1995) Rapid inactivation of depletion-activated calcium current (ICRAC) due to local calcium feedback, *J Gen Physiol 105*, 209-226.
215. Bakowski, D., Glitsch, M. D., and Parekh, A. B. (2001) An examination of the secretion-like coupling model for the activation of the Ca2+ release-activated Ca2+ current I(CRAC) in RBL-1 cells, *J Physiol 532*, 55-71.
216. Jacob, R. (1990) Agonist-stimulated divalent cation entry into single cultured human umbilical vein endothelial cells, *J Physiol 421*, 55-77.
217. Parekh, A. B. (1998) Slow feedback inhibition of calcium release-activated calcium current by calcium entry, *J Biol Chem 273*, 14925-14932.
218. Zweifach, A., and Lewis, R. S. (1995) Slow calcium-dependent inactivation of depletion-activated calcium current. Store-dependent and -independent mechanisms, *J Biol Chem 270*, 14445-14451.
219. Nowak, L., Bregestovski, P., Ascher, P., Herbet, A., and Prochiantz, A. (1984) Magnesium gates glutamate-activated channels in mouse central neurones, *Nature 307*, 462-465.
220. Lytton, J. (2007) Na+/Ca2+ exchangers: three mammalian gene families control Ca2+ transport, *Biochem J 406*, 365-382.
221. Airey, J. A., Grinsell, M. M., Jones, L. R., Sutko, J. L., and Witcher, D. (1993) Three ryanodine receptor isoforms exist in avian striated muscles, *Biochemistry 32*, 5739-5745.
222. Coronado, R., Morrissette, J., Sukhareva, M., and Vaughan, D. M. (1994) Structure and function of ryanodine receptors, *Am J Physiol 266*, C1485-1504.
223. Nakai, J., Imagawa, T., Hakamat, Y., Shigekawa, M., Takeshima, H., and Numa, S. (1990) Primary structure and functional expression from cDNA of the cardiac ryanodine receptor/calcium release channel, *FEBS Lett 271*, 169-177.

224. Sorrentino, V., and Volpe, P. (1993) Ryanodine receptors: how many, where and why?, *Trends Pharmacol Sci 14*, 98-103.
225. Sutko, J. L., and Airey, J. A. (1996) Ryanodine receptor Ca2+ release channels: does diversity in form equal diversity in function?, *Physiol Rev 76*, 1027-1071.
226. McPherson, P. S., and Campbell, K. P. (1993) The ryanodine receptor/Ca2+ release channel, *J Biol Chem 268*, 13765-13768.
227. Ogawa, Y. (1994) Role of ryanodine receptors, *Crit Rev Biochem Mol Biol 29*, 229-274.
228. Pozzan, T., Rizzuto, R., Volpe, P., and Meldolesi, J. (1994) Molecular and cellular physiology of intracellular calcium stores, *Physiol Rev 74*, 595-636.
229. Tarroni, P., Rossi, D., Conti, A., and Sorrentino, V. (1997) Expression of the ryanodine receptor type 3 calcium release channel during development and differentiation of mammalian skeletal muscle cells, *J Biol Chem 272*, 19808-19813.
230. Caswell, A. H., and Brandt, N. R. (1989) Does muscle activation occur by direct mechanical coupling of transverse tubules to sarcoplasmic reticulum?, *Trends Biochem Sci 14*, 161-165.
231. Rios, E., and Brum, G. (1987) Involvement of dihydropyridine receptors in excitation-contraction coupling in skeletal muscle, *Nature 325*, 717-720.
232. Schneider, M. F. (1994) Control of calcium release in functioning skeletal muscle fibers, *Annu Rev Physiol 56*, 463-484.
233. Somlyo, A. P., and Somlyo, A. V. (1986) Electron probe analysis of calcium content and movements in sarcoplasmic reticulum, endoplasmic reticulum, mitochondria, and cytoplasm, *J Cardiovasc Pharmacol 8 Suppl 8*, S42-47.
234. Fill, M., and Copello, J. A. (2002) Ryanodine receptor calcium release channels, *Physiol Rev 82*, 893-922.
235. Proenza, C., O'Brien, J., Nakai, J., Mukherjee, S., Allen, P. D., and Beam, K. G. (2002) Identification of a region of RyR1 that participates in allosteric coupling with the alpha(1S) (Ca(V)1.1) II-III loop, *J Biol Chem 277*, 6530-6535.
236. Protasi, F. (2002) Structural interaction between RYRs and DHPRs in calcium release units of cardiac and skeletal muscle cells, *Front Biosci 7*, d650-658.
237. Tanabe, T., Beam, K. G., Adams, B. A., Niidome, T., and Numa, S. (1990) Regions of the skeletal muscle dihydropyridine receptor critical for excitation-contraction coupling, *Nature 346*, 567-569.
238. Tanabe, T., Mikami, A., Niidome, T., Numa, S., Adams, B. A., and Beam, K. G. (1993) Structure and function of voltage-dependent calcium channels from muscle, *Ann N Y Acad Sci 707*, 81-86.
239. Block, B. A., Imagawa, T., Campbell, K. P., and Franzini-Armstrong, C. (1988) Structural evidence for direct interaction between the molecular components of the transverse tubule/sarcoplasmic reticulum junction in skeletal muscle, *J Cell Biol 107*, 2587-2600.
240. Ikemoto, N., Antoniu, B., and Kim, D. H. (1984) Rapid calcium release from the isolated sarcoplasmic reticulum is triggered via the attached transverse tubular system, *J Biol Chem 259*, 13151-13158.
241. Kasai, M., and Ide, T. (1996) Regulation of calcium release channel in sarcoplasmic reticulum, *Ion Channels 4*, 303-331.
242. Lamb, G. D. (1992) DHP receptors and excitation-contraction coupling, *J Muscle Res Cell Motil 13*, 394-405.
243. Margreth, A., Damiani, E., and Tobaldin, G. (1993) Ratio of dihydropyridine to ryanodine receptors in mammalian and frog twitch muscles in relation to the mechanical hypothesis of excitation-contraction coupling, *Biochem Biophys Res Commun 197*, 1303-1311.
244. Sun, X. H., Protasi, F., Takahashi, M., Takeshima, H., Ferguson, D. G., and Franzini-Armstrong, C. (1995) Molecular architecture of membranes involved in excitation-contraction coupling of cardiac muscle, *J Cell Biol 129*, 659-671.

245. Cannell, M. B., and Soeller, C. (1997) Numerical analysis of ryanodine receptor activation by L-type channel activity in the cardiac muscle diad, *Biophys J 73*, 112-122.
246. Sham, J. S., Cleemann, L., and Morad, M. (1995) Functional coupling of Ca2+ channels and ryanodine receptors in cardiac myocytes, *Proc Natl Acad Sci U S A 92*, 121-125.
247. Ferreri-Jacobia, M., Mak, D. O., and Foskett, J. K. (2005) Translational mobility of the type 3 inositol 1,4,5-trisphosphate receptor Ca2+ release channel in endoplasmic reticulum membrane, *J Biol Chem 280*, 3824-3831.
248. Otsu, H., Yamamoto, A., Maeda, N., Mikoshiba, K., and Tashiro, Y. (1990) Immunogold localization of inositol 1, 4, 5-trisphosphate (InsP3) receptor in mouse cerebellar Purkinje cells using three monoclonal antibodies, *Cell Struct Funct 15*, 163-173.
249. Ross, C. A., Meldolesi, J., Milner, T. A., Satoh, T., Supattapone, S., and Snyder, S. H. (1989) Inositol 1,4,5-trisphosphate receptor localized to endoplasmic reticulum in cerebellar Purkinje neurons, *Nature 339*, 468-470.
250. Foskett, J. K., White, C., Cheung, K. H., and Mak, D. O. (2007) Inositol trisphosphate receptor Ca2+ release channels, *Physiol Rev 87*, 593-658.
251. Berridge, M. J. (1993) Inositol trisphosphate and calcium signalling, *Nature 361*, 315-325.
252. Clapham, D. E. (1995) Calcium signaling, *Cell 80*, 259-268.
253. Thomas, A. P., Bird, G. S., Hajnoczky, G., Robb-Gaspers, L. D., and Putney, J. W., Jr. (1996) Spatial and temporal aspects of cellular calcium signaling, *FASEB J 10*, 1505-1517.
254. Zhang, Z., Lewis, D., Strock, C., Inesi, G., Nakasako, M., Nomura, H., and Toyoshima, C. (2000) Detailed characterization of the cooperative mechanism of Ca(2+) binding and catalytic activation in the Ca(2+) transport (SERCA) ATPase, *Biochemistry 39*, 8758-8767.
255. Rizzuto, R., Bernardi, P., and Pozzan, T. (2000) Mitochondria as all-round players of the calcium game, *J Physiol 529 Pt 1*, 37-47.
256. Rizzuto, R., Simpson, A. W., Brini, M., and Pozzan, T. (1992) Rapid changes of mitochondrial Ca2+ revealed by specifically targeted recombinant aequorin, *Nature 358*, 325-327.
257. Isaeva, E. V., and Shirokova, N. (2003) Metabolic regulation of Ca2+ release in permeabilized mammalian skeletal muscle fibres, *J Physiol 547*, 453-462.
258. Green, D. R., and Reed, J. C. (1998) Mitochondria and apoptosis, *Science 281*, 1309-1312.
259. McCormack, J. G., and Denton, R. M. (1990) The role of mitochondrial Ca2+ transport and matrix Ca2+ in signal transduction in mammalian tissues, *Biochim Biophys Acta 1018*, 287-291.
260. Berchtold, M. W., Brinkmeier, H., and Muntener, M. (2000) Calcium ion in skeletal muscle: its crucial role for muscle function, plasticity, and disease, *Physiol Rev 80*, 1215-1265.
261. Farah, C. S., and Reinach, F. C. (1995) The troponin complex and regulation of muscle contraction, *FASEB J 9*, 755-767.
262. Henrotte, J. G. (1952) A crystalline constituent from myogen of carp muscles, *Nature 169*, 968-969.
263. Fohr, U. G., Weber, B. R., Muntener, M., Staudenmann, W., Hughes, G. J., Frutiger, S., Banville, D., Schafer, B. W., and Heizmann, C. W. (1993) Human alpha and beta parvalbumins. Structure and tissue-specific expression, *Eur J Biochem 215*, 719-727.
264. Kasri, N. N., Torok, K., Galione, A., Garnham, C., Callewaert, G., Missiaen, L., Parys, J. B., and De Smedt, H. (2006) Endogenously bound calmodulin is essential for the function of the inositol 1,4,5-trisphosphate receptor, *J Biol Chem 281*, 8332-8338.
265. Wright, N. T., Prosser, B. L., Varney, K. M., Zimmer, D. B., Schneider, M. F., and Weber, D. J. (2008) S100A1 and calmodulin compete for the same binding site on ryanodine receptor, *J Biol Chem 283*, 26676-26683.
266. Donoso, P., and Hidalgo, C. (1989) Sodium-calcium exchange in transverse tubules isolated from frog skeletal muscle, *Biochim Biophys Acta 978*, 8-16.
267. Berridge, M. J. (2012) OFF Mechanisms

Cell Signalling Biology.

268. Neher, E. (1998) Vesicle pools and Ca2+ microdomains: new tools for understanding their roles in neurotransmitter release, *Neuron 20*, 389-399.
269. Prakriya, M., Solaro, C. R., and Lingle, C. J. (1996) [Ca2+]i elevations detected by BK channels during Ca2+ influx and muscarine-mediated release of Ca2+ from intracellular stores in rat chromaffin cells, *J Neurosci 16*, 4344-4359.
270. Mogami, H., Nakano, K., Tepikin, A. V., and Petersen, O. H. (1997) Ca2+ flow via tunnels in polarized cells: recharging of apical Ca2+ stores by focal Ca2+ entry through basal membrane patch, *Cell 88*, 49-55.
271. Berridge, M. J., Bootman, M. D., and Roderick, H. L. (2003) Calcium signalling: dynamics, homeostasis and remodelling, *Nat Rev Mol Cell Biol 4*, 517-529.
272. el-Hayek, R., Lokuta, A. J., Arevalo, C., and Valdivia, H. H. (1995) Peptide probe of ryanodine receptor function. Imperatoxin A, a peptide from the venom of the scorpion Pandinus imperator, selectively activates skeletal-type ryanodine receptor isoforms, *J Biol Chem 270*, 28696-28704.
273. Esteve, E., Smida-Rezgui, S., Sarkozi, S., Szegedi, C., Regaya, I., Chen, L., Altafaj, X., Rochat, H., Allen, P., Pessah, I. N., Marty, I., Sabatier, J. M., Jona, I., De Waard, M., and Ronjat, M. (2003) Critical amino acid residues determine the binding affinity and the Ca2+ release efficacy of maurocalcine in skeletal muscle cells, *J Biol Chem 278*, 37822-37831.
274. Lukacs, B., Sztretye, M., Almassy, J., Sarkozi, S., Dienes, B., Mabrouk, K., Simut, C., Szabo, L., Szentesi, P., De Waard, M., Ronjat, M., Jona, I., and Csernoch, L. (2008) Charged surface area of maurocalcine determines its interaction with the skeletal ryanodine receptor, *Biophys J 95*, 3497-3509.
275. Chen, L., Esteve, E., Sabatier, J. M., Ronjat, M., De Waard, M., Allen, P. D., and Pessah, I. N. (2003) Maurocalcine and peptide A stabilize distinct subconductance states of ryanodine receptor type 1, revealing a proportional gating mechanism, *J Biol Chem 278*, 16095-16106.
276. Altafaj, X., France, J., Almassy, J., Jona, I., Rossi, D., Sorrentino, V., Mabrouk, K., De Waard, M., and Ronjat, M. (2007) Maurocalcine interacts with the cardiac ryanodine receptor without inducing channel modification, *Biochem J 406*, 309-315.
277. Esteve, E., Mabrouk, K., Dupuis, A., Smida-Rezgui, S., Altafaj, X., Grunwald, D., Platel, J. C., Andreotti, N., Marty, I., Sabatier, J. M., Ronjat, M., and De Waard, M. (2005) Transduction of the scorpion toxin maurocalcine into cells. Evidence that the toxin crosses the plasma membrane, *J Biol Chem 280*, 12833-12839.
278. Ram, N., Aroui, S., Jaumain, E., Bichraoui, H., Mabrouk, K., Ronjat, M., Lortat-Jacob, H., and De Waard, M. (2008) Direct peptide interaction with surface glycosaminoglycans contributes to the cell penetration of maurocalcine, *J Biol Chem 283*, 24274-24284.
279. Boisseau, S., Mabrouk, K., Ram, N., Garmy, N., Collin, V., Tadmouri, A., Mikati, M., Sabatier, J. M., Ronjat, M., Fantini, J., and De Waard, M. (2006) Cell penetration properties of maurocalcine, a natural venom peptide active on the intracellular ryanodine receptor, *Biochim Biophys Acta 1758*, 308-319.
280. Altafaj, X., Cheng, W., Esteve, E., Urbani, J., Grunwald, D., Sabatier, J. M., Coronado, R., De Waard, M., and Ronjat, M. (2005) Maurocalcine and domain A of the II-III loop of the dihydropyridine receptor Cav 1.1 subunit share common binding sites on the skeletal ryanodine receptor, *J Biol Chem 280*, 4013-4016.
281. Poillot, C., Bichraoui, H., Tisseyre, C., Bahemberae, E., Andreotti, N., Sabatier, J. M., Ronjat, M., and De Waard, M. (2012) Small efficient cell-penetrating peptides derived from scorpion toxin maurocalcine, *J Biol Chem 287*, 17331-17342.
282. Stasiuk, G. J., Tamang, S., Imbert, D., Poillot, C., Giardiello, M., Tisseyre, C., Barbier, E. L., Fries, P. H., de Waard, M., Reiss, P., and Mazzanti, M. (2011) Cell-permeable Ln(III) chelate-functionalized InP quantum dots as multimodal imaging agents, *ACS Nano 5*, 8193-8201.

283. Futaki, S., Nakase, I., Tadokoro, A., Takeuchi, T., and Jones, A. T. (2007) Arginine-rich peptides and their internalization mechanisms, *Biochem Soc Trans 35*, 784-787.
284. Wike-Hooley, J. L., Haveman, J., and Reinhold, H. S. (1984) The relevance of tumour pH to the treatment of malignant disease, *Radiother Oncol 2*, 343-366.
285. Garcia-Martin, M. L., Herigault, G., Remy, C., Farion, R., Ballesteros, P., Coles, J. A., Cerdan, S., and Ziegler, A. (2001) Mapping extracellular pH in rat brain gliomas in vivo by 1H magnetic resonance spectroscopic imaging: comparison with maps of metabolites, *Cancer Res 61*, 6524-6531.
286. Etter, E. F., Kuhn, M. A., and Fay, F. S. (1994) Detection of changes in near-membrane Ca2+ concentration using a novel membrane-associated Ca2+ indicator, *J Biol Chem 269*, 10141-10149.
287. Fernandez-Arguelles, M. T., Yakovlev, A., Sperling, R. A., Luccardini, C., Gaillard, S., Medel, A. S., Mallet, J. M., Brochon, J. C., Feltz, A., Oheim, M., and Parak, W. J. (2007) Synthesis and characterization of polymer-coated quantum dots with integrated acceptor dyes as FRET-based nanoprobes, *Nano Lett 7*, 2613-2617.
288. Gaillard, S., Yakovlev, A., Luccardini, C., Oheim, M., Feltz, A., and Mallet, J. M. (2007) Synthesis and characterization of a new red-emitting Ca2+ indicator, calcium ruby, *Org Lett 9*, 2629-2632.
289. Yakovlev, A. V., Zhang, F., Zulqurnain, A., Azhar-Zahoor, A., Luccardini, C., Gaillard, S., Mallet, J. M., Tauc, P., Brochon, J. C., Parak, W. J., Feltz, A., and Oheim, M. (2009) Wrapping nanocrystals with an amphiphilic polymer preloaded with fixed amounts of fluorophore generates FRET-based nanoprobes with a controlled donor/acceptor ratio, *Langmuir 25*, 3232-3239.
290. Bruchez, M., Jr., Moronne, M., Gin, P., Weiss, S., and Alivisatos, A. P. (1998) Semiconductor nanocrystals as fluorescent biological labels, *Science 281*, 2013-2016.
291. Shah, C. P., Rath, M., Kumar, M., and Bajaj, P. N. (2010) Precursor concentration and temperature controlled formation of polyvinyl alcohol-capped CdSe-quantum dots, *Beilstein J Nanotechnol 1*, 119-127.
292. Lacoste, T. D., Michalet, X., Pinaud, F., Chemla, D. S., Alivisatos, A. P., and Weiss, S. (2000) Ultrahigh-resolution multicolor colocalization of single fluorescent probes, *Proc Natl Acad Sci U S A 97*, 9461-9466.
293. Zhang, Q., Li, Y., and Tsien, R. W. (2009) The dynamic control of kiss-and-run and vesicular reuse probed with single nanoparticles, *Science 323*, 1448-1453.
294. Ishihama, Y., and Funatsu, T. (2009) Single molecule tracking of quantum dot-labeled mRNAs in a cell nucleus, *Biochem Biophys Res Commun 381*, 33-38.
295. Liu, L. W., Hu, S. Y., Pan, Y., Zhang, J. Q., Feng, Y. S., and Zhang, X. H. (2014) Optimizing the synthesis of CdS/ZnS core/shell semiconductor nanocrystals for bioimaging applications, *Beilstein J Nanotechnol 5*, 919-926.
296. Collot, M., Loukou, C., Yakovlev, A. V., Wilms, C. D., Li, D., Evrard, A., Zamaleeva, A., Bourdieu, L., Leger, J. F., Ropert, N., Eilers, J., Oheim, M., Feltz, A., and Mallet, J. M. (2012) Calcium rubies: a family of red-emitting functionalizable indicators suitable for two-photon Ca2+ imaging, *J Am Chem Soc 134*, 14923-14931.
297. El-Andaloussi, S., Jarver, P., Johansson, H. J., and Langel, U. (2007) Cargo-dependent cytotoxicity and delivery efficacy of cell-penetrating peptides: a comparative study, *Biochem J 407*, 285-292.
298. Tisseyre, C., Ahmadi, M., Bacot, S., Dardevet, L., Perret, P., Ronjat, M., Fagret, D., Usson, Y., Ghezzi, C., and De Waard, M. (2014
) Quantitative evaluation of the cell penetrating properties of an iodinated Tyr-L-maurocalcine analog, *Biochim Biophys Acta 1843*, 2356-2364.

299. Aroui, S., Dardevet, L., Ajmia, W. B., de Boisvilliers, M., Perrin, F., Laajimi, A., Boumendjel, A., Kenani, A., Muller, J. M., and De Waard, M. (2015) A Novel Platinum-Maurocalcine Conjugate Induces Apoptosis of Human Glioblastoma Cells by Acting through the ROS-ERK/AKT-p53 Pathway, *Mol Pharm 12*, 4336-4348.
300. Xu, G., Yong, K. T., Roy, I., Mahajan, S. D., Ding, H., Schwartz, S. A., and Prasad, P. N. (2008) Bioconjugated quantum rods as targeted probes for efficient transmigration across an in vitro blood-brain barrier, *Bioconjug Chem 19*, 1179-1185.